Radiation Doses and Risks from Paediatric Computed Tomography

Zoe Brady
B.Sc. (Hons)

A thesis submitted for the degree of
Doctor of Philosophy

School of Applied Sciences
College of Science, Engineering and Health
RMIT University

February 2012

Declaration

I certify that except where due acknowledgement has been made, the work is that of the author alone; the work has not been submitted previously, in whole or in part, to qualify for any other academic award; the content of the thesis is the result of work which has been carried out since the official commencement date of the approved research program; any editorial work, paid or unpaid, carried out by a third party is acknowledged; and, ethics procedures and guidelines have been followed.

Zoe Brady
February 2012

Supervisors

Prof. Peter N. Johnston
Branch Director, Medical Radiation Services
Australian Radiation Protection and Nuclear Safety Agency (ARPANSA)
Commonwealth Government of Australia
Adjunct Professor, RMIT University
Melbourne, Australia

Dr. Timothy M. Cain
Director, Medical Imaging
Royal Children's Hospital (RCH) Melbourne
Melbourne, Australia

Acknowledgements

Thank you to my supervisors Prof Peter Johnston and Dr Tim Cain who have provided insightful guidance. Luke Wilkinson at St Vincent's Hospital and Matthew Haynes at the William Buckland Radiotherapy Centre (WBRC) in Melbourne have provided invaluable advice, both intellectually and personally. I would also like to thank a number of people who have been very helpful with providing resources, support and assistance. These include Anthony Wallace at ARPANSA; John Mathews, Anna Forsythe and Jo Chesson at the University of Melbourne; Greta Toncheva at Duke Medical Centre in the US; Paul Shrimpton and Jan Jansen at the UK Health Protection Agency; Choonsik Lee at the US National Cancer Institute; Corynne Smythe and Mark Fitzgerald at the Australian Department of Health and Ageing; Rick Franich at RMIT; the physics/engineering staff at the Peter MacCallum Cancer Centre in East Melbourne: Tomas Kron, Jim Cramb and Jim Hagekyriakou; the physics/engineering staff at WBRC: Craig Lancaster, Neil Brouwer and Trevor Ackerly; and my employers, Australian Radiation Services Pty Ltd and Alfred Health. A special thank you to all of the staff, including Fiona Ramanauskas and Mita Pedersen, in the Medical Imaging Department at the Royal Children's Hospital Melbourne. Finally, thank you to Cam, Annie, Scott, Dave, Jack, Emily and Evie and my other family and friends who have supported me throughout and experienced this rewarding, yet challenging, journey with me.

Contents

List of Figures

List of Tables

List of Abbreviations

2D	Two dimensional
AEC	Automatic Exposure Control
ALARA	As low as reasonably achievable
AP	Anterior-posterior
ARL	Australian Radiation Laboratory (now ARPANSA)
ARPANSA	Australian Radiation Protection and Nuclear Safety Agency (formerly ARL)
BEIR	Biological Effects of Ionising Radiation
CIRS	Computerized Imaging Reference Systems
CT	Computed Tomography
CTDI	Computed Tomography Dose Index
$CTDI_{vol}$	Volumetric Computed Tomography Dose Index
$CTDI_{w}$	Weighted Computed Tomography Dose Index
CT-Expo	Monte Carlo CT dosimetry calculator (Stamm and Nagel, 2011b)
DDREF	Dose and Dose Rate Effectiveness Factor
DLP	Dose Length Product
DRL	Diagnostic Reference Level
EAR	Excess Absolute Risk
ERR	Excess Relative Risk
FWHM	Full Width Half Maximum
GSF	German National Research Centre for Environment and Health
Gy	Gray
HPA	United Kingdom Health Protection Agency (formerly NRPB)
HVL	Half Value Layer
HREC	Human Research Ethics Committee
IAEA	International Atomic Energy Agency
ICRP	International Commission on Radiological Protection
ICRP 26	ICRP Publication 26: 1977 Recommendations (ICRP, 1977)
ICRP 60	ICRP Publication 60: 1990 Recommendations (ICRP, 1991)
ICRP 103	ICRP Publication 103: 2007 Recommendations (ICRP, 2007b)

ICRU	International Commission on Radiation Units and Measurements
ImPACT	Monte Carlo CT dosimetry calculator (ImPACT, 2011)
kV	kilovoltage
kV$_p$	peak kilovoltage
LAR	Lifetime Attributable Risk
LDRL	Local Diagnostic Reference Level
LET	Linear Energy Transfer
LiF	Lithium fluoride
LiF:Mg,Cu,P	Lithium fluoride doped with magnesium, copper and phosphorous (TLD-100H)
LiF:Mg,Ti	Lithium fluoride doped with magnesium and titanium (TLD-100)
LNT	Linear No Threshold
mAs	Current (mA) multiplied by time (seconds)
LSS	Life Span Study
MDCT	Multiple row Detector CT
MOSFET	Metal oxide semiconductor field effect transistor
MRI	Magnetic Resonance Imaging
MSAD	Multiple Slice Average Dose
NRPB	United Kingdom National Radiological Protection Board (now HPA)
ORNL	Oak Ridge National Laboratory
PA	Posterior-anterior
PCXMC	Monte Carlo radiography dosimetry calculator (STUK, 2008)
QUDI	Quality Use of Diagnostic Imaging
RANZCR	Royal Australian and New Zealand College of Radiologists
RBM	Red Bone Marrow
RCH	Royal Children's Hospital Melbourne
RR	Relative Risk
SNR	Signal to Noise Ratio
SPR	Society for Pediatric Radiology
Sv	Sievert
TLD	Thermoluminescence Dosimetry/Dosemeters
TLD-100	LiF:Mg,Cu,P
TLD-100H	LiF:Mg,Ti
UF	University of Florida
UK	United Kingdom
UNSCEAR	United Nations Scientific Committee on the Effects of Atomic Radiation
US	United States

Summary

The use of computed tomography (CT) worldwide has increased dramatically since its introduction. In Australia, more than two million CT services are billed to the government health care system every year and the rate of imaging is increasing beyond population growth. CT imaging currently accounts for the largest source of ionising radiation exposure to the population from all diagnostic procedures. There is a small, theoretical risk of carcinogenesis attributable to low doses of ionising radiation based on epidemiological evidence at higher doses and dose rates. The doses from CT examinations fall into this low dose range. Recognition of the potential radiation risks combined with the high utilisation of CT imaging has led to greater awareness of population health risks. Furthermore, the exposure risks from radiation are higher for children than for adults due to their increased radiosensitivity and greater prospective life expectancy. There is only limited information on Australian paediatric CT imaging rates, doses and risks. This thesis aims to assess the medical radiation exposure of children in Australia from CT examinations.

For the past 10 years, there has been an international focus on the risks to children from CT scanning. Despite this, it is acknowledged that radiation doses and risks in CT still need to be addressed. Since radiation induced cancer risk is specific to the organ or tissue irradiated, there is a particular need for CT organ dosimetry. In this thesis, a method has been developed using thermoluminescence dosemeters (TLDs) placed in a physical anthropomorphic phantom to measure organ and tissue absorbed doses. This method takes into account the energy dependency of photon interaction processes, electronic disequilibrium in small bone cavities and bone marrow and trabecular bone distributions which vary with age. In addition, a TLD material (LiF:Mg,Cu,P) which is new to diagnostic radiology applications has been used for the absorbed dose measurements. This material is more sensitive to low radiation doses and has a relatively linear energy and dose response allowing calibration at megavoltage energies on a linear accelerator. This ensured uniformity and reproducibility of output for the calibration exposures, which are limitations of using conventional TLD materials at diagnostic energies.

The TLD dosimetry method was used to quantify organ absorbed doses for typical paediatric CT examinations of the brain, chest and abdomen/pelvis for clinical protocols in use at the Royal Children's Hospital (RCH) Melbourne, Australia. The measurements

were undertaken using a physical anthropomorphic phantom representative of a 10 year old child. The mean absorbed dose to an organ is the appropriate quantity for assessing the detrimental stochastic effects of radiation exposure. However, for radiation protection purposes, effective dose is a more useful quantity allowing comparison of different partial body exposure situations to assess risk in more general terms and facilitate optimisation. Therefore, effective dose has been estimated from the measured organ absorbed doses for the typical paediatric CT examinations and the impact of the newly introduced tissue weighting factors by the International Commission on Radiological Protection has been evaluated.

The ability to reliably estimate organ absorbed doses and effective dose in the clinical environment is necessary to ensure that the principles of radiation protection are being employed. Therefore, the experimentally measured organ absorbed doses and the derived effective doses were compared with doses calculated using several different computational methods in order to identify a feasible clinical tool for paediatric CT dosimetry. The methods investigated included standard CT dose calculators which make use of pre-existing Monte Carlo data sets of organ dose conversion coefficients. A novel application of a Monte Carlo simulation tool designed for radiography exposure situations was also utilised to simulate the CT exposure situation. Further emerging scanner-independent methodologies based on normalised organ doses as a function of patient size were also assessed. Finally, simpler conversion methods for estimating effective dose were compared. A variety of anthropomorphic phantoms including physical, mathematical (stylised), voxel and hybrid models were used in the range of CT dosimetry methods assessed.

A retrospective audit of patient CT dose records at the RCH was also undertaken. This allowed the derivation of local diagnostic reference levels (DRLs), which is considered an essential process for dose optimisation. Furthermore, the patient data was used to verify the measurements made with the physical anthropomorphic phantom. A method for assessing and benchmarking the sampled dose data was developed and this will be of use to other practices undertaking dose surveys, which is now a regulatory requirement in most Australian jurisdictions. The benchmarking process also recognised protocols for which significant dose reductions at the RCH have already been achieved.

The first comprehensive analysis of paediatric CT imaging frequency and trends in Australia was undertaken. This involved assessing the amount of paediatric CT imaging that is funded by the government health care system and determining a process to reflect current Australian usage. These results provide an important foundation for paediatric CT research in Australia.

Finally, using the measured organ absorbed doses and Australian CT imaging frequency, cancer risk projections for CT examinations on Australian children have been made. It was found that the risk to an individual patient is small when compared with the overall natural cancer rate. A CT examination for an individual child is justified if there is

reasonable likelihood that it will produce a health benefit or inform patient management. The population is advantaged when the summed positive health benefits from those whose management is positively influenced by the imaging are greater than the summed detrimental effects. The net positive health effects of the CT examination will be greater when appropriate imaging is performed and is optimised for both image quality and dose. However, in a society where the threshold for conducting a CT examination is becoming ever lower, it is important that we remain attentive to the overall population health detriment from medical imaging radiation exposure.

This thesis provides an experimental method for paediatric CT organ dosimetry and a comprehensive evaluation of paediatric CT doses and imaging trends in Australia. Typical doses for paediatric CT examinations have been quantified using various methods, both experimental (direct) and computational (indirect). Local DRLs have been established based on the dose distributions from patient data and will provide a useful benchmark for future local and national dose surveys. Finally, cancer risk projections for incidence and mortality from paediatric CT scanning have been made for the Australian population.

Chapter 1

Introduction

1.1 Background

X-ray diagnostic imaging is one of the most useful and valuable medical tools available today. It allows us to non-invasively "peer" inside the human body to study anatomy and physiology, and to diagnose and investigate disease. Advances in technology have led to improved image quality and the ability to gain added diagnostic information that affects patient management. However, there is potential for the increased risk of radiation induced cancer to offset these benefits. This risk arises not only from higher dose techniques, but also from the increased uptake of imaging. As with all fields of medicine, diagnostic imaging involves an element of risk that must be balanced by the benefit that it provides.

Many studies have investigated the correlation between radiation exposure and cancer risk. Epidemiological studies, such as the Life Span Study of the atomic bomb survivors, medical studies and experimental animal research have established a relationship between exposure and cancer induction and cellular damage. However, there is a lack of consensus on the effects of radiation at low doses and low dose rates, with the linear no threshold hypothesis being widely accepted and the basis of the international system of radiation protection (ICRP, 2007b). Medical radiation exposure for diagnostic purposes usually falls into this low dose category, where the radiation risks are yet to be observed and modelled by epidemiological studies.

Amongst diagnostic imaging modalities, computed tomography (CT) has been shown to account for the highest contribution to population dose (NCRP, 2009). Despite the uncertainties inherent in risk assessments for low dose exposures, some researchers (Brenner et al., 2001a; Brenner and Hall, 2007) have contended that when considering population health, the lifetime cancer risk attributable to CT examinations is not negligible. Furthermore, this risk is higher in children who are more radiosensitive than adults and have

a longer remaining lifetime for cancer to become evident. Since 2001 and the publication of a series of articles (Brenner et al., 2001a; Donnelly et al., 2001; Paterson et al., 2001) about the risks of radiation induced cancer in children from diagnostic CT scans, there has been a strong international focus on paediatric CT dose.

It is remarkable that CT has been used in medicine for almost 40 years, yet only recently has the radiation exposure from CT become more widely recognised as a public health issue. Worldwide, there is a large volume of published material on CT and radiation attributable risk, although there is a lack of specific information for the Australian population that combines these aspects, particularly for children. Furthermore, in practice, it has been observed that there is limited understanding of the magnitude of doses and associated risks. Therefore, there is a strong research interest in this area from the medical, public and government sectors in Australia.

1.2 Thesis Scope and Objectives

The objective of this thesis is to assess the medical radiation exposure of children in Australia from CT examinations. The risk of radiation induced cancer is anatomy-specific and therefore determined from organ and tissue absorbed doses. Currently, the most accurate and reliable methods of determining these doses are by measurement or Monte Carlo radiation transport simulation. This thesis evaluates both experimental and computational dosimetry methods for paediatric CT. An important emphasis was on assessing clinical practice rather than theoretical exposure conditions. This is becoming increasingly important with modern CT technology, which utilises features such as tube current modulation rather than fixed exposures. This results in organs being exposed to different X-ray beam output depending on the attenuation characteristics in each body region, hence making the examination patient-specific.

There are very few publications describing organ absorbed dose measurements in the context of paediatric CT using clinical protocols (Fujii et al., 2007, 2009; Hollingsworth et al., 2007; McDermott et al., 2009; Nishizawa et al., 2008). In this thesis, an experimental method using thermoluminescence dosemeters (TLDs) was implemented to measure organ absorbed doses for standard paediatric clinical protocols using a physical anthropomorphic phantom representing a 10 year old child. High sensitivity TLD chips (LiF:Mg,Cu,P) were used for the dose measurements. There are limited applications using these TLDs for measuring doses encountered in the diagnostic energy range (Brisse et al., 2009b; Duggan et al., 2003). However, this type of TLD material exhibits a relatively linear energy and dose response compared with conventional TLD material (LiF:Mg,Ti). This allowed calibration to be undertaken on a linear accelerator at a megavoltage energy overcoming limitations of output reproducibility and uniformity associated with traditional calibration on CT scanners or beam quality matched diagnostic X-ray units. This was considered a significant advantage in using the high sensitivity TLD material and ensured greater

precision for measuring the relatively low doses common to paediatric CT. Using this type of TLD material necessitated the development of a calibration technique at megavoltage energy, which was validated against a calibration performed at kilovoltage energy on a superficial X-ray therapy unit.

This thesis is not limited to a basic measurement of organ absorbed dose, but rather develops a detailed formalism for calculating organ and tissue absorbed doses for children from TLD measurements. This takes into account the energy dependence of photon interactions in different tissues in the energy range typical of CT spectra and the lack of secondary electron equilibrium in the small cavities containing bone marrow. Furthermore, the distribution of active marrow, inactive marrow and trabecular bone varies with age and this has been considered in the organ and tissue absorbed dose calculations. Due to the complexity of determining the absorbed dose to the bone marrow and bone surface, these types of considerations are generally only taken into account for Monte Carlo simulations (Lee et al., 2006b).

Measurement of organ absorbed dose is impractical in the diagnostic radiology clinical environment as it is time and resource intensive. Therefore, several computational dosimetry methods were also evaluated in this thesis. While there are some assessments between experimental and computational methods in the literature for CT examinations (Brix et al., 2004; Geleijns et al., 1994; Groves et al., 2004; Lechel et al., 2009), these are for adults and do not include inter-comparison of the breadth of methods considered in this thesis. The different methods were compared using parameters and conditions that best matched the "real-life" scenario to assess their reliability for clinical implementation. It is often challenging to use these tools for dose estimates when the clinical conditions are difficult to simulate.

Epidemiological studies are necessary to model the relationship between radiation exposure and risk, but these are impeded by the large cohort sizes needed to observe effects at low radiation doses. However, risk projection models are useful for providing more timely theoretical estimates of radiation detriment to the population. In order to project the population cancer risks in this thesis, the Australian paediatric CT imaging trends and the number of examinations undertaken nationally needed to be quantified. This information is difficult to collate as there is no single repository of diagnostic imaging data in Australia. Previous studies have relied on the government health care system data (Wise and Thomson, 2004), which is limited in its completeness. A more thorough approach was used in this thesis involving multiple sources of paediatric imaging data over longer time scales. This permitted more realistic estimates of the number of CT examinations performed in Australia on children. This information is essential for any research and analysis being conducted in the area of paediatric CT. Furthermore, it considerably extends the current literature on trends and patterns of paediatric CT imaging, both nationally and internationally.

1.3 Thesis Structure

Chapter 2 provides an overview of medical radiation exposure. The current knowledge of risk associated with exposure to low radiation doses is explored and worldwide trends in CT imaging are considered. These issues are further discussed in relation to children and dose reduction techniques for paediatric CT are reviewed. More detailed background information on CT scanner design, operation, image quality and dosimetry is provided in Appendix A.

Chapter 3 outlines a TLD measurement method for paediatric CT dosimetry using a physical anthropomorphic phantom representing a 10 year old child. Organ and tissue absorbed doses are quantified for CT brain, chest and abdomen/pelvis examinations performed at the Royal Children's Hospital (RCH) Melbourne, Australia. Chapter 3 also provides estimates of effective dose for the three types of CT examinations assessed. The differences, predominantly due to changes in tissue weighting factors, between recent definitions of effective dose according to the Recommendations of the International Commission on Radiological Protection (ICRP, 1991, 2007b) are discussed. Appendix B provides further information on effective dose and Appendix C on TLDs.

While TLD organ dosimetry is currently the most widely accepted physical measurement method, it is unlikely to find regular application in the clinical environment as it is a laborious technique. Chapter 4 provides a comparison of a subset of the TLD measurements with dose measurements made using metal oxide semiconductor field effect transistors (MOSFETs). It is envisaged that MOSFETs may become a viable alternative to TLDs for organ dosimetry in the future and may be more readily implemented in the clinical environment.

Several computational methods for calculating organ absorbed dose and effective dose for paediatric CT are assessed in Chapter 5. In total, 11 computational methods were investigated and compared with TLD measured doses. Evaluation of these methods also involved assessment of several anthropomorphic phantoms, including physical, mathematical (stylised), voxel and hybrid models. The computational methods investigated included standard CT dose calculators that make use of pre-existing Monte Carlo generated data sets of organ dose conversion coefficients; a novel application of a radiography Monte Carlo program; emerging methodologies based on normalised organ doses that were generally size-specific and in some cases scanner-independent; and simpler conversion methods for estimating effective dose.

Chapter 6 provides the results of a retrospective audit undertaken at RCH of paediatric patient CT records. An assessment method for analysing the local scan parameters to enable identification of areas for optimisation is also presented. In the audit, the parameters used for the CT protocols and the dose indicators were sampled, along with patient demographics. This allowed comparison with the dose indicators resulting from scanning

the physical phantom and the effective doses values derived from the TLD measurements. From the sampled data, local diagnostic reference levels (DRLs) were established based on the mean value of the patient dose distribution for each age group and type of CT examination. The local DRLs were compared with other Australian published data and international DRLs to facilitate benchmarking.

The paediatric CT imaging trends in Australia are explored in Chapter 7 based on Medicare and RCH data. This is the first comprehensive analysis of paediatric CT imaging trends in Australia. A limitation of the Medicare data is that it does not capture CT services that are not funded by the public health care system. Therefore, Chapter 7 describes a method for adjusting Medicare paediatric CT data to account for non-funded services.

The measured anatomy-specific doses combined with Australian paediatric CT imaging trends enabled cancer risk projections, which are detailed in Chapter 8. For the information from this thesis to be useful on a day-to-day basis it is essential to provide a context for the risk from a CT scan. Few people, particularly members of the public, understand what a specific radiation dose means. The results in this chapter allow members of the medical profession to better explain the risks associated with CT examinations of children for the doses actually received in an Australian hospital. Risk comparators in terms of other causes of death to the Australian population are also provided. Although projected cancer risk estimates are limited by the substantial uncertainties involved and caution should be exercised in their use and application, these risk projections for Australian children will be of significant value and interest.

1.4 Ethical Considerations

1.4.1 Assessment of CT Imaging Trends

Approval was granted by the RCH Human Research Ethics Committee (HREC) to conduct a clinical audit/quality assurance activity (reference no. CA29052, 5 May 2009) to assess the number of CT scans performed at the RCH. An exemption was granted by the RMIT Human Research Ethics Network of the College of Science Engineering & Health to utilise Medicare and RCH data to assess CT imaging trends in Australia. The exemption was provided on the basis that ethics approval to collect the data had been given by the appropriate ethics bodies (RCH HREC) and/or is publicly available (Medicare data), and the project involves analysis of coded and non-identifiable data (reference no. 41-09, 18 August 2009).

1.4.2 Patient Dose Survey

Approval was granted by the RCH HREC to conduct a clinical audit/quality assurance activity (reference no. CA30013, 5 February 2010) to derive local diagnostic reference levels based on an analysis of extracted information from a sample of patient CT examinations. The RMIT Human Research Ethics Network of the College of Science Engineering & Health endorsed and affirmed the decision made by the RCH HREC (reference no. 21-10, 15 April 2010).

1.5 List of All Publications Arising from this Thesis

1.5.1 Peer-Reviewed Publications

1. **Brady, Z.**, Cain, T. M. and Johnston, P. N., *Comparison of organ dosimetry methods and effective dose calculation methods for paediatric CT*, Australasian Physical & Engineering Sciences in Medicine, 2012 (*published online 11 April 2012*) (Brady et al., 2012b).

2. **Brady, Z.** and Einsiedel, P. *A Computed Tomography wish list, from a medical physicist's perspective*, Australasian Physical & Engineering Sciences in Medicine, 2012, 35:1-5 (*Invited Editorial*) (Brady and Einsiedel, 2012).

3. **Brady, Z.**, Cain, T. M. and Johnston, P. N., *Paediatric CT imaging trends in Australia*, Journal of Medical Imaging and Radiation Oncology, 2011, 55:132-142 (Brady et al., 2011d).

4. **Brady, Z.**, Cain, T. M. and Johnston, P. N., *Differences in using the International Commission on Radiological Protection's Publications 60 and 103 for determining effective dose in paediatric CT examinations*, Radiation Measurements, 2011, 55:132-142 (Brady et al., 2011e).

5. **Brady, Z.**, Cain, T. M. and Johnston, P. N., *Justifying referrals for paediatric CT*, Medical Journal of Australia, 2012 *(accepted)* (Brady et al., 2012a).

6. **Brady, Z.**, Ramanauskas, F., Cain, T. M. and Johnston, P. N., *Assessment of paediatric CT dose indicators for the purpose of optimisation*, British Journal of Radiology, 2012 *(accepted)* (Brady et al., 2012c).

1.5.2 Conference Presentations

* = Invited Presentation

1. ***Brady, Z.**, *Doses and risks in paediatric imaging in Australia*, presented at the Siemens Low Dose Academy, 2012, Sydney, Australia (Brady, 2012a).

2. *__Brady, Z.__, *DLP practical breakdown - how best to adjust parameters to reduce dose*, presented at the Siemens Low Dose Academy, 2012, Sydney, Australia (Brady, 2012b).

3. __Brady, Z.__, Cain, T. M. and Johnston, P. N., *Effective dose calculation in CT using high sensitivity TLDs (EPSM ABEC 2010 Conference Proceedings)*, Australasian Physical & Engineering Sciences in Medicine, 2011, 34(1):111 (Brady et al., 2011b).

4. __Brady, Z.__, Cain, T. M. and Johnston, P. N., *Calculations of effective dose for paediatric CT examinations* presented at the 16th International Conference on Solid State Dosimetry, 2010, Sydney, Australia (Brady et al., 2010b).

5. __Brady, Z.__, Cain, T. M. and Johnston, P. N., *Assessing CT protocols in a paediatric hospital using a patient dose survey (EPSM ABEC 2011 Conference Proceedings)*, Australasian Physical & Engineering Sciences in Medicine, 2011, 34(4):590 (Brady et al., 2011c).

6. __Brady, Z.__, Cain, T. M. and Johnston, P. N., *Paediatric CT in Australia - trends and risk (EPSM ABEC 2010 Conference Proceedings)*, Australasian Physical & Engineering Sciences in Medicine, 2011, 34(1):110 (Brady et al., 2011a).

7. *__Brady, Z.__, *Radiation - a risky business?* presented at the Medical Imaging Nurses Association Victorian State Conference, 2010, Melbourne, Australia (Brady, 2010).

8. *__Brady, Z.__, Ackland, H.M. and Varma, D.K. *Too much radiation in trauma?* presented at the SWAN XVIII Trauma Conference, 2010, Sydney, Australia (Brady et al., 2010a).

9. *__Brady, Z.__, Cain, T. M. and Johnston, P. N., *Computed tomography - are we imaging more or less?* presented at the RANZCR/AIR/FRO/ACPSEM Combined Scientific Meeting, 2009, Brisbane, Australia (Brady et al., 2009).

Chapter 2

Medical Radiation Exposure

2.1 Introduction

Ionising radiation is indispensable to modern medicine for diagnosis and treatment. In countries with advanced health care systems, there is now more than one diagnostic examination performed per person across the population every year (UNSCEAR, 2010a). Medical practices involving ionising radiation include diagnostic examinations, interventional procedures and radiotherapy treatments typically undertaken in radiology, nuclear medicine and radiation oncology departments or clinics. Globally, approximately 3.6 billion diagnostic examinations and six million therapeutic treatments are performed annually (UNSCEAR, 2010a).

Primarily the people exposed to ionising radiation for medical purposes are the patients themselves. These exposure situations are deliberate and voluntary with some diagnostic or therapeutic health benefit to be gained (ICRP, 2007b,c). However, excluding therapeutic exposure, the intention is not to deliver a radiation dose, although this is an inevitable outcome. Recent figures show that diagnostic medical exposures, including radiology and nuclear medicine, account for about one-fifth of the average annual per caput dose to the global population from all sources (UNSCEAR, 2010a). Amongst diagnostic modalities, CT is the highest contributor to population dose, although it accounts for a much smaller proportion of the total number of examinations (NCRP, 2009).

There is irrefutable evidence from epidemiological studies that ionising radiation exposure at high doses is associated with an increase in cancer incidence and morbidity (ICRP, 2005). However, quantifying this risk in the low dose range, typical of CT doses, is complex and contentious. Despite the uncertainty surrounding low dose exposure, the societal risk may not necessarily be negligible and must still be considered (Brenner and Hricak, 2010; Brenner et al., 2003). This risk is even higher for children who are more radiosensitive than adults. Due to the sample size required to have the necessary statistical power to

establish a low dose response, it is unlikely that risks at these very low levels will ever be precisely known (Brenner et al., 2003; ICRP, 2005).

The following discussion reviews the current stance of major groups regarding risk from radiation exposure at the low doses encountered in medical imaging. The largest diagnostic imaging contributor to population dose, CT, is then considered in more detail, including global examination frequency and dose. This leads to a more focused discussion of the radiation risks associated with paediatric CT and a summary of current attitudes towards this topic. Finally, a literature review of dose reduction techniques for paediatric CT is provided.

2.2 Radiation and Risk

Epidemiological studies provide a major source of information for quantifying the risk of radiation induced cancer. It is often acknowledged that these types of studies in the low dose range below 100 millisieverts (mSv) are inherently difficult to collate due to the need to obtain sufficient sample sizes and include extensive follow-up to account for radiation induced cancer latency (Brenner et al., 2003; ICRP, 2005, 2007a,b). It is extremely difficult to observe the weak carcinogenic effects of radiation above the high natural cancer incidence with any statistical significance, and consequently the risks at very low levels of exposure may never be precisely known (Brenner et al., 2003; ICRP, 2005). Another source of data for estimating the risk of cancer induction is provided by situations in which high radiation exposures have occurred, such as medical treatments for radiotherapy patients (UNSCEAR, 2000). Furthermore, radiobiological data based on animal studies, as well as medical, occupational, and environmental data on cancer incidence, also inform radiation induced cancer risk determination (ICRP, 2007b). However, observational epidemiological studies largely remain the basis for radiation risk modelling (ICRP, 2007b; NRC, 2006; UNSCEAR, 2000).

The most important epidemiological study is the Life Span Study (LSS) of the atomic bomb survivors because of the large exposed cohort, including men, women and children, and the extensive long-term follow-up that has been undertaken (Preston et al., 2003). Furthermore, the doses for the exposed individuals are reasonably well characterised by individual dose estimates for 85% of the exposed cohort (Brenner et al., 2003; Preston et al., 2003). The study group includes 86,572 people with specific dose estimates, almost 40% of whom received an estimated dose of between 5 to 100 mSv (Preston et al., 2003). The lifetime follow-up of the group is almost complete, with the remaining cohort comprising mainly those survivors who were younger than 20 years of age at exposure (NRC, 2006).

The most recent results from the LSS appear to confirm a linear response of excess solid tumours with dose (Preston et al., 2003). In the lower dose region (<100 mSv) there is

no statistical difference between a linear or linear-quadratic fit for solid cancer incidence relative to the uncertainties in the risk estimation (Figure 2.1). Since the linear-quadratic model offers no significant improvement over the linear model, the latter is adopted (NRC, 2006). The latency period (time from exposure to cancer induction) for leukaemia is less than that for solid tumours, and earlier LSS results show that most excess deaths from leukaemia occurred in the first 15 years post exposure (Pierce et al., 1996). Leukaemia exhibits a linear-quadratic dose response (see inset of Figure 2.1), while for much higher doses (>3 Sv) responses for both leukaemia and solid tumours flatten out, most likely due to cell death (Heggie et al., 1997).

Based predominantly, but not solely, on the analysis and review of LSS data, the United Nations Scientific Committee on the Effects of Atomic Radiation (UNSCEAR) and the US National Academy of Sciences (NAS)/National Research Council (NRC) Committee on the Biological Effects of Ionising Radiation (BEIR) demonstrate that a linear dose-response exists at low doses (NRC, 2006; UNSCEAR, 2000). The International Commission on Radiological Protection (ICRP) has a mandate to make recommendations for a system of radiological protection and provide guidance on managing the risks of radiation exposure. The latest ICRP recommendations based on all available evidence consider a linear no threshold (LNT) model to be the best practical approach for radiation protection purposes (ICRP, 2007b). The use of this dose response hypothesis infers that any increase in dose will lead to the same increase in the probability of incurring cancer or heritable effects attributable to radiation. Furthermore, the International Atomic Energy Agency (IAEA) also adopt the LNT model based on the recommendations of the ICRP and are responsible for publishing Safety Standards to establish basic requirements for protection against radiation risks (IAEA, 1996). However, there are other organisations such as the American Nuclear Society (ANS, June 2001) and the French Academy of Sciences and National Academy of Medicine (30 March 2005) that believe insufficient evidence exists to support this model.

There is some evidence of protective effects from low doses of radiation or a hormetic response, but these are yet to be confirmed through epidemiological studies (Sykes and Day, 2007). Furthermore, there is no observable increase in cancer incidence in areas of high background radiation such as Kerala, India (Nair et al., 2009). At present, the LNT model remains the most reasonable assumption regarding the dose response relationship at low levels despite the lack of epidemiological evidence (ICRP, 2007b). The LNT model is often described as conservative (Blecher, 2010; Mendelson et al., 2010), however other plausible extrapolations in the low dose region demonstrate that the linear model may overestimate some risks, but underestimate others (Brenner et al., 2003).

To account for the extrapolation from high doses and dose rates to low doses and dose rates, a Dose and Dose Rate Effectiveness Factor (DDREF) is used. The ICRP (2007b) recommend a factor of two in agreement with UNSCEAR (2000), while the BEIR VII

Report (NRC, 2006) uses a factor of 1.5 for solid tumours and one for leukaemia. However, the ICRP acknowledge that a factor of two corresponds with the data used to derive the BEIR VII factors and that the DDREF includes uncertainty and is not intended as a precise figure (ICRP, 2007b). Various DDREFs in the range from 2-10 have been proposed (Preston, 2008; Wall et al., 2006), which fall within the large uncertainty in the value (Hricak et al., 2011).

Another issue that arises in applying risk estimations from the LSS to other populations is the method of "transporting" the risk from the Japanese population. One method termed relative risk transport assumes excess risk is proportional to the baseline risks for that population (i.e. the additional risk from radiation exposure multiplies the population cancer rate by a specific amount (Berrington de Gonzalez and Darby, 2004)). Therefore, in this model excess relative risk (ERR) will be the same for the Japanese population as for any other population. An alternative model is one of absolute risk, where it is assumed that excess risk does not depend on baseline risk, but is added to the population rate. In this case, excess absolute risk (EAR) will be the same between populations. The BEIR VII Committee (NRC, 2006) use a weighted average of both ERR and EAR risk models to transport risk from the Japanese population to the US population. The weighting is site-specific. For example, for breast and thyroid cancer, the risk models use a combined cohort from the LSS and medically irradiated groups that include Caucasians. The risk models are combined to give a lifetime attributable risk (LAR) representing the probability that an individual will develop (incidence) and may die (mortality) from cancer associated with radiation exposure.

Based on these calculations, the BEIR VII Committee (NRC, 2006) finds that for the US population, rates for all radiation attributable cancer incidence are about twice the rates for mortality. This ratio varies significantly on a site-specific comparison. The highest LAR for radiation induced cancer mortality in males and females is for the lung, based on a population of mixed ages. For radiation induced cancer incidence, "other solid cancers" have the highest LAR for males, while the lung, breast, and other solid cancers all have relatively high LARs for females. For leukaemia, incidence LAR is approximately 30% higher than mortality LAR for both males and females due to radiation exposure.

The overall LAR for cancer incidence and mortality attributable to radiation exposure averaged over all ages is given in Table 2.1. Similar estimates (Wise, 2003) of lifetime risk for incidence and mortality of solid cancer due to radiation exposure were calculated for the Australian population based on LSS data to 1990 and Australian background cancer incidence and mortality rates. However, more recent analyses have not been published.

Radiation induced cancer incidence and mortality are dependent on sex and age at exposure. The BEIR VII Report (NRC, 2006) provides site-, age- and sex-dependent lifetime risk estimates that can be applied to different exposure situations. Figure 2.2 shows over-

Table 2.1: BEIR VII Committee's preferred estimates of lifetime attributable risk (10^{-2} Gy^{-1}) for solid cancer and leukaemia incidence and mortality due to radiation exposure (NRC, 2006).

Exposed Population[a]	**Solid Cancer**[b,c]		**Leukaemia**[b,d]	
	Incidence	**Mortality**	**Incidence**	**Mortality**
Males	8.00	4.10	1.00	0.69
Females	13.1	6.10	0.72	0.52

[a] Estimates apply for a population of mixed ages.
[b] LAR is calculated from the weighted average of the relative and absolute risk transport models.
[c] DDREF of 1.5 is applied.
[d] Estimates based on a linear-quadratic model.

all cancer incidence and mortality for males and females as a function of age at exposure. This model shows an increased risk of cancer incidence and mortality for persons younger than 30 years of age at exposure and for ages above 30 the difference is less distinct. Children are considerably more radiosensitive than adults because their cells are not yet mature and still developing and they have more years of remaining lifetime in which a radiation induced cancer may appear. For example, the lifetime risk of radiation induced fatal cancer resulting from radiation exposure of a girl aged 10 years is almost double the risk due to the same radiation exposure of a woman at 30 years of age. However, a recent study (Shuryak et al., 2010) suggests that the risks in middle age have potentially been underestimated and this may warrant consideration in the future.

The ICRP (2007b) recommends the use of nominal risk coefficients for stochastic effects after radiation exposure which are averaged over sex and age at exposure and based on cancer incidence data, mainly from the LSS. Similar to the method applied by the BEIR VII Committee (NRC, 2006), lifetime EAR and ERR are determined. In the case of the ICRP, these are averaged across the sexes and then weighted to transfer risks across populations. A DDREF of two is applied (except for leukaemia, which is again based on a linear-quadratic model) and these risk estimates are then applied across a composite population baseline cancer rate computed by the ICRP. A radiation detriment is then applied which takes into account lethality, loss of quality of life, and life impairment (number of years lost) and is a sum of the site-specific detriments. The ICRP detriment-adjusted nominal risk coefficients for all radiation induced cancers are given in Table 2.2. For the whole population, these are averaged over age and sex, while adult specific coefficients exclude children. The risk of heritable effects in the whole population associated with gonad exposure is included in the total risk coefficient. The overall fatal risk coefficient recommended for use by the ICRP is rounded to 5% per sievert (ICRP, 2007b).

Figure 2.1: Excess relative risk of solid cancer due to radiation exposure based on data from the Life Span Study. The inset shows the linear-quadratic fit for leukaemia (from the BEIR VII Report (NRC, 2006)).

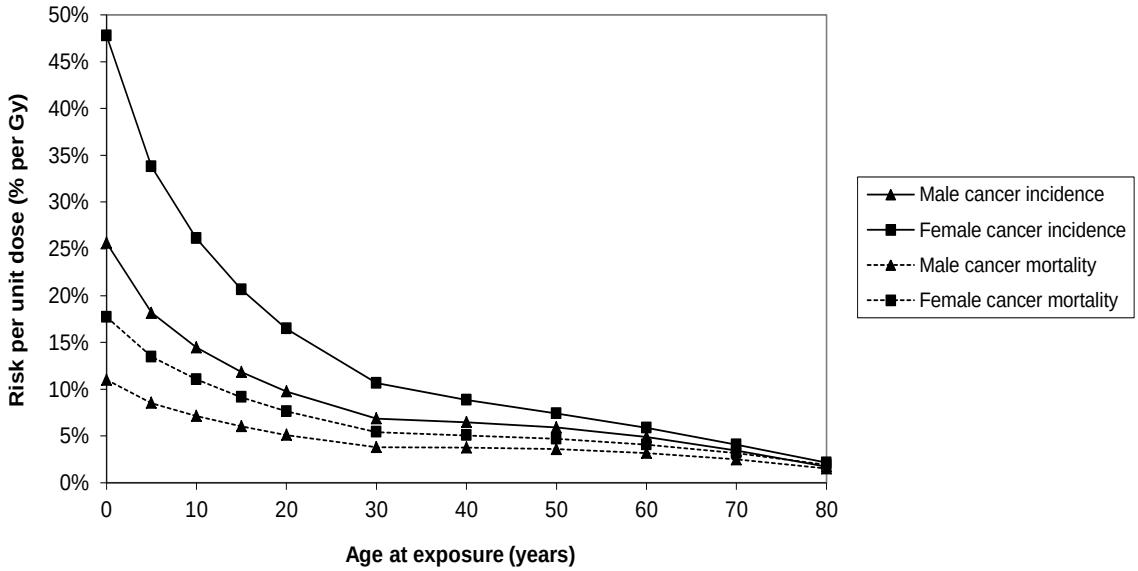

Figure 2.2: Overall cancer incidence and mortality due to radiation exposure for all solid cancers and leukaemia for males and for females (BEIR VII Report (NRC, 2006)).

Table 2.2: Detriment adjusted nominal risk coefficients (10^{-2} Sv^{-1}) for stochastic effects after exposure to radiation at a low dose rate (ICRP, 2007b).

Exposed Population[a]	Cancer	Heritable Effects	Total
Whole	5.5	0.2	5.7
Adult[b]	4.1	0.1	4.2

[a] Estimates are averaged over age and sex.
[b] The adult population excludes children, which are included in the whole population.

2.3 Radiation Exposure from CT

The cancer risk associated with radiation exposure due to medical diagnostic imaging has been receiving considerable attention in recent years (Berrington de Gonzalez et al., 2009; Brenner et al., 2001a; Brenner, 2002; Brenner and Hall, 2007; Einstein et al., 2007a; Fazel et al., 2009; Frush et al., 2003; Giles, 2004; Hall and Brenner, 2008; Hammer et al., 2011; Kleinerman, 2006; Smith-Bindman, 2010; Smith-Bindman et al., 2009; Wall et al., 2006). In particular, discussion has focused on CT as a relatively high dose modality, which is potentially over-utilised. Even deterministic effects, such as hair loss, have been reported in incidents in the US from apparent erroneous over-doses due to CT brain perfusion scans (FDA, 2009a,b, 2010a). These, and radiotherapy incidents covered in the general news media, have led to US Congressional hearings, FDA initiatives regarding medical equipment regulations (FDA, 2010b) and new legislation for medical radiation safety (California Senate Bill No. 1237). However, this focus on CT exposure has only been relatively recent, considering that CT has been in use for almost 40 years.

The first clinical CT images were published in 1973 by Godfrey Hounsfield and James Ambrose (Ambrose, 1973a,b; Ambrose and Hounsfield, 1973; Ambrose, 1973c; Hounsfield, 1973). However, the theoretical basis for this type of imaging dates back to 1917 and the research of mathematician Johann Radon (Carlton and Adler, 1996). Allan Cormack published work in the mid-sixties on the theoretical basis of CT and Hounsfield, while working for EMI Ltd (Hayes, Middlesex, UK), was the first to build a CT scanner in 1971 and realise its clinical applications. The Nobel Prize for Medicine was jointly awarded to Cormack and Hounsfield in 1979.

CT uses the attenuation of X-rays by the patient's body to produce a tomographic cross-sectional image (or slice) of the body, which can be reformatted into three dimensional reconstructions on some modern scanners. CT differs from conventional radiography whereby the full three dimensional structure of the body is collapsed into a two dimensional projection. A major disadvantage of radiography is the lack of spatial resolution in the direction of the X-ray beam, which can be referred to as "depth scrambling" (Webb, 1988). Conversely, a CT image is formed by scanning a volume of tissue from all direc-

tions, giving multiple projections through the object, and reconstructing an image of the object from these projections. The resultant image appears as though a slice has been physically removed from the body and overlying structures can be differentiated. Different scanners operate on various geometries and utilise a range of technology, which have evolved considerably over time. Appendix A provides background to the development of CT scanner design and technology.

When first introduced CT had limited application and could only be used for brain scans, where the patient's head was immobilised by a water bag that accommodated the large changes in flux adjacent to the head (Bushberg et al., 2001). Despite the increased applications available with advanced CT scanners, it was predicted that magnetic resonance imaging (MRI) would eventually reduce the CT workload (Kalra et al., 2004a; Rehani and Berry, 2000; Vock, 2005). However, with the introduction of multiple row detector CT (MDCT) scanners and sub-second rotation times, the ease and speed of CT scanning has ensured its viability. Furthermore, emerging CT technologies have also influenced the age profile of CT usage (UNSCEAR, 2010a) as it becomes possible to perform more paediatric imaging with newer, faster scanners. There is generally no longer the need to use a general anaesthetic to keep the child still for the duration of the scan and hence there is more likelihood for paediatric CT imaging to be used, where previously it may have been avoided due to the anaesthetic risks.

An early Australian survey found that there were 334 CT scanners nationally, approximately 18 per million people in the mid-nineties (Thomson and Tingey, 1997). By 2007, this number had increased by about 30% (UNSCEAR, 2010a). Similarly, worldwide surveys conducted by UNSCEAR have also shown increases in other countries (Table 2.3), with Japan having a considerably higher number of scanners relative to the population (UNSCEAR, 2000, 2010a).

Table 2.3: Increase in the number of CT scanners per million population by country (UNSCEAR, 2000, 2010a).

Country	**CT Scanners (per million population)**		**Percentage Increase**
	1991-1996	**1997-2007**	
Australia	18.8	24.5	30.3
Japan	63.7	92.6	45.4
New Zealand	8.2	12.0	46.3
UK	6.0	6.7	11.7
US	26.2	-	-

In the UNSCEAR 2000 report (UNSCEAR, 2000) CT constituted approximately 6% of all medical diagnostic procedures in countries with advanced health care systems (Level I) (Table 2.4). In the more recent report (UNSCEAR, 2010a) published in 2010 this had increased to 10%. The increase for other countries with less advanced health care is even more significant. In the earlier survey (UNSCEAR, 2000), 34% of the annual global dose

due to medical exposures was due to CT. For the period 1997-2007 this had risen to 43% (UNSCEAR, 2010a).

Table 2.4: Contribution of CT to medical diagnostic imaging examinations and the effective dose from these examinations (UNSCEAR, 2000, 2010a).

Health Care Level[a]	**Percentage contribution of CT to total number of medical examinations**		**Percentage contribution of CT to dose from medical examinations**	
	1991-1996	**1997-2007**	**1991-1996**	**1997-2007**
I	6	10	41	46
II	1	2	5	15
III/IV[b]	0.4	15	2	65
Global average	**5**	**7**	**34**	**43**

[a] Health care levels are defined by the number of physicians per head of population. Level I has at least 1 per 1,000; Level II has 1 per 1,000-3,000; Level III has 1 per 3,000-10,000; Level IV has 1 per >10,000.

[b] There is great uncertainty in the frequency and doses for health care level III/IV countries (UNSCEAR, 2010a).

Similarly, data from the US (NCRP, 1989, 2009) shows that in 1980 CT accounted for 1.8-2.5% of all radiological examinations and delivered approximately 5% of the collective dose for medical procedures. By 2001, CT accounted for 13% of procedures and 30% of the collective dose (Nickoloff and Alderson, 2001) and results for 2006 show CT contributed 17% of all procedures (excluding dental) and 49% of the dose (Mettler et al., 2009, 2008). In the UK, the collective dose from CT almost doubled over a ten year period (to 2002) to account for 47% of the dose from all medical X-ray examinations (Hart and Wall, 2004), whereas by 2003/2004 CT only accounted for 9% of all examinations (Shrimpton et al., 2006). In the late nineties, Australian estimates show that medical exposures accounted for 35% of the dose from all sources, while CT contributed 45% of the dose from these medical sources (Webb et al., 1999; Wise and Thomson, 2004).

Although CT remains a small percentage of the total number of medical examinations, it is evident that it contributes a significant proportion of the collective dose to the population. For countries with advanced health care, the average dose per CT examination has increased significantly since its inception in the seventies (UNSCEAR, 2010a) (Table 2.5). Conversely, the average dose for a chest radiograph has been decreasing. In the earliest results (1970-1979) only doses for CT head scans were included and hence the dramatic increase in the survey for the following decade (1980-1990). However, using the average dose as an indicator of CT dose levels may be misleading. A number of studies and surveys (Moss and McLean, 2006; Muhogora et al., 2010; Shrimpton et al., 2006; Smith-Bindman et al., 2009; Wallace et al., 2010) have found that substantial variation in dose for the same type of CT examination is observed between sites.

Since children are more sensitive to radiation than adults, it is meaningful to analyse

Table 2.5: Changes over time in the average dose for CT examinations and chest radiographs for countries with advanced health care systems (UNSCEAR, 2010a). Percentage increases on previous time period are shown in brackets.

Year	Average dose per CT exam (mSv)	Average dose per chest radiograph (mSv)
1970-1979	1.3	0.25
1980-1990	4.4 (238%)	0.14 (-44%)
1991-1996	8.8 (100%)	0.14 (0%)
1997-2007	7.4 (-16%)	0.07 (-50%)

paediatric CT doses and imaging trends. The more recent UNSCEAR survey results (UNSCEAR, 2010a) provide a breakdown of CT trends for particular protocols by age and sex. However, this data is relatively incomplete and lacks the detail necessary for a meaningful global analysis. The only age groups provided are 0-15 years, 16-40 years and over 40 years. At an UNSCEAR meeting in August 2010 it was agreed to commence preliminary investigations that focus specifically on children (UNSCEAR, 2010b). There are already some smaller scale surveys that have been conducted on paediatric CT utilisation rates (Blackwell et al., 2007; Dorfman et al., 2011; Larson et al., 2011; Mettler et al., 2000; Townsend et al., 2010; Wiest et al., 2002) and the IAEA is assessing paediatric CT utilisation in developing countries (Muhogora et al., 2010).

2.4 Children and CT

In February 2001 a series of three featured articles (Brenner et al., 2001a; Donnelly et al., 2001; Paterson et al., 2001) and an editorial (Rogers, 2001) in the American Journal of Roentgenology generated significant media coverage in the US regarding the dose to children from CT scanning. The day that the articles were published the front page of the newspaper USA Today carried a headline "*CT scans in children linked to cancer later*" (Donnelly and Frush, 2001). This resulted in a strong public reaction, but also encouraged the medical community to become more aware of paediatric CT dose. Interestingly, prior to this, concerted efforts from CT manufacturers to reduce dose were limited (Donnelly, 2005). The first paper on paediatric CT dose reduction appeared as early as 1986 (Brenner et al., 2001b; Robinson et al., 1986), but it was not until the publication of these articles in 2001 that attention was properly drawn to the issue.

One of the important realisations was that CT protocols for adults were in some cases being used on children. While early scanners did not allow adjustment of parameters, advancing technology provided operators with the ability to lower the dose for younger/smaller patients although it appeared that this was not being utilised in some cases. A paediatric hospital survey of CT examinations performed on children at outside institutions found that no appreciable adjustment of parameters was being made based on the examination

type or patient age (Paterson et al., 2001). To compound the problem, the number of CT scans being performed on children appeared to be increasing (Blackwell et al., 2007; Brenner et al., 2001a; Wiest et al., 2002). This growth in CT utilisation can be attributed to advances in technology allowing faster scanning times and hence greater feasibility for conducting scans on uncooperative, young and/or sick patients. Furthermore, the availability of CT scanners makes them readily accessible and it has become an expectation of some patients or their families that CT imaging be performed.

The combination of using adult parameters and the higher radiation risk for children compared with adults leads to a significantly higher attributable lifetime cancer mortality rate in children (Brenner et al., 2001a). According to Brenner et al. (2001a), based on 600,000 abdominal and head CT scans performed annually in the US on children under the age of 15 years, approximately 500 of these children might ultimately die of radiation induced cancer. These figures, used in isolation, may cause considerable concern particularly for parents with children requiring a CT scan. However, it is important to make a comparison with the background cancer rate from causes other than radiation. Approximately 140,000 of the 600,000 children will eventually die from cancer from non-radiation related causes and the radiation induced cancer risk increases this rate by only 0.35% (Brenner et al., 2001a).

Furthermore, the health benefit of the CT scans must also be considered. The radiation attributable cancer rate, calculated by Brenner et al. (2001a), equates to about 1 in every 1,200 abdominal and head CT scans leading to a fatal cancer in the age group under 15 years. It is expected that a significant proportion, ideally all, of these examinations would have a diagnostic benefit changing patient management and even have been life saving. The risk to benefit ratio must be regarded in this context and is ultimately a decision that the child's clinician must make. Furthermore, the risks calculated by Brenner et al. (2001a) are likely to be high, since they are based on the use of adult parameters. For a properly optimised and clinically justified examination, these risks are lower.

The Society for Pediatric Radiology (SPR) responded (Pediatric Radiology, 2001) to the press coverage of the articles as unbalanced and potentially dangerous and stated that the benefits of CT imaging had not been highlighted. Brenner et al. (2001c) agreed that the risks are almost always outweighed by the benefits, but when the risks are applied to such a large population they become a public health issue. For an individual patient the benefits are justified, but from a population perspective the risks must be considered.

The emphasis on risk is prevalent in the commentary surrounding CT paediatric dose. Defining what is acceptable in terms of risk will always be a challenging question. Human nature tends to lead us to overreact when presented with a small risk, while larger risks, such as dying from lung cancer due to smoking are often disregarded (Picano, 2004). Donnelly (2002) draws the parallel with the introduction of X-ray imaging in medicine and the delay in realising its harmful effects. He cautions that over-utilisation can result

from the successful introduction of new technology, without realising its unforseen dangers which leads to belated optimisation of techniques and implementation of appropriate safety and protection measures.

A symposium on dose reduction in the US held in 2002 concluded that the clinical value of CT is unquestioned, but that further optimisation of the dose to children is necessary (Linton and Mettler, 2003). A radiologist is quoted from the symposium keynote address as remarking that "the truth is that we were asleep at the switch on the issue of CT dose" (Linton and Mettler, 2003). Despite the known controversy regarding quantifying the risk associated with low radiation doses, it was becoming apparent in the literature, particularly from 2001 onwards, that dose reduction was needed for paediatric CT.

2.4.1 Dose Reduction Techniques

There are numerous ways of reducing and optimising the dose to the patient from CT exposure. However, dose is inextricably linked to image quality and the factors contributing to each must be balanced to ensure images are of diagnostic quality, while dose is minimised. Both image quality and dose also depend on patient size (Nickoloff, 2002; Nickoloff et al., 2003; Siegel et al., 2004), which must be taken into account. Optimisation is not a simple process and the danger exists that a diagnosis may be missed due to poor image quality (Cohen, 2009) or that the dose is not as low as reasonably achievable. The aim is to achieve acceptable, rather than optimal, image quality (Frush, 2009) with the least dose.

Identifying an appropriate level of noise so that images are considered diagnostic is one of the current challenges (Lewis, 2005). As highlighted in the 2001 articles (Brenner et al., 2001a; Donnelly et al., 2001; Paterson et al., 2001) what is relevant for adults may not necessarily apply equally to children. Children do not usually have the same fat planes between tissues and organs as adults and therefore do not have the same inherent contrast and tissue differentiation (ICRP, 2007a; McCollough et al., 2006; Nievelstein et al., 2010; Vock, 2005). Additionally, details of interest are smaller in children and this translates into a higher contrast to noise requirement. It follows that a constant level of noise across adults and children is inadequate and that children will generally require a less noisy image (McCollough et al., 2006; Nievelstein et al., 2010). There will be some clinical situations that may tolerate more noise in areas of higher contrast such as the skeleton and lung parenchyma (Frush, 2008).

Following the discussion generated from the articles in 2001, an Alliance for Radiation Safety in Pediatric Imaging was formed in 2007 (including the SPR, American Society of Radiological Technologists, American College of Radiology, American Association of Physicists in Medicine and other medical organisations and agencies) (Goske et al., 2008a,b). The Royal Australian and New Zealand College of Radiologists (RANZCR) subsequently became a member (2010). The central message of the Alliance through their

Image Gently campaign (http://www.pedrad.org/associations/5364/ig/) is to "child-size" CT scans. The key recommendations are (Goske et al., 2008b; Strauss et al., 2010):

1. Reduce or child-size the amount of radiation used.
2. Scan only when necessary.
3. Scan only the indicated region.
4. Scan once: multiphase scanning is usually not necessary in children.

These simple messages in fact encompass the essence of dose reduction. Before examining practical ways of reducing dose, the issue of justification of the CT scan deserves further consideration. Clinically, the decision to request a scan is the first opportunity to mitigate the dose if it is decided that the scan is not necessary at all.

Justification of the Scan

Eliminating unnecessary or inappropriate CT examinations is the most effective method of reducing dose (Donnelly, 2005). A CT examination for an individual child is justified if there is reasonable likelihood that it will produce a health benefit or inform patient management, otherwise the child only receives the potential detrimental radiation effects. The population is advantaged when the summed positive health benefits from those whose management is positively influenced by the imaging are greater than the summed detrimental effects. The net positive health effects of the CT examination will be greater when unnecessary studies are not performed and the studies performed are optimised for both image quality and dose.

The principle of justification applied to medical exposure situations requires the medical practitioner to weigh the benefits of the procedure against the risks of radiation detriment due to the exposure to ensure that there is a net benefit (ICRP, 2007b,c). One of the impediments to determining the risk-benefit ratio for diagnostic imaging is that the indication for the examination is a current medical problem with the imaging potentially providing an immediate benefit, while the radiation effects relate to possible future risks. The ICRP (2007b; 2007c) defines three levels of justification that must be met when considering medical exposures (Table 2.6).

Firstly, the use of radiation in medicine is well proven as being beneficial and doing more good than harm. Hence, justification is taken for granted at this top tiered level. The second level of justification applies to defined radiological practices (e.g. chest radiography for the diagnosis of serious pulmonary conditions (ICRP, 2007c)). These procedures are justified at a national or international level by professional bodies. The third level of justification relates to the individual patient procedure. In this case, the medical practitioner should consider the objective of the exposure and also the individual involved. Alternative procedures including initial physical examination and those that do not involve ionising

radiation, such as magnetic resonance imaging (MRI) or ultrasound, should be considered. Prior imaging for the individual should also be checked to see if the required diagnostic information has been previously acquired.

Table 2.6: Levels of justification for medical exposures in the ICRP system of radiation protection (ICRP, 2007b,c).

Level of Justification	**Description**	**Responsible Person**
Level 1	Use of radiation in medicine	Justification is taken for granted
Level 2	Specified procedures with a specified objective	Decided by national and international professional bodies
Level 3	Individual patient procedure	Decided by medical practitioner

There are numerous reasons that unnecessary scans may be undertaken including defensive medicine for fear of litigation from not performing a CT scan, pressure from the public to use high end technical examinations and in some cases there is a financial incentive to perform more CT examinations (Brenner and Hricak, 2010; Broder, 2008; Donnelly, 2005; Hendee et al., 2010; Studdert et al., 2005). The medical practitioners peer review group in Australia recently reported that CT scans were being initiated without appropriate clinical justification (PSR, 2010). The report suggested that lack of knowledge about particular imaging modalities and using imaging instead of undertaking adequate clinical assessment may also be contributors to inappropriate CT use (PSR, 2010). Furthermore, opportunities to educate referrers on inappropriate requests may be missed, leading to over-utilisation of imaging (Hendee et al., 2010).

CT imaging should not be the default choice, particularly in the trauma setting. In a retrospective review (Fenton et al., 2004) of the results in more than 2,000 trauma CT scans of children (January 1999 to October 2003), it was found that more than 50% were normal. CT "is wonderful, but not every time for every patient" (Linton and Mettler, 2003). An informal poll (Pediatric Radiology, 2002) of paediatric radiologists revealed that approximately one third of requests are likely to be unnecessary. Recent Australian media commentary (Margo, 12 March 2009) highlighted that the "rapid gratification" felt by patients by receiving quick results from a CT scan seemed to imply that the small and remote risk of cancer later on was outweighed. Furthermore, patients were pressuring doctors to order CT scans, yet the doctors were "not always up to date" with the risks associated with CT exposure and therefore unable to make an informed clinical decision (Margo, 12 March 2009), especially about alternative imaging. However, the availability of non-ionising imaging techniques (e.g. MRI and ultrasound) must also be sufficient so that CT is not the easiest, default imaging option (Klig, 2006).

The ICRP state that justification is the shared responsibility of the requesting clinician and the radiologist (ICRP, 2007a). Some authors have suggested that paediatric CT request forms should be vetted by consultant radiologists (Paterson and Frush, 2007) or even

informed consent obtained from the patient (de Campo and de Campo, 2010). However, other authors comment on the difficulty in obtaining consent for procedures involving radiation because the risk is age-dependent and cumulative (Brink et al., 2011; Goske and Bulas, 2009) or because of the risk of a parent refusing a justified CT scan (Karsli et al., 2009). Alternatively, consent above a certain dose level (Baerlocher and Detsky, 2010, 2011) may be warranted combined with a clear radiation risk communication strategy such as the graphical depiction suggested by Picano (2004). Informed decision making may provide a viable alternative to informed consent (Goske and Bulas, 2009) and would educate the patient providing an opportunity for shared decision making (Merck et al., 2011). One study (Larson et al., 2007) surveyed parents of children undergoing CT scans, before and after providing a brochure on radiation safety and found that the level of consenting to the CT scan did not change.

Other studies (Hadley et al., 2006; Kuppermann, 2008; Osmond et al., 2010) encourage the use of clinical decision rules and potentially incorporating these into software, as long as they are simple, accurate and well-founded. An online tool called Diagnostic Imaging Pathways (www.imagingpathways.health.wa.gov.au) has been developed in Australia to support informed decision making. Furthermore, a consumer and referrer information database called "InsideRadiology" (www.insideradiology.com.au) on medical imaging has been established to encourage informed choice. The value of education should not be underestimated as one of the most important steps in changing trends in the ordering of CT scans.

Recent discussions (Margo, 12 March 2009; Street et al., 2009) in Australia have also highlighted the need for a central register of medical exposures. This would provide both individuals and their doctors with information regarding their exposure history allowing more information for justification of procedures. A study (Sodickson et al., 2009) covering a US institution's records for a period of 22 years found that 33% of patients underwent five or more CT examinations and 5% had undergone between 22 and 132 examinations. A US study (Dorfman et al., 2011) of medical imaging utilisation for children found that over a three year period 45% of the cohort receiving CT imaging had two or more scans, and 14% had three or more scans during that time. An Israeli study (Chodick et al., 2006) over a five year period found that 15% of the cohort (0-18 years) had a prior CT scan within that time frame and a Japanese survey (Ghotbi et al., 2006) found that almost a quarter of children had repeat scans during a one year time period. It is conceivable that some individuals have numerous CT examinations across different hospitals and practices during their lifetime with no real knowledge of their cumulative radiation exposure.

One way to reduce the number of scans per individual is to ensure that imaging is not repeated unnecessarily after transfer between health care facilities (Bagg et al., 2008; Chwals et al., 2008; Cook et al., 2010; Street et al., 2009). This is an issue that affects patients of all ages. CT scans may be repeated if the outside images do not arrive with the patient,

are in an unreadable format, or if the quality and outside protocol is questioned. Repeat imaging should only be undertaken if there is a clinical indication for doing so.

Child-Size the Exposure

For the same exposure factors, the dose to a child or small adult will be greater than for a larger person. Although the energy imparted is less in the child, the absorbed energy is distributed in a smaller organ and hence dose to the organ (absorbed energy in the mass) will in fact be higher (Brenner, 2002; Frush et al., 2003; Huda, 2002; McNitt-Gray, 2002; Paterson and Frush, 2007). Furthermore, when an organ is proximal to the X-ray tube, an adult and a child will receive the same incident exposure from the X-ray beam. When that organ is on the opposite side to the tube, the patient's body will provide some shielding to the organ. In a child, this self-shielding will be less, which results in a higher dose to the organ (Brenner, 2002). These factors combined with the higher risk of related cancer induction because of a child's radiosensitivity and remaining length of life, are key drivers for reducing the dose during CT scans of children.

A simple method of dose reduction is to minimise the overall exposure by decreasing the area exposed and scanning only the indicated region (ICRP, 2007a; Vock, 2005). Due to the shorter scan times in MDCT, there is a tendency to increase the scan region (Campbell et al., 2005). This should be avoided and only the minimum length required for diagnostic purposes should be included in the scan. Reducing the scan region in follow-up CT examinations in patients with certain clinical indications (e.g. cystic fibrosis) is also possible based on prior scanning of the patient (Jimenez et al., 2006). Furthermore, whenever possible for helical scans, the scan length should be scanned in one large block rather than two or more contiguous blocks because of the contribution to dose from over-ranging due to data interpolation (Heggie et al., 2006).

Multi-phase (e.g. pre- and post-contrast) examinations should not be conducted for children, or avoided unless absolutely necessary (ICRP, 2007a; Paterson and Frush, 2007; Vock, 2005). For example, it rarely changes a child's management when searching for a calcification to conduct a pre-contrast scan in addition to the post-contrast study (Paterson and Frush, 2007). Another method is the use of shielding, such as bismuth shielding, to limit dose to the breast, thyroid or eyes during the scan (Coursey et al., 2008; Fricke et al., 2003; Heaney and Norvill, 2006; Hopper, 2002; Kim et al., 2010; Mukundan et al., 2007; Parker et al., 2008). However, more recently, there has been debate as to whether reducing the tube current instead of using bismuth shielding is a more effective measure (Geleijns et al., 2010). Additionally, preparing the child psychologically for the CT scan and/or having a parent or carer remain in the room during the scan if necessary, may assist in acquiring an optimised examination (Nievelstein et al., 2010; Strauss et al., 2010).

Adjusting the parameters used for the examination is a more direct way of influencing dose for a given protocol. The dose to a patient is proportional to the number of photons in

the X-ray beam, which is quantified by the tube current in milliamperes (mA) multiplied by the time for a single rotation of the X-ray tube in seconds (s) to give mAs. CT is a quantum noise limited system (Huda et al., 2002), which means the image quality can be improved by increasing mAs. Noise is inversely proportional to the square root of mAs and hence an increase in the number of photons will provide better counting statistics, lowering quantum noise, but increasing the dose to the patient. Beam collimation, slice width and pitch will also affect dose and image quality, although changes in these individual parameters typically improve image quality at the expense of increasing the dose.

Manufacturers have introduced automatic tube current modulation (see Section A.2, Appendix A), which is perhaps one of the most important dose saving tools available on modern scanners (Kalra et al., 2004b; McCollough, 2008). The scanner software determines the necessary current required, based on the size of the patient, to achieve a setting predefined by the user. In addition to this automated dose optimisation feature, the operator (typically a radiographer) can also influence the techniques used. It should now be standard practice to adjust parameters for children based on age, weight, size or a combination of these and there is much literature addressing these techniques (Boone et al., 2003; Donnelly et al., 2001; Haaga, 2001; Huda et al., 2000; Lucaya et al., 2000; Paterson and Frush, 2007; Suess and Chen, 2002; Verdun et al., 2004). Paterson et al. (2007) provide an excellent review of some of the suggested protocols for children and manufacturers now provide age- or weight-based technique charts that can be utilised.

Age can be a difficult parameter to use as a reference for technique selection. Children vary significantly in size, particularly if they are sick and applying a protocol based on general age groups may be insufficient. The exception may be for head protocols, as the skull develops with age and is the main attenuator in the head (Ghotbi et al., 2006; ICRP, 2007a; Suess and Chen, 2002). Furthermore, the head shows rapid growth in the first two years, but then gradually plateaus (Kleinman et al., 2010). Weight can be used (Ghotbi et al., 2006; Kim and Newman, 2010; Singh et al., 2009), although patient diameter or girth is more likely the most accurate measure as it directly correlates with the pathway traversed by the beam (Boone et al., 2003; Haaga, 2001; Kleinman et al., 2010). The initial scan projection radiograph can be used to take a measurement of the patient's anatomy on which to base the scan parameter selection. The clinical indication can also be used as an input for protocol selection (Singh et al., 2009).

Donnelly et al. (2001) created a look-up table based on weight which they used for their single-slice helical CT scanner (CT/I, GE Healthcare, Waukesha, Wisconsin, US). In some rare instances they needed to increase the protocol defined current by 50 mA to decrease noise in order to identify very small lesions (e.g. in the evaluation of an immuno-compromised child for fungal liver disease). Boone et al. (2003) investigated suitable parameters for children by assessing the dose, noise and contrast to noise ratio (CNR) for a series of measurements on a 16 MDCT scanner (LightSpeed, GE Healthcare,

Waukesha, Wisconsin, US) using cylindrical phantoms. They freely provide technique charts in Excel (Microsoft Office) spreadsheet format that calculate the mAs required for a paediatric exposure to maintain the same CNR as the equivalent adult CT scan for abdominal and head examinations. The dose reduction factor is determined based on the patient's abdomen or head diameter.

Huda et al. (2000) tried a different approach and determined the mAs and voltage values required to achieve the same detector energy fluence as for specific adult protocol parameters. Lucaya et al. (2000) found that there was no difference in the image quality scores between 50 and 180 mAs for high resolution chest CT scans and that dose could be dramatically decreased (72% reduction). Suess and Chen (2002) provide percentage reductions in mAs for head protocols and body protocols based on the child's age and weight, respectively. Verdun et al. (2004) proposed using a dose efficiency descriptor (defined as noise reduction per unit dose) and determined dose values and a noise level for specific weight classes. Brisse et al. (2009a) extended this concept to use relative low contrast detectability to determine appropriate parameters based on patient diameter.

The Image Gently campaign (www.pedrad.org/associations/5364/ig) provides guidelines for an alternative method for determining paediatric parameters. Baseline techniques are established based on adult head and abdomen scans. This allows a correlation between all types of scanners using the phantoms currently used for quality assurance tests. A table of reduction factors is then provided to determine the paediatric parameters based on posterior-anterior (PA) thickness. This method is based on existing American College of Radiology (ACR) national CT accreditation dose recommendations for adult protocols and may not be directly utilised by a dedicated paediatric institution, for example. More recent ACR accreditation requirements include a dose recommendation for paediatric abdomen examinations (ACR, 13 September 2010).

The voltage of the X-ray tube is a more difficult parameter to adjust as the effect on image quality is more complex. Furthermore, the dose relationship is not simply explained as it depends on the filtration of the beam (beam quality) and scanner geometry, which are unique to individual machines. Huda and Slone (2003) have shown that an increase in tube voltage from 80 to 140 kV_p will increase the dose by a factor of five, while Nickoloff (2002) shows that increasing from 120 to 140 kV_p will increase the dose by about 30-45%. Increasing the voltage, while keeping all other parameters constant, will degrade the low contrast resolution, but simultaneously decrease noise due to more photons penetrating the patient and the contrast to noise ratio may actually increase or be maintained.

With the range of protocols that can be applied, another issue that has been considered is the ease of following the protocol in clinical practice where parameters need to be manually adjusted depending on patient size. Frush et al. (2002) have shown that a colour coded format based on weight was found to be strongly preferred by the CT scanner operator because it was easier to use and/or understand. Although more sheets of paper were

required (each weight category was presented on a separate sheet rather than in a single table) it was found that this lead to less errors. It has been suggested (Saxena et al., 2005) that software modifications should be made by manufacturers to allow the use of pre-programmed weight based protocols. However, Frush et al. (2002) consider that although a weight based system could be entered, the parameters often need changing and hence there are grounds for maintaining a paper based system. Singh et al. (2009) assessed compliance with weight based colour coded protocol selection determined by clinical indication and found that non-compliance was typically due to patients being older, heavier or larger in size. In their implementation of the colour coded scheme, the protocols were programmed into the scanner for easy selection once the decision had been made on which protocol to use.

Benchmarking and awareness of dose levels are essential to the process of dose optimisation. Diagnostic reference levels (DRLs) are becoming more common for medical imaging modalities, especially CT. DRLs represent the lower bound of potentially unacceptable practice, rather than being an upper limit not to be exceeded (Shrimpton and Wall, 2000). These can be set at a practice, regional and/or national level and are calculated by surveying doses for standard patients across practices and generally established at the third quartile value. Dose surveys can then be conducted at a practice level and compared with national DRLs to determine when local practice should be reviewed, particularly when the DRL is consistently exceeded. DRLs have been used for some time in European countries (Bongartz et al., 2004). A summary of DRLs relating to paediatric CT procedures is provided in Table D.1 (Appendix D).

Education

The critical factors in any of the dose reduction techniques discussed are education and collaboration. Without knowledge and understanding of the key issues affecting dose and close cooperation between referrers, radiologists, radiographers, technologists and physicists, the full potential of dose reduction will not be achieved. Furthermore, training is an important step in the installation of any new scanner. Advances in technology do not automatically translate to more skilled use of that technology (Chodick et al., 2009).

A survey (Arch and Frush, 2008) of SPR members has assessed the effectiveness of education on optimisation since the 2001 articles (Brenner et al., 2001a; Donnelly et al., 2001; Paterson et al., 2001) and found that parameters for CT scans are being adjusted. Despite a relatively high response rate of "unknown" for questions regarding protocols (22%; 13/59) and current or voltage (49%; 29/59), of the respondents who did answer the questions 98% reported that tube current was based on either patient weight (78%) or age (20%). Only one respondent used the same tube current regardless. A lower percentage of respondents selected "unknown" compared with a survey conducted five years earlier. Similarly, reductions in voltage were found, with no respondents using more than 120 kV_p

for routine chest and abdomen scans.

Other evidence is emerging that demonstrates that the education campaign since 2001 has had a mixed effect on paediatric CT utilisation rates. A survey of North American paediatric facilities found that the proportion of diagnostic imaging (including ultrasound, MRI and CT imaging) that was attributable to CT had declined steadily since 2003 (Townsend et al., 2010). However, the study did not report absolute utilisation rates and hence overall trends are less clear. Other evidence reveals that paediatric CT usage is still increasing, particularly for pre-surgical diagnosis of appendicitis where it is replacing ultrasound based primarily on availability after hours, cost and the high level of skill required by the ultrasound operator (Brenner and Hall, 2007; Frush, 2008; Partrick et al., 2003; Reed, 2008; Sivit, 2008; Wagner, 2002). A preliminary result from a US study has demonstrated an apparent deceleration in growth for CT imaging of children, although overall utilisation is still increasing (Wiest et al., 2002).

Explanation of radiation dose to a patient undergoing a CT scan or their family appears to be provided in only some circumstances. A survey (Lee et al., 2004) conducted in the US found that over a two week period in a hospital's emergency department, 93% of patients did not receive information about radiation exposure before undergoing a CT scan. A recent Australian survey (Zhou et al., 2010) of medical students and interns found that over half underestimated the dose from common examinations, while a quarter incorrectly identified MRI as producing ionising radiation, a result repeated in another Australian survey (Keijzers and Britton, 2010) of emergency department doctors. This survey found that the clinical scenario was a determinant of whether a patient was informed of radiation risk (Keijzers and Britton, 2010). Other surveys have also found the misconception that MRI involves ionising radiation (Jacob et al., 2004; Soye and Paterson, 2008) and in most radiation doses were underestimated (Quinn et al., 1997; Rice et al., 2007; Shiralkar et al., 2002; Soye and Paterson, 2008). Interestingly, most surveys reveal a relatively low proportion of the medical profession having any formal radiation safety training (Jacob et al., 2004; Keijzers and Britton, 2010; Quinn et al., 1997; Soye and Paterson, 2008).

Education does not need to be restricted to the medical profession and users of CT. The Image Gently alliance have released a campaign on their website (www.pedrad.org/associations/5364/ig) to help inform parents. A medical record card can be used to track their child's exposure to ionising radiation and brochures explaining medical exposure are also provided. Online risk calculators for paediatric CT scans have also started to emerge (Alessio and Phillips, 2010). In addition, the Image Gently concept has broadened to include Step Lightly, which addresses dose issues in paediatric interventional radiology (Sidhu et al., 2009) and the Image Wisely campaign (www.imagewisely.org) has been established which focuses on adult radiation protection in medicine (Brink and Amis, 2010).

2.5 Conclusions

It is agreed that there is uncertainty in the extrapolation of risks from the LSS to the lower doses typical of CT imaging and debate on this topic continues. However, the most reasonable assumption for radiation protection purposes is that even low doses of ionising radiation are potentially harmful, particularly for children. It will require large scale, long-term epidemiological studies of patients who have undergone CT scans to quantify the risk. These types of studies are inherently difficult in terms of obtaining sufficient sample sizes and the extensive follow-up required to account for radiation induced cancer latency. Although these studies are commencing, the results may take many years to publish and may even then be equivocal.

In the past decade the risks associated with paediatric CT scanning have received increasing attention. In the context of the growth in paediatric CT utilisation and the use of parameters which were leading to higher than necessary radiation doses, the health risks for the cohort of children undergoing CT scans are no longer considered to be negligible. Therefore, the impetus is to decrease the population health risks by reducing unnecessary imaging, educating and informing all those involved in the process from the referring clinician to the patient and ensuring that when a CT scan is clinically indicated, it is performed with an optimal technique. The exposure risks associated with diagnostic medical imaging using ionising radiation are unavoidable, but the risks can be appropriately managed and reduced.

2.6 Publications Arising from this Chapter

1. **Brady, Z.**, Cain, T. M. and Johnston, P. N., *Justifying referrals for paediatric CT*, Medical Journal of Australia, 2012 *(accepted)* (Brady et al., 2012a).

Chapter 3

Experimental Dosimetry

3.1 Introduction

There has been much discussion and increasing awareness of the potential adverse population health effects due to radiation exposure from paediatric CT scans (Brenner et al., 2001a; Frush et al., 2003; Hall and Brenner, 2008). Quantifying the dose from these scans is necessary for assessing potential risk and to enable optimisation. However, there are a variety of dose measures and indicators that are used for CT dosimetry (see Appendix A.5 for a discussion of these) and it is often difficult to determine the most appropriate quantity to use. Typically, a combination of these quantities is necessary to adequately describe the exposure situation.

The organ or tissue absorbed dose is the most relevant quantity to assess radiation detriment. This can be measured experimentally by placing dosemeters in an anthropomorphic phantom, which mimics the human body in terms of the physical characteristics of size and shape, but is also equivalent in terms of material properties that affect X-ray photon interaction and dose deposition. The types of dosemeters generally employed for diagnostic radiology dosimetry include thermoluminescence dosemeters (TLDs) (Brisse et al., 2009b; Chapple et al., 2002; Nishizawa et al., 2008) and, more recently, metal oxide semiconductor field effect transistors (MOSFETs) (Bower and Hintenlang, 1998; Mukundan et al., 2007; Yoshizumi et al., 2007).

Both TLD and MOSFET dosimetry methods are time consuming. TLDs are particularly labour intensive due to the additional steps of annealing and read out, compared with MOSFETs which allow real time dose determination. However, both dosimetry methods require careful calibration by reference to an ionisation chamber measurement. While an ionisation chamber is considered the "gold standard" of radiation dosimetry, TLDs are routinely used in medical dosimetry because of their reliability, small size and tissue equivalence. A more detailed discussion of TLD dosimetry is provided in Appendix C.

Measuring organ absorbed doses is also restricted by the number of dosemeters that can be used for the dose assessment. This is particularly relevant for dispersed and large organs and tissues such as the bone marrow, bone surface, muscle and skin. Furthermore, the attenuation properties of different tissues needs to be taken into account, particularly at the photon energies relevant to CT, and in some cases electronic equilibrium will not exist (for example in marrow cavities). Due to the complexity and required time and resources, experimental dosimetry in diagnostic radiology is infrequently performed in the clinical setting.

There are only a limited number of studies where physical anthropomorphic phantoms and dosemeters have been used to measure organ doses for paediatric CT. Chapple et al. (2002) used a range of paediatric anthropomorphic phantoms (representing neonate, 1, 5, 10 and 15 year old children) and TLDs to measure CT organ absorbed doses for four non-overlapping regions of the head, chest, abdomen and pelvis using fixed, non-clinical scan parameters. However, the aim of the study was to develop a scanner-independent dose conversion method for calculating effective dose for any of these anatomical regions using the dose length product (DLP) and hence effective dose rather than organ doses are reported.

Brisse et al. (2009b) also used a range of phantoms (representing newborn, 1, 5 and 10 year old children) with 69-74 high sensitivity LiF:Mg,Cu,P TLDs to assess the effect of automatic tube current modulation on organ absorbed dose. This study was conducted on an earlier four row multiple detector CT (MDCT) scanner and total body helical examinations were performed for each phantom. Therefore, reported organ absorbed doses do not demonstrate the effects of scattered radiation or over-ranging from standard clinical scan lengths. The authors comment on the lack of measured organ absorbed dose data in the literature for MDCT scanners.

Fujii et al. (2007; 2009) used an anthropomorphic phantom representing a six year old Japanese child with 32 silicon spherical photodiodes to measure organ absorbed doses for chest and abdominal CT examinations. Nishizawa et al. (2008) used the same phantom and 160 BeO and $CaSO_4$:Tm TLDs to assess organ absorbed dose for CT brain and chest examinations. The Fujii et al. (2007; 2009) and Nishizawa et al. (2008) studies are similar to work undertaken in this thesis, although they have been undertaken with a phantom representing a younger child of Japanese nationality. Furthermore, the Fujii et al. studies (2007; 2009) have been performed with a limited number of photodiodes. The Nishizawa et al. study (2008) comments on the lower sensitivity of BeO TLDs and the energy dependence of the $CaSO_4$:Tm TLDs.

McDermott et al. (2009) used an anthropomorphic phantom representing a five year old child and measured point doses for eight organ and tissue locations with TLDs for head and chest CT protocols on a 64 MDCT scanner. The authors remark on the lack of published information regarding measured paediatric CT organ doses. Again, this study

is comparable to the current work, although undertaken on a smaller sized phantom and with far fewer measurement locations.

Hollingsworth et al. (2007) used an anthropomorphic phantom of a five year old child and 20 MOSFET detectors to measure organ absorbed doses for cardiac-gated CT angiography. Coursey et al. (2008) used the same anthropomorphic phantom and also 20 MOSFET detectors placed in the chest region to assess the effect of bismuth breast shielding on organ absorbed doses. Similarly, Mukundan et al. (2007) used the same phantom and 20 MOSFET detectors placed in the head region to assess the effect of bismuth shielding on the dose to the eye for children. All of the MOSFET studies are limited by the small number of dosemeters used and in the case of Coursey et al. (2008) and Mukundan et al. (2007) only a small region of the body was assessed.

In this part of the thesis, absorbed dose to radiosensitive organs and tissues was directly measured using 101 high sensitivity TLDs for typical CT examinations of the brain, chest and abdomen/pelvis at a paediatric hospital (The Royal Children's Hospital (RCH) Melbourne). A subset of measurements was repeated with MOSFETs to compare with the TLD measurements. The comparison of the two dosimetry techniques is discussed in Chapter 4. In a later part of this thesis, the measured organ absorbed doses were compared with computed doses, which is discussed in Chapter 5.

Due to the limitation of performing organ dosimetry regularly in the clinical setting, effective dose is a single parameter that is often used as an estimate of radiation detriment. It is not a directly measurable quantity, but a means of expressing a non-uniform, partial body exposure in terms of an "effective" whole body dose (Christner et al., 2010; ICRP, 2007b; McCollough et al., 2010). This allows comparison of relative radiation risk between different imaging modalities and even other sources of exposure. For example, it allows comparison of the relative risk from a chest X-ray, a chest CT scan and a nuclear medicine cardiac scan.

Effective dose is derived from the mean organ and tissue absorbed doses weighted for the type of radiation and the organ or tissue radiosensitivity. A more complete discussion of computing effective dose is given in Appendix B. Radiation and tissue weighting factors are provided by the International Commission on Radiological Protection (ICRP) and the factors are updated over time based on advances in the scientific understanding of the effects of radiation on the human body. The most recent recommendations published in 2007 are contained in ICRP Publication 103 (ICRP 103) (ICRP, 2007b), which updated ICRP Publication 60 (ICRP 60) (ICRP, 1991). In this thesis, the effective dose is determined according to both the ICRP 60 and ICRP 103 definitions from the organ and tissue absorbed doses measured using TLDs. The changes in the effective dose definition, which are primarily due to altered tissue weighting factors, are investigated when applied to paediatric CT scans.

3.2 Methods

3.2.1 CT Examinations

Organ and tissue absorbed doses were measured using TLDs for typical CT examinations undertaken at the RCH on a 16 MDCT scanner (Siemens Sensation 16, Erlangen, Germany). The commonly performed CT protocols that were assessed included brain, chest and abdomen/pelvis examinations. Depending on the type of examination, CT protocols at the RCH are categorised into several age groups: 0-6 months, 6 months-3 years, 3-6 years (or under 5 years), 6-10 years (or 5-10 years) and over 10 years. In this thesis, the currently used protocols at the RCH for a child aged over 10 years were assessed. This selection was made by an experienced radiographer based on the size and representative age of the anthropomorphic phantom. The parameters used are summarised in Table 3.1.

Table 3.1: Current CT protocols at the RCH for a child aged over 10 years.

Examination	**kV$_p$**	**Q$_{ref}$ mAs**[a]	**Rotation time (s)**	**Pitch**	**Beam Collimation**
CT Brain	120	270	0.75	axial	12x1.5 mm
CT Chest	120	80	0.5	1	16x1.5 mm
CT Abdomen/Pelvis	120	60	0.5	1.25	16x1.5 mm

[a] Q_{ref} is the Imaging Quality Reference mAs, which is a Siemens specific setting used for automatic tube current modulation (CARE Dose 4D), which is set by the user for each protocol. This value is adjusted based on image quality requirements and the amount of noise acceptable in the image. It is defined in terms of the effective mAs (actual mAs divided by pitch).

The CT brain examination is undertaken in axial mode to allow angulation of the gantry to reduce the dose to the lens of the eye, whereas both the chest and abdomen/pelvis examinations are performed in helical mode with differing pitches. For both body examinations the scanned volume is larger compared with the head examination and therefore motion artefacts can become problematic, hence the need to use a faster helical scanning protocol. A higher pitch value is used for abdomen/pelvis scans where contrast resolution, rather than spatial resolution, has the higher priority. Higher values of pitch lead to a faster scan, but also a spreading of the slice sensitivity profile and hence a decrease in spatial resolution.

CT X-ray Spectra

The effective energy of the CT beam was calculated using IPEM Report No. 78 (Cranley et al., 1997) and the associated program Spectrum Processor (Reilly and Sutton, 1997). All CT protocols were performed at 120 kV$_p$ utilising either the inherent body or head filter depending on the type of examination being performed. The half value layer (HVL)

of the X-ray beam is 7.5±0.2 mm Al at 120 kV_p with the head filter and 8.8±0.2 mm Al at 120 kV_p with the body filter (Siemens Manual). Typical X-ray photon spectra at 120 kV_p for these filters are shown in Figure 3.1. The effective energy range at 120 kV_p is approximately 60-70 keV depending on the filter being used, which is similar to the value used by other authors (Fujii et al., 2007; Nishizawa et al., 2008).

CTDI Measurements

The following tests were undertaken to determine the accuracy of alignment at the isocentre of the scanner: agreement between the internal and external scan plane lights; coincidence of the internal scan plane lights and scan plane; and alignment of the coronal and sagittal plane lights with the scan plane. CTDI measurements were performed with a calibrated 3 cm^3 Radcal ion chamber with 100 mm length, model 10X5-3CT and a model 9095E electrometer (Radcal Corp., Monrovia, California, US). For a discussion of CT dosimetry formalism refer to Section A.5, Appendix A. Reproducibility of the beam output was assessed using $CTDI_{100}$ in air measurements at the isocentre. $CTDI_{vol}$ measurements in both the body (32 cm diameter) and head (16 cm diameter) CT dosimetry phantoms were also undertaken. Correct alignment of the ion chamber and dosimetry phantoms for all measurements was assessed according to the ImPACT protocol (ImPACT, 1997).

3.2.2 Anthropomorphic Phantom

In paediatric diagnostic radiology applications, it is not feasible to conduct in vivo dosimetry on real subjects. However, an anthropomorphic phantom which simulates the human body can be used for this purpose. There are several commercially available anthropomorphic phantoms, including a paediatric range. In this thesis, a Computerized Imaging Reference Systems (CIRS) anthropomorphic phantom of a 10 year old child was used (Figure 3.2, Model 706-D, CIRS, Inc., Norfolk, Virginia, US).

CIRS manufacture five paediatric phantoms, each representative of an age bracket as shown in Table 3.2. Organ dimensions for children within each bracket do not vary by more than 15% and the phantoms are representative of ethnic variations and both sexes (Varchena, 2002). For children, height is more indicative of body size than age, particularly when considering children suffering from an illness who may be undergoing CT examinations in a hospital. Hence, for dosimetry purposes, children falling within the height ranges specified in Table 3.2 are best represented by the corresponding phantom. The phantom used in this thesis represents children 124-156 cm tall, which broadly corresponds to 7 to 13 year olds.

The CIRS Model 706-D phantom used in this thesis consisted of 31 slab sections each 25 mm thick, which assemble to form the head and trunk of the body (legs and arms are not included). The phantom is made from epoxy resins, with photon attenuation values

Table 3.2: CIRS paediatric anthropomorphic phantom range (Varchena, 2002).

Phantom Name	Age Range (years)	Height Range (cm)
Newborn	0-0.5	Up to 66
1 yo	0.5-3	66-95
5 yo	3-7	95-124
10 yo	7-13	124-156
15 yo	13-17	156-168

within 1% for bone and soft tissue and 3% for lung tissue at photon energies from 30 keV to 20 MeV, as claimed by the manufacturer (CIRS, 2006; Varchena, 2002) (Figure 3.3). The material specifications are shown in Table E.1 (Appendix E). The CIRS Model 706-D phantom provides 214 locations for dosimetry devices in 19 inner organs (CIRS, 2006). These are located by holes in the slabs which are plugged when not in use with tissue-, bone-, and lung-equivalent material depending on their location.

For TLD measurements in this thesis, the plugs were halved and a small amount of plug material removed so that a TLD chip could be inserted between the halves (CIRS, 2006; Yoshizumi et al., 2007). The TLD chips were always handled with vacuum tweezers to avoid contamination and damage of the TLDs (Figure 3.4).

3.2.3 Thermoluminescence Dosimetry

The paediatric CT organ and tissue absorbed doses to be measured in this thesis are in the range of 10 μGy to 100 mGy. These are relatively low compared with radiotherapy doses which routinely exceed 1 Gy. Therefore high sensitivity TLDs were used. These consisted of 3.175x3.175x0.889 mm^3 chips of lithium fluoride doped with magnesium, copper and phosphorous (LiF:Mg,Cu,P) (TLD-100H, Thermo Scientific, Franklin, Massachusetts, US), with a detection range of 1 μGy to 10 Gy (Thermo, 2007). The glow curve consists of three low temperature peaks (70-160°C), a main dosimetry peak at about 220°C and a high temperature peak at 300°C (Moscovitch and Horowitz, 2007). Appendix C provides further information on thermoluminescence dosimetry.

TLD Annealing

The TLDs were annealed before each irradiation in an annealing tray with the lid removed in a micro-processor controlled oven (Scientific Equipment Manufacturers (South Australia) Pty Ltd, Adelaide, South Australia, Australia) located at the Peter MacCallum Cancer Centre (East Melbourne, Victoria, Australia). The annealing cycle consisted of three segments including a 19 minute heat up cycle to 240°C, 15 minutes maintained at 240°C and an oven cool down for five minutes. The TLDs were then left to cool in the oven to ensure a consistent cooling rate and duration after each anneal.

A recognised disadvantage of LiF:Mg,Cu,P is the potential for residual signals from peaks above the main dosimetry peak which remain after the relatively low temperature anneal. However, annealing the TLDs at a higher temperature is a destructive process, with the TLDs irreversibly losing their sensitivity (Duggan et al., 2004). Recently, the manufacturer has succeeded in reducing this residual signal to less than 1% after changes to the TLD production stream (Ramlo et al., 2007).

TLD Read Out

TLDs were read out on a Model 5500 automatic thermoluminescent reader (Harshaw, Thermo Electron Corporation, Ohio, US) located at the William Buckland Radiotherapy Centre (WBRC, Melbourne, Victoria, Australia). The read out cycle included a preheat segment at 155°C for eight seconds, an acquire phase for 26.7 seconds with a linear ramp rate of 20°C/s to 240°C. A post anneal followed for 10 seconds at 240°C. The gain setting for the reader was set to high. This temperature profile is similar to that used by others for this type of TLD material (Bartolotta et al., 1995; Davis et al., 2003; Dong et al., 2002; Duggan et al., 2004; Kron et al., 1996; Lupke et al., 2006; Moscovitch and Horowitz, 2007). The preheat is effective in removing the contribution of the low temperature peaks (Moscovitch and Horowitz, 2007). All TLDs were read out within 24 hours of being irradiated to limit effects of fading, although fading is considered negligible for this type of TLD material (Dong et al., 2002; Duggan and Kron, 1999).

The annealing tray was specifically designed for these TLDs and was also used for storage. The tray was cleaned in an ultrasound bath and heated multiple times before its first use. Ten TLDs were initially placed in the tray for storage. These TLDs were irradiated and read out and the process then repeated to confirm that no contaminants remained from the manufacturing process of the tray. The mean difference in response between the two read outs was ∼2%.

TLD Calibration

Individual calibration factors (CF) for each TLD were derived from a series of three calibration irradiations of 100 mGy each using a 6 megavoltage (MV_p) photon beam. The calibration factor is given by:

$$CF = \frac{1}{3}\left[\sum_{i=1}^{3} \frac{d_i}{r_i - b_i}\right] \tag{3.1}$$

where d_i is the calibration dose relative to water at 6 MV_p in milligray (mGy), r_i is the TLD reading in nanocoulombs (nC) after the calibration irradiation and b_i is the mean reading in nC for a batch of unirradiated TLDs. The calibration factor has units of $mGy{\cdot}nC^{-1}$. The background reading was measured for the entire batch of TLDs after

being prepared and treated in the same way as when the batch was calibrated. The same mean background measurement was used for each calibration.

During measurements of CT doses, the measured dose relative to water (D_i) at location i for a TLD with calibration factor CF was calculated by:

$$D_i = CF \times (R_i - B) \tag{3.2}$$

where R_i is the TLD reading in nC after the CT exposure and B is the mean reading in nC for a set of unirradiated TLDs from the same batch.

The TLD set (106 TLDs) was irradiated for calibration using a 6 MV_p 10x10 cm^2 X-ray photon beam on a linear accelerator (linac). The TLDs were placed in a Perspex holder with sufficient distance between adjacent TLDs to limit scattering effects (Figure 3.5).

Three different linacs located at WBRC were used for calibration of the TLDs. Before each calibration the output of the linac was checked with a calibrated 0.6 cm^3 Farmer-type NE2581 ion chamber (NE Technology, Reading, UK) and Scanditronix Wellhofer Dose 1 electrometer (IBA Dosimetry, Louvain-la-Neuve, Belgium) with calibration traceable to a national primary standard (Australian Radiation Protection and Nuclear Safety Agency, Yallambie, Victoria, Australia) (Figure 3.6). Ion chambers are calibrated to cobalt-60 and then corrected for linac energies. Temperature and pressure corrections were automatically applied to the ion chamber reading and a correction factor was determined for each linac output (range 0.992-1.008). Each batch of TLDs in the Perspex holder was placed 100 cm from the source. Slabs of solid water with a total thickness of 5 cm were placed on the TLDs and a dose of 100 mGy was used for each calibration. TLD readings that were not reproducible to within 4% over the three calibration measurements were not used. This left a batch of 101 out of 106 TLDs for use. The coefficient of variation of the calibration factors for the batch of utilised TLDs was 4.2%.

The major advantages of calibrating the TLDs using a linac are reproducibility and uniformity of output. This is possible with LiF:Mg,Cu,P compared with other TLD materials, because it exhibits relatively linear energy and dose response (Duggan, 2002; Duggan et al., 2004). Typically for measurement of CT dose using traditional LiF:Mg,Ti TLDs (e.g. TLD-100), calibration is undertaken on a general X-ray unit with beam quality matched to the CT beam using additional filtration (Brix et al., 2004; Cohnen et al., 2006; Lechel et al., 2009; Nawfel et al., 2000; Yoshizumi et al., 2007). Alternative calibration methods include using a CT scanner (Groves et al., 2004) or a superficial X-ray therapy (SXRT) unit (Duggan et al., 2003; Smith et al., 1998).

A comparative calibration of the TLDs was also performed on an SXRT unit (Therapax S3, Pantak, Branford, Connecticut, US) for a batch of 100 TLDs to compare calibration

factors with those derived from the 6 MV_p linac exposure. The desired CT beam quality was 120 kV_p with a half value layer (HVL) of 7.5±0.2 mm Al and/or 8.8±0.2 mm Al (Siemens Sensation 16 CT Scanner HVL for head and body filters respectively (Siemens Manual)). The closest beam quality match on the superficial unit was achieved with an energy of 120 kV_p and 1.1 mm Al and 0.3 mm Cu filters resulting in a HVL of 8.1 mm Al and effective beam energy of 66 keV (Reilly and Sutton, 1997). The output of the SXRT unit was checked with the same calibrated Farmer ion chamber used to verify the linac output and a correction factor of 0.981 was subsequently used. The ion chamber output measurements were made in air at a focus to detector distance (FDD) of 25 cm and a cone steel applicator was attached to the X-ray tube head for a beam size of 10 cm diameter. A cone applicator with FDD of 25 cm and beam diameter 15 cm was fixed to the X-ray tube head for the TLD irradiations to ensure all TLDs were fully irradiated.

The TLD batches were placed in the same Perspex holder as used for the linac calibrations and in contact with the cone applicator. A correction for the change in beam area was applied to calculate the time required (0.11 min) to apply a dose of 100 mGy to the TLDs. The TLDs were read out using the same methodology as for the 6 MV_p linac calibration exposures and individual calibration factors for each TLD (dose to water divided by background corrected TLD reading) were derived. The calibration factors from the 6 MV_p calibration, including an energy correction for the TLD energy response based on Duggan et al. (2004), were compared with the calibration factors derived from the SXRT calibration. On average the SXRT derived calibration factors were 4.2% higher than the 6 MV_p derived calibration factors.

TLD Measurement Uncertainty

The calculation of uncertainty for TLD measurements was based on the International Organization for Standardization (ISO) Guide to the Expression of Uncertainty in Measurement (Bentley, 2005; ISO, 1993 (corrected & reprinted, 1995)) and the UK Institute of Physical Sciences in Medicine (IPSM) analysis of TLD uncertainties for patient dose measurements (IPSM, 1992). The treatment of uncertainties took into account random (Type A) and systematic (Type B) errors (Table 3.3).

Table 3.3: Random and systematic uncertainties for TLD calibration and measurement (IPSM, 1992).

Random (Type A) Uncertainties	**Systematic (Type B) Uncertainties**
TLD calibration reading	Dose meter calibration
TLD background reading (calibration)	TLD energy response
Calibration dose	TLD dose linearity
TLD measurement reading	TLD signal fading
TLD background reading (measurement)	Temporal variation of TLD reader

Referring to equation (3.1), the uncertainty in the background reading (b_i) and the cali-

bration dose (d_i) are considered negligible compared with the variation in the TLD reading (r_i). Hence, the random error in the calibration factor (CF) for a single TLD is simply the standard deviation in the calibration factor (σ_{CF}) for the three irradiations given by:

$$\sigma_{CF} = \left[\frac{1}{3}\sum_{i=1}^{3}\left(CF_i - CF\right)^2\right]^{1/2} \tag{3.3}$$

The dose (D_i) at TLD measurement location i in the anthropomorphic phantom for a CT examination is given by equation (3.2). The total random error in the dose measurement (σ_{D_i}) using propagation of errors is given by:

$$\begin{aligned}
\sigma_{D_i} &= \left[\left(\frac{\partial D_i}{\partial R_i}\right)^2\sigma_{R_i}^2 + \left(\frac{\partial D_i}{\partial B}\right)^2\sigma_B^2 + \left(\frac{\partial D_i}{\partial CF}\right)^2\sigma_{CF}^2\right]^{1/2} \\
\sigma_{D_i} &= \left[CF^2\sigma_{R_i}^2 + CF^2\sigma_B^2 + (R_i - B)^2\sigma_{CF}^2\right]^{1/2} \\
\sigma_{D_i} &= D_i \times \left[\frac{\sigma_{R_i}^2+\sigma_B^2}{(R_i-B)^2} + \frac{\sigma_{CF}^2}{CF^2}\right]^{1/2}
\end{aligned} \tag{3.4}$$

where σ_B is the standard deviation in the background readings of the unirradiated batch of TLDs and σ_{R_i} is zero since there is only one measurement. Multiple TLDs were placed in each organ of the anthropomorphic phantom. Random errors for the organ doses were combined using propagation of errors.

The systematic errors identified for the measurements are given in Table 3.4. The total systematic error was ±4% (two standard deviations). This is lower than a similar analysis conducted by Broadhead et al. (1997) for the use of TLD-100 (LiF:Mg,Ti) which found the total non-random uncertainty to be ±9%. The overall uncertainty is calculated by combining the random and systematic uncertainties in quadrature. This typically ranged from 4% to 10% for this batch of TLDs.

Absorbed Dose to Tissue

For each CT examination assessed in this thesis, the TLDs were irradiated three times using an identical protocol before being read out to improve counting statistics and increase the dose to be measured. The resultant measured dose was divided by three to calculate the organ or tissue absorbed dose per examination. This method has been used in other studies (Geleijns et al., 1994; Groves et al., 2004; Hunold et al., 2003).

The TLDs were calibrated at an energy of 6 MV_p (effective energy 2 MeV (Kron et al., 1998)) on a linac. Although the energy response for the high sensitivity TLDs is more linear than the energy response of LiF:Mg,Ti (Figure C.1, Appendix C), a CT spectrum weighted energy correction factor for keV energies ($C_{keV}(E)$) was applied based on published energy

Table 3.4: Values for systematic uncertainties (two standard deviations) in TLD measurements.

Systematic (Type B) Uncertainties	**Value**	**Reference**
Dose meter calibration	±1%	ARPANSA Calibration Certificate[a]
TLD energy response	±1%	Duggan et al. (2004), Kron et al. (1998)
TLD dose linearity[b]	±1%	Harris et al. (1997)
TLD signal fading[b]	±1%	Moscovitch and Horowitz (2007)
Temporal variation of TLD reader	±4%	Calculated from experiment[c]

[a] Calibrated by ARPANSA to a traceable national standard.
[b] Negligible.
[c] Standard deviation of mean readings for the light response checks carried out on the TLD reader across calibration and measurement readings. The temporal response of the reader was more consistent at the commencement of the experimental work and it is expected that the increased variation and hence relatively high uncertainty in the above table is due to either drift in the system or an accumulation of dirt on the photomultiplier tube lens. After servicing of the system, this variation appears to have been corrected.

response modelling which provides a dose response ratio when normalised to high photon energy radiation (Figure C.1, Appendix C) (Duggan et al., 2004; Kron et al., 1998). The correction takes into account the response of the TLDs at the CT energy compared with the linac calibration energy, although the correction is close to unity (Duggan et al., 2004). The energy correction factor ($C_{keV}(E)$) was calculated to be 1.03 using an energy spectrum weighting (averaged over the CT spectra for the head and body filter given in Section 3.2.1). Beam hardening changes due to tissue, muscle and bone attenuation were considered and the change to the energy correction factor was negligible. Therefore, the energy correction factor does not include changes in the beam spectrum due to attenuation by the phantom or scattering within the phantom. The changes in the beam spectrum due to attenuation have been considered for the systematic uncertainty in the TLD energy response.

Furthermore, an energy dependent tissue conversion factor ($f_T(E)$) was used to estimate the dose relative to tissue from the calculated organ absorbed doses relative to water, given by:

$$f_T(E) = \frac{\left[\frac{\mu_{en}}{\rho}(E)\right]_T}{\left[\frac{\mu_{en}}{\rho}(E)\right]_W} \tag{3.5}$$

where $[\mu_{en}/\rho(E)]_T$ is the mass energy absorption coefficient for tissue at photon energy E and $[\mu_{en}/\rho(E)]_W$ is the mass energy absorption coefficient for water at photon energy E. The ratio of mass energy absorption coefficients for tissue to water using the same spectrum weighting applied for the energy correction factor gives a tissue conversion factor of 1.02 (Hubbell and Seltzer, 2004; ICRU, 1989; Johns and Cunningham, 1983). Mass energy absorption coefficients were used from Report No. 44 from the International Commission

on Radiation Units and Measurements (ICRU, 1989) as made available in tabulated form by the US National Institute of Standards and Technology (NIST) (Hubbell and Seltzer, 2004). Both the energy correction factor ($C_{keV}(E)$) and tissue conversion factor ($f_T(E)$) were also applied to the calculated uncertainties.

The absorbed dose to tissue ($D_{T,i}$) in milligray (mGy) at location i in the anthropomorphic phantom measured with TLD j is then given by:

$$D_{T,i} = [CF_j \cdot C_{keV}(E) \cdot f_T(E)] \times (R_{i,j} - B) \tag{3.6}$$

where $R_{i,j}$ is the reading on TLD j in nC after the exposure and B is the mean background reading in nC for a set of unirradiated TLDs from the same batch.

Further correction for differences in mass energy absorption coefficients were taken into account for organs and tissues where the ratio of mass energy absorption coefficients relative to tissue weighted over the CT spectrum differed from that of soft tissue. The corrected organ or tissue absorbed doses $D_{org,i}$ at location i were calculated by:

$$D_{org,i} = D_{T,i} \times \frac{\left[\frac{\mu_{en}}{\rho}(E)\right]_{org}}{\left[\frac{\mu_{en}}{\rho}(E)\right]_{T}} \tag{3.7}$$

where $D_{T,i}$ is the dose to tissue at location i given by equation (3.6), $[\mu_{en}/\rho(E)]_{org}$ is the mass energy absorption coefficient for the organ or tissue of interest at photon energy E and $[\mu_{en}/\rho(E)]_T$ is the mass energy absorption coefficient for tissue at photon energy E. Table 3.5 shows the organs/tissues for which a correction factor was applied. The corrections applied for the dose to the bone surface are addressed separately below (Section 3.2.4).

Table 3.5: Ratio of photon mass energy absorption coefficients for various organs and tissues relative to soft tissue weighted over the CT spectrum (Hubbell and Seltzer, 2004; ICRU, 1989).

Organ/Tissue (*org*)	$[\mu_{en}/\rho(E)]_{org} / [\mu_{en}/\rho(E)]_T$
Brain	1.01
Lung	1.01
Testes	0.99
Eye lens	0.93
Red bone marrow	0.90
Breast	0.88

3.2.4 Measurement of Organ and Tissue Absorbed Dose

For large or extended organs and tissues, the average absorbed dose is challenging to measure. Ideally, a large number of TLDs should be placed at all available locations in the phantom. Furthermore, multiple TLDs at each location improves the accuracy of measurement. Scalzetti et al. (2008) recommend a system involving 187 measurement locations to properly obtain average organ absorbed dose in a phantom of an adult male. Studies (Groves et al., 2004; Hollingsworth et al., 2007; Hunold et al., 2003; Hurwitz et al., 2007b; Kawaura et al., 2006; Scalzetti et al., 2008) using TLDs and/or MOSFETs for assessment of effective dose in CT have used a varying number of measurement locations ranging from 20 to 66 (Table F.1, Appendix F).

In this thesis 90 measurement locations have been used, mainly limited by the number of TLDs available. The TLDs were placed in organs and tissues identified in the recent ICRP 103 Recommendations (ICRP, 2007b), which provides the most extensive list to date (refer to Table B.2, in Appendix B). The selection of these points was based on a methodology similar to Scalzetti et al. (2008) where the number of locations was guided by organ size and the relative importance for dosimetry purposes based on the ICRP 103 tissue weighting factors (ICRP, 2007b). The TLD measurement locations used are shown in Figure F.1 (Appendix F).

One option considered was to place more TLDs in the area of the phantom exposed to the primary X-ray beam based on the protocol used (i.e. brain, chest or abdomen/pelvis). However, it was decided that for consistency, TLDs would be used in the same location independent of the examination type. The one exception was for TLDs used to measure skin dose. Six TLDs were used for this purpose and all were placed in the primary beam. The bone marrow, bone surface, skin, lung and liver were considered to be large organs or tissues and therefore a higher number of TLDs were placed in these areas. The bone surface dose was calculated from the bone marrow dose, necessitating only one group of TLDs for these measurements.

Effective dose using the ICRP 60 and ICRP 103 definitions was calculated from the measured organ and tissue absorbed doses according the formalism in Appendix B. Further detail regarding specific organ absorbed dose estimates is provided below.

Dose Variation within an Organ and Reproducibility

A preliminary measurement was undertaken with a smaller batch of calibrated TLD-100H chips to investigate the variation in dose within large organs and the reproducibility of TLD measurements. Seven TLD measurement locations were selected in both the lung and in the liver (total of 14 TLDs) in the anthropomorphic phantom of a 10 year old child (Figure 3.7). A CT chest examination was performed and repeated three times using an identical protocol without removing the TLDs to improve counting statistics. This

procedure was then repeated three times with three different sets of 14 TLDs to assess measurement reproducibility.

It was found that the absorbed dose varied by up to 21% within each organ (where the range of measured absorbed doses for the organ has been expressed as a percentage of the mean measured absorbed dose for the organ). This variation in dose highlighted the necessity to use multiple measurement locations in organs and tissues, particularly those that are large, in order to determine the mean organ or tissue absorbed dose. The ICRP recommends averaging the absorbed dose over an organ or tissue to take account of the heterogeneity of exposure and states that the mean organ or tissue absorbed dose is associated with the radiation detriment due to stochastic effects with adequate accuracy (ICRP, 2007b). The ICRP also observes that averaging of the absorbed dose across an organ relies on a linear dose-response relationship (ICRP, 1991). The 21% variation in point dose measurements was expected based on the size of the organs and the partial exposure. For the repeated measurements, it was found that the absorbed doses measured at each location were reproducible on average to within 3.4% (two standard deviations; range 0.5%-8.0%).

Mean Absorbed Dose

For an organ or tissue with multiple TLDs the mean absorbed dose to the organ or tissue (D_{org}) was calculated with an equal weighting for each TLD, as follows:

$$D_{org} = \frac{1}{n}\sum_{i=1}^{n} D_{org,i} \tag{3.8}$$

where $D_{org,i}$ is given by equation (3.7), $D_{org,i} = D_{T,i}$ for soft tissue, and n is the number of TLDs placed in that organ or tissue. The locations of TLDs in large organs and tissues were selected to ensure that the dose measurement was representative of the dose across the entire organ or tissue.

Gonads Absorbed Dose

The gonads absorbed dose (D_{gonads}) was calculated from the equally weighted average of the absorbed dose to the testes (D_{testes}) and ovaries ($D_{ovaries}$), given by (ICRP, 1991, 2007b):

$$D_{gonads} = \frac{D_{testes} + D_{ovaries}}{2} \tag{3.9}$$

Equivalent dose was calculated from the averaged gonad absorbed dose using the sex-averaged tissue weighting factor. However, the separate testes and ovaries organ absorbed doses have been reported separately, where applicable.

Substituted Organ Absorbed Doses

For the oral mucosa and salivary glands, the absorbed dose to the mandible was used as no specific location is provided in the anthropomorphic phantom for these tissues. Similarly, the heart is not specified in the anthropomorphic phantom and instead a point identified as the oesophagus was used as a surrogate. The measurement for this TLD was used for the heart absorbed dose and was also combined with the other oesophageal TLD measurements to calculate the average oesophagus absorbed dose. The extrathoracic (ET) region was approximated by the thyroid absorbed dose and the lymphatic nodes by the muscle absorbed dose. These approximations are also used by the ImPACT group (ImPACT, 2011).

TLDs were also placed at the lens of the eye, which is not specified in the organs and tissues at risk of stochastic effects by the ICRP. The dose to the eye was measured in order to assess deterministic effects.

Colon Absorbed Dose

The ICRP 103 Recommendations (ICRP, 2007b) specify that the absorbed dose to the colon is calculated as the mass-weighted mean of the absorbed dose to the upper large intestine (D_{ULI}) and lower large intestine (D_{LLI}). The upper large intestine was listed as a remainder organ in ICRP 60 and the lower large intestine absorbed dose was used for the colon absorbed dose, although this definition was revised in ICRP Publication 69 (ICRP, 1995). The original ICRP 60 definition has been used for the colon equivalent dose calculation in this thesis, although the difference to the effective dose calculation is negligible (<1.5%).

The organ masses for a 10 year old child given in ICRP Publication 89 (ICRP, 2002) and the mass weightings used for the ICRP 103 method are given in Table 3.6. The absorbed dose to the ULI is the mass-weighted average of the absorbed dose to the ascending (D_{asc}) and transverse colon (D_{trans}) and the absorbed dose to the LLI is the mass-weighted average of the absorbed dose to the descending (D_{desc}) and rectosigmoid colon (D_{recto}).

Table 3.6: Upper and lower large intestine organ masses and percentages (mass weightings) for a 10 year old (ICRP, 2002).

Organ	Organ Mass (g)	Mass Weighting (%)
Ascending (inc caecum)	51	43
Transverse	68	57
ULI	*119*	*57*
Descending	51	56
Rectosigmoid	40	44
LLI	*91*	*43*
Colon	**210**	**100**

Therefore, for a 10 year old the colon absorbed dose (D_{colon}) according to ICRP 103 is calculated by:

$$D_{colon} = 0.57D_{ULI}+0.43D_{LLI} = 0.57\,(0.43D_{asc} + 0.57D_{trans})+0.43\,(0.56D_{desc} + 0.44D_{recto}) \tag{3.10}$$

Red Bone Marrow Absorbed Dose

Bone tissue consists of an outer continuous hard layer of cortical (compact) bone and an underlying layer of trabecular (cancellous or spongiosa) bone. The shafts of long bones and the outer layers of short, flat and irregular bones consist of cortical bone. Trabecular bone, found in the ends of long bones and throughout the interior of flat bones, is a lattice of bone structures called trabeculae. Red bone marrow (RBM) fills the spaces between trabeculae and is involved in red blood cell production and is therefore considered active marrow. A fatty yellow inactive marrow fills lumen in the cortical bone. At birth, all bone marrow is predominantly red marrow. With age and depending on the site of the bone, red marrow gradually transforms to yellow marrow with only about a third of marrow being active by adulthood (ICRP, 2002).

The absorbed dose to the RBM is included in the calculation of effective dose, because of the red marrow radiosensitivity and in particular, the risk of leukaemia induction as a result of exposure. The bone marrow measurement locations in the anthropomorphic phantom were selected based on the six highest bone marrow fractions for a 10 year old (Cristy, 1981; Cristy and Eckerman, 1987) as shown in Table G.1 (Appendix G). Weight fractions for an adult (40 years of age) have been included for comparison. It was considered that the extremities (arms and legs) would receive a negligible dose since they are not in the primary X-ray beam. Furthermore, they are not included on the anthropomorphic phantom and hence could not be used for a bone marrow measurement. Only the clavicles and upper spine skeletal regions were not allocated any TLD measurement locations. The bone marrow in these regions accounts for less than 3% of the total bone marrow and hence will have an insignificant contribution to the total bone marrow dose.

Photoelectrons produced in the ionisation process may have a longer range than the smallest dimension of the cavities containing RBM (Johns and Cunningham, 1983). Hence, electrons produced in the RBM are likely to leave it without depositing all their energy and electrons produced in the adjacent bone will likely contribute energy to the RBM. The number of electrons produced in the bone will be much higher because of the high atomic number and hence increased probability of photoelectric interactions. Therefore, secondary electron equilibrium in the RBM cannot be assumed. To correct for this an energy dependent dose enhancement factor ($f_{de,b}\,(E)$) derived by King and Spiers (King and Spiers, 1985) is applied for different types of bone. Considering equation (3.7), for

the dose to the RBM at location i in a type of bone b, ($D_{RBM,i,b}$), this becomes:

$$D_{RBM,i,b} = D_{T,i} \times \frac{\left[\frac{\mu_{en}}{\rho}(E)\right]_{RBM}}{\left[\frac{\mu_{en}}{\rho}(E)\right]_{T}} \times (1 + f_{de,b}(E)) \tag{3.11}$$

where $D_{T,i}$ is the dose relative to tissue at location i, as given by equation (3.6), and the ratio of mass energy absorption coefficients is given in Table 3.5. The dose enhancement factor depends on the bone (b) for which the bone marrow dose is being determined (King and Spiers, 1985).

The dose enhancement factors for different bone types provided by King and Spiers (1985) were matched to the bone measurement locations used in this thesis according to the method of Eckerman and Stabin (2000). The bone matching is shown in Table G.2 (Appendix G). The dose enhancement factor is energy dependent, with a maximum for all types of bone at 50 keV. Therefore, it is insufficient to use a monoenergetic dose enhancement factor based on the effective energy of the CT beam, which is close to the energy at which the maximum dose enhancement occurs. For example, the dose enhancement factor for an effective energy of 60 keV would overestimate the dose by approximately 15% in all bones compared with using a dose enhancement factor based on the CT photon energy spectrum. Therefore, the dose enhancement factors were calculated by weighting over the CT spectrum (attenuation by the phantom neglected) and are summarised in Table G.2 (Appendix G).

The red marrow absorbed dose in the bone must then be summed to derive the total red bone marrow absorbed dose. A weighted sum was applied using the bone marrow weight fractions for a child shown in Table G.1 (Appendix G) (Kawaura et al., 2006; Nishizawa et al., 2008; Yoshizumi, 12-13 June 2009). The total red bone marrow absorbed dose (D_{RBM}) was calculated according to:

$$D_{RBM} = \sum_{b,i} \left[D_{RBM,i,b} \times \left(\frac{M_{RBM,b}}{M_{RBM}} \right) \right] \tag{3.12}$$

where $D_{RBM,i,b}$ is given in equation (3.11) and measured at each of the locations selected for bone marrow measurements and the second term is the mass weight fraction of bone marrow at each of those locations (mass of red bone barrow in bone b, $M_{RBM,b}$, divided by total mass of red bone marrow in the skeleton M_{RBM}) (Table G.1, Appendix G).

Various methods can be used for calculating the absorbed dose to the RBM (Caracappa et al., 2009; Eckerman and Stabin, 2000; Kramer et al., 2003; Lee et al., 2006b). Each provides an approximation that attempts to model the complex structure of the bone and energy deposition. The disequilibrium of energy deposition in bone marrow and the distribution of red bone marrow in the body for a child have been considered in the approach

used in this thesis. However, a recognised limitation is that only six locations for bone marrow measurement were selected.

Bone Surface Absorbed Dose

The endosteal tissue (or bone surface) is the layer of tissue covering trabeculae surfaces in regions of trabecular spongiosa and the cortical surfaces of the medullary cavities of the shafts of all long bones (ICRP, 2009). In adults, the medullary endosteum contributes approximately 1% to the total endosteum mass[i]. Assuming similar proportions in children, the dose to the medullary endosteal will be negligible compared with the dose to the endosteal tissue of the spongiosa and therefore can be discarded (Lee et al., 2006b). Similar to the bone marrow calculation, secondary electron equilibrium cannot be assumed in the absorbed dose measurement and calculation for the bone surface. However, the depth defining the bone surface has recently been reconsidered[ii] and new dose enhancement factors are not yet available[i]. In previous studies, the absorbed dose to the homogeneous skeletal tissue has been used as a conservative estimate of the absorbed dose to the bone surface (Kramer et al., 2003; Lee et al., 2006b). In this thesis, the average absorbed dose to the spongiosa has been substituted for the absorbed dose to the endosteum (Schlattl et al., 2007)[i].

Spongiosa bone consists of trabeculae and active and inactive bone marrow. The mass of each depends on the bone and varies with age. The percentage of active marrow in bones for a 10 year old are known from Cristy and Eckerman (1987) and for inactive marrow and trabecular bone from Eckerman and Stabin (2000) (Table G.3, Appendix G). The total mass of each in the skeleton is provided in ICRP Publication 89 (ICRP, 2002) and hence the mass of active and inactive marrow and trabecular bone for a 10 year old can be calculated using the percentage mass distributions (Table G.4, Appendix G). The resulting percentage distributions of active and inactive marrow and trabecular bone in the spongiosa bone for different skeletal regions in a 10 year old are given in Table G.5 (Appendix G). There is a large amount of variation in the composition of the spongiosa in different bones. Furthermore, the overall composition for a 10 year old is different from an adult (37%, 37%, 27% active marrow, inactive marrow and trabecular bone respectively in total spongiosa in the skeleton compared with 33%, 33%, 33% for adults (ICRU, 1992)). Therefore, it is warranted to consider the spongiosa composition in each bone in the calculation of the absorbed dose to the spongiosa. Hence, the dose to the bone surface (D_{bs}) is approximated by the average dose to the spongiosa ($D_{spongiosa}$):

[i] J Jansen [UK Health Protection Agency] 2011, pers. comm., 17 January.

[ii] In contrast to previous assumptions, recent studies have indicated that the cells at risk for bone cancer induction are localised out to 50 µm (previously assumed: 10 µm) from both the trabecular surfaces and interior cortical surfaces of the medullary cavities, but not within the Haversian canals of cortical bone (Bolch et al., 2007; ICRP, 2009).

$$D_{bs} \approx D_{spongiosa} = \sum_{b,i} \left[D_{T,i} \times \left(\frac{\left[\frac{\mu_{en}}{\rho}(E)\right]_{spongiosa}}{\left[\frac{\mu_{en}}{\rho}(E)\right]_{T}} \right) \times \left(\frac{M_{spongiosa,b}}{M_{spongiosa}} \right) \right] \tag{3.13}$$

where $D_{T,i}$ is the dose relative to tissue at location i, as given by equation (3.6), and measured at each of the locations selected for bone marrow measurements in bone b, the second term is the ratio of mass energy absorption coefficients for spongiosa in bone b relative to soft tissue, and the last term is the mass weight fraction of spongiosa at each location (mass of spongiosa in bone b, $M_{spongiosa,b}$, divided by total mass of spongiosa in the skeleton $M_{spongiosa}$ as given in Table G.6, Appendix G).

Based on the selected measurement locations, the dose to approximately 52% of the spongiosa will be determined. However, 44% of the remaining spongiosa is in the arms and legs and therefore will have a negligible dose since they are not directly in the X-ray beam. The clavicles and upper spine were the only other skeletal regions not allocated any TLD measurement locations, as for the bone marrow measurements. The spongiosa in these regions accounts for 4% of the total spongiosa and hence will have an insignificant contribution to the total bone surface absorbed dose.

The mass energy absorption coefficient for spongiosa depends on the bone and is a weighted summation for the proportion of active and inactive marrow and trabecular bone for that bone. The spongiosa to tissue ratio of mass energy absorption coefficients for each bone considered in this thesis are also given in Table G.6, Appendix G. The spongiosa mass energy absorption coefficients were determined from ICRU Report 46 (ICRU, 1992) using the energy dependent coefficients for adult red marrow, adult yellow marrow and cortical bone for a 10 year old child[iii].

Skin Absorbed Dose

Skin absorbed dose was measured using TLDs placed on the anterior, posterior and left and right lateral surfaces of the phantom. The TLDs were placed in the scan region to ensure that they were irradiated by the primary X-ray beam. The average absorbed dose measured by n TLDs was scaled by the ratio of the irradiated area to the overall phantom surface area (P_{SA}). This method was used as ICRP 60 assumes that the risk of skin cancer is proportional to the irradiated skin area (ICRP, 1991). The skin surface area proportions for a 10 year old are summarised in Table 3.7. The proportion of surface area irradiated for each CT protocol assessed is shown in Table 3.8. Other authors (Fujii et al., 2007; Kawaura et al., 2006; Nishizawa et al., 2008) have used a similar method. Nishizawa et al. (2008) calculated that the exposed area for a CT chest examination for an anthropomorphic phantom of a six year old child was 17.5%, and 25% for an abdominal-pelvic

[iii] In ICRU Report 46, spongiosa is a composition of cortical bone, red and yellow marrow (ICRU, 1992).

examination, which are similar to the irradiated surface area proportions used in this thesis.

Therefore, the absorbed dose to the skin (D_{skin}) was calculated by:

$$D_{skin} = \frac{P_{SA}}{n} \sum_{i}^{n} D_{T,i} \tag{3.14}$$

where $D_{T,i}$ is the absorbed dose to tissue at location i as given in equation (3.6).

Table 3.7: Skin surface area proportions for 10 year old (ICRP, 2002).

Region	**Skin surface area proportion**
Head	10.9%
Trunk	33.6%
Upper extremities	19.4%
Lower extremities	36.2%

Table 3.8: Irradiated proportion of skin surface area for 10 year old for specific CT examinations.

Examination	**Area irradiated**	**Irradiated skin surface area proportion** (P_{SA})
CT Brain	67% of head area	7.19%
CT Chest	50% of trunk	16.8%
CT Abdomen/Pelvis	60% of trunk	20.2%

Muscle Absorbed Dose

The muscle absorbed dose was calculated from an approximation of the absorbed dose to all soft tissue measured by the TLDs. It was assumed that muscle is uniformly distributed in the head and trunk. The average absorbed dose directly in the beam and outside of the beam to the head and trunk was calculated for all TLD locations that were classified as soft tissue (TLD locations inside bone, lens of the eye and on the skin surface were excluded). The total average absorbed dose to soft tissue in the head and the trunk was then calculated by weighting the average absorbed dose inside and outside of the beam by the volume of the head or trunk directly and indirectly irradiated, respectively. The total muscle absorbed dose was determined by weighting the head and trunk total average soft tissue absorbed doses by the muscle mass ratio for that region to the whole body muscle mass based on adult ratios (ICRP, 2009; Na et al., 2010), assuming that the ratios are similar between children and adults. From these ratios, 3% of muscle mass is in the head and 51% in the trunk. The remainder is in the extremities, which were considered to receive a negligible exposure. Some authors (Fujii et al., 2007) exclude the muscle

absorbed dose calculation as part of the remainder organ absorbed dose based on the difficulty in deriving a value for this tissue.

3.3 Results

Alignment of the laser lights with the X-ray scan planes was first assessed. The laser lights are used to position a patient at the isocentre of the scanner. In the State of Victoria in Australia, it is required that agreement must be within ±2 mm (DoH, 2007). External laser lights, at a small distance from the centre of the gantry, are provided in the axial, coronal and sagittal scan planes to more easily align a patient. Internal laser lights are also provided in the axial plane only. It was found that the external laser light was not co-incident with the internal laser light in the axial plane (difference of 4-5 mm). It was confirmed that the internal laser light was co-incident with the scan plane (estimated deviation less than 0.75 mm) and therefore the internal laser light was used for alignment in this plane. The normalised measured $CTDI_{vol}$ values and displayed values are given in Table 3.9 and demonstrate good agreement, even for the tilted gantry.

Table 3.9: Values of normalised $CTDI_{vol}$ displayed on the console and measured. The percentage difference between the values is also provided.

Filter	**kV_p**	**Beam Collimation (mm)**	**Normalised $CTDI_{vol}$ (mGy/100 mAs)**		**Percentage Difference**
			Console	**Measured**	
Head	120	10	16.8	16.9	1%
	120	18[a]	19.2	18.0	-6%
Body	120	10	6.3	6.0	-5%

[a] Performed with a tilted gantry to simulate experimental measurements.

Automatic tube current modulation was used on all CT examinations undertaken. The average current (mA), $CTDI_{vol}$, DLP and scan length values for each CT examination performed on the TLD loaded phantom are summarised in Tables 3.10 and 3.11.

The TLD measured organ and tissue absorbed doses for the three paediatric CT examinations assessed in this thesis are shown in Table 3.12 and Figure I.1 (Appendix I). The highest average absorbed dose is to the brain (33.6 mGy) and eye lens (19.3 mGy) for the brain examination. The highest mean absorbed dose for the chest examination is for the thyroid and ET region (10.9 mGy) and for the abdomen/pelvis examination is the stomach (8.9 mGy). The range of measured absorbed doses and mAs and $CTDI_{vol}$ normalised absorbed doses have also been provided in Tables I.1 to I.3 (Appendix I). Organs on the periphery of the scan volume can have a significant variation in absorbed dose across the organ due to partial irradiation. For example, the measurement points in the kidney for the chest examination resulted in doses of 2.8, 1.7 and 0.9 mGy (cranial to caudal). For the brain and abdomen/pelvis examinations where the kidney was either completely

Table 3.10: Values of tube current (mA) and rotation time product (mAs) for the phantom CT examinations.

Examination	Average mA (min, max)[a]	Average Actual mAs[b]	Average Effective mAs[c]	Q_{ref} Effective mAs[d]
CT Brain	345 (102, 379)	259	259	270
CT Chest	155 (112, 199)	78	78	80
CT Abdomen/Pelvis	160 (114, 175)	80	64	60

[a] The average current was derived from a single CT examination performed on a TLD loaded CIRS anthropomorphic phantom of a 10 year old child by averaging the mA values for each single rotation.
[b] The average actual mAs was calculated by multiplying the average current (mA) by the rotation time (sec).
[c] The average effective mAs was calculated by dividing the average actual mAs by the pitch.
[d] Q_{ref} is the Imaging Quality Reference mAs, which is a Siemens specific setting used for automatic tube current modulation (CARE Dose 4D), which is set by the user for each protocol. This value is adjusted based on image quality requirements and the amount of noise acceptable in the image. It is defined in terms of the effective mAs (actual mAs divided by pitch).

outside the scanned volume or located directly within it, the absorbed doses were more consistent.

The absorbed dose to soft tissue for the colon, red bone marrow and bone surface measurement locations are shown in Table 3.13. The absorbed doses for these organs and tissues are not based on the simple average of multiple TLDs in each organ (as detailed in the Methods Section) and have therefore been provided individually. As expected, the colon absorbed doses are all negligible for the brain examination. They are slightly higher for the CT chest examination, particularly for the transverse colon in the upper large intestine which is closest to the scanned volume for a chest scan. The measured colon absorbed doses are all higher for the abdomen/pelvis examination where the colon is directly irradiated. The measured absorbed doses vary considerably for the locations selected for the red bone marrow and bone surface calculations. This is expected since these locations range from the skull to the pelvis and therefore may be directly irradiated, partially irradiated or completely outside of the scanned volume. This is evident in the range of measured absorbed doses for all examinations, although it can be most readily seen in the brain examination where the absorbed dose to the skull measurement locations is 41 mGy, while all other locations are less than 1 mGy.

A further comparison of individual TLD measured absorbed doses from all three CT examinations is shown in Figure 3.8. These graphs show the individual TLD measurements from the top of the phantom (cranial, slab 1) to the base (caudal, slab 31). Out-of-field doses demonstrated a gradual reduction in dose with distance from the scanned volume for each examination, as expected. The extent of over-ranging for the helical examinations has also been indicated on these graphs.

Table 3.11: Average values of $CTDI_{vol}$, DLP and scan length for the phantom CT examinations.

Examination	**Average $CTDI_{vol}$[a,b] (mGy)**	**Average DLP[a,b] (mGy·cm)**	**Average Scan Length[a,c] (cm)**
CT Brain	40.0±0.3	640±5	16.006±0.005[b]
CT Chest	5.72±0.08	152±10	26.6±1.5
CT Abdomen/Pelvis	4.56	168±3	36.9±0.7

[a] The average $CTDI_{vol}$, DLP and scan length were calculated from a series of three CT examinations using identical protocols performed on a TLD loaded CIRS anthropomorphic phantom of a 10 year old child. The range is two standard deviations calculated from the series of three examinations.

[b] Dose indicators for the CT brain examination were displayed on the CT scanner in terms of the 16 cm diameter phantom and in terms of the 32 cm diameter phantom for the CT chest and abdomen/pelvis examinations.

[c] The scan length for the tilted brain scan on the CT scanner is taken as the length perpendicular to the beam axis. This is not the actual length scanned on the patient.

The effective doses calculated from the measured absorbed doses using the ICRP 60 and ICRP 103 formalisms are shown in Table 3.14. The effective dose computed using ICRP 103 was 22% lower for the CT brain examination, 16% higher for the CT chest examination and only 4% lower for the CT abdomen/pelvis examination when compared with the effective dose computed using ICRP 60. The differences are predominantly due to revision of the tissue weighting factors.

3.4 Discussion

3.4.1 Comparison of Organ and Tissue Absorbed Doses

Table 3.12 and Figure I.1 (Appendix I) provide a comparison of mean organ and tissue absorbed doses from the TLD measurements for the three CT examinations assessed. Without taking into account the relative radiosensitivities of the organs and tissues, the highest absorbed doses are to the bone surface, brain and eye lenses for the CT brain examination. Despite the angling of the gantry, the eye lenses still receive a significant dose. The highest thyroid absorbed dose is from the CT chest examination and this is dependent on each individual scan and the selection of collimation as the thyroid may or may not be within the scan volume. Even when it is outside the scan volume it is likely to receive a dose from scattered radiation, over-beaming and over-ranging in the case of helical examinations when the chest is being imaged. As expected, organs within the scan volume receive higher absorbed doses than those outside the scan volume.

Lens Absorbed Dose

The lens of the eye does not need to be considered for stochastic effects. However, it is useful to consider the deterministic effects, such as cataracts, which have a threshold of

Table 3.12: TLD measured organ and tissue absorbed doses in an anthropomorphic phantom of a 10 year old child for different CT examinations.

Organ/Tissue	**Absorbed Dose (mGy)**[a] **Mean±2σ**		
	CT Brain	**CT Chest**	**CT Abdomen/Pelvis**
Bone Marrow	6.1±0.3	2.4±0.1	3.2±0.1
Colon	0.026±0.001	0.52±0.03	8.0±0.4
Lung	0.46±0.02	9.9±0.4	4.1±0.2
Stomach	0.068±0.003	4.8±0.2	8.9±0.4
Breast	0.27±0.01	9.1±0.4	1.29±0.06
Gonads	0.0127±0.0006	0.080±0.004	3.7±0.2
Bladder	0.0111±0.0006	0.080±0.004	6.9±0.3
Oesophagus	0.48±0.02	9.2±0.4	3.3±0.1
Liver	0.118±0.005	10.5±0.5	8.5±0.4
Thyroid	1.67±0.07	10.9±0.5	0.24±0.01
Bone Surface	5.0±0.2	3.4±0.2	3.6±0.2
Brain	33.6±1.4	0.22±0.01	0.033±0.001
Salivary Glands	2.7±0.1	1.32±0.06	0.117±0.005
Skin	2.0±0.3	1.38±0.09	1.7±0.1
Total Remainder	0.49±0.02	4.4±0.2	4.9±0.2
Adrenals	0.094±0.005	5.1±0.3	6.9±0.3
ET Region	1.67±0.07	10.9±0.5	0.24±0.01
Gall Bladder	0.054±0.003	2.7±0.2	8.6±0.5
Heart	0.51±0.02	8.6±0.4	1.02±0.05
Kidney	0.064±0.003	1.80±0.09	8.3±0.4
Lymph Nodes	0.53±0.02	2.5±0.1	2.8±0.1
Muscle	0.53±0.02	2.5±0.1	2.8±0.1
Oral Mucosa	2.7±0.1	1.32±0.06	0.117±0.005
Pancreas	0.084±0.004	6.4±0.3	8.7±0.4
Prostate	0.0087±0.0007	0.057±0.005	5.8±0.4
Small Intestine	0.023±0.001	0.36±0.02	8.5±0.4
Spleen	0.156±0.007	9.2±0.4	7.9±0.4
Thymus	0.47±0.02	9.3±0.4	0.81±0.04
Uterus/Cervix	0.0126±0.0009	0.115±0.008	6.6±0.4
Eye Lenses	19.3±0.9	0.191±0.009	0.040±0.002
Testes	0.0115±0.0007	0.029±0.003	0.99±0.05
Ovaries	0.0139±0.0008	0.131±0.007	6.4±0.3

[a] Errors are expressed as two standard deviations of the combined random and systematic errors.

Table 3.13: TLD measured absorbed doses to soft tissue in the colon consisting of the upper large intestine (ULI) and lower large intestine (LLI) and the bone locations for the red bone marrow (RBM) and bone surface (BS) measurements in an anthropomorphic phantom of a 10 year old child for different CT examinations.

Organ/Tissue	**Absorbed Dose to Soft Tissue (mGy)**		
	CT Brain	**CT Chest**	**CT Abdomen/Pelvis**
Ascending colon (ULI)	0.03	0.34	8.50
Transverse colon (ULI)	0.03	1.04	8.28
Descending colon (LLI)	0.03	0.33	8.63
Rectosigmoid colon (LLI)	0.01	0.12	6.04
Pelvis (RBM/BS)	0.01	0.10	6.06
Ribs (RBM/BS)	0.49	9.09	4.66
Skull (RBM/BS)	41.09	0.14	0.03
Spine – middle (RBM/BS)	0.16	7.73	4.52
Spine – lower (RBM/BS)	0.02	0.32	5.59
Scapulae (RBM/BS)	0.55	8.05	0.59

Table 3.14: Values of effective dose for standard paediatric CT examinations calculated from TLD measurements of absorbed dose using the ICRP 60 ($E_{TLD,60}$) and ICRP 103 ($E_{TLD,103}$) formalisms. The percentage difference between the values is also provided.

Examination	$\mathbf{E}_{TLD,60}$ **(mSv)**	$\mathbf{E}_{TLD,103}$ **(mSv)**	$(\mathbf{E}_{TLD,103}\text{-}\mathbf{E}_{60})/\mathbf{E}_{60}$
CT Brain	1.8	1.4	-22%
CT Chest	4.3	5.0	16%
CT Abdomen/Pelvis	5.0	4.8	-4%

about 0.5 Gy (ICRP, 2011). The TLD measured absorbed dose to the lens was 19 mGy for the CT brain examination. This is similar to the absorbed dose (15±2 mGy) measured in another study (Heaney and Norvill, 2006) for adult CT head examinations with gantry angulation. Despite angling the gantry as a dose saving technique, the lens dose remains relatively high although well below the deterministic threshold. This dose may have resulted from scattered radiation or over-beaming, where the penumbral region of the X-ray beam is not used for image formation. This ensures uniform exposure of the MDCT detectors, but results in exposure of the patient that does not contribute to the data acquisition. The portion of the beam missing the detectors is greater for smaller collimations as was the case for the brain examination.

Directly Irradiated Organs

Measured absorbed doses for multiple TLDs located in directly irradiated large organs varied throughout the organ volume. This is due to differences in photon attenuation for measurement locations that are superficial compared with those that are deeper within

an organ and/or relative to the body and other structures (e.g. bony) within it. The individual measured absorbed doses in the brain for the scan of the head region ranged from 25.9 to 41.2 mGy. This variation in dose is also attributable to non-uniformity in the exposure because of gantry angulation. The range of absorbed doses in the lung for the chest examination was 8.4 to 11.4 mGy and in the liver was 7.3 to 9.8 mGy for the abdomen/pelvis examination. It is therefore necessary to use multiple measurement locations across larger organs, so that the mean absorbed dose adequately reflects the heterogeneity in dose deposition.

Partially Irradiated Organs

Organs on the periphery of the scan volume can have a significant variation in absorbed dose across the organ due to partial irradiation. For example, as already discussed, the measurement points in the kidney for the chest examination resulted in absorbed doses of 2.8, 1.7 and 0.9 mGy (cranial to caudal). For the brain and abdomen/pelvis examinations where the kidney was either completely outside the scanned volume or located directly within it, the absorbed doses were more consistent. For the brain examination the three kidney measurement points were all 0.1 mGy and, cranial to caudal, the kidney absorbed doses were 8.3, 8.2 and 8.4 mGy for the abdomen/pelvis examination. Averaging of multiple measurement points is necessary for organs which are partially irradiated.

Selecting the location of an organ or tissue can have a considerable effect on the measured absorbed dose when the organ or tissue is located on the edge of the scan volume. The thyroid is on the periphery of the scan range for the chest examination and therefore may or may not be directly exposed depending on operator technique. For the chest examination performed on the anthropomorphic phantom, the dose to the thyroid (10.9 mGy) appears to indicate that it is in the primary beam. However, this dose may also be due to over-beaming and/or over-ranging.

It is clear from Figure 3.8 that absorbed doses of equivalent magnitude to those in the directly irradiated scanned volume were measured outside of the imaged range. The dotted lines on these figures represent the estimated additional scan length due to over-ranging (van der Molen and Geleijns, 2007) necessary for data interpolation in helical scans. The additional length at the beginning and end of the imaged volume correlates well with absorbed doses measured beyond the imaged volume. Over-ranging is greater for larger beam collimation and higher pitch, which may reduce scan times, but at the cost of increased dose in the over-ranging region (Fujii et al., 2009).

The extrathoracic (ET) region is included as a remainder organ in ICRP 103. It was difficult to determine a location in the anthropomorphic phantom for this tissue and instead the thyroid absorbed dose was used as a substitute. This may be a poor approximation when the scan volume is adjacent to this region since the thyroid may be in the scan range, while the ET region is not, but it will still be allocated a dose as though it were ex-

posed to the primary beam. This is a recognised limitation of substituting organ absorbed doses.

Out-of-Field Doses

Out-of-field doses have been measured for tissues and organs outside the scanned volume for all three CT examinations (Figure 3.8). There is a gradual reduction in dose with distance from the scanned volume for each examination. The extent of out-of-field doses is greatest for the brain examination where the mAs (current exposure time product) is more than three times higher than either body examination and where the gantry was angled towards the body for the examination. It is interesting to note that organs and tissues outside of the scanned volume for the brain examination, such as the lung, breast, oesophagus, thymus, heart and liver, have all received a small absorbed dose. This may result from the uncertainty in measurement for the TLDs at low doses or may arise from scattered radiation. The increased photon flux and/or gantry angulation may have resulted in a higher scattered radiation dose to distant organs for this examination. Alternatively, since the brain is located at a distal part of the body, there is greater body length for the scattered dose to be deposited and hence measured, compared with an examination of the chest or abdomen/pelvis.

3.4.2 ICRP 60 versus ICRP 103 Effective Dose

The ICRP defines effective dose as a parameter for expressing stochastic risk from radiation exposure and recommends its use only for radiation protection purposes (ICRP, 2007b). However, effective dose has found widespread application in evaluating doses from medical exposure due to its effectiveness in condensing a complex set of parameters for any exposure situation into a single quantity (McCollough et al., 2010). It is routinely used to compare doses resulting from variations in protocols or from different modalities. However, while taking into account the nature of the exposure, characteristics of a specific individual are not considered. Hence, effective dose provides a broad, generic estimate and is an indication only of the typical dose. Although it should not be applied to the individual, it is often used for incident dose assessments and other situations involving specific patients to express a "relative" risk. Despite its use when inappropriate, effective dose is a useful parameter for expressing risk.

Over time the definition of effective dose has changed, as the effects of radiation on different organs and tissues is continually revised in accordance with scientific knowledge. These changes are primarily due to tissue weighting factors, although the inclusion of additional organs and tissues to be considered for stochastic risk has also occurred. Effective dose is derived from the mean organ and tissue absorbed doses and any changes to tissue weighting factors will not affect the absorbed dose. Therefore, it is useful to measure organ and tissue absorbed doses and from these effective dose may be computed using

various ICRP definitions.

The measurements undertaken using the TLD loaded anthropomorphic phantom were used to derive effective dose based on both the ICRP 60 and ICRP 103 formalisms ($E_{TLD,60}$ and $E_{TLD,103}$ respectively). A comparison of these values show that the ICRP 103 definition leads to a lower effective dose for a CT brain examination, a higher value for a CT chest examination and approximately the same value for a CT abdomen/pelvis examination (Table 3.14). It is expected that the effective dose for examinations involving the brain will decrease using the ICRP 103 definition. Since the brain is directly irradiated the tissue weighting factor according to ICRP 60 is 0.025 (remainder splitting rule), whereas for ICRP 103 the brain is identified as a primary organ with a weighting factor of 0.01, accounting for the decrease in effective dose. Similarly, Christner et al. (2010) found a 39% reduction for CT brain examinations for adults.

However, there are other studies (Deak et al., 2010; Huda et al., 2011) that show an increase in the effective dose estimate for CT brain examinations based on the ICRP 103 definition, when compared with the ICRP 60 definition. The ICRP 60 effective dose estimates made by Deak et al. (2010) for CT brain examinations appear to apply a tissue weighting factor of 0.005, rather than 0.025, for the brain dose and consequently underestimate the ICRP 60 effective dose. Therefore, Deak et al. (2010) conclude that the ICRP 103 effective dose estimate for brain examinations increases relative to the ICRP 60 estimate, which does not agree with the findings of this thesis.

The study by Huda et al. (2011) similarly reports an increase in effective dose estimates for CT head examinations for adults according to ICRP 103, when compared with ICRP 60 effective dose estimates. They have made use of the ImPACT CT Patient Dosimetry Calculator (version 1.0) for effective dose estimates according to either ICRP 60 or ICRP 103. ImPACT does employ the ICRP splitting rule for ICRP 60 effective dose calculations. However, the effective dose estimates in ImPACT are based on Monte Carlo simulations, which use a mathematical anthropomorphic phantom. Not all of the organs and tissues specified in the ICRP 103 effective dose estimate were included in the Monte Carlo calculations and the method of substituting known organ absorbed doses has been used by ImPACT. For example, the salivary glands and oral mucosa in ImPACT have been allocated the brain absorbed dose. Since the brain absorbed dose is relatively high when directly irradiated in a CT brain examination, the salivary glands and oral mucosa are allocated this same absorbed dose, even though it is most likely that they would not be directly irradiated in this type of scan. Therefore, the ICRP 103 effective dose estimates in ImPACT are higher relative to the ICRP 60 effective dose estimates for a brain examination due to the inappropriately high absorbed doses allocated to these tissues, which are only included in the ICRP 103 effective dose estimate and not the ICRP 60 effective dose. These differences are discussed further in Chapter 5.

One of the significant changes to tissue weighting factors in ICRP 103 was the increase

from 0.05 to 0.12 for the breast weighting factor. This is demonstrated by a 16% increase in the effective dose using ICRP 103 tissue weighting factors for a CT chest examination, which reflects the increased radiosensitivity attributed to the breast. Li et al. (2011a) also found a 16% increase and Fujii et al. (2009) a 19% increase in effective dose for paediatric CT chest examinations when using ICRP 103 instead of ICRP 60.

The tissue weighting factor for the gonads also changed significantly, decreasing from 0.20 to 0.08 in ICRP 103. However, the effective dose for a CT abdomen/pelvis examination using ICRP 103 is only 4% lower than the ICRP 60 value. In this case, the reduction in the gonad tissue weighting factor is balanced by an increase in the weighting factor for the remainder organs from 0.05 to 0.12. Fujii et al. (2009) also found a 4% decrease in the ICRP 103 effective dose for CT abdomen/pelvis examinations (Fujii et al., 2009). For adults, Christner et al. (2010) similarly found a 14% increase for CT chest examinations and 7% decrease for CT abdomen/pelvis examinations.

3.5 Conclusions

Organ and tissue absorbed doses have been measured for CT brain, chest and abdomen/pelvis examinations using high sensitivity TLDs loaded in an anthropomorphic phantom of a 10 year old child and for currently used protocols on the RCH CT scanner. When considering stochastic effects, the highest measured absorbed dose was to the brain as a result of radiation exposure from a CT brain examination. However, a lower absorbed dose to a more radiosensitive organ may in fact lead to a greater stochastic risk. The relative radiosensitivities of the organs and tissues have only broadly been taken into account in the present analysis using the averaged tissue weighting factors intended for adults. Chapter 8 provides a detailed assessment of the radiation induced cancer incidence and mortality risks associated with the measured organ absorbed doses, using age-specific organ risk factors.

The TLD measurements demonstrated some of the issues in estimating average absorbed dose to an organ or tissue. Directly and fully irradiated organs and tissues lead to more consistent dose measurements throughout their volume. Organs and tissues on the periphery of the scan volume had a range of dose measurements and were also affected by over-ranging in helical scanning. Even organs distant from the scanned volume had a small amount of radiation exposure, likely due to scattered radiation.

From the measured absorbed doses, effective doses have been derived based on ICRP 60 and ICRP 103 formalisms. Effective dose is not a physical quantity but an estimate of biological detriment reflecting the risk from radiation exposure. It is a useful generic quantity that can be used for optimisation in diagnostic radiology. However, differences arise in the effective dose for paediatric CT depending on whether the ICRP 60 or ICRP 103 formalism is used. These changes reflect the lower weighting now applied to the brain for

direct irradiation, the increased assessed radiosensitivity of the breast and the remainder organs collectively and the decrease in assessed radiosensitivity for the gonads.

3.6 Publications Arising from this Chapter

1. **Brady, Z.**, Cain, T. M. and Johnston, P. N., *Differences in using the International Commission on Radiological Protection's Publications 60 and 103 for determining effective dose in paediatric CT examinations*, Radiation Measurements, 2011, 55:132-142 (Brady et al., 2011e).
2. **Brady, Z.**, Cain, T. M. and Johnston, P. N., *Effective dose calculation in CT using high sensitivity TLDs (EPSM ABEC 2010 Conference Proceedings)*, Australasian Physical & Engineering Sciences in Medicine, 2011, 34(1):111 (Brady et al., 2011b).
3. **Brady, Z.**, Cain, T. M. and Johnston, P. N., *Calculations of effective dose for paediatric CT examinations* presented at the 16th International Conference on Solid State Dosimetry, 2010, Sydney, Australia (Brady et al., 2010b).

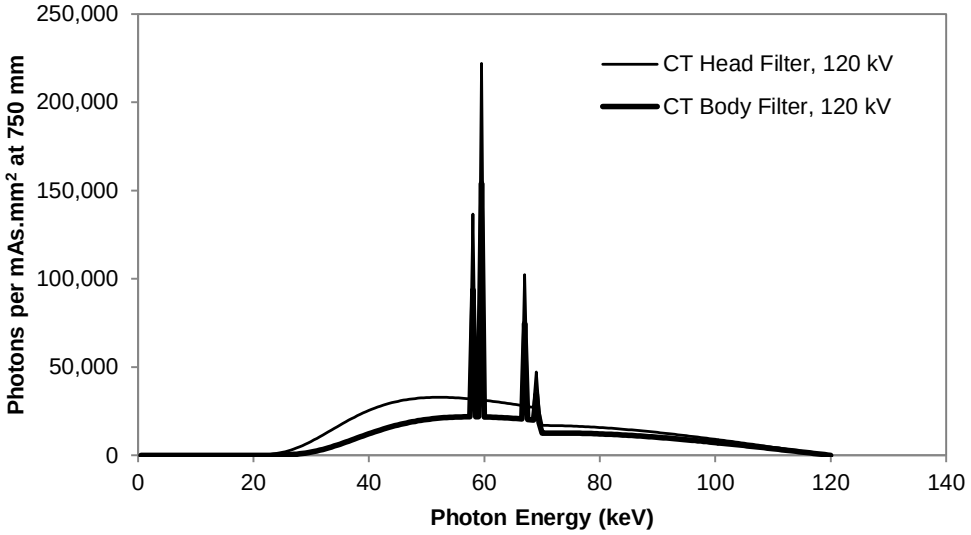

Figure 3.1: X-ray photon spectra at 120 kV_p for the Siemens Sensation 16 CT scanner using the head filter (7.5 mm Al HVL [input parameter: 7 mm Al filtration], mean photon energy 63 keV) and body filter (8.7 mm Al HVL [input parameter: 11.1 mm Al filtration], mean photon energy 66 keV) (Reilly and Sutton, 1997).

a) b)

c) d)

Figure 3.2: CIRS anthropomorphic phantoms a) examples of phantoms of a male adult, female adult and baby, b) RCH CIRS phantom of a 10 year old child assembled (without assembly frame), c) RCH CIRS phantom of a 10 year old child's head showing some slab sections removed, d) with head slab sections disassembled.

Figure 3.3: Anterior-posterior and lateral views of the anthropomorphic phantom of a 10 year old child, with 3D reconstruction of the skeleton shown on the left.

Figure 3.4: Slab from phantom with TLDs being loaded from storage and annealing tray using vacuum tweezers. Each plug was halved with the TLDs placed between the two halves.

Figure 3.5: TLD-100H chips (x25) placed in Perspex holder for calibration irradiations.

Figure 3.6: Linac output check prior to calibration of the set of TLDs. Solid water blocks were used and a 0.6 cm^3 Farmer ion chamber was placed at 100 cm from the focus with 5 cm of solid water between the source and ion chamber.

a) b)

c) d)

Figure 3.7: TLD measurement locations in the anthropomorphic phantom of a 10 year old child in the lung (circled in images a and b) and in the liver (circled in images c and d). The phantom slab numbers are a) 13, b) 15, c) 17 and d) 18.

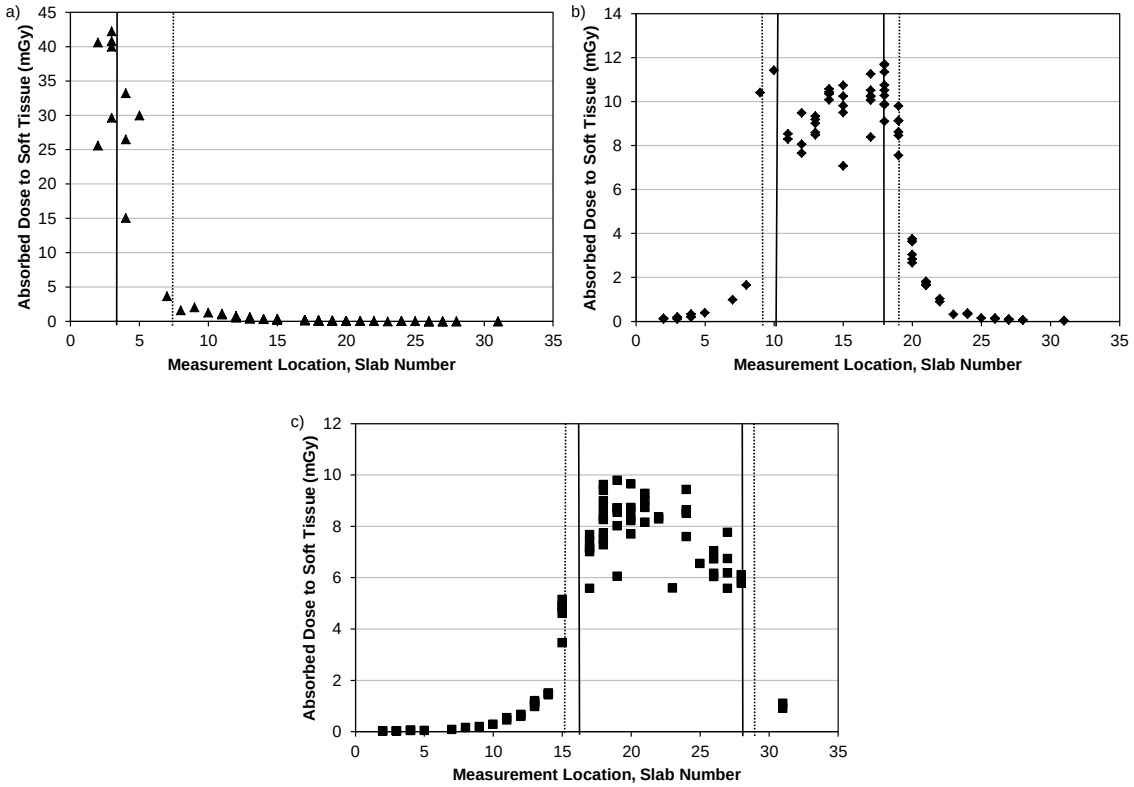

Figure 3.8: Individual absorbed dose to soft tissue measurements for various CT examinations of the TLD loaded anthropomorphic phantom of a 10 year old child. The horizontal axis corresponds to the slab number of the phantom (slabs 1-31), where a single slab may be loaded with multiple TLDs. a) CT brain examination: the axial scan range was from above the head and because of the tilt of the gantry only fully irradiated down to slab 3 (solid vertical line), and partially irradiated down to slab 7 (dotted line). b) CT chest examination: the scan range included the entire thorax anatomy from slab 10 (first solid vertical line) to half way through the liver, slab 18 (second solid vertical line). The dotted lines represent the extent of over-ranging for the helical scan (van der Molen and Geleijns, 2007). c) CT abdomen/pelvis examination: the scan range was from just above the diaphragm, slab 16 (first solid vertical line) to symphysis pubis, slab 28 (second solid vertical line). The dotted lines represent the extent of over-ranging for the helical scan (van der Molen and Geleijns, 2007).

Chapter 4

MOSFET Dosimetry Comparison

4.1 Introduction

A measurement device that is finding increased application in the diagnostic imaging field (Bower and Hintenlang, 1998; Dong et al., 2002; Frush and Yoshizumi, 2006; Hollingsworth et al., 2007; Hurwitz et al., 2007a,b, 2009; Jones et al., 2005; Miksys et al., 2010; Mukundan et al., 2007; Peet and Pryor, 1999; Sessions et al., 2002; Wang et al., 2005; Yoshizumi et al., 2007, 2003) is the metal oxide semiconductor field effect transistor (MOSFET) (Figure 4.1). A MOSFET consists of a silicon n-type substrate, with a polysilicon conducting gate electrode mounted on a silicon dioxide (SiO_2) layer grown on the substrate. Doped (p^+) source and drain terminals are separated by the gate region.

When a negative voltage is applied to the gate, holes (positively charged) are attracted to the gate electrode and are trapped at the substrate-SiO_2 interface. When there is an accumulation of charge a conduction channel (p-channel) is formed. The required voltage to generate the conduction channel is called the threshold voltage. When ionising radiation is incident on the MOSFET and passes through the SiO_2 layer, electron-hole pairs are created which changes the charge carrier trapping within the device. Holes move towards the substrate-SiO_2 interface where they become trapped, while electrons move away from the gate. The overall effect is to change the threshold voltage required to initiate the conduction channel. It is the shift in threshold voltage which is measured (before and after irradiation by ionising radiation) which is proportional to the radiation dose.

The major advantage of MOSFETs is that they are real time. However, there are other factors, such as angular and energy dependence, that must be taken into consideration when using MOSFETs instead of TLDs. MOSFETs were used in this thesis with the

anthropomorphic phantom of a 10 year old child to repeat a limited number of the TLD measurements. This allowed a comparison between the two dosimetry methods. The MOSFETs used were a trial set on loan to the RCH from Best Medical Canada (Ottawa, Ontario, Canada).

4.2 Methods

High sensitivity MOSFET dosemeters (TN-1002RD, Best Medical Canada, Ottawa, Ontario, Canada) were used to repeat some of the measurements undertaken with the TLD-100H chips. Five individual MOSFETs were connected to each bias module, which transferred data wirelessly to a laptop. Two bias modules with 10 high sensitivity MOSFETs were calibrated and used (Figure 4.2).

The MOSFETs were calibrated using a general radiography X-ray tube (Optimus 80, Philips Healthcare, Andover, Massachusetts, US) matched to the CT scanner beam quality to be used during the measurements. This was achieved on the general X-ray tube by using 125 kV_p and adding 1 mm Al and 0.2 mm Cu filters. This model of X-ray tube is limited to selection of 117 kV_p and 125 kV_p at higher kV_p, hence 120 kV_p could not be used. When measured with a calibrated Unfors Xi solid state detector (Unfors, Billdal, Sweden), the HVL of the beam was 8.1 mm Al. For calibration, each set of five MOSFETs connected to a bias module was placed adjacent to a 6 cm^3 Model 10X6-6 ion chamber connected to a Radcal 9095E electrometer (Radcal, Monrovia, California, US) and a calibrated Unfors Xi solid state detector (Figure 4.3).

Each MOSFET wire was colour coded and connected to the same terminal in the same bias reader for calibration and subsequent measurements. Three exposures were made at approximately 10 mGy and millivolt to centrigray (mV/cGy) conversion factors were computed using the MOSFET software (D_XPOSURE Software, Version 2.2, Best Medical Canada, Ottawa, Ontario, Canada). All MOSFET measurements were read out immediately after exposure to avoid any additional charge build up. Figure 4.4 shows differences in conversion factors for different beam qualities with HVL ranging from 3-8 mm Al (measured by the Unfors Xi). The values are consistent and hence a single conversion factor was used.

The CIRS anthropomorphic phantom of a 10 year old child used for TLD measurements was also used for the MOSFET measurements. When using MOSFETs all portions of the plug were removed from the phantom slab and the MOSFET and wire were inserted into the hole. Electrical tape was used to cushion the MOSFET wires between the slabs (Yoshizumi et al., 2007). The combination of the MOSFET wire and tape resulted in a small gap between adjacent phantom slabs. Care was taken when moving the phantom for the experimental set up as the MOSFET wires protruded when the phantom was fully assembled (Figure 4.5).

Figure 4.1: Schematic of a metal oxide semiconductor field effect transistor (MOSFET) (Hallil, 12-13 June 2009).

Figure 4.2: Two Mobile MOSFET bias modules with five high sensitivity MOSFETs connected to each module. The wires of each MOSFET are colour coded for easy identification. In the photograph, protective casings are around the individual MOSFETs.

Figure 4.3: MOSFET calibration configuration.

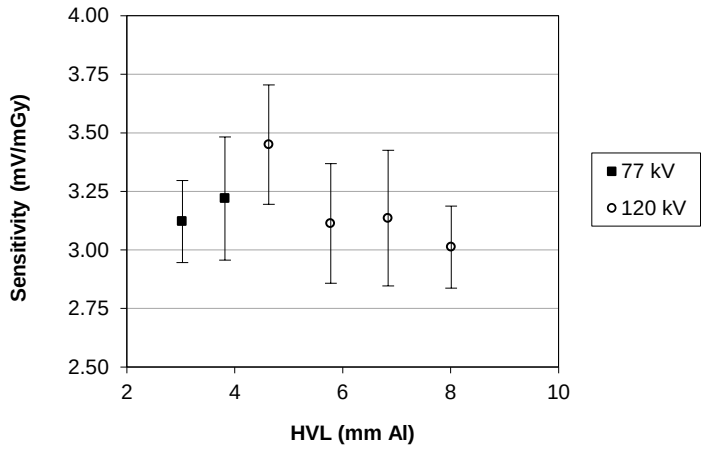

Figure 4.4: MOSFET sensitivity for different beam qualities. Error bars are two standard deviations based on three measurements at each beam quality.

Figure 4.5: MOSFET wires protrude when the phantom is fully assembled.

For measurements of absorbed dose for CT examinations, the MOSFETs were placed inside the liver and lung within the anthropomorphic phantom. The tissue absorbed dose (D_T) was calculated from the measurement of absorbed dose in air (D_{air}), taking into account the mass energy absorption coefficient (μ_{en}/ρ) of the MOSFET oxide coating (Sessions et al., 2002), by:

$$D_T\,[\mathrm{Gy}] = D_{air}\frac{\left[\mu_{en}/\rho\right]_T}{\left[\mu_{en}/\rho\right]_{air}} = X\,[\mathrm{R}] \times 0.00876\left[\frac{\mathrm{J}}{\mathrm{kg}}\mathrm{R}^{-1}\right]\frac{\left[\mu_{en}/\rho\right]_{oxide}}{\left[\mu_{en}/\rho\right]_{air}}\frac{\left[\mu_{en}/\rho\right]_T}{\left[\mu_{en}/\rho\right]_{oxide}} \quad (4.1)$$

The conversion factor calculated for each MOSFET relative to the Unfors dose measurement already takes into account the conversion from roentgen to gray (0.00876 Gy per R). The ratio of mass energy absorption coefficients (tissue to air) at 60 keV (effective energy of the CT beam, Figure 3.1) for soft tissue is 1.07 and for the lung is 1.08 (Hubbell and Seltzer, 2004). These were applied when calculating the absorbed dose for the relevant tissues.

4.3 Results

The ratio of MOSFET to TLD measured absorbed doses for seven locations in the liver and lung are shown in Figure 4.6. These were obtained using the protocol for a CT chest examination for children aged over 10 years (Table 3.1). The MOSFET measurements are on average 9% higher than the TLD measurements.

4.4 Discussion

TLDs have traditionally been the gold standard for medical dosimetry. However, they are not easy to use and require careful, reproducible preparation and calibration. Furthermore, they are passive dosemeters and do not provide a real time result. MOSFETs are finding increased application as a potential dosimetry tool for medical exposures. Although they have not yet gained widespread acceptance, there are numerous studies based on MOSFET measurements for diagnostic radiology (Bower and Hintenlang, 1998; Dong et al., 2002; Ehringfeld et al., 2005; Frush and Yoshizumi, 2006; Hurwitz et al., 2007a,b, 2009; Jones et al., 2005; Miksys et al., 2010; Peet and Pryor, 1999; Yoshizumi et al., 2007), including articles assessing paediatric CT doses (Coursey et al., 2008; Hollingsworth et al., 2007; Mukundan et al., 2007).

Some of the known limitations of MOSFETs are the energy and angular dependence, particularly for lower energies encountered in diagnostic radiology (Dong et al., 2002; Ehringfeld et al., 2005; Jones et al., 2005; Wang et al., 2005). However, these may be addressed to some extent with consistent positioning and appropriate correction factors.

Dong et al. (2002) have demonstrated an increased sensitivity of high sensitivity MOSFETs at low doses (below about 5 mGy) compared with TLD-100H chips which varied less than 3% over the same dose range suggesting that TLDs may be more suitable at the very low doses typical of plain radiography.

In this thesis, the absorbed doses measured with the MOSFETs were within reasonable agreement (on average within 9%) of the TLD measurements (Figure 4.6). Yoshizumi et al. (2007) compared the same high sensitivity MOSFETs against TLD-100 chips for CT examinations in an adult anthropomorphic phantom. They found the difference between the dosimetry methods ranged from 1% to 27% in the scanned volume (Yoshizumi et al., 2007). The disparity was much greater for organs outside of the field of view, due to the lower limit of detection for MOSFETs (1.4 mGy compared with 0.20 mGy for TLDs) (Yoshizumi et al., 2003). Of the individual TLD measured absorbed doses for CT brain, chest and abdomen/pelvis examinations (Chapter 3), only 48% of the measured doses were greater than 1.4 mGy. This was for all TLDs, including those placed distant from the scanned volume (e.g. testes for a CT brain examination). However, for the TLDs placed in the directly irradiated volume, the measured absorbed doses were predominantly above 5 mGy (Figure 3.8). Therefore, MOSFETs appear to be a reasonable alternative to TLDs for measuring CT organ absorbed doses in the scanned volume.

The main advantage of MOSFETs is the ability to make an immediate measurement. They can be placed in the same locations as TLDs, hence making real time organ and tissue dosimetry plausible. This benefit may even outweigh any limitations, since real time measurement will facilitate optimisation of protocols and simplify dosimetry in the clinical environment. For example, in Chapter 3 TLDs were used to measure organ and tissue doses in an anthropomorphic phantom for typical CT examinations including the initial topogram dose. The measured dose was attributable to both the topogram and scan doses. Using the MOSFETs it was quickly verified that for the measurement positions in the liver and the lung the topogram absorbed dose was on average only 2% (maximum 4%) of the total absorbed dose from the examination. This was not readily undertaken with the TLDs.

4.5 Conclusions

MOSFETs offer an alternative dosimetry method that is fast and easy to use. However, they do require initial calibration and conversion factors must be derived for all beam qualities and energies that are to be used. This is performed at acceptance and is labour intensive. Further studies are required to assess the necessary frequency of calibration, both over time and relative to the cumulative dose that each MOSFET receives. Furthermore, MOSFETs have a lifetime related to cumulative exposure and hence must be replaced on a semi-regular basis. TLDs also require labour intensive calibration, although TLD-100H material has the advantage of a relatively linear energy response. Both TLDs

and MOSFETs are small, fragile and require careful handling. TLDs remain the gold standard and are the more accurate method for undertaking dosimetry. However, considering that effective dose is intended to be a broad estimate of typical dose, the real time nature of MOSFETs may lead to the acceptance of some of these limitations. In the future, MOSFETs may become indispensable to medical imaging clinical dosimetry.

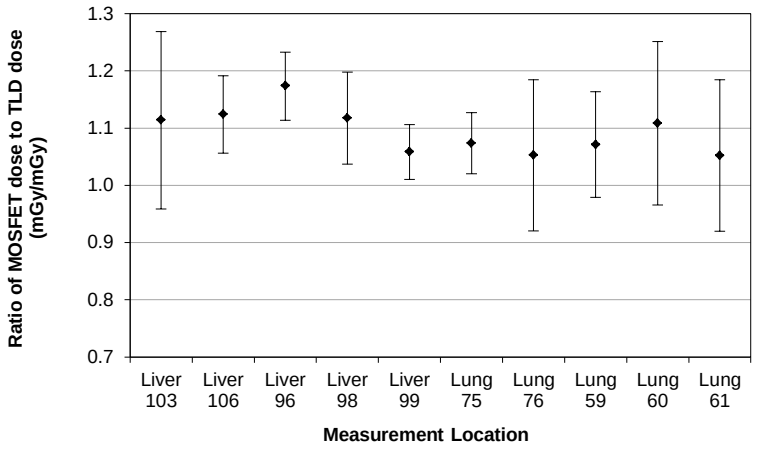

Figure 4.6: Ratio of MOSFET to TLD measured doses for the liver and lung. The number after the organ (e.g. Liver 103) refers to the position number in the anthropomorphic phantom. Errors are two standard deviations calculated from the combined errors from a series of three MOSFET and TLD measurements.

Chapter 5

Computational Dosimetry

5.1 Introduction

Estimates of organ absorbed dose and effective dose are frequently required for CT examinations in order to assess stochastic risk or to assist in the process of optimisation. Experimental dosimetry measurements, for example with thermoluminescence dosemeters (TLDs) or metal oxide semiconductor field effect transistors (MOSFETs) placed in an anthropomorphic phantom, are difficult to implement in the diagnostic radiology clinical environment. These methods require significant resources in terms of equipment, time and skilled staff, which often prevent radiology practices from performing experimental dosimetry. Therefore, it is necessary to have alternative, indirect or computational methods for determining CT dose.

Existing dose computational methods for medical exposure situations are predominantly based on Monte Carlo radiation transport simulations. For exposures from CT examinations there are various Monte Carlo-based dose calculators available (ImPACT, 2011; Kalender et al., 1999; Le Heron, 1993; Stamm and Nagel, 2011b). These are dependent on the type of CT scanner used and provide estimates of organ and tissue absorbed dose for a reference person of a standardised size and shape. More recent methods using Monte Carlo simulations for CT exposures provide a technique for estimating organ and tissue absorbed doses that is specific to the size of the patient and is independent of the CT scanner (Li et al., 2011a; Turner et al., 2011).

Currently there is no definitive method for undertaking CT dosimetry and multiple experimental and computational approaches exist. The choice between dosimetry methods is often more difficult when considering children, since the dose estimates need to be age-specific or reflect the range of ages necessary to accurately represent the paediatric population. Furthermore, with a wide variety of methods available, there is potential for doses to differ. Since organ and tissue absorbed doses are used for risk assessment and

effective dose for radiation protection purposes, it is important to assess the extent of the variability between different methods. There are only a limited number of studies comparing CT doses using experimental and/or computational techniques (Brix et al., 2004; Geleijns et al., 1994; Groves et al., 2004; Kim et al., 2011; Lechel et al., 2009; Lee et al., 2011), particularly for paediatric CT imaging (Deak et al., 2008; Li et al., 2011c).

The objective of this part of the thesis was to compare different computational methods for paediatric CT organ dosimetry and effective dose estimation to assess their reliability for clinical implementation. The types of anthropomorphic phantoms and categories of CT computational methods that can be used to assess medical exposures are reviewed in the background section. Several of the available computational dose methods for paediatric CT examinations were investigated using standard clinical protocols. The computed absorbed doses were compared with absorbed doses measured using TLDs placed in a physical anthropomorphic phantom representing a 10 year old child (Chapter 3). Different methods of determining effective dose were also assessed and compared with the effective doses calculated from the measured organ and tissue absorbed doses.

5.2 Background

5.2.1 Computational Anthropomorphic Phantoms

For most computational organ dosimetry methods, the patient must be modelled by an anthropomorphic phantom, which represents an idealised form of human anatomy (Lee and Bolch, 2006; Martin, 2007; Xu and Eckerman, 2010). The first type of computational phantom (1960s to 2000s) is often referred to as a stylised or mathematical phantom (Xu and Eckerman, 2010) and was originally developed by the Oak Ridge National Laboratory (ORNL) for the Medical Internal Radiation Dosimetry (MIRD) Committee (Snyder et al., 1969). This phantom represented a hermaphrodite adult and anatomical structures were defined by solid geometrical objects such as elliptical cylinders and cones. An independent set of ORNL phantoms, including children, were later developed by Cristy and Eckerman (Cristy, 1980; Cristy and Eckerman, 1987). The German National Research Centre for Environment and Health (GSF) also used the initial hermaphrodite adult phantom to develop an adult male and adult female for external dosimetry (Kramer et al., 1982).

The next class or generation (1980s to 2000s) of computational phantom is referred to as a voxel phantom (Xu and Eckerman, 2010). These phantoms were constructed by voxel segmentation from CT and magnetic resonance imaging (MRI) cross-sectional images of humans (Caon et al., 1999; Fill et al., 2004; Kramer et al., 2003; Lee et al., 2006a,c; Petoussi-Henss et al., 2002; Saito et al., 2001; Zankl et al., 1988). More recently a third generation of hybrid phantoms (2000s to present) have emerged (Xu and Eckerman, 2010), which use boundary representation (BREP) where exterior surfaces are defined by non-uniform rational B-splines (NURBS) and polygon mesh (PM) surfaces (Lee et al., 2007b,

2008a, 2010; Li et al., 2008, 2011a,b,c; Segars et al., 2008; Xu et al., 2007). The BREP modelling technique provides more anatomically realistic models that also allow deformation of surfaces, which is useful for organ motion or sizing (Xu and Eckerman, 2010) and scaling for different body morphometrics (Lee et al., 2010). Both voxel and hybrid phantoms are patient-specific, based on the images that were initially captured. Therefore, the standard technique is to scale the organs to match ICRP recommended reference organ masses (ICRP, 2002, 2006).

5.2.2 CT Scanner-Dependent Computational Methods

There are two main Monte Carlo data sets of normalised organ absorbed doses from CT exposures. These were generated by the UK National Radiological Protection Board (NRPB, now the Health Protection Agency, HPA) (Jones and Shrimpton, 1993, 1991) and the GSF (Zankl et al., 1991, 1993). These data sets provide organ absorbed dose data normalised to the CTDI measured in air at the isocentre ($CTDI_{air}$) of the CT scanner and are dependent on the type of scanner modelled in the Monte Carlo simulation. The NRPB data set is used via an Excel (Microsoft Office) interface in the "CT Patient Dosimetry Calculator" provided by the UK ImPACT group (ImPACT, 2011) and similarly the GSF data set is used via an Excel interface in the commercially available "CT-Expo" calculator (Stamm and Nagel, 2011b). Other calculators are also available (CTDOSE (Le Heron, 1993), CT-Dose, ImpactDose (formerly WinDose (Kalender et al., 1999)).

The design and specifications of the CT scanner are predictably proprietary information and as a result, Monte Carlo models generally simulate only a limited number of CT scanners. There are 23 data sets from the NRPB, modelling 27 scanners from Siemens, Picker, CGR, GE, and Philips that were clinically operational in the late eighties to early nineties (Jones and Shrimpton, 1993; Shrimpton and Edyvean, 1998). Notably, these are all single detector CT (SDCT) scanners. The GSF data set models the Siemens Somatom DRH scanner (Brix et al., 2004; Zankl et al., 1991), which was also included in the NRPB data set.

Since the data sets were generated for older scanners their relevance to new CT technology is potentially limited. However, the ImPACT group have addressed this by using an ImPACT Factor which matches new CT scanners to the existing NRPB Monte Carlo data sets using output dependent conversion factors (Lewis et al., 2000). The GSF data set similarly utilises the ImPACT method for matching new scanners to a set of scanner-specific correction factors which are related to the single scanner that was originally modelled (Nagel, 2002; Shrimpton and Edyvean, 1998). The scanner matching technique is a recognised limitation of using the existing data sets (Christner et al., 2010; Shrimpton, 2004).

The ImPACT dose calculator uses Monte Carlo data generated from simulating an exposure of a single hermaphrodite adult mathematical phantom (Jones and Shrimpton, 1993, 1991), while CT-Expo uses data for adult male and adult female mathematical phantoms

(Kramer et al., 1982; Zankl et al., 1991) and baby and child voxel phantoms (Veit et al., 1989; Zankl et al., 1993, 1995).

In addition to these traditional CT dose calculators, it is expected that a CT dose calculator using Monte Carlo data sets based on the University of Florida (UF) family of hybrid phantoms (Lee et al., 2010) will be available in the future[i]. Another research group at Duke University are investigating segmenting a range of clinical images for patients of all ages and weight percentiles to produce a library of Monte Carlo dose estimates using the patient-specific hybrid phantoms allowing patient-specific dose estimation by matching a patient's characteristics to one in the database (Li et al., 2008, 2011a,b,c).

5.2.3 CT Scanner-Independent Computational Methods

Shrimpton (2004) was first to propose a method of estimating organ absorbed dose using coefficients normalised to the weighted CTDI ($CTDI_w$), which takes into account the scanner output characteristics and the impact on dose deposition in standardised dosimetry phantoms. Measurements are made in a polymethyl methacrylate (PMMA) homogeneous, cylindrical phantom and $CTDI_w$ is calculated from a weighted average of measurements at the centre and periphery, which includes the effects of the scanner beam shaping filter on dose. The standard phantoms used for CT dosimetry are a 32 cm diameter phantom representing an adult's body and a 16 cm diameter phantom representing the head of an adult or child, or in some cases a child's body.

Normalising doses to a quantity, such as $CTDI_w$, which takes account of the influence of the scanner design on dose deposition in a patient (standardised phantom), removes some of the scanner dependence which was a feature of the original Monte Carlo CT dose data sets which were normalised to $CTDI_{air}$. The feasibility of this method was demonstrated by normalising effective dose across different age groups for three types of scanners (Shrimpton, 2004). The variability in the effective dose coefficients normalised to $CTDI_w$ for each age group and examination type was less than 10% (Shrimpton, 2004).

Turner et al. (2010) further demonstrated the viability of this method using Monte Carlo simulations for four modern multi-detector CT (MDCT) scanners and one of the GSF voxel phantoms (Fill et al., 2004; Petoussi-Henss et al., 2002). Organ and effective doses were normalised to the volumetric CTDI ($CTDI_{vol}$), which is calculated by dividing the $CTDI_w$ by the pitch for helical scans. The mean variance across scanners for all organs was 5.2% and only 4.2% for effective dose (Turner et al., 2010). Turner et al. (2011) further assessed estimating scanner-independent organ absorbed doses for CT abdominal examinations across a range of GSF computational phantoms (Fill et al., 2004; Petoussi-Henss et al., 2002) to take into account varying patient size, including children. They concluded that the method was feasible for fully irradiated organs and showed a dependence on patient

[i] C Lee [US National Cancer Institute] 2011, pers. comm., 18 May.

size (Turner et al., 2011). The method was more variable for partially irradiated organs due to the organ size, proximity to the scan region and relative organ position between different phantoms (Turner et al., 2011).

Li et al. (2008; 2011a) have shown a similar correlation between organ absorbed dose and patient size for CT chest examinations using Monte Carlo modelling for a single MDCT scanner and multiple patient-specific hybrid phantoms developed from paediatric patient clinical images. They demonstrated that changes in beam collimation, pitch and tube voltage had little effect (<7%) on $CTDI_{vol}$-normalised lung doses for CT chest examinations and they predict that this may also apply to other centrally located organs in the scan volume (Li et al., 2011a).

Traditional DLP to effective dose conversion methods (Chapple et al., 2002; Khursheed et al., 2002; Shrimpton and Wall, 2000; Shrimpton et al., 2006; Shrimpton, 2004) utilise the same principle. Since the DLP is based on the $CTDI_{vol}$, these conversion methods also provide a generic approach for estimating effective dose across different scanners. Similarly, these methods all demonstrate a dependence on the size of the patient and in the past have predominantly been defined relative to the age of the patient. Conversion coefficients are readily utilised and easily understood in the clinical setting and are useful for providing a sufficiently precise estimate of effective dose (Shrimpton and Wall, 2009), considering the uncertainty in the value for a reference patient is about ±40% (Martin, 2007).

5.3 Methods

Twelve methods for determining CT doses have been evaluated using three clinical paediatric CT protocols. One method was experimental and based on dose measurements (Chapter 3), while the remainder were computational. The methods are summarised in Table 5.1 and detailed further below. The clinical protocols were all designed for use on a Siemens Sensation 16 MDCT scanner (Siemens, Erlangen, Germany) using automatic tube current modulation (CARE Dose 4D). The standard parameters for the CT protocols used when scanning a 10 year old patient are given in Tables 3.1 and 3.10 and these were used as input parameters for the various computational methods. In the experimental method, the CT brain examination was performed with a tilted gantry to minimise dose to the lens of the eye. It was not possible to simulate this in many of the computational methods and instead the dose estimates were made with the axis of rotation parallel to the long axis of the phantom where necessary.

The scan lengths for all examinations were defined by matching the anatomical regions exposed on the physical phantom with the same regions on the computational phantoms (Table 5.2). The inferior slice of the brain examination extended between the supraorbital ridge and first cervical vertebra and the scan continued to just beyond the vertex, the

chest examination included the entire thorax and half of the liver and the abdomen/pelvis examination began slightly superior to the diaphragm and ended at the symphysis pubis. Each of the phantoms is shown in Figure J.1 (Appendix J) with scan regions indicated for the three CT examinations. The reference patient considered in the dose estimates was a 10 year old child, or the next closest age where this was not available.

Method 1: Experimental Method - TLD Measurements

Organ and tissue absorbed doses were measured and reported in Chapter 3 using TLDs placed in a physical anthropomorphic phantom representing a 10 year old child. All experimental measurements were undertaken at the Royal Children's Hospital (RCH) Melbourne on a Siemens Sensation 16 MDCT scanner. Effective dose was estimated from the absorbed dose measurements as described in Chapter 3 using both ICRP 60 and ICRP 103 tissue weighting factors.

Methods 2 and 3: ImPACT and CT-Expo - CT Dose Calculators

Organ and tissue absorbed doses and effective doses were derived using ImPACT (ImPACT, 2011) and CT-Expo (Stamm and Nagel, 2011b). Since the NRPB data set utilised by ImPACT was generated using a mathematical phantom representing an adult, paediatric modifying factors (Khursheed et al., 2002) derived from Monte Carlo modelling using the ORNL Cristy and Eckerman (1987) mathematical phantoms representing children were applied when calculating effective dose. The paediatric modifying factors only apply to the effective dose and hence the organ and tissue absorbed doses were determined from the adult phantom, although paediatric factors for the kilovoltage, tube current and rotation time were used. In CT-Expo organ and tissue absorbed doses and gender-averaged effective dose were calculated using the GSF voxel phantom representing the seven year old child (Veit et al., 1989; Zankl et al., 1993, 1995). Both ImPACT and CT-Expo provide effective dose estimates using the ICRP 60 and ICRP 103 Recommendations.

Method 4: PCXMC - Radiography Dose Calculator

A dose calculator called PCXMC Dose Calculations (STUK, 2008) designed for two-dimensional (2D) radiography and fluoroscopy applications (Tapiovaara and Siiskonen, 2008) was used to simulate the CT examinations using multiple 2D projections. PCXMC is a PC-based program, which runs a Monte Carlo simulation based on an X-ray beam projection and other user specified examination conditions, including the X-ray spectrum, to calculate organ and tissue absorbed doses and effective dose. Twenty projection angles using a beam collimation equivalent to the total CT scan region were summed to simulate a 360 degree rotational CT scan. A large focal to source distance was used to produce unidirectional photons, allowing greater control over the defined scan volume. The beam was angled to simulate the tilted gantry for the CT brain examination. PCXMC runs Monte

Table 5.1: Summary of organ and effective dose derivation methods and quantities compared in this thesis.

Method	**Tool**[a]	**Phantom**		**ICRP Publication**[c]	**Quantity**
		Type[b]	**Representative Age**		
Measurement[d]	TLD	Physical	10 yo	ICRP 60	$E_{TLD,60}$
				ICRP 103	$E_{TLD,103}$
ImPACT[e,f]	MC	Stylised ORNL	Adult	ICRP 60	$E_{ImPACT,60}$
				ICRP 103	$E_{ImPACT,103}$
CT-Expo[e,g]	MC	Voxel GSF	7 yo	ICRP 60	$E_{EXPO,60}$
				ICRP 103	$E_{EXPO,103}$
PCXMC[e,h]	MC	Stylised ORNL	10 yo	ICRP 60	$E_{PCXMC,60}$
				ICRP 103	$E_{PCXMC,103}$
Lee et al.[e,i]	MC	Stylised ORNL	10 yo	ICRP 60	$E_{ORNL,60}$
		Voxel UF	11 yo	ICRP 60	$E_{UF,60}$
Li et al.[e,j]	MC	Hybrid	Patient specific	ICRP 103	$E_{Li,103}$
Turner et al.[e,k]	MC	Voxel GSF	Patient specific	NA[f]	NA[f]
k coefficient[e,l]	MC	Stylised ORNL	10 yo	ICRP 60	$E_{DLP,60}$
Deak et al.[e,m]	MC	Stylised ORNL	10 yo	ICRP 60	$E_{DEAK,60}$
				ICRP 103	$E_{DEAK,103}$
Chapple et al.[e,n]	TLD	Physical	10 yo	ICRP 60	$E_{CHAPPLE,60}$
k_w coefficient[e,o]	MC	Stylised ORNL	10 yo	ICRP 60	$E_{CTDI,60}$

[a] Tool used for dose calculation: either thermoluminescence dosemeters (TLD) or Monte Carlo (MC) modelling.
[b] Phantom types including physical or stylised (mathematical), voxel and hybrid computational phantoms developed by various groups including the Oak Ridge National Laboratory (ORNL) (Cristy and Eckerman, 1987), German National Research Centre for Environment and Health (GSF) (Veit et al., 1989; Zankl et al., 1993, 1995), and University of Florida (UF) (Lee et al., 2006c).
[c] The ICRP Publication used for calculation of effective dose.
[d] Experimental method.
[e] Computational methods.
[f] ImPACT Dose Calculator (ImPACT, 2011).
[g] CT-Expo Dose Calculator (Stamm and Nagel, 2011b).
[h] PCXMC Dose Calculator (STUK, 2008).
[i] Lee et al. (2007a).
[j] Li et al. (2011a).
[k] Turner et al. (2011) provide a method for organ dose estimation only, not effective dose.
[l] Shrimpton et al.(2006).
[m] Deak et al. (2010).
[n] Chapple et al. (2002).
[o] Shrimpton (2004).

Table 5.2: Scan length parameters for the computational and physical phantoms.

Examination	CT-Expo[a]			ImPACT[a]			PCXMC	TLD[b]
	Start	End	Length (cm)	Start	End	Length (cm)	Length (cm)	Length (cm)
CT Brain	48.0	63.0	15.0	80.0	94.0	14.0	13.0	16.0[c]
CT Chest	24.0	43.0	19.0	37.5	69.5	32.0	25.0	26.6
CT Abdomen/Pelvis	4.00	30.0	26.0	6.00	46.0	40.0	30.0	36.9

[a] Start and End scan length parameters for CT-Expo and ImPACT are input parameters specific to these CT dose calculators.
[b] The average scan length was calculated from a series of three CT examinations using identical protocols performed on the TLD loaded physical anthropomorphic phantom representing a 10 year old child (see Table 3.11).
[c] The scan length for the tilted brain scan on the CT scanner is taken as the length perpendicular to the beam axis. This is not the actual length scanned on the patient.

Carlo simulations using mathematical hermaphrodite phantoms based on the ORNL Cristy and Eckerman phantoms (1987), with some modifications that improve the head and neck modelling, correct the thyroid location and model organs and tissues specified in ICRP 103 (Tapiovaara and Siiskonen, 2008). Absorbed doses were calculated using the phantom representing a 10 year old child. PCXMC provides effective dose estimates using both ICRP 60 and ICRP 103 definitions.

Methods 5 and 6: Lee et al. (2007a) ORNL 10 yo and UF 11 yo mAs-Normalised Doses

Lee et al. (2007a) provide mAs-normalised organ and tissue absorbed doses and effective dose for several types of CT examinations based on Monte Carlo simulations using a range of ORNL mathematical (Cristy and Eckerman, 1987) and the University of Florida (UF) patient-specific voxel phantoms (Lee et al., 2006c). The computed doses used for the assessment in this thesis were based on simulations using the ORNL phantom representing a 10 year old child and the UF phantom representing a male 11 year old child (Table K.1, Appendix K). The same CT scanner and kV_p considered in this thesis were used in the simulations by Lee et al. (2007a). The beam collimations for the current protocols were wider (18 mm for brain examinations and 24 mm for body examinations), compared with the simulated 12 mm beam in the other study. However, Lee et al. (2007a) concluded that organ and effective dose did not vary significantly for different beam collimations. Li et al. (2011a) also support this finding for organ absorbed doses in the scan volume, although they also observe that collimation can have an effect on organs located at the edge of scan, likely due to over-ranging for helical scans. Effective dose was calculated by Lee et al. (2007a) using the ICRP 60 formalism, modified to produce a gender-specific estimate according to the methodology of Zankl et al. (2002).

Method 7: Li et al. (2011a) $CTDI_{vol}$-Normalised, Size-Specific Doses

Organ and tissue absorbed doses for the CT chest examination were calculated according to a relationship suggested by Li et al. (2011a) derived from Monte Carlo modelling using multiple patient-specific hybrid phantoms (Li et al., 2011b,c). They found that the $CTDI_{vol}$-normalised organ and tissue absorbed dose (in terms of the 16 cm dosimetry phantom) ($nH_T\left(d_{\text{chest}}\right)$) is given by (Li et al., 2011a):

$$nH_T\left(d_{\text{chest}}\right) = \frac{e^{(\alpha_T d_{\text{chest}} + \beta_T)}}{12.19} \tag{5.1}$$

where α_T and β_T are organ specific fitting parameters provided in Table K.2 (Appendix K) and d_{chest} is the average chest diameter between the lung apex and base. For the calculated absorbed doses in this thesis, the chest diameter of the physical phantom (21 cm) from the experimental method was used. Equation (5.1) was used to calculate the absorbed dose for all organs specified by Li et al. (2011a), although it is recognised that the correlation with chest diameter is only strong for large organs (e.g. lung) and centrally located tubular organs (e.g. oesophagus) inside the scan volume. The correlation is weaker for small organs inside the scan volume (e.g. thyroid and breast) and organs on the periphery or outside the scan volume (e.g. liver and small intestine) and distributed organs (e.g. bone surface and red bone marrow).

Effective dose normalised to DLP (k) as a function of the average chest diameter (d_{chest}) was calculated according to (Li et al., 2011a):

$$k\left(d_{\text{chest}}\right) = e^{(\alpha_k d_{\text{chest}} + \beta_k)} \tag{5.2}$$

where $\alpha_k = -0.093\ \text{cm}^{-1}$ and $\beta_k = -2.01$. This conversion coefficient is based on effective dose calculated according to the ICRP 103 definition.

Method 8: Turner et al. (2011) $CTDI_{vol}$-Normalised, Size-Specific Doses

Organ absorbed doses were calculated for fully irradiated organs in the CT abdomen/pelvis examination using the size-corrected, scanner-independent organ absorbed dose estimates provided by Turner et al. (2011). They found through Monte Carlo simulations using a range of computational anthropomorphic phantoms and different scanner models that the $CTDI_{vol}$-normalised organ absorbed dose (in terms of the 32 cm dosimetry phantom) averaged over different scanner models $\left(n\bar{D}_{P,O}\right)$ can be given by (Turner et al., 2011):

$$n\bar{D}_{P,O} = A_0 e^{(B_0 \times \text{perimeter})} \tag{5.3}$$

where P refers to the phantom model, O to the organ and the perimeter (in cm) is defined

at the central slice for the abdomen component of the scan. The parameters A_0 and B_0 are given in Table K.3 (Appendix K). The abdomen perimeter for the physical phantom used in this thesis was 59 cm. The method by Turner et al. (2011) does not provide an estimate of effective dose.

Methods 9-11: DLP to Effective Dose Conversion Coefficients

The effective dose (E) for each examination was estimated from the DLP (Table 3.11) using anatomy- and age-dependent conversion coefficients, k ($\mathrm{mSv \cdot mGy^{-1} \cdot cm^{-1}}$), according to:

$$E = k \cdot DLP \tag{5.4}$$

Three different sets of conversion coefficients were utilised. Firstly, the widely employed conversion coefficients (Khursheed et al., 2002; Shrimpton et al., 2006) derived using Monte Carlo dose estimates based on the Cristy and Eckerman (1987) paediatric mathematical phantoms were used (Table K.4, Appendix K). These conversion coefficients are applicable to effective dose estimates according to ICRP 60 only.

Secondly, Deak et al. (2010) have recently provided sex- and age-specific conversion coefficients as a function of X-ray tube voltage for effective dose estimates for both ICRP 60 and ICRP 103 definitions. The coefficients for estimating effective dose for a 10 year old child undergoing CT examinations at 120 $\mathrm{kV_p}$ (Table K.5, Appendix K) have been utilised in this thesis. These coefficients were derived from Monte Carlo modelling of an MDCT scanner and the ORNL Cristy and Eckerman (1987) mathematical phantoms with modifications to incorporate organs and tissues specified in ICRP 103. It should be noted that Deak et al. (2010) were not recommending the replacement of existing conversion coefficients, but aimed to provide information regarding voltage-, age- and sex-dependency using modelling of a specific CT scanner.

Finally, Chapple et al. (2002) proposed a size dependent equation for determining DLP conversion coefficients (k) for children undergoing CT examinations, given by:

$$k = y_0 + A_1 e^{-x/t_1} \tag{5.5}$$

where y_0, A_1 and t_1 are fitting parameters given in Table K.6 (Appendix K) and x is the height of the patient for head examinations or equivalent diameter of the region being scanned for body examinations. The equivalent diameter is calculated from both height and weight and therefore takes into account density, which may provide a better correlation with energy imparted than the perimeter (Lindskoug, 1992). For the calculated effective doses in this thesis, the dimensions of the physical phantom from the experi-

mental method were used. The height of the physical phantom was 140 cm (including legs, which were not physically present on the phantom) and the equivalent diameter was 17 cm (calculated using a height of 140 cm and weight of 32 kg). Equation (5.5) was derived from TLD measurements made in a range of physical paediatric anthropomorphic phantoms (representing neonate, 1, 5, 10 and 15 year old children). This effective dose estimate is based on the ICRP 60 definition.

Method 12: $CTDI_w$ to Effective Dose Conversion Coefficients

An alternative method proposed by Shrimpton (2004) for estimating the effective dose for axial scans from $CTDI_w$ rather than DLP was also used. In this model, the effective dose (E) using the ICRP 60 formalism is calculated according to (Shrimpton, 2004):

$$E = k_w \cdot \mathrm{CTDI_w} \tag{5.6}$$

where k_w is a conversion coefficient with units $\mathrm{mSv \cdot mGy^{-1}}$ as given in Table K.7 (Appendix K). It follows for helical scans that since the dose is inversely proportional to pitch (Goldman, 2008; McCollough and Zink, 1999), effective dose may be calculated using equation (5.6) and substituting $CTDI_{vol}$ for $CTDI_w$ since $CTDI_{vol}$ is calculated by dividing $CTDI_w$ by the helical pitch.

5.4 Results

The mean organ and tissue absorbed doses measured with TLDs have previously been presented in Table 3.12. Comparison of the measured and computed organ and tissue absorbed doses are provided in Figure 5.1 for a paediatric CT brain examination, Figure 5.2 for a paediatric CT chest examination and Figure 5.3 for a paediatric CT abdomen/pelvis examination. The largest disparities between the measured and computed absorbed doses were for the salivary glands and oral mucosa resulting from the CT brain examination (up to a 15-fold difference). This was also found for the same tissues for the CT chest examination, although the difference was smaller (up to a 4-fold difference). For the CT abdomen/pelvis examination the computed absorbed doses to the testes showed the greatest variation from the measured absorbed doses (up to a 7-fold difference).

Overall, computed absorbed doses to organs and tissues fully and directly irradiated on all phantoms demonstrated the best agreement with the measured absorbed doses. For the CT brain examination the maximum variation of the computed absorbed dose to the brain from the measured absorbed dose was 31% resulting from the CT-Expo calculation. For the CT chest examination the maximum variation from the measurements was 18% for the lung (PCXMC), 14% for the thymus (PCXMC and Li 2011), 24% for the oesophagus (UF 11 yo), 32% for the heart (Li 2011) and 31% for the breast (PCXMC).

The CT abdomen/pelvis examination included several fully and directly irradiated organs in the scan volume. The greatest variation in the calculated absorbed doses compared with the measured absorbed doses was 26% for the liver (ORNL 10 yo), 19% for the spleen (ORNL 10 yo), 24% for the stomach (ORNL 10 yo), 14% for the gall bladder (ImPACT), 26% for the adrenals (Turner 2011), 32% for the pancreas (ORNL 10 yo), 16% for the kidneys (ORNL 10 yo), 49% for the small intestine (ORNL 10 yo), 45% for the colon (UF 11 yo), 19% for the uterus (CT-Expo), 25% for the ovaries (CT-Expo), 18% for the bladder (ImPACT) and 38% for the prostate (CT-Expo). The largest differences between measured and computed absorbed doses were mainly seen in the calculations using the ORNL 10 year old phantom.

Absorbed doses to organs and tissues that were partially irradiated on the edge of the scan volume showed larger variation between the methods. For example, the maximum variation from the measured absorbed dose was 190% for the lens of the eye computed absorbed dose for the CT brain examination (CT-Expo), 84% for the thyroid computed absorbed dose for the CT chest examination (PCXMC) and 77% for the lung computed absorbed dose for the CT abdomen/pelvis examination (PCXMC). Similarly, extended tissues, such as the skin, muscle, bone marrow and bone surface, demonstrated larger variance in dose. For example, the greatest deviation in the computed skin absorbed dose from the measured value was 125% for the CT brain examination and 118% for both the CT chest and abdomen/pelvis examinations. The maximum variation in skin absorbed dose was due to the CT-Expo calculation for all three types of CT examination.

The values of effective dose estimated from the experimental and computational methods are given in Table 5.3. The effective dose according to ICRP 60 ranged from 1.5-2.5 mSv for the CT brain examination, 3.0-4.7 mSv for the CT chest examination and 4.3-5.7 mSv for the CT abdomen/pelvis examination (excluding the adult ImPACT doses). The effective dose according to ICRP 103 ranged from 1.4-2.3 mSv for the CT brain examination, 3.6-6.2 mSv for the CT chest examination and 3.9-5.4 mSv for the CT abdomen/pelvis examination (excluding the adult ImPACT dose). The range of effective dose values is shown in Figure 5.4.

The values of effective dose using the ICRP 60 methodology were normalised to $E_{TLD,60}$ and are shown in Figure 5.5. Similarly, the calculated ICRP 103 effective dose values relative to $E_{TLD,103}$ are shown in Figure 5.6. For the ICRP 60 formalism, the effective doses estimated from the computational methods varied from the effective doses determined from the absorbed dose measurements by -30% to 35% and for the ICRP 103 methodology the variation was -29% to 41%. Table 5.4 gives the DLP to effective dose conversion coefficients calculated by dividing the computed effective dose by the DLP values given in Table 3.11 for all methods investigated.

Table 5.3: Values of effective dose from the experimental and computational methods investigated.

Quantity	Effective Dose (mSv)		
	CT Brain	**CT Chest**	**CT Abdomen/Pelvis**
$E_{TLD,60}$	1.8	4.3	5.0
$E_{ImPACT,60}$	1.6 (1.9-2.1)[a]	3.3 (3.6-4.6)[a]	3.8 (4.6-5.7)[a]
$E_{EXPO,60}$	2.5	4.7	5.3
$E_{PCXMC,60}$	1.8	4.4	4.6
$E_{ORNL,60}$	2.0	3.4	4.8
$E_{UF,60}$	1.9	3.0	4.9
$E_{DLP,60}$	2.0	4.1	5.3
$E_{DEAK,60}$	1.5	3.3	4.5
$E_{CHAPPLE,60}$	2.3	3.6	4.7
$E_{CTDI,60}$	1.7	3.1	4.3
$E_{TLD,103}$	1.4	5.0	4.8
$E_{ImPACT,103}$	1.8 (2.2-2.3)[a]	4.0 (4.4-5.6)[a]	3.6 (4.3-5.4)[a]
$E_{EXPO,103}$	2.0	5.3	5.1
$E_{PCXMC,103}$	1.4	5.3	4.1
$E_{Li,103}$	-	6.2	-
$E_{DEAK,103}$	1.7	3.6	3.9

[a] ImPACT recommends scaling the effective dose calculated for the adult by paediatric scaling factors derived by Khursheed et al. (2002). A range is provided for the recommended factors and the bracketed terms in the Table above represent the lower and upper limits of this range for a 10 year old child.

5.5 Discussion

For medical exposures, the risk to an individual is assessed from the mean absorbed dose to radiosensitive organs and tissues, since the probability of cancer induction depends on the anatomy exposed, the level of exposure and the age and gender of the individual (ICRP, 2007c). The homogeneity of absorbed dose in an organ or tissue depends on the exposure situation and also the size or physical distribution of that organ or tissue. For CT examinations, the exposure is a partial irradiation of the body which leads to heterogeneity of the absorbed dose distribution in some organs and tissues, particularly those that are not completely located within the scan volume. Furthermore, distributed tissues such as the skin and bone marrow will always exhibit a varying absorbed dose distribution for CT examinations due to the nature of the exposure. These factors contribute to the difficulty and variability in CT organ dosimetry.

The exposure risk will also depend on the type of radiation, expressed by the equivalent dose (ICRP, 2007b), although for CT examinations this is numerically equal to the absorbed dose. The effective dose reflects the combined detriment from the risk of stochastic effects in different organs and tissues averaged over all ages and both sexes. The ICRP makes recommendations regarding radiation and tissue weighting factors, which are re-

Table 5.4: Calculated DLP to effective dose conversion coefficients.

k **(mSv/mGy·cm)**[a]	**CT Brain**	**CT Chest**	**CT Abdomen/Pelvis**
$E_{TLD,60}$/DLP	0.0029	0.014	0.014
$E_{ImPACT,60}$/DLP	0.0025 (0.0030-0.0033)[b]	0.010 (0.011-0.015)[b]	0.011 (0.013-0.016)[b]
$E_{EXPO,60}$/DLP	0.0039	0.015	0.015
$E_{PCXMC,60}$/DLP	0.0028	0.014	0.013
$E_{ORNL,60}$/DLP	0.0031	0.011	0.014
$E_{UF,60}$/DLP	0.0030	0.009	0.014
$E_{DLP,60}$/DLP	0.0032	0.013	0.015
$E_{DEAK,60}$/DLP	0.0023	0.010	0.013
$E_{CHAPPLE,60}$/DLP	0.0036	0.011	0.013
$E_{CTDI,60}$/DLP	0.0026	0.010	0.012
$E_{TLD,103}$/DLP	0.0022	0.016	0.014
$E_{ImPACT,103}$/DLP	0.0028 (0.0034-0.0037)[b]	0.013 (0.014-0.018)[b]	0.010 (0.012-0.015)[b]
$E_{EXPO,103}$/DLP	0.0031	0.017	0.014
$E_{PCXMC,103}$/DLP	0.0022	0.017	0.012
$E_{Li,103}$/DLP	-	0.020	-
$E_{DEAK,103}$/DLP	0.0027	0.011	0.011

[a] The conversion factors (k) were calculated by dividing the effective dose by the dose length product (DLP) obtained from the CT examinations using the physical phantom representing a 10 year old child. The DLP values were 640 mGy·cm, 317 mGy·cm and 350 mGy·cm for the CT brain, chest and abdomen/pelvis examinations respectively. These DLP values are all relative to the 16 cm dosimetry phantom. The conversion coefficients can be multiplied by a factor of approximately 2 to give coefficients relative to the 32 cm dosimetry phantom for the body examinations.

[b] ImPACT recommended paediatric scaling factors (Khursheed et al., 2002) used and range is shown in brackets.

vised to take account of new scientific information regarding the biological effectiveness of radiation and tissue and organ radiosensitivity. Recommendations in ICRP Publication 60 (ICRP, 1991) have been in use for about 20 years and these have been recently revised in ICRP Publication 103 (ICRP, 2007b).

In the diagnostic radiology clinical environment, it is beneficial to estimate both absorbed dose and effective dose from CT examinations for assessment of risk and to reduce dose. Furthermore, the BEIR VII Report (NRC, 2006) has highlighted the need for epidemiological research studies, especially to follow-up children receiving CT scans. Several studies investigating the effects of low dose radiation have commenced (Bernier et al., 2012; Brady et al., 2011f; Hricak et al., 2011; Pearce et al., 2011) and these require reconstruction of paediatric CT doses. Therefore, CT dose calculation methods that are applicable to children are required in both the clinical and research contexts.

Several methods of estimating CT dose have been investigated in this thesis. Actual clinical scenarios have been evaluated by using typical CT protocols that a 10 year old child may undergo at a children's hospital. As the tools assessed here are often used for dose assessment, it is useful to examine the extent of the differences between the methods when calculating paediatric CT doses. There are several important influencing factors on

the measured and calculated absorbed doses that need to be considered. These include the models used to represent the organs and their position in the body, the type/model of CT scanner being used and/or modelled in the calculation and the scan parameters used in simulating the X-ray exposure. It should be noted that the clinical conditions could not be matched exactly in the computational methods and therefore, various assumptions and approximations had to be made. Consequently, the variables associated with each method could not be strictly controlled, but rather the conditions that have been used for each method provide the best match to the clinical scenario.

5.5.1 Patient Modelling

The most significant difference between the various methods is due to the phantom used to model the patient. The PCXMC computational phantom is the closest model in age and size to the physical phantom used for the experimental measurements. However, the elemental compositions of these phantoms differ and are shown in Figure E.1 and Table E.2 (Appendix E). The dimensions of the PCXMC and CT-Expo child phantoms are compared in Table E.3 (Appendix E) with dimensions of the physical phantom used for TLD measurements. In addition to the differences in composition and overall size between the phantoms, there are other internal disparities such as the location of organs that will also affect dose estimates.

Organ Positioning

Differences between phantoms in terms of organ depth, the exterior shape of the trunk of the phantom and diameter relative to the incoming radiation beam will affect the dose (Lee et al., 2007a; Zankl et al., 2005). As summarised in Table 5.1, the methods investigated utilise physical, stylised (or mathematical), voxel and hybrid phantoms representing 7-11 year old children and an adult to which paediatric scaling factors were applied. Even for the voxel and hybrid phantoms where the organ masses are scaled to represent a reference person, some of the organ topology of the individual whose images were originally segmented to construct the phantom will remain (ICRP, 2009). Therefore, it is expected that some variation in the calculated doses will be evident and, in fact, unavoidable across the different methods.

The thyroid and ET region absorbed doses for the CT chest examination demonstrate a wide variation between the dosimetry methods. Lee et al. (2011) have previously identified that the vertical placement of the thyroid can lead to significant differences in absorbed dose estimates. In the mathematical phantoms the thyroid is located in the neck region, whereas for other phantoms including the physical and UF phantoms, it is partially in the upper trunk region. In this more realistic anatomy, the thyroid will also receive some shielding from the clavicles and scapulae (Lee et al., 2007a), but may also be directly irradiated in a chest examination leading to variations in the dose calculation.

Abdominal organs such as the adrenals, pancreas and kidneys are typically positioned higher in the earlier phantom models (Lee et al., 2011). Therefore, for the CT chest examination (Figure 5.2), the computed absorbed doses to these organs using the earlier mathematical phantoms tend to be higher compared with the other methods. For this exposure situation when these organs are located higher within the phantom model, they are closer to the direct scan volume or are even positioned partially within it leading to the higher absorbed doses.

The location of the testes can also lead to a difference in absorbed dose, which is evident in Figure 5.3 for the CT abdomen/pelvis examination. The testes location can vary between phantoms relative to the mid-femoral neck (Lee et al., 2011). Therefore, if the scan extends to the mid-femoral neck anatomical landmark, the testes may be fully or partially irradiated or even outside the scan region depending on the phantom. Lee et al. (2007a) also comment that the depth of the testes between the legs can lead to a greater shielding effect for lateral projections in some phantoms. This shielding is observed in the lower absorbed dose to the testes in the UF 11 year old phantom compared with the ORNL 10 year old phantom where the scan length extended to mid-testes on both phantoms (Figure 5.3). For the other methods, the testes are predominantly outside of the scan volume.

In addition, the overall size of a phantom will affect the absorbed dose to organs outside of the scan volume. In smaller phantoms, such as the one used in CT-Expo which represents a seven year old child, the closer relative proximity of organs to the scanned volume will increase doses. On the other hand, for an adult phantom, as in ImPACT, these organs will be further away from the directly irradiated area (see for example the kidney absorbed doses in Figure 5.2).

Organ Absorbed Dose Substitution

Some of the phantoms do not model all organs and tissues listed in ICRP 60 and ICRP 103 and often other organ absorbed doses are used as a substitute to approximate these doses. For example, for measurements made in the physical phantom, the thyroid absorbed dose approximated the absorbed dose to the ET region. An example in ImPACT is for the salivary gland and oral mucosa absorbed doses, which are approximated by the brain absorbed dose (ImPACT, 2011). In CT-Expo the absorbed dose to the heart is not calculated or included in the effective dose calculation as conversion factors are not available for determining the absorbed dose to this organ for the child phantom[ii].

The effect of organ absorbed dose substitution can be seen in Figure 5.1 in the high absorbed doses assigned to the salivary glands and oral mucosa in the ImPACT calculations for the CT brain examination. As the experimental method demonstrates, the absorbed

[ii]G.Stamm [Institute of Diagnostic and Interventional Radiology, Germany] 2011, pers. comm., 29 September.

dose to these tissues is in fact considerably less than the brain absorbed dose. This will also influence the effective dose estimate.

For all dosimetry methods, except for ImPACT and Deak et al. (2010), the effective dose for a CT brain examination using ICRP 103 tissue weighting factors is lower than the estimate using the ICRP 60 tissue weighting factors. This is due to the lower tissue weighting factor allocated to the brain using ICRP 103. However, by substituting the brain absorbed dose for the salivary glands and oral mucosa absorbed doses in ImPACT, the ICRP 103 effective dose for a CT brain examination is incorrectly higher than the ICRP 60 effective dose. This is because the inappropriately high absorbed doses allocated to these tissues are only included in the ICRP 103 effective dose estimate and not the ICRP 60 effective dose.

The effective dose for a CT brain examination derived using the Deak et al. (2010) conversion factors also demonstrates an increase between the ICRP 60 effective dose and ICRP 103 effective dose. However, for the ICRP 60 effective dose calculation it appears that the remainder splitting rule has not been applied and hence the brain has been considered a remainder organ when it should have been allocated a tissue weighting factor of 0.025 rather than 0.005. This consequently underestimates the ICRP 60 effective dose for the CT brain examination. A more detailed discussion of the effects of the changed tissue weighting factors in ICRP 103 on paediatric CT doses is given in Section 3.4.2 (Chapter 3).

5.5.2 CT Scanner Modelling

Another significant difference, which applies to the scanner dependent methods assessed in this thesis, is the type of CT scanner that was modelled in the dose calculations. ImPACT and CT-Expo both use methods of scanner matching to allow dose estimates for scanners which were not modelled in the original Monte Carlo data sets. PCXMC is not designed for CT dose estimates and therefore it was necessary to simulate the CT X-ray spectra using appropriate filtration. However, this did not take into account the shaped beam filter used in most modern scanners, which likely led to the wider variation in organ absorbed doses calculated with PCXMC.

The CT scanner used for the TLD measurements in this thesis has a Straton X-ray tube (Siemens, Erlangen, Germany). The ImPACT dose calculator demonstrates that the output in air at the isocentre using the body filter is 12% higher at 120 kV_p and 24 mm beam collimation for the Straton tube compared with earlier Siemens X-ray tubes (ImPACT, 2011). The $CTDI_w$ is 9% higher for the Straton tube using the same exposure conditions. Although the dose conversion coefficients provided by Lee et al. (2007a) are based on Monte Carlo simulations with the same type of CT scanner as used for the TLD measurements in this thesis, it is not clear whether a Straton X-ray tube was used. Similarly, CT-Expo does not explicitly mention the Straton tube and therefore it is not clear

whether it has been considered.

Geleijns et al. (1994) have previously compared the NRPB (ImPACT) and GSF (CT-Expo) data sets and found that only the NRPB data set models the shaped beam filters typically used in CT scanners. This leads to significant differences in the organ absorbed dose conversion factors between the two data sets. In CT-Expo a further scanner specific correction factor (k_{CT}) is applied to the GSF data set conversion factors to take into account differences in scanner geometry, beam filtration and beam-shaping (Brix et al., 2004; Nagel, 2002). For the Siemens Sensation 16 CT scanner, this correction factor is 0.9 (Brix et al., 2004; Nagel, 2002; Stamm and Nagel, 2011b).

The modelling provided by Li et al. (2011a) and the conversion coefficients produced by Deak et al. (2010) are both derived from Monte Carlo modelling of 64 MDCT scanners. The other DLP and CTDI conversion methods (Chapple et al., 2002; Shrimpton et al., 2006; Shrimpton, 2004) attempt to provide more generic conversion coefficients by averaging over several scanners. Turner et al. (2011) investigated the feasibility of scanner independent conversion factors, although these are currently limited to organs in the scan region for an abdominal examination.

To assess differences resulting from the CT scanner modelling, the output of the scanners in the CT dose calculators ImPACT and CT-Expo were compared with the output measured on the CT scanner used for the TLD measurements. Measurements of $\mathrm{CTDI_{100}}$ were made in air ($\mathrm{CTDI_{100,air}}$) at the isocentre with a calibrated 3 $\mathrm{cm^3}$ Radcal ion chamber with 100 mm length, model 10X5-3CT and a model 9095E electrometer (Radcal Corp., Monrovia, California, US) for various beam collimations and utilising both the inherent head and body filters. The ImPACT $\mathrm{CTDI_{100,air}}$ values are available for all scanners included in the dose calculator. A correction factor for beam collimation is provided to calculate $\mathrm{CTDI_{100,air}}$ values relative to those for a 10 mm beam collimation.

The $\mathrm{CTDI_{100,air}}$ values are not as readily accessible in CT-Expo, although they can be calculated from the normalised $\mathrm{CTDI_w}$ values which are provided with respect to the head (H) and body (B) CT dosimetry phantoms ($_n\mathrm{CTDI_{w,H/B}}$), as follows (Brix et al., 2004; Nagel, 2002):

$$ {}_n\mathrm{CTDI_{100,air}} = \frac{{}^{\mathrm{n}}\mathrm{CTDI_{w,H/B}}}{\mathrm{P_{H/B}}} \tag{5.7} $$

where $P_{H/B}$ represents "phantom factors" defined by the above CTDI ratio. A reference value is used in the CT-Expo dose calculator ($_n\mathrm{CTDI_{w,H/B,ref}}$) and corrections applied for different slice collimations (k_{OB}) and voltages (U) from the reference conditions. The reference conditions for the Siemens Sensation 16 scanner are 120 $\mathrm{kV_p}$ and 24 mm beam collimation (Brix et al., 2004; Nagel, 2002; Stamm and Nagel, 2011b). For any other combination of parameters, the weighted CTDI is defined as (Brix et al., 2004):

$$ {}_{n}\mathrm{CTDI}_{\mathrm{w,H/B}} = {}_{\mathrm{n}}\mathrm{CTDI}_{\mathrm{w,H/B,ref}} \cdot \mathrm{k_{OB}} \cdot \left(\frac{\mathrm{U}}{\mathrm{U_{ref}}}\right)^{2.5} \tag{5.8} $$

The slice collimation factor (k_{OB}) corrects for both differences in the collimation and for over-beaming effects. Therefore, equations (5.7) and (5.8) can be used to calculate ${}_{n}\mathrm{CTDI}_{\mathrm{air}}$.

A comparison of the ImPACT and CT-Expo $\mathrm{CTDI}_{100,\mathrm{air}}$ values with the measured values is given in Table 5.5. For the CT chest and abdomen/pelvis examinations assessed in this thesis, a 24 mm beam collimation was used. However, this collimation is only available in helical mode and therefore could not be replicated in axial mode for the $\mathrm{CTDI}_{100,\mathrm{air}}$ measurement. The next widest collimation width was assessed (18 mm). For ImPACT there is better agreement for the 10 mm collimation over all voltages than for the other collimation widths. The 10 mm collimation is the reference condition in ImPACT. For the wider beam collimations used for the examinations in this thesis, it does appear that the ImPACT $\mathrm{CTDI}_{100,\mathrm{air}}$ values will be slightly higher. The converse is true for CT-Expo. There is better agreement with the measurements for the wider collimations. For CT-Expo the reference condition is 24 mm. However, it is interesting to note that for the measured values and ImPACT the $\mathrm{CTDI}_{100,\mathrm{air}}$ values increased with changing beam collimation from 10 mm to 18 mm while the voltage remained constant, whereas CT-Expo demonstrated a decrease in $\mathrm{CTDI}_{100,\mathrm{air}}$ for these beam collimations.

Table 5.5: Comparison of measured CTDI_{100} values with ImPACT and CT-Expo for various $\mathrm{kV_p}$ and beam collimations.

Filter	**$\mathrm{kV_p}$**	**Beam Collimation (mm)**	**CTDI_{100} in Air (mGy/100 mAs)**		
			Measured	**ImPACT**[a]	**CT-Expo**[a,b]
Head	120	10	23.3	24.3 (4%)	28.1 (21%)
	120	18	25.8	28.4 (10%)	25.2 (-2%)
Body	80	10	5.5	5.7 (4%)	7.2 (30%)
	100	10	10.6	10.9 (3%)	12.5 (18%)
	120	10	16.5	17.2 (4%)	19.7 (20%)
	120	18	18.2	20.1 (11%)	17.7 (-3%)
	120	24	-	19.1	17.0

[a] Percentage difference from the measured values is shown in brackets.
[b] The k_{OB} factors are 1.16, 1.04 and 1.00 for 10 mm, 18 mm and 24 mm beam collimations, respectively. The phantom factor ($P_{H/B}$) is 0.76 for the head filter and 0.77 for the body filter for examinations on a child (Stamm and Nagel, 2011b).

Values for the normalised $\mathrm{CTDI_w}$ calculated from the dose indicators displayed on the CT scanner for the TLD measurements and provided in ImPACT and CT-Expo are given in Table 5.6 for the three types of paediatric CT examinations investigated. ImPACT displays $\mathrm{CTDI_w}$ values, but uses only $\mathrm{CTDI_{air}}$ to calculate organ and effective dose. The $\mathrm{CTDI_w}$ value is used to calculate the DLP, which ImPACT also displays for information, although

it is not used in the dose calculations. CT-Expo uses $CTDI_w$ for organ and effective dose calculations. The differences in the $CTDI_w$ values for the CT brain examination may be due to the tilted gantry, which is not simulated in ImPACT or CT-Expo. For the body CT examinations of the chest and abdomen/pelvis, the CT scanner and ImPACT normalised $CTDI_w$ are both relative to the 32 cm dosimetry phantom, whereas the CT-Expo values are relative to the 16 cm dosimetry phantom. The CT-Expo values have been divided by a factor of two to allow comparison. All $CTDI_w$ values for the body examinations are within 10% of the scanner displayed values. The ImPACT values are slightly higher, while the CT-Expo values are slightly lower.

Table 5.6: Comparison of $CTDI_w$ values from the CT examinations performed on the physical phantom with ImPACT and CT-Expo values for the same examinations.

Examination	**$CTDI_w$ (mGy/100 mAs)**			
	CT Scanner[a]	**ImPACT**[b]	**CT-Expo**[b]	**Scaled CT-Expo**[b,c]
CT Brain	15.4	19.9 (29%)	19.1 (24%)	-
CT Chest	7.3	7.8 (7%)	13.1 (79%)	6.6 (-10%)
CT Abdomen/Pelvis	7.1	7.8 (10%)	13.1 (85%)	6.6 (-8%)

[a] The CT scanner $CTDI_w$ values were calculated from $CTDI_{vol}$·pitch and the mAs displayed during the CT examinations on the TLD loaded physical phantom representing a 10 year old child. Note that $CTDI_{vol}$ and mAs values displayed on the CT scanner are an average for the examination since tube current modulation was employed for each scan.
[b] Percentage difference from the CT scanner values is shown in brackets.
[c] The CT-Expo $CTDI_w$ values for body examinations on children are relative to the 16 cm dosimetry phantom. These have been scaled by 0.5 to allow comparison with the scanner displayed values and ImPACT which are both relative to the 32 cm dosimetry phantom.

The method of matching CT scanners in ImPACT using an ImPACT Factor (ImF) was also assessed. The factor is defined by (ImPACT, 2011):

$$ImF = a\frac{CTDI_c}{CTDI_{air}} + b\frac{CTDI_p}{CTDI_{air}} + c \tag{5.9}$$

where the centre and periphery CTDI values ($CTDI_c$, $CTDI_p$) are measured in the CT dosimetry phantoms at a particular tube voltage and $a = 0.4738$, $b = 0.8045$ and $c = 0.0752$ using a 10 mm beam collimation. The ImF is then matched to the closest ImF for a scanner in the original Monte Carlo data set. The CTDI values and the matched data sets are shown in Table 5.7. It is evident that the scanner matching is dependent on the CTDI values and variations between measurement and ImPACT values which are averaged values will invariably exist. For this case, different data sets would have been selected depending on whether measurements on the specific scanner or ImPACT averaged values were used.

Table 5.7: Calculation of the ImPACT Factor to enable scanner matching.

Region	Method	$CTDI_{air}$	$CTDI_c$	$CTDI_p$	ImPACT Factor (*ImF*)	Matched Data Set
		(mGy/100 mAs)				
Head	Measured	23.3	15.5	17.5	0.993	14
	ImPACT	24.3	15.6	17.7	0.965	17
Body	Measured	16.5	3.6	7.2	0.529	10
	ImPACT	17.2	4.3	8.4	0.587	16

5.5.3 Scan Parameters

Tube Current

The scan parameters used to simulate the exposure situation are a further source of variation between the different methods assessed. For all computational methods a constant tube current was assumed, whereas the CT examinations on the physical phantom utilised a range of current values varied during the examination to reduce dose to the patient while maintaining adequate image quality (Appendix H). For the experimental method, the ranges of tube current values were 102-379 mA, 112-199 mA and 114-175 mA for the CT brain, chest and abdomen/pelvis examinations respectively. Using a physical phantom representing a 10 year old child, Brisse et al. (2009b) have shown that modulating the tube current in the z-direction decreases the absorbed dose to organs in areas of low attenuation, such as the lungs, but increases the absorbed dose to organs such as the bladder and ovaries due to the high density pelvic bones. In this thesis, x-y-z tube current modulation was used, but the effects on organ absorbed doses are likely to be similar to those noted by Brisse et al. (2009b).

Scan Length

Scan length was another parameter that varied between each of the methods assessed (Table 5.2). In ImPACT, CT-Expo and PCXMC the scan volume was determined by matching the anatomy scanned on the physical phantom, rather than using the actual scan length. This was necessary, in particular for ImPACT where the adult phantom differed considerably in size to the child physical phantom. Matching anatomy will also lead to differences in the scan length due to the different placement of some organs between the various phantoms, as previously discussed. Furthermore, identifying the matching start and end locations on the mathematical and voxel phantoms in the dose calculators was not straightforward as many organs are not clearly described for the phantom models. For the other computational methods used, the scan length was predetermined by the modelling undertaken in each study and therefore could not be influenced by any selections made in this thesis. This is likely to have the greatest effect on the dose to organs at the edge of a scan volume.

The effect of varying the scan length is best demonstrated by the absorbed dose to the thyroid from the CT chest examination (Figure 5.2) and the absorbed dose to the testes from the CT abdomen/pelvis examination (Figure 5.3). The thyroid has been directly irradiated in the experimental method and in the computational methods using CT-Expo and based on Li et al. (2011a) and therefore the absorbed doses from these methods are much higher. Similarly, the CT abdomen/pelvis examination in Lee et al. (2007a) partially included the testes, resulting in the higher absorbed doses than calculated or measured in the other methods. Therefore, both the organ placement in a phantom and the scan length will affect the absorbed dose to organs at the periphery of the imaging. Lechel et al. (2009) had similar findings regarding organs on the border or partly inside the scan volume, recommending that organ absorbed dose comparisons between different methods could only be reliably made for those organs completely irradiated in all phantoms. Li et al. (2011a) and Turner et al. (2011) confirmed this finding for CT chest and abdomen examinations respectively.

Over-Ranging

Another important factor that affects the absorbed dose to organs at the start and end of a scan volume is the additional length included for data interpolation for helical examinations. The "exposed" length is longer than the "imaged" length and depends on the pitch, beam collimation and reconstruction algorithm (van der Molen and Geleijns, 2007). For the CT scanner used for the experimental method, the over-ranging length for a pitch of 1-1.25 is approximately 5-6 cm (van der Molen and Geleijns, 2007), with half of this length added to each end of the scan. CT-Expo can optionally apply a correction for over-ranging in helical examinations and for the helical CT protocols assessed in this thesis, the CT-Expo over-ranging length was 4.8 cm for the chest examination and 5.5 cm for the abdomen/pelvis examination which had a higher pitch. Figure 3.8 clearly demonstrates the effects of over-ranging for the helical examinations, where the TLD measurements show the additional dose outside of the "imaged" scan length. The user can allow for over-ranging by including additional length in the dose calculation. However, determining the extra length is complex and currently not displayed on the CT scanner. In PCXMC, helical examinations could not be simulated and an adjustment was made to the scanner output to account for the pitch. However, this incorrectly assumed that the scan volume was uniformly irradiated from all directions by a beam with constant output.

5.5.4 Which Method(s) is Best?

Organ Dosimetry

There are many factors affecting the derivation of organ and tissue absorbed doses and it was anticipated that differences would exist between the dosimetry methods. However, these differences should not be considered limitations. Rather, the variation demonstrates

the non-uniform nature of the human body (the uniqueness of each individual) and the difficulty in specifying phantoms to be representative of broad populations. Although reference phantoms are designed to reflect ICRP organ reference masses, the placement of the organ within the body and the proximity relative to other organs are not standardised and have an important influence on dose estimates. Furthermore, while in this thesis computed absorbed doses have been assessed against measured absorbed doses, these may not equate to the "true" absorbed dose. There is uncertainty associated with the TLD measurements, limitations due to the number of TLDs used and the design of the physical anthropomorphic phantom will affect the measured result. In addition, the clinical conditions such as a tilted gantry, tube current modulation and over-ranging were not necessarily incorporated into the computational tools. Therefore, the measured absorbed doses serve as a reference point for comparing the wide range of methods assessed.

In this thesis it was found that there was less variation in the absorbed doses to organs that are directly and fully irradiated, whereas for organs on the periphery of the scan volume the dose variation was more pronounced. For the CT brain examination, the brain was the only directly irradiated organ and the measured and computed absorbed doses were all within approximately 30%. For the CT chest examination, the calculated absorbed doses for directly irradiated organs were similarly within approximately 30% of the measured absorbed doses for all methods. There was slightly more variation in the absorbed doses for directly irradiated organs and tissues for the CT abdomen/pelvis examination. The majority of computed absorbed doses were within approximately 30% of the measured values, except for the absorbed dose to the small intestine, colon and prostate which were all within 50%. Therefore, for directly irradiated organs all computational methods were considered suitable for dose estimation.

Although limited to organs that were directly irradiated for a CT abdomen/pelvis examination only, the scanner-independent $CTDI_{vol}$-normalised organ absorbed doses provided by Turner et al. (2011) demonstrated the best correlation with the measured absorbed doses. These were all within 7% of the measured absorbed doses, except for the adrenals absorbed dose, which was 26% higher than the measured absorbed dose. Expressing the measured organ absorbed doses from this thesis as $CTDI_{vol}$-normalised organ absorbed doses (in mGy to tissue per mGy of $CTDI_{vol}$ for the 16 cm dosimetry phantom) for the brain was 0.8 mGy/mGy for the CT brain examination and 0.7-0.9 mGy/mGy for directly irradiated organs for both the CT chest and abdomen/pelvis examinations (Tables I.1 to I.3, Appendix I). It may be worthwhile expressing absorbed doses in this way in the future when comparing different dose estimates.

For absorbed doses to organs and tissues on the periphery of the scanned volume, the variation in doses was significant. These differences are predominantly due to the notable variation in organ positioning between phantoms, although the defined scan length also contributed to the differences in dose. Overall, CT-Expo provided estimates of absorbed

dose that were closest to the measured values for organs that were located in the neck and chest regions and on the periphery of the scan volume. This may be due to the incorporation of the over-ranging length for helical scans in the CT-Expo calculation, which a user may opt to do manually on other software. Interestingly, for organs located in the abdomen/pelvis region that were partially irradiated, no one method was better than the others. This may reflect the influence that organ depth has on dose variability, since this region can be thicker than other parts of the body and hence organs will be shielded to a different extent between the phantoms.

For distributed tissues, such as the bone marrow, bone surface, skin, lymph nodes and muscle, there was a wide variability in absorbed dose. Some computational methods provided estimates that were in good agreement with the measured absorbed doses, although there was no single method that demonstrated consistently good agreement for all distributed tissues for a particular type of examination or for a single distributed tissue across the different examinations. For organs and tissues that were distant to the scan region, there were also large dose differences. However, the necessity of calculating absorbed doses for organs that will receive distant scattered radiation exposure should be considered as these doses are generally very low and in fact negligible when assessing potential stochastic effects. The ability to reliably calculate these doses is most likely inconsequential.

Effective Dose

The effective dose estimates that were in best agreement with the values derived from the experimental method across all CT examinations for both ICRP 60 and ICRP 103 definitions of effective dose were those calculated using PCXMC. This was unexpected as the tool was designed to simulate 2D radiography exposures and does not model various aspects of the CT scanner geometry and design. However, it should be noted that the organ and tissue absorbed doses calculated with PCXMC did not demonstrate the same correlation with the measured absorbed doses. It is likely that the over- and under-estimation of organ absorbed doses have balanced to provide a reasonably good approximation of effective dose when compared with measurement. This arises from the weighting applied to equivalent doses when deriving the effective dose, which means that each organ or tissue absorbed dose only has a partial contribution to the total effective dose. Hence, the weighted sum used to calculate effective dose to some extent compensates for errors in organ absorbed dose estimates.

Overall, some of the computational methods overestimated the TLD derived effective dose and some underestimated the dose. For the body examinations, the computational methods were more likely to underestimate the dose. Geleijns et al. (1994) found that calculated effective doses for body examinations on adults were about 40% lower than effective doses derived from measurement, while Groves et al. (2004) found that the doses calculated from Monte Carlo modelling were 18% lower. Brix et al. (2004) also

demonstrated a consistent underestimation of effective dose on MDCT scanners using an earlier version of CT-Expo compared with effective dose derived from measurement. They suggested that this was due to the effects of over-ranging which were not incorporated in most of the dose calculations considered here, but were included in the measurements. The results in this thesis tend to support this, since CT-Expo effective dose estimates (which now incorporate over-ranging) for body examinations are in close agreement with the values derived from measurement. When calculating doses due to helical CT scans, an estimated additional length should be included to allow for over-ranging when defining the start and end positions of the scan.

The experimental method employed here is impractical to use routinely in the clinical environment and some of the computational methods, such as PCXMC, are also not readily applied as they are time intensive. Overall, the CT dose calculators which were assessed (ImPACT and CT-Expo) were the most user-friendly and comprehensive methods for calculating CT doses. The simplest, quickest method and the one used most regularly in radiology practices is the DLP conversion method (Shrimpton et al., 2006). DLP conversion coefficients have been derived from all of the effective doses calculated in this thesis (Table 5.4). It is not the intention that any of these replace existing values, particularly since they are derived from effective doses calculated for a single examination with set parameters and the associated value of DLP, but they provide a useful overview and demonstrate the variable range that may arise depending on the dose calculation methodology used. Generally, all of the methods assessed provided an estimate of effective dose that was within a reasonable range (40%) of the value derived from measurement.

5.6 Conclusions

In this part of the thesis, eleven computational CT dose calculation methods were assessed and compared with experimental measurements for paediatric CT clinical protocols for a 10 year old patient. Often the clinical scenario is difficult to simulate in the available dose calculation methodologies and it is useful to assess the reliability of the available tools given this significant limitation. There was a greater level of consistency between absorbed doses calculated for organs and tissues completely and directly irradiated in the scan volume. The greatest disparities were between doses to those organs and tissues partially irradiated on the periphery of the scan volume. The variation between doses for distributed organs was found to be lower than expected. Overall, the organ and tissue absorbed doses demonstrated greater variation than the estimated effective doses. All computational methods investigated provided an effective dose estimate within approximately 40% of the effective dose derived from absorbed dose measurements.

Size-dependent functions providing $CTDI_{vol}$-normalised organ absorbed doses appear to be one of the most promising calculation methods, particularly as these are scanner independent. It will be interesting to see in the future if these methods can be modified to

apply equally well to organs and tissues that are partially irradiated or distributed through the body and whether the effects of tube current modulation and an angled gantry can be accommodated.

5.7 Publications Arising from this Chapter

1. **Brady, Z.**, Cain, T. M. and Johnston, P. N., *Comparison of organ dosimetry methods and effective dose calculation methods for paediatric CT*, Australasian Physical & Engineering Sciences in Medicine, 2012 *(published online 11 April 2012)* (Brady et al., 2012b).

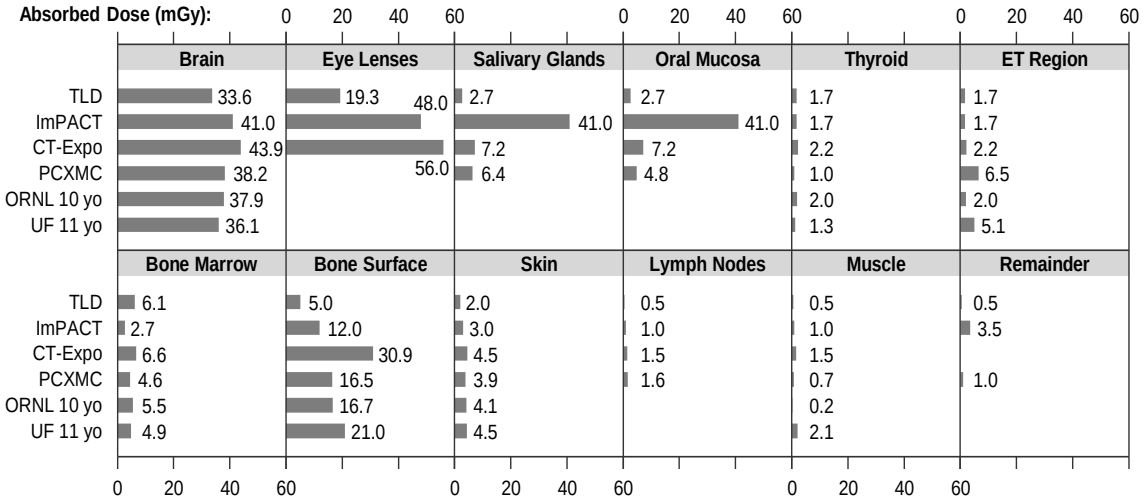

Figure 5.1: Organ and tissue absorbed doses in milligray (mGy) for a paediatric CT brain examination measured with TLDs placed in a physical phantom representing a 10 year old child and calculated using ImPACT (ImPACT, 2011), CT-Expo (Stamm and Nagel, 2011b), PCXMC (Tapiovaara and Siiskonen, 2008) and organ conversion coefficients for the ORNL 10 year old phantom and the UF 11 year old phantom as described by Lee et al. (2007a). The absorbed dose to the remainder organs and tissues as defined in ICRP 103 is also shown.

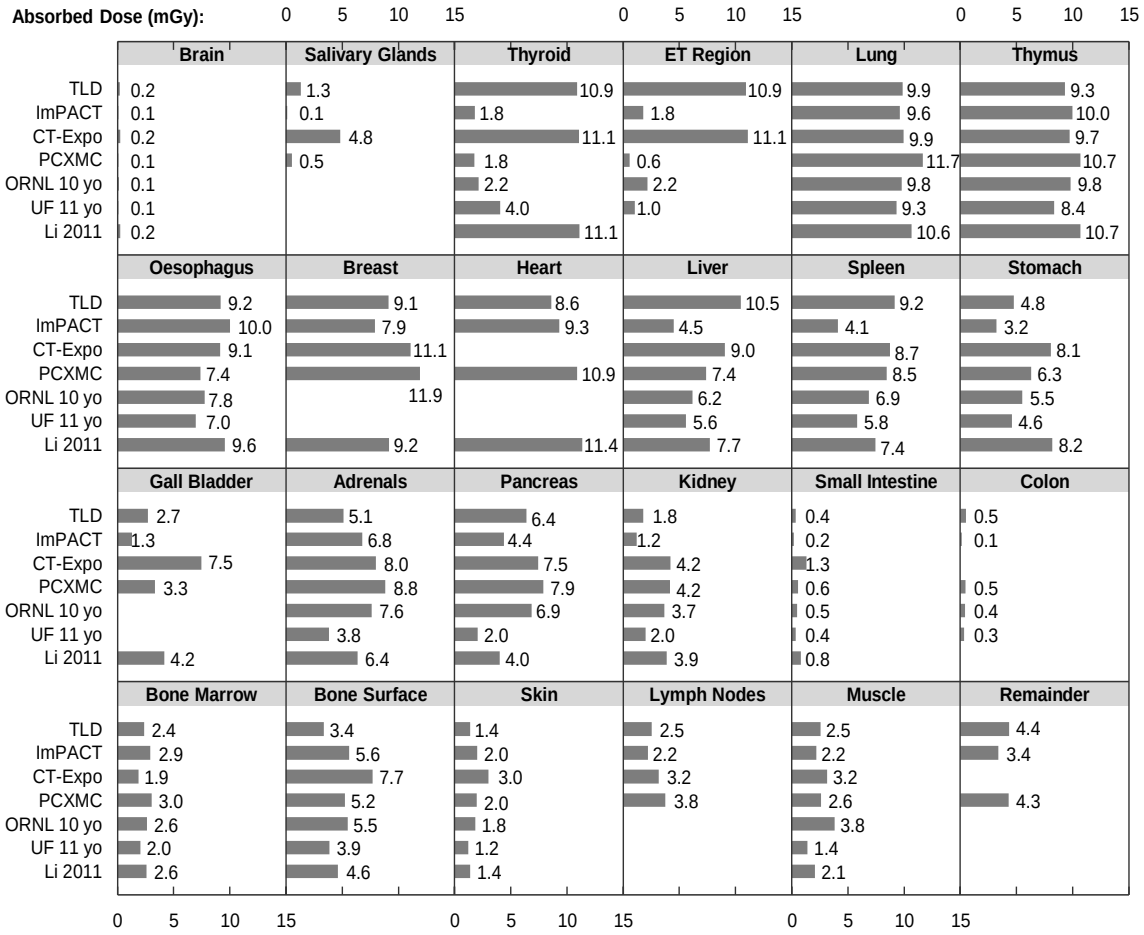

Figure 5.2: Organ and tissue absorbed doses in milligray (mGy) for a paediatric CT chest examination measured with TLDs placed in a physical phantom representing a 10 year old child and calculated using ImPACT (ImPACT, 2011), CT-Expo (Stamm and Nagel, 2011b), PCXMC (Tapiovaara and Siiskonen, 2008), organ conversion coefficients for the ORNL 10 year old phantom and the UF 11 year old phantom as described by Lee et al. (2007a) and size-specific conversion coefficients provided by Li et al. (2011a). The absorbed dose to the remainder organs and tissues as defined in ICRP 103 is also shown.

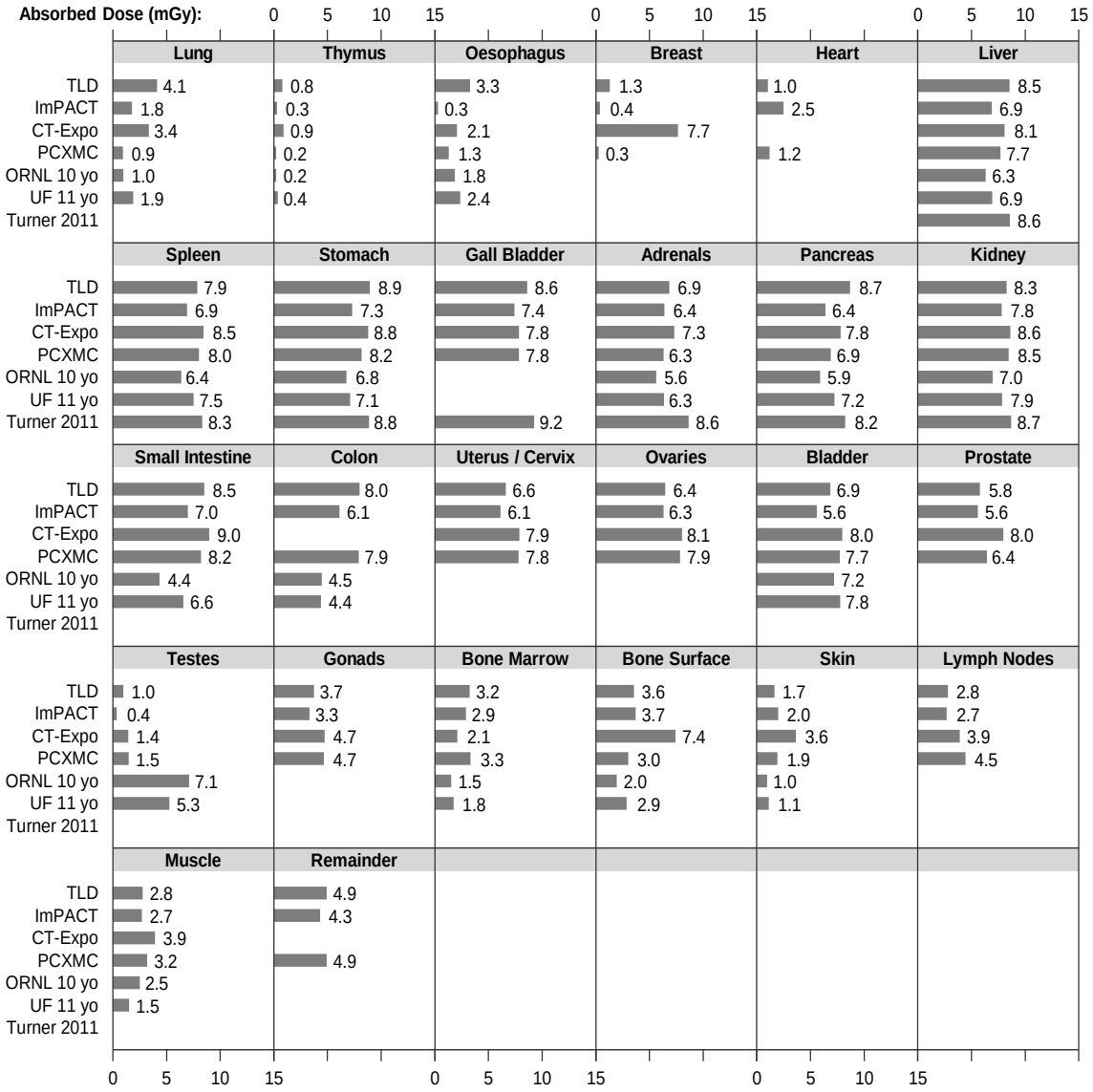

Figure 5.3: Organ and tissue absorbed doses in milligray (mGy) for a paediatric CT abdomen/pelvis examination measured with TLDs placed in a physical phantom representing a 10 year old child and calculated using ImPACT (ImPACT, 2011), CT-Expo (Stamm and Nagel, 2011b), PCXMC (Tapiovaara and Siiskonen, 2008), organ conversion coefficients for the ORNL 10 year old phantom and the UF 11 year old phantom as described by Lee et al. (2007a) and size-specific conversion coefficients provided by Turner et al. (2011). The absorbed dose to the remainder organs and tissues as defined in ICRP 103 is also shown.

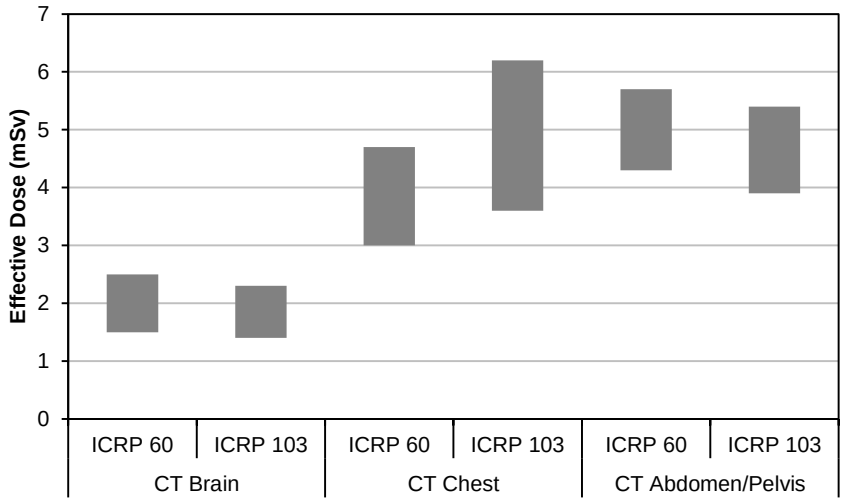

Figure 5.4: The range of effective dose values for all measurement and theoretical methods investigated (excluding adult ImPACT doses) according to ICRP 60 and ICRP 103 methods.

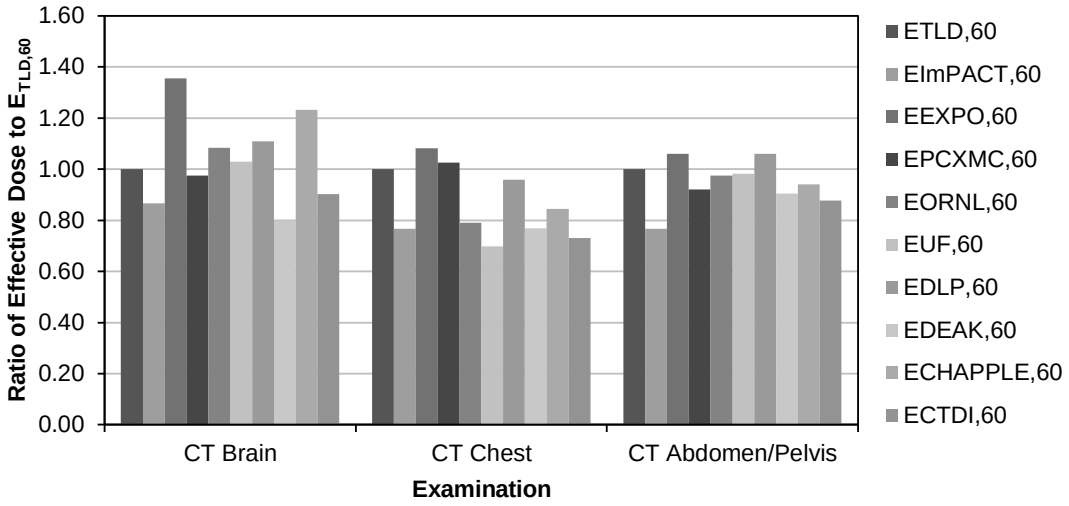

Figure 5.5: Ratio of various effective dose values based on ICRP 60 calculated from computational methods to the effective dose based on ICRP 60 estimated from TLD measurements ($E_{TLD,60}$) in a physical phantom representing a 10 year old child for paediatric CT brain, chest and abdomen/pelvis examinations.

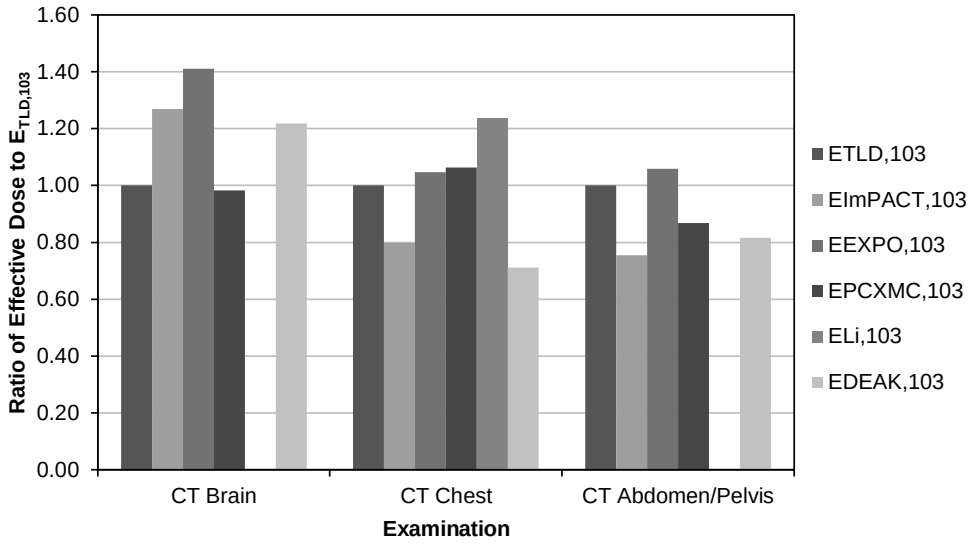

Figure 5.6: Ratio of various effective dose values based on ICRP 103 calculated from computational methods to the effective dose based on ICRP 103 estimated from TLD measurements ($E_{TLD,103}$) in a physical phantom representing a 10 year old child for paediatric CT brain, chest and abdomen/pelvis examinations.

Chapter 6

Survey of Patient Doses in Paediatric CT to Establish Local DRLs at RCH

6.1 Introduction

In the internationally adopted system of radiation protection, a medical procedure involving the exposure of a patient to ionising radiation must be both justified and optimised (ICRP, 2007c). A dose limit or constraint is not applicable in these situations, as the exposure will depend on the medical question being investigated and a higher radiation risk may be warranted in cases where there is potential for greater clinical gain. A procedure involving exposure to radiation will result in net patient benefit if undertaken according to appropriate clinical guidance which incorporates the radiation protection principles of justification and optimisation. However, a number of surveys (Dougeni et al., 2012; Moss and McLean, 2006; Muhogora et al., 2010; Shrimpton et al., 2006; Smith-Bindman et al., 2009; Wallace et al., 2010) of doses from CT examinations have observed substantial differences between practices for the same type of examination, suggesting that exposures may not be suitably optimised. The extent of the variation indicates these differences are not solely attributable to patient factors, such as size and shape, but must also be a result of the exposure parameters and protocols used. Therefore, optimisation of CT protocols is essential, particularly for children who are more radiosensitive than adults (NRC, 2006).

The ICRP introduced diagnostic reference levels (DRLs) as an optimisation tool for managing dose from medical imaging procedures (ICRP, 1991, 1996a, 2001, 2007c). DRLs are defined for common diagnostic examinations as the typical dose level for groups of standard sized patients or standard phantoms for broadly defined types of equipment (ARPANSA,

2008b; IPEM, 2004). A DRL is not a static quantity and it is the regular update, review and assessment of dose trends, rather than the precise value, that is of importance to the optimisation process (Oestmann, 1998). As the contribution of medical imaging to collective population dose continues to grow (UNSCEAR, 2010a), there is greater awareness and utilisation of tools such as DRLs to reduce and manage dose.

Modality and exam specific DRLs are typically set by regulatory authorities at a national level, at the third quartile value of the dose distribution from a substantive survey of patient doses (Bongartz et al., 2004; ICRP, 2001; IPEM, 2004; Shrimpton et al., 2005). One objective of establishing DRLs and reviewing the values is to improve the dose distribution for a type of examination over time (ICRP, 2007c). Ultimately a narrow range of values representing good practice may be derived (ICRP, 2007c). Furthermore, it is conceivable that a lower level may also be relevant to indicate a value below which image quality is questionable (ICRP, 2001). Both image quality and dose are factors that must be considered for optimisation, although currently the focus of DRLs is as a dose indicator.

In Australia, the Australian Radiation Protection and Nuclear Safety Agency (ARPANSA) has issued a Code of Practice regarding radiation protection in medicine (ARPANSA, 2008b). The new requirements make it necessary to implement a dose monitoring program at a practice level to facilitate comparison with DRLs (ARPANSA, 2008b). It is the intention that DRLs are not used as a constraint, but rather a level, which if consistently exceeded warrants investigation (ICRP, 1996a). By periodically undertaking patient dose surveys, a facility can determine if local levels of exposure are acceptable in terms of Australian practice (ARPANSA, 2008a). National DRLs have yet to be established, although ARPANSA have commenced a survey to determine values for CT (ARPANSA, 2011).

The new Australian requirements also recommend that local DRLs (LDRLs) be established with regard to national values where these exist (ARPANSA, 2008a). In practices in which the LDRL is significantly lower than the national DRL, it is preferable that the lower level be utilised in order to encourage optimisation. Furthermore, it may be relevant for a practice to have an LDRL that is higher than the national DRL (e.g. specific trauma imaging), although these protocols must be clearly justified and regularly reviewed. The Institute of Physicists and Engineers in Medicine (IPEM) in the United Kingdom (UK) originally discouraged the use of LDRLs due to the lack of statistical significance in the small sample sizes available within a single institution (George et al., 2004). However, later guidelines recommend that LDRLs may be calculated from the mean of the dose distribution, rather than the third quartile (IPEM, 2004). Establishing the value at the third quartile incorrectly conveys that 25% of patient doses are always at a level warranting investigation. Therefore, the mean value LDRL represents the typical dose level for a protocol at that institution, reflecting the local situation. These values should be

reviewed more frequently than national DRLs, allowing greater local control and increased opportunity for management and optimisation of doses.

The aim of this part of the thesis was to conduct a survey of CT doses for typical examinations performed at the Royal Children's Hospital (RCH) in Melbourne, Australia. As the hospital is currently being redeveloped and the CT scanner will be decommissioned, this survey will provide a useful baseline for comparison of doses after installation of a new scanner. The dose levels were compared with other Australian published data and international DRLs to facilitate benchmarking.

6.2 Methods

A retrospective audit of patient records at the RCH for CT brain, chest and abdomen/pelvis examinations was undertaken. Approval was gained from the institutional Human Research Ethics Committee to access this data. The RCH is a major Australian specialist paediatric hospital and the only dedicated paediatric hospital in both Victoria and Tasmania. It was established in 1870 and in the 2007-2008 financial year treated approximately 35,000 inpatients, 130,000 outpatients and had 68,000 emergency department attendances (RCH, 2008). The RCH performed 3,685 CT examinations in 2008.

All CT scans included in this survey were performed on a Sensation 16 multidetector CT (MDCT) scanner with a Straton X-ray tube (Siemens, Erlangen, Germany) utilising automatic tube current modulation (CARE Dose4D). This is the only CT scanner located at the RCH. The gender, age, parameters used (kV_p, time per rotation, detector configuration, beam collimation, pitch, effective mAs) and dose indicators, volumetric computed tomography dose index ($CTDI_{vol}$) and dose length product (DLP) were recorded for each patient (see Section A.5, Appendix A for a discussion of CT dosimetry terms).

In clinical practice at the RCH, the protocol to be used for an individual patient is typically selected based on the age of the patient for head examinations and the weight of the patient for body examinations. However, all protocols are programmed into the RCH CT scanner in terms of patient age and are given in Table L.1 (Appendix L). Depending on the type of examination, the RCH CT protocols are categorised into several age groups including 0-6 months, 6 months-3 years, 3-6 years (or under 5 years), 6-10 years (or 5-10 years) and over 10 years. Body weight is not a parameter that is recorded at the RCH and since this survey was retrospective, the age of the patient was used to group the surveyed records. It is recommended that when assessing doses from a patient survey at a practice level, the sample should consist of at least 10 patients (Bongartz et al., 2004; IPEM, 2004). In this survey, samples of 20 patients were selected for each age group in each of the three study protocols. The CT protocols were not changed during the survey period. Only those patient examinations where there were no obvious indicators that the examination was atypical were sampled. For example, patients with metal implants were excluded. For

CT examinations of the brain, only those performed without contrast were included in the survey. CT examinations of the chest and abdomen/pelvis were included whether they were performed with or without intravenous contrast, as all post-contrast examinations were single phase only and the same protocol was used. Consecutive patient records were included in the survey if they met the inclusion criteria. The patient records were sampled from 2009 to early 2011. When 20 patient records were accumulated for an examination type and age category, then no earlier records were required.

On most modern CT scanners, the $CTDI_{vol}$ and DLP values are displayed as projected values following the CT localiser radiograph (also called the scout/surview/topogram/ scanogram) and the itemised values resulting from each individual part of the examination and total values are displayed at the conclusion of an examination based on the scan parameters used. At RCH this final dose screen is recorded for each patient so that these values could readily be collected for use in the survey. The $CTDI_{vol}$ values represent standardised dose measurements made in two different polymethyl methacrylate (PMMA) homogenous, cylindrical phantoms. The measurements are made at the periphery and centre of the cylinder and weighted accordingly to take into account the varying dose distribution with depth in the phantom during a CT scan. Typically, a 16 cm diameter dosimetry phantom is used to represent the head of an adult or child (or child's body) and a 32 cm diameter dosimetry phantom to represent an adult's body. Some jurisdictions now require the phantom size for the $CTDI_{vol}$ and DLP calculations to be displayed on the final dose screen, although this was not a feature of the RCH scanner.

It was found from TLD measurements earlier in this thesis that there were limitations in using the dose indicators displayed on the CT scanner console after an examination (Chapter 3, Chapter 5). The displayed dose indicators on the RCH scanner for paediatric body examinations were based on the 32 cm dosimetry phantom. This displayed dose considerably underestimated the dose measured with TLDs and supports the recommendation by Shrimpton and Wall (2000) that all CT dose indicators should be expressed in terms of the 16 cm dosimetry phantom for children regardless of age or scan location. Displayed dose indicators for head examinations were expressed in terms of the 16 cm dosimetry phantom, which more closely reflected TLD measurements. To distinguish between the values, $CTDI_{vol,16}$ and DLP_{16} will be used for doses relative to the 16 cm dosimetry phantom and $CTDI_{vol,32}$ and DLP_{32} for doses relative to the 32 cm dosimetry phantom.

Since this study relates to children, doses expressed in terms of the 32 cm dosimetry phantom were converted to doses relative to the 16 cm dosimetry phantom following the methodology of Huda et al. (2010) taking into account the X-ray beam filtration used for the scan. This is necessary since the 16 cm dosimetry phantom is generally reserved for head imaging and therefore the head, rather than the body, filter is used on the CT scanner. Using the ImPACT CT Dosimetry Tool (ImPACT, 2011) and the methodology of Huda et al. (2010), a conversion factor of 2.08 was determined to convert body doses in

terms of $CTDI_{vol,32}$ and DLP_{32} into $CTDI_{vol,16}$ and DLP_{16}, respectively. The UK National Radiological Protection Board (NRPB, now the Health Protection Agency) use a factor of "about two" when deriving DRLs for paediatric CT to convert from the 32 cm to the 16 cm dosimetry phantom dose (Shrimpton et al., 2005). Siegel et al. (2004) also found a similar dose ratio between the two phantoms.

The DLP is calculated by multiplying the $CTDI_{vol}$ by the scan length. For helical scans, this represents the imaged length, rather than the exposed length as it does not take into account the additional over-ranging length required for helical data interpolation on many CT scanners (van der Molen and Geleijns, 2007). The imaged scan length was calculated from the recorded $CTDI_{vol}$ and DLP values for each patient in the survey.

Recommendations were made regarding establishing LDRLs in terms of $CTDI_{vol}$ and DLP for the RCH based on mean dose values from the survey. These dose indicators do not take into account the relative radiosensitivity of the organs and tissues exposed or the amount of the body directly irradiated and therefore effective dose was estimated. Effective dose is designed to provide a measure of overall radiation detriment due to stochastic effects and is to be used for prospective dose assessment to facilitate planning and optimisation (ICRP, 2007b). While not intended for retrospective use for estimation of doses to individuals, it is utilised here as an optimisation tool that will allow comparison with similar procedures undertaken at different hospitals. The surveyed median DLP values were used with published (Shrimpton et al., 2006) age- and region-specific conversion coefficients (Table K.4, Appendix K) to calculate effective dose according to the 1990 Recommendations of the ICRP (ICRP 60 (ICRP, 1991)). These conversion coefficients were matched to the age groups used in this survey to estimate effective dose. Where some age groups included a range of ages incorporating two different conversion coefficients, these values were averaged.

Conversion coefficients derived earlier in this thesis based on TLD measurements (Chapter 5) and the 2007 Recommendations of the ICRP (ICRP 103 (ICRP, 2007b)) were also used to convert DLP values to effective dose. These conversion coefficients were derived from measurements made in a physical phantom representing a 10 year old child. The values were scaled for all other age groups according to the relative ratios of the published ICRP 60 conversion coefficients (Shrimpton et al., 2006). This method is approximate, but suitable for the purpose of providing broad estimates of effective dose using the two different ICRP Recommendations (ICRP, 1991, 2007b). These conversion coefficients are compared with other published ICRP 103 paediatric conversion coefficients in Table 6.1. Deak et al. (2010) provide conversion coefficients specific to a 64 MDCT scanner and Alessio and Phillips (2010) derive conversion coefficients based on adult effective doses, adjusted for paediatric sizes. It is evident that a wide range of values currently exists in the literature. The conversion coefficients based on earlier TLD measurements (Chapter 3) were used for effective dose estimates in this thesis because they are specific to this

scanner and calculated directly from a paediatric anthropomorphic phantom, rather than an adult phantom.

6.3 Results

The age and gender distribution of patients included in the survey are shown in Table M.1 (Appendix M). For the three types of examination, overall more records for males than females were recorded. For CT chest examinations for children aged 5-10 years, there were very few female patient records (15%) that met the study inclusion criteria in the time period surveyed. The parameters set in the age-dependent standard, pre-programmed protocols are given in Table L.1 (Appendix L). In addition, the mean value of the tube current, scan length and the dose indicators from the patient records survey are also provided in Table L.1 (Appendix L).

Figure 6.1 shows $CTDI_{vol,16}$ values plotted against DLP_{16} for all age groups, with a linear fit and zero y-intercept. The gradient of each line gives the average scan length of the pooled data. Values of DLP_{16}, $CTDI_{vol,16}$ and scan length as a function of patient age are shown in Figure 6.2. The $CTDI_{vol}$ increased with age for all types of examination, regardless of whether the examination was of the body or head region. The DLP increased with age for each type of examination, although the increase was less for brain examinations than for body examinations. Scan length did not substantially change with age for CT brain examinations, while for body examinations it increased with age, particularly for the youngest age groups.

The range and median values for $CTDI_{vol,16}$, DLP_{16}, mAs and scan length are shown for each age group in Figure 6.3. These graphs demonstrate the wider range of scan lengths for body examinations compared with head examinations. The bottom panel of Figure 6.3 shows a graph of $CTDI_{vol,16}$ normalised to 100 mAs for each age group and each examination. Since this quantity is independent of both the examination mAs and the scan length, it reflects the influence on dose of the protocol parameters initially selected.

Recommended LDRLs in terms of both $CTDI_{vol}$ and DLP are given in Table 6.2 based on the survey results. These are rounded values of the mean of the age group for each type of examination. The values have been provided in terms of both the 16 cm and 32 cm dosimetry phantoms for the body examinations. Effective dose according to ICRP 60 and ICRP 103 definitions was calculated using the median DLP value and age- and site-specific conversion factors. The values of effective dose are given in Table 6.3.

6.4 Discussion

Repeat surveys conducted in the UK have shown that DRLs assist in reducing radiation doses over time (Shrimpton et al., 2005). DRLs for paediatric CT examinations were

Table 6.1: Dose length product (DLP) to effective dose (E) conversion coefficients.

Examination	**Age Group**[a]	**E/DLP Conversion Coefficient ($mSv \cdot mGy^{-1} \cdot cm^{-1}$)**[b]			
		ICRP 60[c]	**ICRP 103**[d]	**ICRP 103**[e]	**ICRP 103**[f]
CT Brain	**0-6 m [0 y]**	0.011	0.0076	0.0085	0.013
	6 m-3 y [1 y]	0.0067	0.0046	0.0053	0.008
	3-6 y [5 y]	0.0040	0.0028	0.0035	0.005
	6-10 y [10 y]	0.0032	0.0022	0.0027	0.004
	>10 y [Adult]	0.0021	0.0014	0.0019	0.002
CT Chest	**<5 y [1 y]**	0.026	0.032	0.026	0.038
	5-10 y [5, 10 y]	0.016	0.019	0.014	0.023
	>10 y [10 y]	0.013	0.016	0.012	0.019
		(0.014)	(0.017)	(0.015)	(0.020)
CT Abdomen/ pelvis	**<5 y [1, 5 y]**	0.025	0.023	0.022	0.026
	5-10 y [5, 10 y]	0.018	0.016	0.014	0.018
	>10 y [10 y]	0.015	0.014	0.012	0.015
		(0.015)	(0.014)	(0.014)	(0.015)

[a] Age groups are defined in terms of months (m) or years (y). The age groups used in the survey were based on the categorisations used for RCH CT protocols. Since conversion coefficients are generally defined for a specific age, these were matched to the age groups used in the survey. The age specific to the conversion coefficients is shown in square brackets in this column. For example, for the 0-6 month age group for CT brain examinations in this survey, the age-specific conversion coefficient for 0 year olds has been used. In some cases an average of conversion coefficients was used based on the distribution of ages in the survey and for these, two ages have been listed in the square brackets.

[b] All values of the conversion coefficients are relative to the 16 cm dosimetry phantom, except those shown in round brackets, which are relative to the 32 cm dosimetry phantom and are for adults. Some of the patients in the >10 year age group will be closer in size to an adult rather than a child.

[c] ICRP 60 conversion coefficients provided by Shrimpton et al. (2006), which are age-specific. These values have been used to calculate the ICRP 60 effective doses given in Table 6.3.

[d] These conversion coefficients were derived from the measurements made in Chapter 3. These values have been used to calculate the ICRP 103 effective doses given in Table 6.3.

[e] ICRP 103 conversion coefficients provided by Deak et al. (2010), which are age-specific and kV-specific. The kV for each protocol is given in Table L.1 (Appendix L). All body conversion coefficients in Deak et al. (2010) have been provided relative to the 32 cm dosimetry phantom and therefore have been divided by two to be expressed relative to the 16 cm dosimetry phantom, except for the values in rounded brackets. Deak et al. (2010) provide separate conversion coefficients for the abdomen and the pelvis. For the CT abdomen/pelvis examinations in the Table above the conversion coefficients for these two regions have been averaged.

[f] ICRP 103 conversion coefficients provided by Alessio and Phillips (2010), which are age-specific. The conversion coefficients given in the Table above for the CT abdomen/pelvis examinations for Alessio and Phillips (2010) relate to the abdomen only.

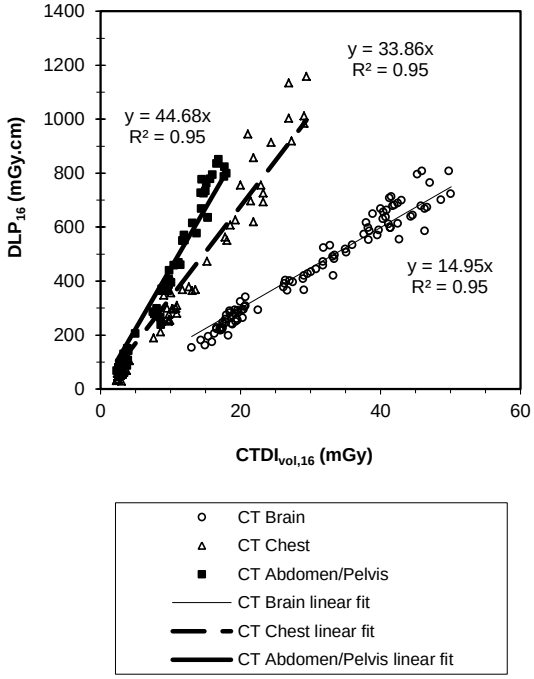

Figure 6.1: DLP_{16} as a function of $CTDI_{vol,16}$ for CT brain, chest and abdomen/pelvis examinations from the RCH paediatric dose survey. A linear fit is shown for each examination with a y-intercept of zero.

Table 6.2: Recommended local diagnostic reference levels (LDRLs) at the RCH for typical paediatric CT examinations.

Examination	**Age Group**[a]	**LDRL (Mean Value)**[b]			
		$CTDI_{vol,32}$ (mGy)[c]	**DLP_{32} (mGy·cm)**[d]	**$CTDI_{vol,16}$ (mGy)**[c]	**DLP_{16} (mGy·cm)**[d]
CT Brain	**0-6 m**	-	-	18	250
	6 m-3 y	-	-	20	300
	3-6 y	-	-	30	450
	6-10 y	-	-	40	650
	>10 y	-	-	45	700
CT Chest	**<5 y**	2	50	3	100
	5-10 y	5	150	11	300
	>10 y	12	400	23	800
CT Abdomen/Pelvis	**<5 y**	2	100	4	150
	5-10 y	5	200	10	400
	>10 y	8	350	15	750

[a] Age groups are defined in terms of months (m) or years (y).

[b] Dose indicators for CT chest and abdomen/pelvis examinations were displayed on the CT scanner as $CTDI_{vol,32}$ and DLP_{32}. These have been multiplied by a factor of 2.08 according to the methodology of Huda et al. (2010), prior to rounding, to give $CTDI_{vol,16}$ and DLP_{16}. The dose indicators for the CT brain examinations were already displayed in terms of $CTDI_{vol,16}$ and DLP_{16} and therefore did not require correction.

[c] $CTDI_{vol}$ values in milligray (mGy) have been rounded up to the nearest whole number.

[d] DLP values have been rounded up to the nearest 50 mGy·cm.

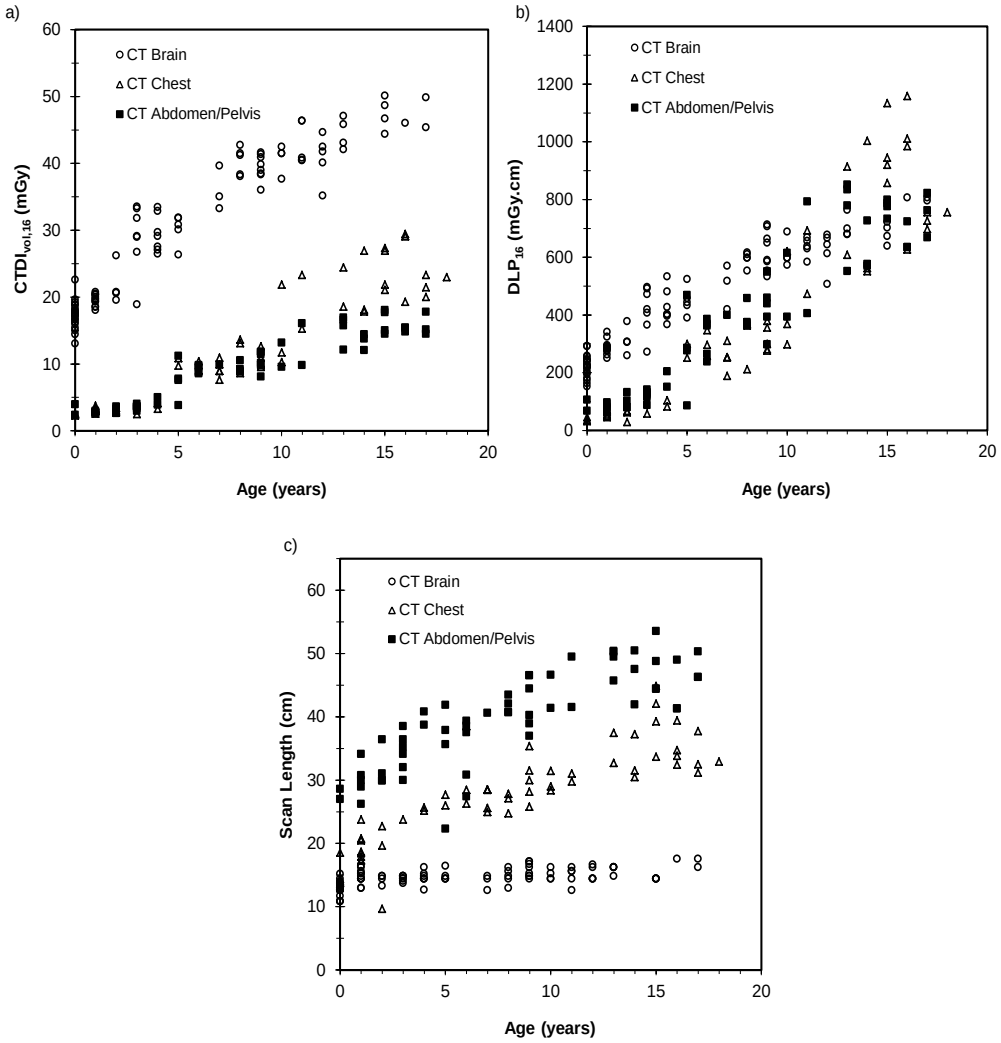

Figure 6.2: a) $CTDI_{vol,16}$, b) DLP_{16} and c) scan length versus patient age for CT brain, chest and abdomen/pelvis examinations from the RCH paediatric dose survey.

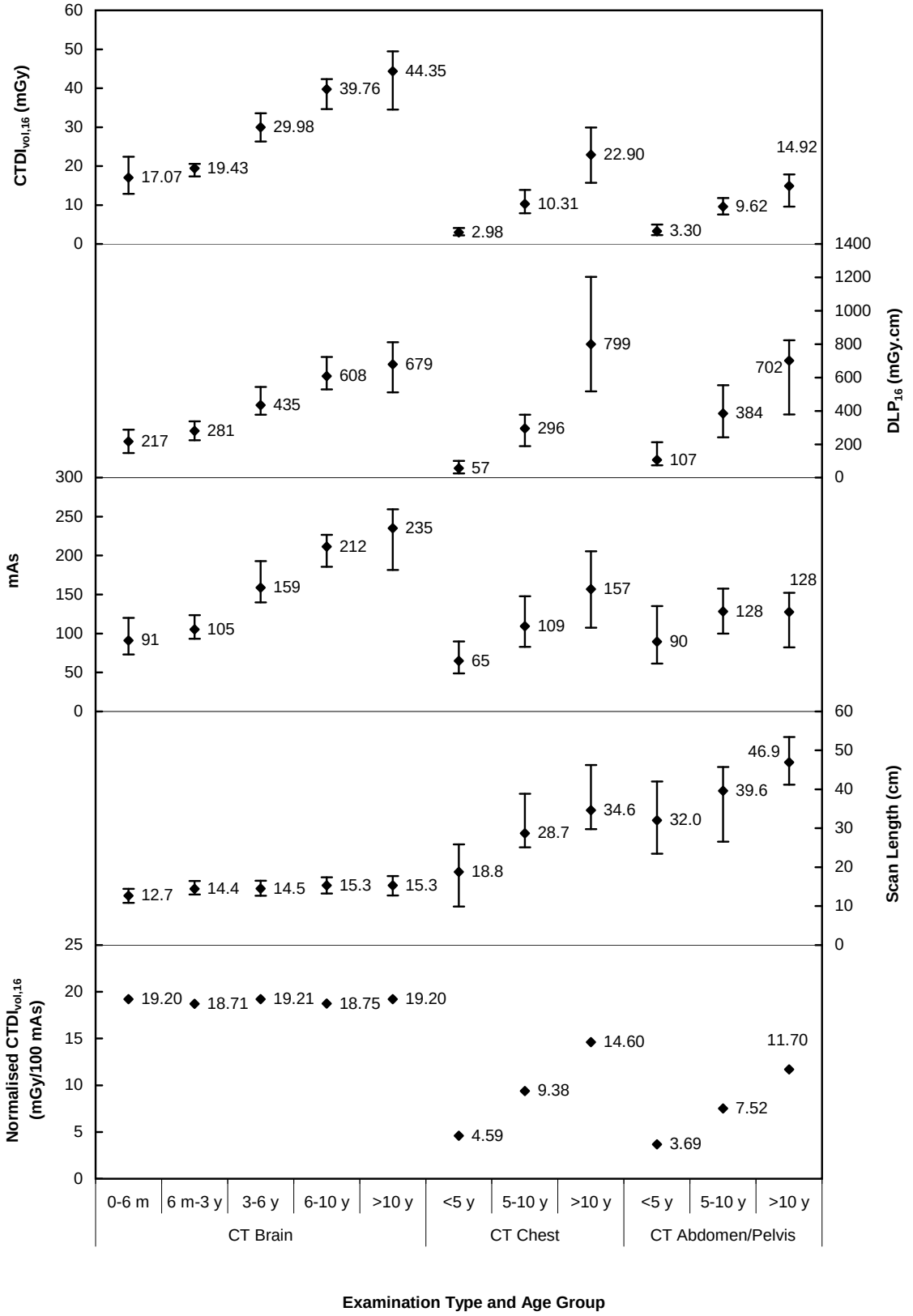

Figure 6.3: $CTDI_{vol,16}$, DLP_{16}, mAs (actual mAs not effective mAs) and scan length, including the median value, for different age groups for typical CT brain, chest and abdomen/pelvis examinations from the RCH paediatric dose survey. The bottom panel shows normalised median $CTDI_{vol,16}$ values.

Table 6.3: Summary of estimated effective doses for typical paediatric CT examinations at the RCH.

Examination	Age Group[a]	Median DLP[b] (mGy·cm)	Effective Dose ICRP 60[c] (mSv)	Effective Dose ICRP 103[d] (mSv)
CT Brain	**0-6 m**	221	2.4	1.7
	6 m-3 y	283	1.9	1.3
	3-6 y	423	1.7	1.2
	6-10 y	597	1.9	1.3
	>10 y	675	1.4	1.0
CT Chest	**<5 y**	60	1.6	1.9
	5-10 y	296	4.6	5.6
	>10 y	755 (363)[e]	9.8 (5.1)[f]	12 (6.3)[f]
CT Abdomen/Pelvis	**<5 y**	99	2.5	2.3
	5-10 y	380	6.6	6.2
	>10 y	729 (351)[e]	11 (5.3)[f]	10 (4.9)[f]

[a] Age groups are defined in terms of months (m) or years (y).

[b] DLP for CT chest and abdomen/pelvis examinations were displayed on the CT scanner as DLP_{32}. These have been multiplied by a factor of 2.08 according to the methodology of Huda et al. (2010), prior to rounding, to give DLP_{16}. The dose indicators for the CT brain examinations were already displayed in terms of DLP_{16} and therefore did not require correction.

[c] The effective dose is calculated from the median DLP_{16} using age- and region-specific published conversion factors (Shrimpton et al., 2006) (Table K.4, Appendix K).

[d] The effective dose is calculated from the median DLP_{16} using age- and region-specific conversion factors derived earlier in this thesis (Chapter 5).

[e] The value in brackets is the DLP_{32} value, which is displayed on the scanner. This has been included for comparison as some of the patients in this age group will be closer to an adult size rather than a child size.

[f] The effective dose in brackets is calculated from the median DLP_{32} using adult region-specific published conversion factors for ICRP 60 (Shrimpton et al., 2006) (Table K.4, Appendix K) or conversion coefficients derived from TLD measurements for ICRP 103.

10-40% lower when comparing surveys at five year intervals (Shrimpton and Wall, 2000; Shrimpton et al., 2005). With an established and widely adopted DRL program, it is envisaged that at some point doses may become relatively constant and DRLs will then be important to protect against unnecessary dose increases. In Australia, there will be a significant initial opportunity for optimisation when national DRLs are established.

At the local level, dose surveys can be undertaken to establish LDRLs which can be compared with national DRLs where these are available. It is useful to conduct surveys based on real patients, which can be repeated at regular intervals to assess CT practice at an institution. Using the dose indicators on the CT display ($CTDI_{vol}$ and DLP) ensures that results will be comparable between different scanners, sites and countries, as long as the dosimetry phantom is specified. Furthermore, Heggie (2005) argues that dose surveys are also an essential tool for understanding local practice when commissioning a new CT scanner to ensure that optimisation is undertaken. Therefore, LDRLs are useful to gauge changes in local practice and techniques and the impact of new imaging technology.

Establishing typical dose levels for children is more challenging than deriving these values for adults. Parameters and hence doses vary considerably with size and age for children. Multiple reference values for a particular examination may be appropriate to account for the variation in size across age ranges. It has been suggested that age may not be an appropriate indicator of size in children and a method for deriving a representative "age" from a size measurement of the patient has been developed (Hart et al., 2000; IPEM, 2004). The diameter of the patient directly correlates with the distance that the X-ray beam travels in the patient and hence is a more direct determinant of dose (Boone et al., 2003; Haaga, 2001; Hart et al., 2000; IPEM, 2004; Kleinman et al., 2010). However, in this survey, dose records were grouped for children based on age and not size. This allowed investigation of the range of doses that may be encountered in a particular age bracket.

6.4.1 Scan Parameters and Patient Age

The results of the patient dose survey undertaken show that the dose indicators, $CTDI_{vol}$ and DLP, increased with patient age (Figure 6.3). Furthermore, the range of these values is widest in the older patients for all types of examinations. This is due to the considerable variation in patient size in the eldest cohort, which spans children aged 10 years to adolescents aged 18 years.

Normalising the $CTDI_{vol}$ values with respect to mAs provides a better indication of the dose dependence on the programmed scan parameters, as it quantifies the intensity of the X-ray beam and reflects the effects of tube voltage, beam collimation and pitch on the dose to the patient, regardless of the patient size. The slight variation in normalised values for protocols using the same parameters evident in the results from this thesis is due to the limitations of using *average* mAs for this calculation (see for example normalised values

for CT brain examinations in the bottom panel of Figure 6.3). For a fixed tube current these values would be identical.

CT brain examinations had the highest value of normalised $CTDI_{vol}$ (Figure 6.3). This is partly attributable to the narrower beam collimation compared with body examinations, which incurs a greater dose penalty due to over-beaming, where the unused penumbral region of the X-ray beam is proportionally higher for narrower collimations. Furthermore, less filtration is used for head scanning, which leads to a greater dose compared with a more filtered beam with higher beam quality for body examinations (Huda et al., 2010). Since the kV_p, beam collimation and pitch did not change for the different age groups for brain examinations, the normalised $CTDI_{vol}$ remained constant.

The beam collimation and pitch also remained constant between the age groups for the body examinations, although the kV_p increased over the three age groups. This is observed in the increasing normalised $CTDI_{vol}$ values in Figure 6.3. The chest and abdomen/pelvis normalised values for the same age groups differ only by the pitch. It is interesting that the values are similar as the two body regions have quite different attenuation and contrast characteristics. It may be expected that the $CTDI_{vol}$ values which reflect the patient dose may be lower for the chest than for the abdomen/pelvis due to the reduced attenuation from the air in the lungs and the increased inherent contrast in this area allowing for lower dose settings. However, this was not always the case, particularly for the oldest age group (Figure 6.3).

Tube Current Modulation

In all examinations assessed, the tube current modulation dose reduction tool was used (CARE Dose4D). This requires a user-defined reference mAs value[i], which is set at a level to achieve the desired image quality. The tube current is modulated based on the size of the patient being scanned relative to the standard sized patient (defined as weighing 20 kg or five years of age for this scanner). Therefore, for very young/small patients it is expected that the range of mAs values for the examination will be less than the reference value and for older/large patients, the mAs will exceed the reference mAs value. This was found to be true in the patient records survey results. For a four day old patient undergoing a CT chest examination the average value for the examination was 49 mAs compared with a reference value of 65 mAs. For a 14 year old adolescent undergoing a CT chest examination the average was 124 mAs and the reference was 80 mAs.

For the brain examinations which were undertaken with a tilted gantry, the average tube current was lower than the reference value for all age groups. Some sections of the scan had a very low tube current where the transmission length through the brain was quite small (e.g. top of the head). Overall, the mAs for the brain examinations increased significantly

[i]In this context Siemens use an effective mAs, which is defined as the actual mAs divided by the pitch. This quantity is referred to as Q_{ref}.

with age, reflecting the higher reference mAs required to achieve the same image quality in older patients with a more radio-dense skull.

For the body examinations, the change in examination mAs reflected both the reference mAs values and/or the increasing size of the older patients. For example, for chest examinations the increase between the younger groups was due to the increasing reference value and/or the increasing size of the patient, whereas the increase in the oldest group was due only to larger patient size since the reference value remained constant. For abdomen/pelvis examinations the patients in the oldest group were larger, which would increase the examination mAs, but this was offset by a lower reference mAs and hence the median examination mAs was the same for the two oldest age groups.

Scan Length

The change of body size as children develop is clearly evident in the longer scan lengths for the body examinations in older children (Figure 6.1c). As expected, variation in scan length is not as readily evident for scans of the head, except in perhaps the youngest patients. The average scan length for brain examinations increased between the two youngest age groups (up to three years old), but was then fairly consistent (Table L.1, Appendix L). This correlates well with the rapid growth of the head in the first two years (Kleinman et al., 2010).

Generally, the greatest change in scan length in body examinations occurred in the first five years. The length of the scan for abdomen/pelvis examinations was 11-13 cm longer on average than for examinations of the chest for all age groups (Table L.1, Appendix L). For children under five years, the average chest scan length was 40% shorter than the abdomen/pelvis scan length, whereas in the older age groups it was only 25% shorter. Regardless of age, the anatomical borders of the scan seldom change. For chest examinations, the entire thorax anatomy and half of the liver are routinely included. For abdomen/pelvis examinations the typical scan range is from just above the diaphragm to symphysis pubis. Hence, it is most likely that anatomical changes as children develop lead to differences in the comparative sizes of the chest and abdomen/pelvis in different age groups, which is reflected in the relative scan lengths from this survey.

For all scans in helical mode, the operator's planned length defines the mid-position of the first and last image to be reconstructed and the length of the table movement for a single rotation (which varies with pitch) is automatically added to this planned length. This additional half-rotation width at each end is part of the imaged length and included in the DLP calculation. An additional scan length due to over-ranging for helical data interpolation is not included in the DLP and van der Molen and Geleijns (2007) have shown that for this scanner with a pitch of 1-1.25, the over-ranging length is 5-6 cm. Therefore, the scan lengths calculated here represent the imaged length and underestimate the total length exposed and consequently the effective dose.

Effective Dose

It is important to distinguish the values of $CTDI_{vol}$ and DLP from the actual dose to the patient. These quantities are measures of dose in a CT dosimetry phantom, whereas effective dose reflects the stochastic risk to the patient from the radiation exposure. Estimates of effective dose have been given in Table 6.3. In the eldest age category, both DLP_{16} and DLP_{32} may be applicable for the range of patient sizes in this age group and hence both values have been reported. A comparison between ICRP 103 and ICRP 60 effective dose estimates for paediatric CT examinations is provided earlier in this thesis (see Section 3.4.2, Chapter 3).

The effective dose estimates for this survey are similar to those found in a multicentre study in Belgium, although these largely related to single detector CT scanners (Pages et al., 2003). A recent study by Thomas and Wang (2008) reported effective doses based on a similar paediatric patient dose survey for an 8 MDCT scanner without tube current modulation. The effective doses in their study were calculated using ICRP 60 conversion coefficients. The ICRP 60 effective dose estimates reported in the current survey are predominantly lower, except for imaging of the chest in the older age groups. This appears to be due to two factors. Firstly, in the other study a higher pitch (1.375) is used, which will reduce dose. Secondly, the mAs was lower than the present survey. However, the earlier study reports that dose ranges within an age group for an examination can be large (Thomas and Wang, 2008).

6.4.2 Comparison with Physical Phantom

In an earlier part of this thesis (Chapter 3), measurements were undertaken using a physical anthropomorphic phantom representing a 10 year old child. The phantom was scanned on the RCH CT scanner using the protocols for a child aged over 10 years (Table 3.1), which were selected by an experienced radiographer. Table 6.4 provides the displayed dose indicators compared with those collected in the survey for a real patient in each examination category who was 10 years of age.

The normalised values of $CTDI_{vol}$ are similar between the phantom and patient for all three types of examination. Since normalised $CTDI_{vol}$ is independent of the patient, it was expected that for any patient or phantom these values would be in agreement. There is a slight variation in the $CTDI_{vol}$ values, which is due to the limitations of using the *average* mAs from the scan for this calculation.

Parameters for the CT brain examination were similar between the phantom and the patient demonstrating that the size of the head and attenuation properties were well matched. However, for the body examinations some variation was evident due to body size. For the CT chest examination, the mAs was considerably lower (47%) for the examination of the physical phantom and consequently the $CTDI_{vol}$ was also lower. The mAs was 28%

Table 6.4: Displayed dose indicators for CT examinations of a physical phantom representing a 10 year old child compared with the dose indicators for CT examinations of 10 year old patients at the RCH.

Parameter	CT Brain[a]		CT Chest[b]		CT Abdomen/Pelvis[b]	
	Phantom	Patient[c]	Phantom	Patient[c]	Phantom	Patient[c]
Effective mAs	231	230	80	150	65	90
Scan length (cm)	16.0	15.6	26.6	28.4	36.9	46.6
$CTDI_{vol}$ (mGy)	40.0	40.8	5.72	10.5	4.60	6.33
DLP (mGy·cm)	640	637	152	298	168	295
Norm. $CTDI_{vol}$ (mGy/100 mAs)	17.3	17.7	7.15	7.00	5.66	5.63

[a] Dose indicators for the CT brain examination are $CTDI_{vol,16}$ and DLP_{16}.
[b] Dose indicators for the CT chest and abdomen/pelvis examinations are $CTDI_{vol,32}$ and DLP_{32}.
[c] A patient was selected from the survey data for each examination based on age to match the phantom.

lower and the scan length was 21% shorter for the CT abdomen/pelvis examination of the phantom when compared with the sampled 10 year old patient. The differences in these parameters suggest that the size of the phantom body was smaller than the 10 year old patients sampled in the survey. However, it is noted that this comparison is based on a single patient for each examination who may or may not be representative of the population.

6.4.3 Optimisation in Australian Paediatric CT Practice

An assessment of dose optimisation at the RCH can be made by comparing the examination parameters and dose indicators from this thesis with other published Australian values. For paediatric CT this includes data from an Australian multi-site survey by Moss and McLean (2006), a project coordinated by the Royal Australian and New Zealand College of Radiologists (RANZCR) under the Quality Use of Diagnostic Imaging (QUDI) Program (Wallace et al., 2007a,b) and paediatric DRLs established at the Royal Children's Hospital Brisbane (RCHB) (Watson and Coakley, 2010).

Australian Survey Data

Table 6.5 provides a comparison of values from the current survey with those published in an earlier Australian survey (Moss and McLean, 2006) in which a range of practices in New South Wales participated during 2001-2002. In the earlier survey, 52 practices responded, including both hospital-based and private sites. Four dedicated paediatric centres participated in the survey, while other respondents returned data if they carried out paediatric CT scans (for most centres this was two or less per month). Two-thirds of the CT scanners for which data was submitted were single slice. All scanners were capable of helical scanning. Although the RCH was not included in the earlier survey, the comparison is still useful to gauge the current practices at RCH.

Table 6.5: Comparison of mean (and maximum) values of RCH examination parameters from the current paediatric dose survey with those collected in an earlier Australian survey (Moss and McLean, 2006).

Examination	Age Group	kV_p	mAs	Pitch	$CTDI_{vol}$ (mGy)	${}_nCTDI_w$ (mGy/100 mAs)	${}_nCTDI_{vol}$ (mGy/100 mAs)
CT Brain	8 week	120 (140)	157 (480)	1.03 (1.50)	28.3 (153)	18.1	18.0
	0-6 m	120 (120)	91 (120)	axial	17.1 (22.6)	18.8	18.8
	5-7 y	125 (140)	226 (411)	1.03 (1.67)	42.0 (139)	18.7	18.6
	3-6 y	120 (120)	159 (189)	axial	30.0 (33.5)	18.9	18.9
	6-10 y	120 (120)	212 (228)	axial	39.8 (42.7)	18.8	18.8
CT Chest	8 week	117 (135)	63 (195)	1.37 (2.00)	10.0 (42.3)	19.7	15.7
	<5 y	80 (80)	65 (90)	1 (1)	1.4 (2.0)	2.2	2.2
	5-7 y	121 (140)	99 (200)	1.35 (2.00)	16.9 (43.4)	20.9	17.1
	5-10 y	100 (100)	109 (145)	1 (1)	5.0 (6.5)	4.5	4.5
CT Abdomen/ pelvis	8 week	118 (130)	67 (195)	1.41 (2.00)	10.8 (42.3)	21.3	15.9
	<5 y	80 (80)	90 (136)	1.25 (1.25)	1.6 (2.4)	2.2	1.8
	5-7 y	121 (140)	123 (400)	1.29 (2.00)	20.6 (52.1)	20.0	16.7
	5-10 y	100 (100)	128 (158)	1.25 (1.25)	4.6 (5.7)	4.5	3.6

[a] Shaded rows are values from the earlier Australian survey (Moss and McLean, 2006). White rows are from the current paediatric dose survey (2010-2011). Age categories have been matched as closely as possible.

[b] Values in brackets are maximum values, while all other values are mean values.

[c] $CTDI_w$ and $CTDI_{vol}$ values from the previous Australian survey have been normalised in terms of mAs for comparison with this survey. $CTDI_w$ and $CTDI_{vol}$ for the current survey are in terms of the 16 cm dosimetry phantom for the brain examinations and the 32 cm dosimetry phantom for the body examinations. The size of the phantom has not been specified in the earlier survey (Moss and McLean, 2006).

[d] Since the same protocol was used within each age group in the current survey the values of kV_p and pitch do not vary within an age group.

[e] Age groups are defined in terms of weeks, months (m) or years (y).

Comparison of the present RCH survey with the earlier results shows that there are some differences in practice. CT brain examinations are not performed at 140 kV_p at the RCH, while some sites had previously used this value. However, the mean value for CT brain scans (120 kV_p) for earlier practices does not differ from current practice at the RCH. Examinations of the chest and abdomen/pelvis are currently performed at a lower kV_p at the RCH, which is a recognised dose saving technique in recent years. The dose reduction is reflected in the normalised CTDI values. This decrease in dose will only be achieved if changes in other parameters, such as the mAs, do not offset the dose saving. This is observed in the $CTDI_{vol}$ values, which are up to seven times lower at the RCH for body examinations.

For all CT brain examinations the average mAs for the RCH patients is less than the average from the previous survey. Furthermore, the maximum values are considerably lower than those reported several years ago. This is also observed for examinations of the chest and abdomen/pelvis where maximum mAs values in all age groups were substantially higher in the earlier survey. This may be a consequence of the number of sites involved in the first survey, which included practices where adult imaging was more common. Hence,

the maximum values may be attributable to sites at which adult parameters were not changed when scanning children and hence were quite high.

For the body examinations, the average values for mAs at the RCH are comparable or higher than the earlier survey values. For the youngest age group this may be due to the difference in the age groupings. The earlier survey values are based on an eight week old baby, whereas the RCH values are derived from a sample of patients aged 0-5 years. Again, the age range is broader for the older children in the RCH evaluation (5-10 years compared with 5-7 years). Furthermore, the mAs may not provide a direct correlation with changes in dose for these examinations, since the kV_p has also varied. The influence of the change in parameters on dose must be considered in the context of all parameters, rather than any one parameter in isolation. Normalised CTDI values provide information on the protocol settings, independent of mAs, while CTDI values reflect the total dose for the examination taking into account the size of the patient and the mAs required to produce a diagnostic image based on the other protocol settings used.

Based on the normalised CTDI values, current protocol settings for CT brain examinations at RCH are commensurate with Australian practice in 2001-2002. Overall, doses from brain scanning have decreased since this time based on the lower mAs now utilised, which is reflected in the lower $CTDI_{vol}$ values. The CTDI values have decreased considerably for body examinations, predominantly due to the lower kV_p values now used. Although some of the dose saving achieved by reducing the kV_p has been offset by lower pitch values and higher mAs values, overall the $CTDI_{vol}$ values demonstrate that the dose reduction in current practice is substantial.

The other contributing factor to dose is the volume scanned. An indication of the dose as a result of scan length is given by the DLP. This data was not provided in the earlier Australian study and hence a comparison cannot be made. In general, it appears that current protocols at the RCH will lead to reduced doses to children from CT examinations compared with typical practices in 2001-2002 in Australia.

QUDI Optimisation Project

The issue of paediatric CT dose optimisation in Australia was assessed in 2006 and 2007 in a pilot project funded by the Australian Department of Health and Ageing under the QUDI Program (Wallace et al., 2007a,b). A survey of standard protocols for a five year old patient across Australian paediatric institutions aimed to determine typical doses in terms of DLP. This was followed by optimisation workshops and then a re-assessment of the typical DLPs. The standard parameters for each protocol were entered into the dosimetry tool CT-Expo (Stamm and Nagel, 2011b) to calculate DLP, rather than using real patient data. It should be noted that these DLPs will include the additional scan length for over-ranging due to helical scanning, which is not included in the RCH reported DLPs for the survey conducted in this thesis. The RCH participated in the QUDI project.

In the initial survey conducted in 2006, it was found that doses varied between sites by more than 11-fold. This variation reduced for some protocols when the sites were re-surveyed in 2007. However, interestingly, some protocols showed an increase in dose disparity. In the QUDI project, DRLs were proposed based on the sixth highest ranked DLP. Almost all DRLs reduced in the second survey, some substantially. This demonstrated the benefits of training and feedback in the optimisation process.

From the second, post-optimisation survey, the QUDI DRL for head examinations (for varying clinical indications) ranged from about 200-500 mGy·cm. The mean DLP in the 3-6 year age category for the current RCH survey based on patient records was 435 mGy·cm. This is within the DRL range suggested in the QUDI study, although at the higher end. It is comparable with the QUDI DRL values for head imaging for trauma or space occupying lesions, which are likely to be the most common types of imaging performed at the RCH. Therefore, the RCH brain imaging protocols in this age group appear appropriate when compared with the QUDI DRLs.

For the body examinations, the dosimetry phantom is not specified in the QUDI project, although it is assumed that it is in terms of the 16 cm phantom as CT-Expo applies this phantom for all paediatric calculations (Stamm and Nagel, 2011b). The chest DRLs are all just above 100 mGy·cm in the QUDI survey. The mean DLP values from the RCH survey for chest examinations were 57 mGy·cm and 296 mGy·cm for the under 5 years and 5-10 year age categories, respectively. While the youngest age group is in line with the QUDI DRL, the next age category significantly exceeds the value. This may be due to the age range being wider for this thesis and the influence of using real patient data.

The UK experience has shown that there can be a wide variation in doses when sites are requested to submit their standard protocols on a questionnaire compared with a sample of actual patient dose records (Shrimpton et al., 2005). They concluded that for some sites, the standard protocols may not reflect general practice. The QUDI project is based on a questionnaire of standard protocols, rather than patient dose surveys and this may also impact on the QUDI DRLs. A practice's standard protocol may be overly optimistic, in terms of dose, compared to what happens in actual practice. Alternatively, this result may suggest that the RCH can review optimisation for their CT chest protocols in the middle age group.

For imaging of the abdomen the QUDI DRL values range from about 300-500 mGy·cm, depending on the clinical indication. It is not clear whether the pelvis is included in this imaging. The mean DLP values from the RCH survey for CT abdomen/pelvis examinations were 107 mGy·cm and 384 mGy·cm for the under 5 years and 5-10 year age categories, respectively. These compare favourably with the QUDI DRL values.

The QUDI project is a valuable tool for paediatric CT dose optimisation in Australia. It provides a useful opportunity to benchmark against current Australian practice. Further-

more, for sites that more commonly scan adults, the QUDI DRLs provide an indication of best practice at paediatric hospitals. It would be beneficial to expand this study design to other paediatric age groups to enable a more comprehensive overview of paediatric CT doses in Australia. This may be achieved when national DRLs are established in Australia (ARPANSA, 2011).

Royal Children's Hospital Brisbane

A comprehensive single-site Australian survey was recently undertaken by Watson and Coakley (2010) at the Royal Children's Hospital Brisbane (referred to as RCHB to distinguish it from the Royal Children's Hospital (RCH) Melbourne) based on paediatric protocols on a 64 MDCT scanner. A comparison with the current survey (Table 6.6) shows that the majority of $CTDI_{vol}$ and DLP values in the Watson and Coakley study are significantly lower. The dose reduction may be attributable to changes in technology between the 16 MDCT scanner used in this thesis and the newer 64 MDCT scanner of their survey. However, it may also be due to optimisation of protocols as some of the dose saving appears to be due to lower mAs values. In particular, the examinations of the brain at RCHB demonstrate a significant reduction in mAs compared with the RCH examinations.

It is not completely clear in the Watson and Coakley paper (2010) whether the $CTDI_{vol}$ values are expressed in terms of the 16 cm or 32 cm dosimetry phantom. For example, for the same subset of patients in the 11-25 kg weight range (average age 4.8 years) undergoing CT chest examinations, the $CTDI_{vol}$ values with the 16 cm and 32 cm dosimetry phantoms as the reference are both 3 mGy. However, it is clear that the DLP values are relative to the 16 cm phantom. Therefore, in Table 6.6 $CTDI_{vol}$ values for body imaging should be compared with caution.

For CT chest imaging, the RCH values are comparable with the RCHB values in the youngest age group. It would be useful to compare normalised $CTDI_{vol}$ values, although this data is not available. For the youngest children, the RCH protocol parameters using a lower kV_p (80 kV_p versus 120 kV_p) and higher pitch (1 versus 0.828) would suggest that the RCH doses will be lower than RCHB doses. However, the $CTDI_{vol}$ values are the same, which appears to indicate that higher mAs values are offsetting any dose saving made with the selection of kV_p and pitch.

In the 5-10 year age category the DLPs for body imaging at RCH are considerably higher than any of the corresponding groups in the RCHB survey, particularly for chest imaging. For example, the mean DLP at RCH in the 5-10 year age group at RCH is 296 mGy·cm, whereas the DLP for the group with average age 9.9 years at RCHB is 152 mGy·cm. One of the significant benefits of the Watson and Coakley study (2010) is that they have access to patient weight and have reported dose values in terms of both age and weight.

Table 6.6: Comparison of examination parameters from the current paediatric dose survey at RCH Melbourne with those collected in an earlier study at RCH Brisbane (Watson and Coakley, 2010).

Examination	Weight Range (kg)	Average Age or Range (y)	kV_p	mAs	Pitch	$CTDI_{vol,16}$ (mGy)	DLP_{16} (mGy·cm)	
							Mean	Range
CT Brain	0-9	1.1	120	60	axial	7	106	76-188
	-	0-0.5	120	91	axial	17	217	152-292
	9-19	2.4	120	75	axial	7	171	70-422
	-	0.5-3	120	105	axial	19	281	227-340
	-	3-6	120	159	axial	30	435	365-532
	>19	9.6	120	125	axial	13	337	155-449
	-	6-10	120	212	axial	40	608	518-712
	-	>10	120	235	axial	44	679	506-807
CT Chest	0-10	0.7	100	-	0.828	3	55	17-100
	-	<5	80	65	1	3	57	29-104
	11-25	4.8	120	-	0.828	3	83	33-163
	-	5-10	100	109	1	10	296	189-379
	26-40	9.9	120	-	0.828	5	152	94-328
	-	>10	120	157	1	23	799	472-1159
	41-60	13.3	120	-	0.828	14[b]	328	184-592
	61-75	14.7	120	-	0.828	18[b]	461	280-716
	>75	14.4	120	-	0.828	32[b]	779	384-950
CT Abdomen/ pelvis	0-10	0.6	120	-	0.828	3	67	33-122
	-	<5	80	91	1.25	3	107	67-204
	11-25	4.5	120	-	0.828	5	153	72-220
	-	5-10	100	128	1.25	10	384	237-549
	26-40	10.4	120	-	0.828	5	313	176-504
	-	>10	120	129	1.25	15	702	406-851
	41-60	13.4	120	-	0.828	8	502	192-976
	61-75	14.5	120	-	0.828	35[b]	1485	1238-1732

[a] Shaded rows are values from the RCHB (2006-2008) (Watson and Coakley, 2010). White rows are from the current paediatric dose survey at RCH (2010-2011).

[b] These values were only given relative to the 32 cm dosimetry phantom and therefore have been multiplied by a factor of two so that all CTDI and DLP values are expressed relative to the 16 cm dosimetry phantom.

6.4.4 International Paediatric CT DRLs

A number of countries have established or proposed DRLs for paediatric CT examinations. The international values have been summarised in Table D.1 (Appendix D). DRLs for children are most commonly provided for the head, chest and abdomen. The mean values of $CTDI_{vol}$ and DLP from the patient dose survey conducted at the RCH in this thesis have been compared with the corresponding international DRL values in Figure 6.4 (where they are quantified in a similar way, e.g. in terms of the same dosimetry phantom, similar age group and examination). The national values established in the other countries were based on surveys that included a range of single detector CT scanners and MDCT scanners in clinical practice at the time. All of the other surveys included the 16 MDCT scanner assessed in this study. For a local dose survey, the mean value is used to represent

the typical dose for a type of examination. DRLs on the other hand generally represent the 75^{th} percentile of a substantive dose survey or measurements made using phantoms and standard protocols. Hence, for this inter-comparison, if the local mean value significantly exceeds a corresponding DRL, this may indicate that further investigation and optimisation is warranted locally.

Germany

The German study (Galanski et al., 2007) was based on a nation-wide survey of paediatric CT practice conducted during 2005-2006 where a questionnaire was used to collect standard protocol settings from facilities that performed more than 100 paediatric CT examinations per year. Forty-two institutions participated in the survey.

The proposed DRLs were calculated using the third quartile values for adults (equivalent to the above 15 years age category used in the survey) for brain examinations and abdomen/pelvis examinations. The adult chest DRLs were based on two-thirds of the abdomen/pelvis value, as the chest values surveyed were considered unnecessarily high. A moderate, rather than strong, adaptation was then made to these values for patient age and weight to calculate the set of proposed paediatric CT DRLs. Therefore, the German DRLs to some extent represent desired practice rather than the results of the survey. Comparison with the third quartile values from the survey reveal that the derived DRLs are comparable, but overall slightly lower than the third quartile survey results. Furthermore, over-ranging effects have been taken into account for the DLP calculation, which were negligible for the brain examinations, but increased the DLP on average by 10-20% for the body examinations. The German study is unique in this respect, as it is more common to use the DLP displayed on the scanner which does not include the effects of over-ranging. For a DRL to be practical, it should reflect the dose quantity used clinically. However, to give a true indication of total dose, effects such as over-ranging need to be included. Either way, as with the size of the phantom, it is essential to define the factors on which the DRLs are based.

The German survey establishes DRLs for the same examinations considered in this thesis: brain, chest and abdomen (including pelvis). There are more age groups defined in the German study including newborn, up to one year, 1-5 years, 6-10 years, 11-15 years and above 15 years, whom were considered adults. The newborn DRLs were not used for comparison. All other age groups matched those used in this thesis fairly well, with the 11-15 year group being matched to the >10 year category in this thesis. One exception was made for chest imaging, since the majority of the group in the >10 year category were in fact 15 years or older in the present survey. Therefore, the above 15 years DRL from the German study was used for chest imaging when comparing to the >10 year group in this thesis.

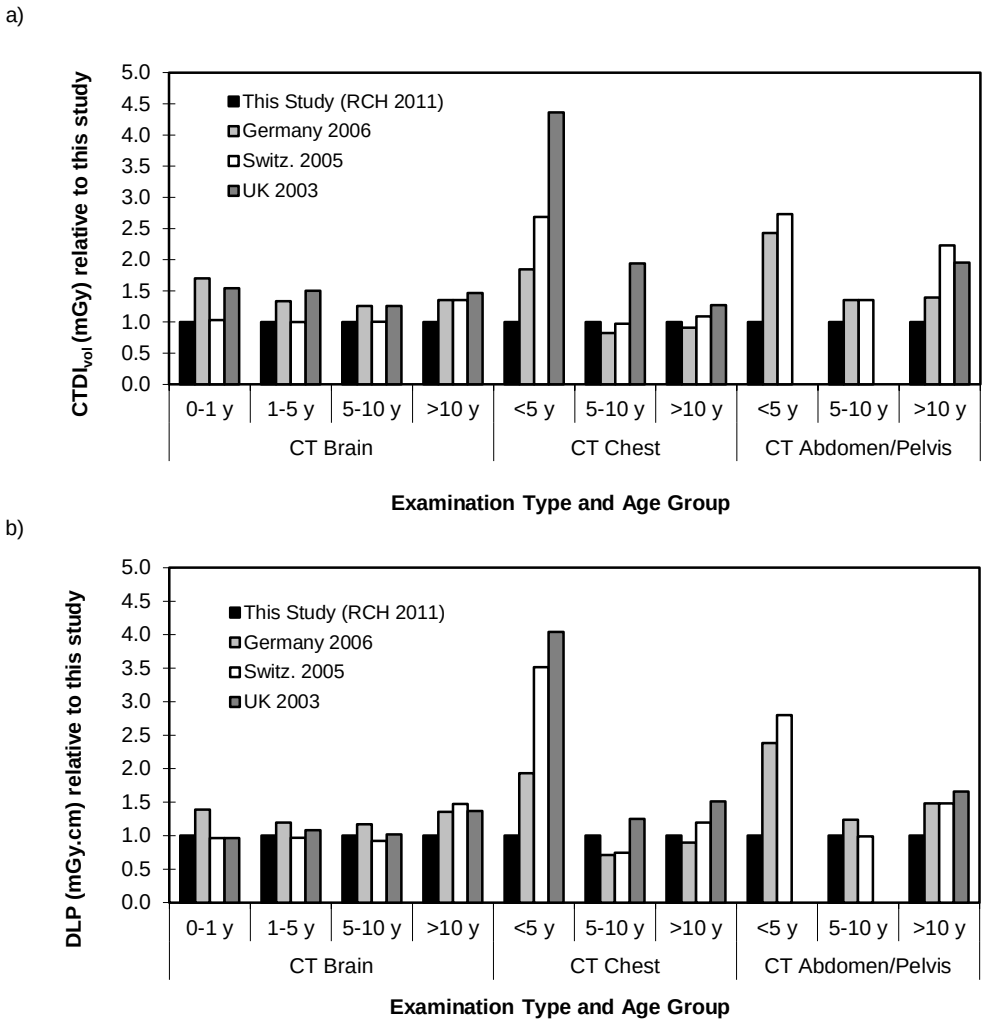

Figure 6.4: Comparison of a) mean $CTDI_{vol}$ values and b) mean DLP values for different age groups for common CT examinations from the paediatric dose survey undertaken in this thesis (RCH 2011) with international DRLs (Germany 2006 (Galanski et al., 2007), Switzerland 2005 (Verdun et al., 2008) and UK 2003 (Shrimpton et al., 2005)). The year indicates the last year of data collection in each of the studies. All values are relative to the mean RCH values from this thesis. All values are relative to the 16 cm dosimetry phantom ($CTDI_{vol,16}$, DLP_{16}) except for the chest and abdomen/pelvis examinations in the >10 year age category, which are relative to the 32 cm dosimetry phantom ($CTDI_{vol,32}$, DLP_{32}).

Switzerland

For the Swiss study (Verdun et al., 2008) undertaken in 2005, dedicated paediatric CT practices submitted standard protocol settings and displayed doses on a questionnaire. This survey method also did not collect data relating to examinations conducted on specific patients. A scaling factor of 1.25 was used to calculate the suggested DRL from the mean survey value. This method has also been used by others to provide a dose level comparable with the third quartile when a dose distribution is not available (Aroua et al., 2004). In this survey the sample size was only small, consisting of eight facilities. It appears that the DLP displayed on the scanner was used to derive the DRLs and hence over-ranging has not been taken into account, as it was in the German study (Galanski et al., 2007).

The CT examinations surveyed in the Swiss study include the clinical indication for the scan. These were trauma for the brain examinations and detection of malignancy for scans of the chest or abdomen. It is not clear whether the pelvis was included in the abdominal scanning and this may have varied between the sites included in the survey. The groups were separated in terms of age and/or weight into <1 year or 10 kg, 1-5 years or 10-20 kg, 5-10 years or 20-35 kg and 10-15 years or >35 kg. This matched closely the age groups used in this thesis.

UK

Paediatric CT DRLs were reported from a UK survey undertaken in 2003 (Shrimpton et al., 2005). This survey collected information on standard protocols, as well as data from scans undertaken on individual patients for a sample of ideally at least 10 patients. For paediatric head imaging, approximately 50 standard protocols were submitted and for paediatric chest imaging approximately 20 different protocols were sampled. Abdomen imaging was not assessed for children in this survey. The UK survey differs from other studies through the collection and analysis of patient data. However, for children, the sample sizes were relatively small. For all head imaging, 56 patient data sets were submitted across all paediatric age groups and for chest imaging only 16 patient records were included. The standard examination protocol data was used to establish DRLs based on rounded third quartile values. Although the effects of over-ranging are acknowledged, the additional scan length is not consistently incorporated as in the German study, due to more limited knowledge regarding this effect at the time of this survey.

Collection of data in the UK study for the paediatric head and chest imaging was based on clinical indications. These were trauma including non-accidental injury for the head imaging of both the posterior fossa or cerebrum and detection of malignancy for the chest examinations. Recommendations for DRLs were provided for 0-1 year olds, five year olds and 10 year olds. This differed from this thesis and the German and Swiss surveys which used age ranges. The 0-1 year old category was matched to the same category for brain

imaging in this thesis. The five year old DRL was compared with the 1-5 year group for brain scans and the <5 year age category for chest and abdominal examinations. The 10 year old age group was matched to the 5-10 year age brackets from this thesis and UK adult DRLs were used for comparison with the >10 year age category of this thesis. This may result in the UK values being at the upper limit for each category.

Dosimetry Phantom

A meaningful comparison of international DRLs for paediatric CT examinations can only be made when the dose indicators are defined in terms of the same CT dosimetry phantom. For adults, it is generally accepted practice to use the 16 cm dosimetry phantom for head examinations and the 32 cm dosimetry phantom for body examinations. Although, even for adults there are some body regions where selection of the relevant phantom is not straightforward, including examinations of the cervical spine, sinuses or the whole body in a single scan (Huda et al., 2010). In these cases it is also important that for adult examinations the phantom is specified. For children, there is little consistency in the choice of phantom used for the dose indicators.

For body examinations, it has been shown that for children the dose indicator should be defined in terms of the 16 cm phantom (Shrimpton and Wall, 2000). The CT scanner at the RCH uses the 32 cm phantom and therefore an adjustment was made to convert $CTDI_{vol}$ and DLP values to be in terms of the 16 cm phantom (Huda et al., 2010). The UK survey also defines DRLs in terms of the 16 cm phantom (Shrimpton et al., 2005). The German study provides values in terms of both dosimetry phantoms where relevant (Galanski et al., 2007). The Swiss study is less clear, as the phantom size is not defined (Verdun et al., 2008). However, in the Swiss study comparisons are made with the UK and German studies, and based on the values of the DRLs derived, it appears that these are also in terms of the smaller dosimetry phantom.

For children or adolescents aged over 10 years, and in particular over 15 years, it may be considered that they are approaching an adult size and the larger 32 cm dosimetry phantom is applicable for expressing the dose for body examinations. The German study provides DRLs for body examinations for 11 years and above only in terms of the 32 cm dosimetry phantom (Galanski et al., 2007). For the comparisons made in this thesis all body doses for chest and abdomen/pelvis imaging in the age group >10 years have been expressed in terms of the 32 cm dosimetry phantom. The exception is the values for the Swiss study, as it is unclear which phantom was originally used.

Brain Examinations

For CT examinations of the brain, the 16 cm dosimetry phantom is consistently used for children and adults ensuring that when inter-comparisons are conducted the same quantity will be evaluated. Figure 6.4a shows that in all age groups for brain examinations the RCH

mean $CTDI_{vol}$ values are equal to or lower than international values. This implies that the protocol settings for brain scans at the RCH are well optimised and reflect current international practice.

In some age groups the mean DLP values at the RCH are slightly higher (<10%) than the corresponding international DRLs (Figure 6.4b). This suggests that the scan lengths may be slightly longer at the RCH. Furthermore, the dose saving evident in the $CTDI_{vol}$ values for the RCH has reduced when comparing the DLPs, conveying that the scan lengths at RCH may on average be slightly longer, offsetting the dose reduction achieved in the parameter selection for the protocols.

It must be noted, there are other contributing factors that may result in a numerical difference in the dose indicators, but not the actual dose to the patient. For axial brain examinations there may be a small component of the scan that extends beyond the top of the skull and scans only air to ensure that the complete region of clinical interest is included in the scan range. For the protocol settings used at the RCH, this will be up to a maximum of a single beam collimation, or 18 mm, of extended scan length which does not directly expose the patient, but increases the DLP and, hence this may account for the observed differences in DLP values. Additionally, the definition of scan length for examinations performed with a tilted gantry will also directly affect the DLP. For example, on this scanner the scan length is measured parallel to the patient's long axis, whereas measurement of the scan length parallel to the axis of rotation would reduce the length by approximately 10%. Therefore, the actual dose to the patient has not changed, but the DLP has, depending on the scan length used. Overall, the RCH values are comparable, if not lower than international values for CT head examinations. It is evident from Figure 6.4 that parameters and doses for CT brain examinations are fairly consistent.

Body Examinations

For body imaging, the RCH mean values are considerably lower than international DRLs in terms of both $CTDI_{vol}$ and DLP in the <5 years age group (Figure 6.4). This is most likely due to the low kV_p (80 kV_p) employed at the RCH, which leads to a considerable dose reduction. For example, the UK survey found that almost 80% of sites conducted chest imaging in this age group at 120 kV_p, with only 5% using 80 kV_p (Shrimpton et al., 2005). This may also explain why the UK DRL is higher than the other values in the 5-10 year age group. Again, 120 kV_p is typically used in the UK, while at the RCH 100 kV_p is used in this age group. The German survey found that in younger patients it was more likely that a lower kV_p would be used for chest imaging than for abdomen/pelvis scans, although in the 2-5 year age group low kV_p chest imaging accounted for just over 30% of the examinations (Galanski et al., 2007).

The German $CTDI_{vol}$ DRLs are up to 15% lower than the mean values at the RCH in the two older age groups for chest imaging (Figure 6.4a). However, it should be noted that

the German survey data resulted in values which they concluded were unnecessarily high for chest imaging when compared with abdomen imaging and therefore the DRLs were modified (decreased), apparently with the intention of encouraging optimisation. The mean values at the RCH are in fact comparable with the third quartile values for chest imaging from the German survey.

The German DRLs in terms of DLP are also lower than the RCH mean values in the two older age groups for chest imaging (Figure 6.4b). As previously discussed, the German chest DRLs are lower than the third quartile values found in their survey and therefore may underestimate current German practice. However, the DLP values in the German study also include the over-ranging length in the helical scans, which was not included in the RCH DLPs. Therefore, it was expected that the German DLP DRLs would be higher than the RCH mean values which do not include this additional length. The third quartile value for the scan length, including over-ranging, in the age group 6-10 years in the German study was 22.7 cm. The mean scan length in the RCH survey for 5-10 year olds was 28.7 cm. Clearly, the RCH scan length is extended. Similarly, the Swiss DLP is lower than the RCH value in the 5-10 year age group. The average scan length for 5-10 year olds in the Swiss study (Verdun et al., 2008) was 23 cm, again shorter than the lengths found at the RCH.

All RCH mean values for abdomen/pelvis examinations across all age groups are equal to or lower than the international DRLs. In the two older age groups, the dose saving achieved through the selection of parameters, evident in the $CTDI_{vol}$ values at the RCH, appears to be offset to some extent by a longer scan length when assessing the DLP values. In particular, the third quartile values in the German survey, which should be longer due to the inclusion of the over-ranging scan length are in fact several centimetres shorter. In the 5-10 year age group the mean RCH scan length was 39.6 cm, while the German survey third quartile value was 31.6 cm. Similarly in the over 10 year category the RCH mean length was 46.9 cm and the German third quartile value was 40.0 cm. Again, there appears to be an opportunity for dose reduction by reviewing the scan length for the RCH examinations. However, overall the RCH average dose values for abdomen/pelvis imaging are lower in comparison.

6.5 Conclusions

Conducting a CT dose survey within a facility is essential for understanding and analysing local practice. The mean values from these surveys are also useful for comparison with national or even international DRLs to facilitate benchmarking and ultimately optimisation of both dose and image quality. A comparison of the average dose values at the RCH with international DRLs for common paediatric CT examinations has shown that the RCH values are typically comparable or lower. In particular, the use of 80 kV_p for both chest and abdomen/pelvis imaging in children under five years of age leads to a significant dose

saving. There is potential for dose optimisation at the RCH by reducing scan lengths for body examinations for children over five years of age. In the short term, a review of these protocols should be undertaken to determine if there is appropriate justification for the extended scan lengths.

In the future, it may be worthwhile deriving LDRLs at the RCH for common protocols based on clinical indication. This may result in narrower ranges for the scan lengths and allow more directed LDRLs. The comparison undertaken in this thesis has shown that it is not simple to compare a practice's dose values against published DRLs. There are many factors that need to be considered and the dose indicators need to be properly defined in terms of the CT dosimetry phantom used and the type of examination. For a more thorough comparison it is essential to also consider the scan length and where possible the normalised $CTDI_{vol}$ values. Using several quantities enables optimisation of protocol parameters, as well as operator technique by isolating the influence of each factor on dose.

It was found in this thesis that comparison of the normalised CTDI values was beneficial as the dependency on mAs was removed. With tube current modulation becoming a common feature of CT scanners today, it is useful to have a quantity that is not influenced by a factor that constantly changes throughout the scan. Furthermore, it is necessary to have a quantity that reflects the parameters, such as kV_p, beam collimation and pitch that are defined when originally establishing protocols. The normalised CTDI values are useful for other sites to consider when assessing parameter choice for common paediatric CT protocols. These values will also provide a point of comparison for the RCH when replacing the current CT scanner.

6.6 Publications Arising from this Chapter

1. **Brady, Z.**, Ramanauskas, F., Cain, T. M. and Johnston, P. N., *Assessment of paediatric CT dose indicators for the purpose of optimisation*, British Journal of Radiology, 2012 *(accepted)* (Brady et al., 2012c).

2. **Brady, Z.**, *DLP practical breakdown - how best to adjust parameters to reduce dose*, presented at the Siemens Low Dose Academy, 2012, Sydney, Australia *(Invited Speaker)* (Brady, 2012b).

3. **Brady, Z.**, Cain, T. M. and Johnston, P. N., *Assessing CT protocols in a paediatric hospital using a patient dose survey (EPSM ABEC 2011 Conference Proceedings)*, Australasian Physical & Engineering Sciences in Medicine, 2011, 34(4):590 (Brady et al., 2011c).

Chapter 7

Assessment of Australian Paediatric CT Imaging Trends

7.1 Introduction

In Australia in 1996, CT imaging was the largest source of radiation exposure from diagnostic radiology procedures, accounting for about 50% of the total dose (Webb et al., 1999). The annual per capita dose from CT examinations was approximately 0.39 millisieverts (mSv) compared with 0.83 mSv from all medical diagnostic exposures (Webb et al., 1999; Wise and Thomson, 2004). CT imaging contributed approximately 17% of the average total annual dose of 2.3 mSv from all natural and non-natural radiation sources. Hence, CT was recognised as a major source of radiation exposure in Australia even more than a decade ago.

There have been several Australian studies investigating CT imaging trends and radiation dose (McLean et al., 2003; Moss and McLean, 2006; Thomson and Tingey, 1997; Wise and Thomson, 2004). The most comprehensive, in terms of the number of sites surveyed, was conducted by the Australian Radiation Laboratory (ARL, now the Australian Radiation Protection and Nuclear Safety Agency, ARPANSA) in 1994/95 (Thomson and Tingey, 1997). The authors estimated that the exposure from CT imaging induced about 280 fatal cancers per year; one in every 4,000 CT examinations. This estimate was based on a mean dose of 6.6 mSv per exam, the linear no-threshold hypothesis and a nominal fatality risk coefficient of 4% per Sv for a population of working age (ICRP, 1991).

Another Australian study provided an assessment of the change in CT radiation doses from 1994 to 2002 (Wise and Thomson, 2004). The authors found that the number of procedures had increased by 60% and that the mean dose per procedure increased from 8.3 to 11.7 mSv over this period, raising the annual per capita dose to 0.9 mSv in 2002 (Wise and Thomson, 2004).

Other Australian studies have surveyed a smaller number of local sites to assess CT radiation dose (McLean et al., 2003; Moss and McLean, 2006). McLean et al. (2003) surveyed nine radiology departments in 2003 regarding paediatric protocols for an 8 week old baby and 7 year old child and made an estimation of effective dose levels using Monte Carlo dose simulations. They found that for chest and abdomen procedures there was a wide range in doses across the different sites, with the specialist paediatric departments having lower doses and a narrower dose range. The average dose was found to be less than 10 mSv with a range of 1-20 mSv.

A wider survey was conducted by Moss and McLean (2006) who included all sites in New South Wales licensed to possess CT scanners in 2001/02. This survey assessed scanning protocols and radiation dose for both adults and children; the latter were based on protocols for 8 week old and 5-7 year old patients. They again found a wide range of doses between sites for comparable examinations. Doses for paediatric head examinations ranged from 1.3-2.0 mSv and for adult head examinations 1.6-2.7 mSv. Chest protocols ranged from 1.9-7.9 mSv for children and 4.9-7.8 mSv for adults, while abdomen imaging resulted in doses of 4.4-14.1 mSv for children and 7.7-13.3 mSv for adults.

This thesis provides an analysis of current paediatric CT imaging trends in Australia for the age range 0-18 years based on examinations that have been billed to Medicare, the universal health care system of the Australian Government. Medicare is administered by the Department of Health and Ageing who are responsible for ensuring that Medicare Benefits Schedule (MBS) payments are made for eligible health services provided to Australian residents by eligible health care providers. Services provided to public patients in a public hospital form the largest group of medical services funded outside the Medicare Benefits Schedule and are not captured in the Medicare data. It has previously been estimated that 24% of CT examinations are non-Medicare funded (Thomson and Tingey, 1997). However, it is not clear if this figure is representative of the situation for paediatric patients. Therefore, in view of the higher risks from radiation exposure in children, this thesis analysed the imaging rate in a major Australian children's hospital for comparison with data from Medicare.

7.2 Methods

A selection of diagnostic imaging services data are made publicly available by Medicare. The information is limited in its completeness for assessing overall imaging rates as it excludes procedures not funded by Medicare. Although care is needed when extrapolating to the total number of medical imaging procedures undertaken, Medicare data are the best currently available resource for describing trends in medical imaging in Australia.

The data relating to imaging services assessed in this thesis were accessed via the statistical reporting function on the Medicare website (www.medicareaustralia.gov.au). The data

retrieved relate to the total number of services, including age and gender distributions, for calendar years from 1994 to 2010. CT services correspond to MBS item codes and may incorporate multiple scans undertaken on a patient during a single visit. The Medicare data is provided in age bands which included 0-4 years, then 10 year age bands to 84 years and a single age band for 85 years and above. Additional data including the total number of services and patients and other de-identified population demographic information including single year of age for patients aged 0-18 years were provided by the Department of Health and Ageing for CT examinations performed from 1986 to 2008. The Medicare definition of a CT service has changed over the last two decades and therefore, where possible, the number of CT patients has been used.

Data on the Australian population were obtained from the Australian Bureau of Statistics in order to calculate imaging rates (ABS, 2008a, June 2009). The Estimated Resident Population (ERP) at the midpoint of each reference year was used. The ERP data was available either by single year of age or in five year age bands and these were combined to match the available Medicare age bands. Imaging rates are expressed as the number of services or patients per 1,000 persons of the ERP in each year corresponding to the Medicare age bands. Indexed rates based on a reference year were calculated to assist in interpreting changes in the data over time. The indexed rate for all other years was calculated by determining the ratio of the comparison period value to the reference period value.

To determine if the Medicare CT data accurately reflects the imaging trends for children and young people aged 0-18 years, CT imaging data was extracted from the Royal Children's Hospital (RCH) Melbourne radiology information system (RMS, Kestral, Australia). The RCH is a major Australian specialist paediatric hospital and the only dedicated paediatric hospital in both Victoria and Tasmania. It was established in 1870 and in the 2007-2008 financial year treated approximately 35,000 inpatients, 130,000 outpatients and had 68,000 emergency department attendances (RCH, 2008). Approval was gained from the RCH Human Research Ethics Committee to retrospectively access this data. Information on the type of CT procedure, date of procedure, and age and gender of the patient was obtained from 1986 to 2008 and the billing code was included for procedures performed from 1999 onwards. Approximate scaling factors were derived from the RCH data to adjust Medicare data for those CT services that are not billed to Medicare.

Data from the RCH were used to calculate the CT imaging trends for patients aged 0-18 years. Each patient visit was counted individually and referred to as CT patients hereafter. The RCH imaging rate was compared with the paediatric data based on number of CT patients over the same time period obtained from Medicare.

7.3 Results

Approximately two million CT services across all age groups were billed to Medicare in Australia in 2010 (Figure 7.1). The annual growth rate in the number of CT services has ranged from 6.3% to 13.3% over the last 16 years, with the only decrease seen in the last year at 3.5%. The recent decrease is promising, but it is too early to be confirmed as an ongoing trend. There was an average annual increase of 7.8% over the last 16 years. Taking population growth into account, the number of CT services per 1,000 persons (imaging rate) has increased by an average of 7.1% per year, or almost tripled in the last 15 years (1994-2009) based on the number of services billed to Medicare (Table 7.1).

Table 7.1: Number of CT services and imaging rate in Australia for services billed to Medicare in 1994 and 2009.

Age at Scan (years)	**No. CT Services (%)**[a]				**CT Imaging Rate (No. services per 1,000 persons**[b]**)**	
	1994		**2009**		**1994**	**2009**
0-4	2,827	(0.5)	2,410	(0.1)	2	2
5-14	17,982	(2.9)	26,890	(1.3)	7	10
15-24	45,813	(7.5)	103,503	(5.0)	17	34
25-34	72,003	(11.8)	157,397	(7.5)	25	51
35-44	96,766	(15.8)	253,374	(12.1)	36	81
45-54	110,155	(18.0)	355,599	(17.0)	52	118
55-64	104,240	(17.0)	433,670	(20.8)	70	175
65-74	100,370	(16.4)	402,426	(19.3)	79	259
75-84	52,748	(8.6)	285,556	(13.7)	80	292
≥ 85	9,533	(1.6)	65,385	(3.1)	53	171
Total	**612,437**	**(100.0)**	**2,086,210**	**(100.0)**	**34**	**95**

[a] CT services billed to Medicare.

[b] Annual imaging rate calculated by dividing the number of CT services billed to Medicare in that year by the Estimated Resident Population at the midpoint of the year, multiplied by 1,000 (ABS, 2008a, June 2009). Note that this does not include non-Medicare funded CT services.

The number of patients for whom CT services were billed to Medicare in the 0-18 year age bracket has more than tripled over the 22 year period from 1986 to 2008, increasing from approximately 17,500 to 58,200 (Figure 7.2). The number of patients undergoing CT examinations at the RCH also demonstrated an increase over this time. In 1986 about 1,500 patients underwent CT examinations at the RCH and by 2008 this had more than doubled to over 3,600 CT patients. For comparison with the annual growth rate of CT services for the entire population over the past 15 years of 8.5%, the average annual change in the number of CT patients aged 0-18 years whose services were billed to Medicare is 4.5% and for RCH CT patients is 5.6% over the same 15 year period.

The age and gender distribution of CT services billed to Medicare compared with the Australian population for 2009 are shown in Figures 7.3 and 7.4. Based on Medicare data, only a small percentage (0.10%) of CT scans are carried out for the very young (0-4 years),

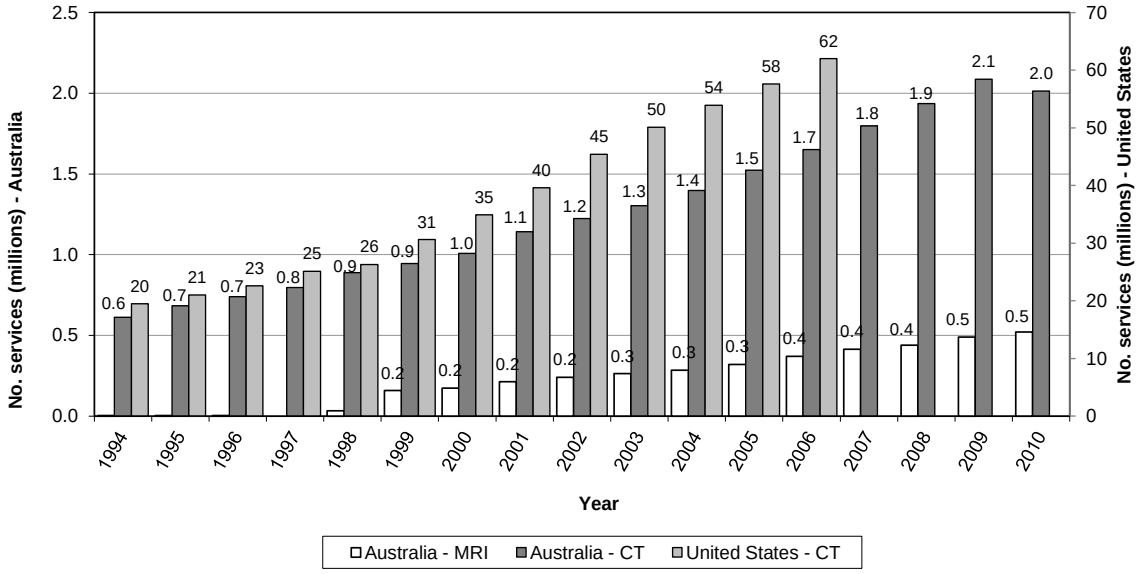

Figure 7.1: Number of MRI (white) and CT (dark grey) services for the Australian population billed to Medicare Australia from 1994 to 2010 and the number of CT procedures (light grey) performed in the United States from 1994 to 2006 (NCRP, 2009).

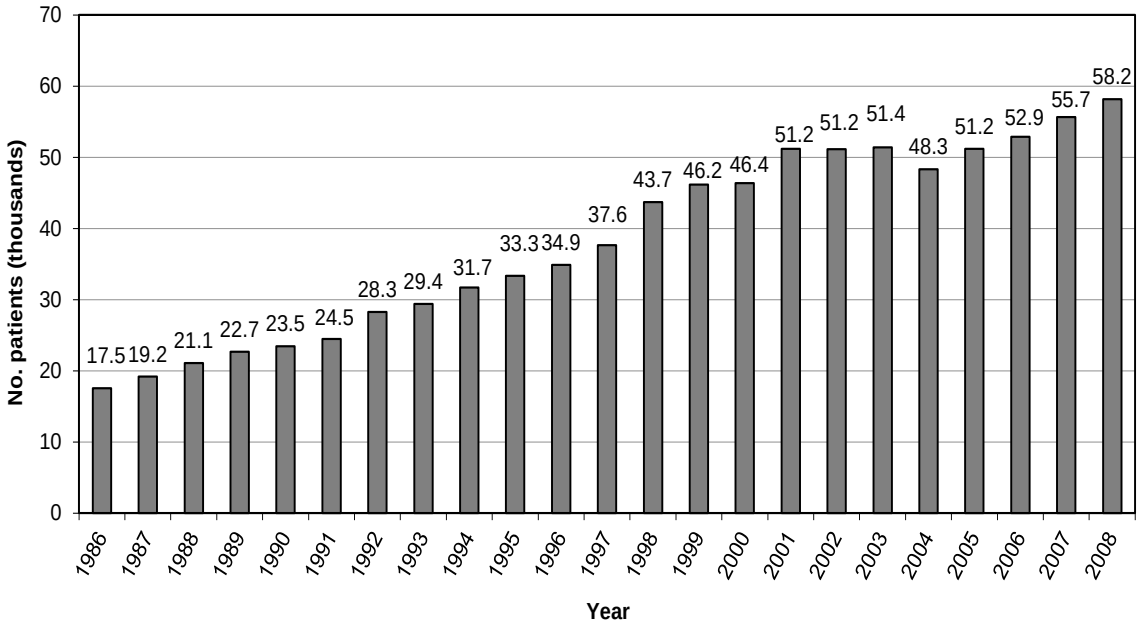

Figure 7.2: Number of patients aged 0 to 18 years for whom CT services were billed to Medicare in Australia from 1986 to 2008 (data provided by the Australian Department of Health and Ageing).

with the bulk of examinations occurring for those aged between 45-74 years (Figure 7.3). A greater percentage of scanning is performed for women aged 15-64 or over 85 years (Figure 7.4). In the youngest age group (0-4 years) the distribution is almost equal and in the group 5-14 years, a slightly higher proportion of males are scanned. Trends in the CT imaging rate for males and females have been similar since 1986 (Figure 7.5). More CT examinations are performed on males aged 0-14 years than on females, while for adolescents aged 15-18 years the imaging rate is similar for both sexes.

There are certain time points where trends in the change in the CT imaging rate are similar between all age groups (circled in Figure 7.6). Figure 7.7 focuses on the CT imaging rate for the 0-18 year age range relative to 1986. The 0-4 and 5-9 year age groups show a decrease in the last five years, while the older age groups show an overall increase in CT imaging rate. This data does not include those services not billed to Medicare.

Data is available from Medicare for other diagnostic modalities from 1994, although the age grouping is limited to 0-4, 5-14 and 15-24 years. Figure 7.8 shows an indexed rate representing the relative change in the CT imaging rate relative to the year 2000 for each modality. The increase in the CT imaging rate in the 0-24 year age group is comparable to increases in the ultrasound imaging rate over the past 15 years. In contrast, diagnostic radiology services (including plain X-ray imaging, fluoroscopy and interventional radiology) have remained fairly constant, while nuclear medicine services have declined. The greatest increase in imaging rate is observed for MRI services, which were first billed to Medicare in 1998 and have seen a dramatic increase since that time. Approximately 2.6 million diagnostic imaging services were billed to Medicare for the 0-24 year age group in 2009. As a proportion of this total number, CT represents 5% of funded services, while nuclear medicine accounts for 1%, MRI 2%, ultrasound 26% and diagnostic radiology 66%.

Billing trends at the RCH were assessed to calculate the percentage of paediatric CT imaging performed that is captured by Medicare data. In 1999, 42% of all CT procedures at the RCH were billed to Medicare and this had decreased to 31% by 2008. The 0-4 year age group had the lowest percentage of Medicare funded procedures performed, dropping to a minimum in 2000 of 19%. Since 1999, CT procedures not billed to Medicare included public in-patients (56%), Transport Accident Commission patients (5%), patients not charged (3%), international patients (1%), and inter-hospital and Work Cover patients (<0.1%). The remaining 35% of patients were captured in Medicare data via billing to Medicare, either directly or through their private health fund.

Approximate scaling factors for children that can be applied to Medicare data to account for those examinations not billed through Medicare are given in Table 7.2. These are calculated from the last seven years of RCH billing data from 2002 to 2008. Other dedicated paediatric hospitals across Australia vary in the number of CT patients billed to Medicare. For the financial year 2008/09 these ranged from 7% in Western Australia,

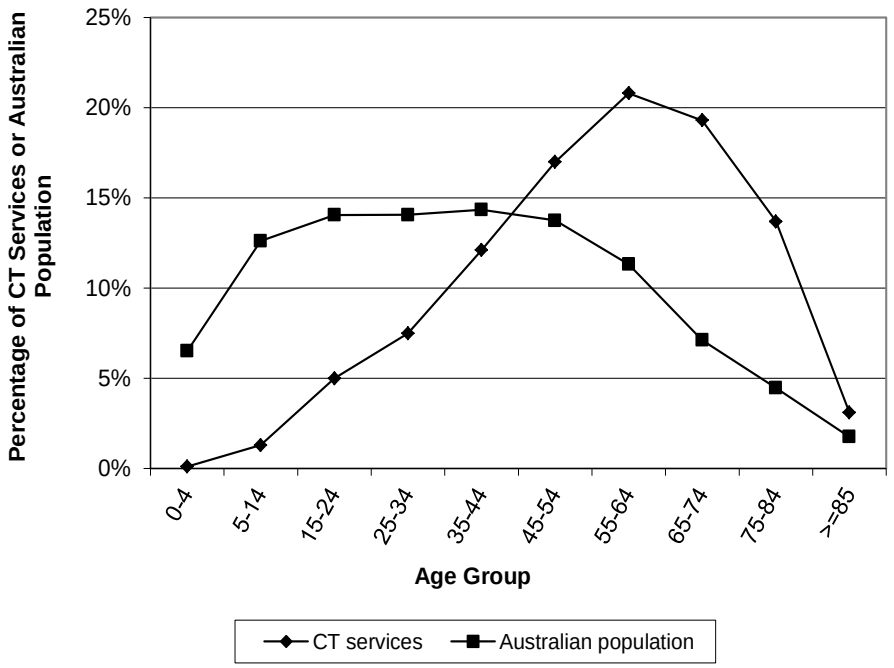

Figure 7.3: Comparison between age distribution for CT services billed to Medicare (diamonds) and of the Australian population (squares) in 2009 (ABS, June 2009; Medicare).

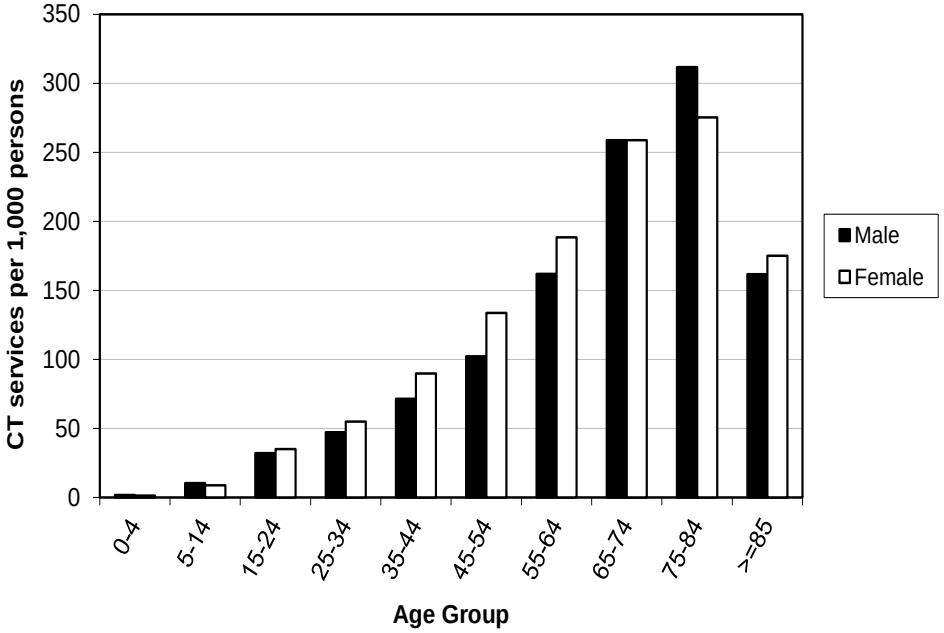

Figure 7.4: Age and gender distribution of the CT imaging rate (number of CT services billed to Medicare Australia per 1,000 people) in 2009 in Australia (ABS, 2008a, June 2009; Medicare).

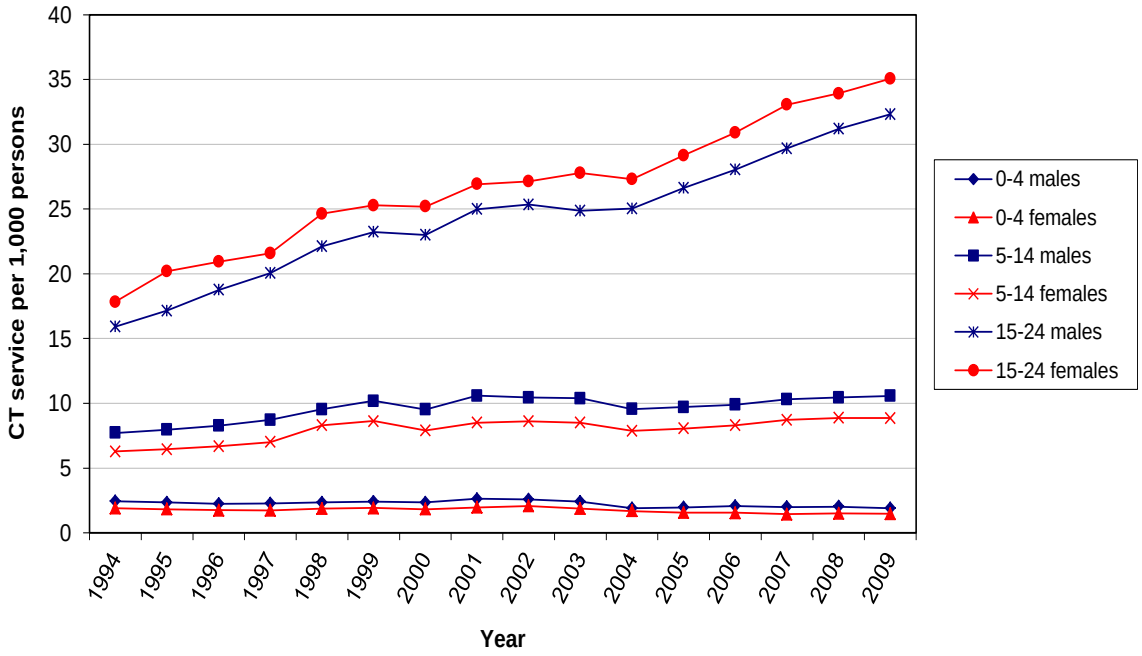

Figure 7.5: CT imaging rates (number of CT services billed to Medicare Australia per 1,000 persons) for males (blue) and females (red) in the younger age ranges (ABS, 2008a, June 2009; Medicare).

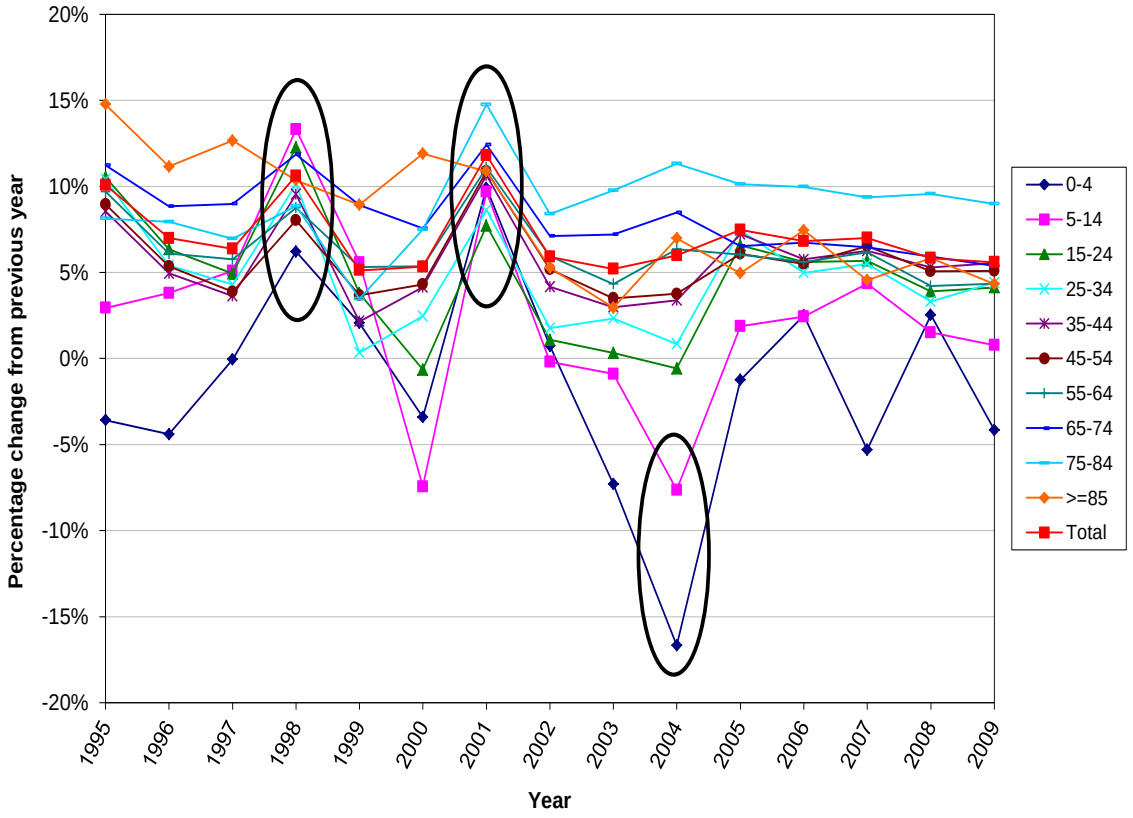

Figure 7.6: Annual percentage change in the imaging rate (number of CT services billed to Medicare Australia per 1,000 people) for each age group since 1995 in Australia (ABS, 2008a, June 2009; Medicare).

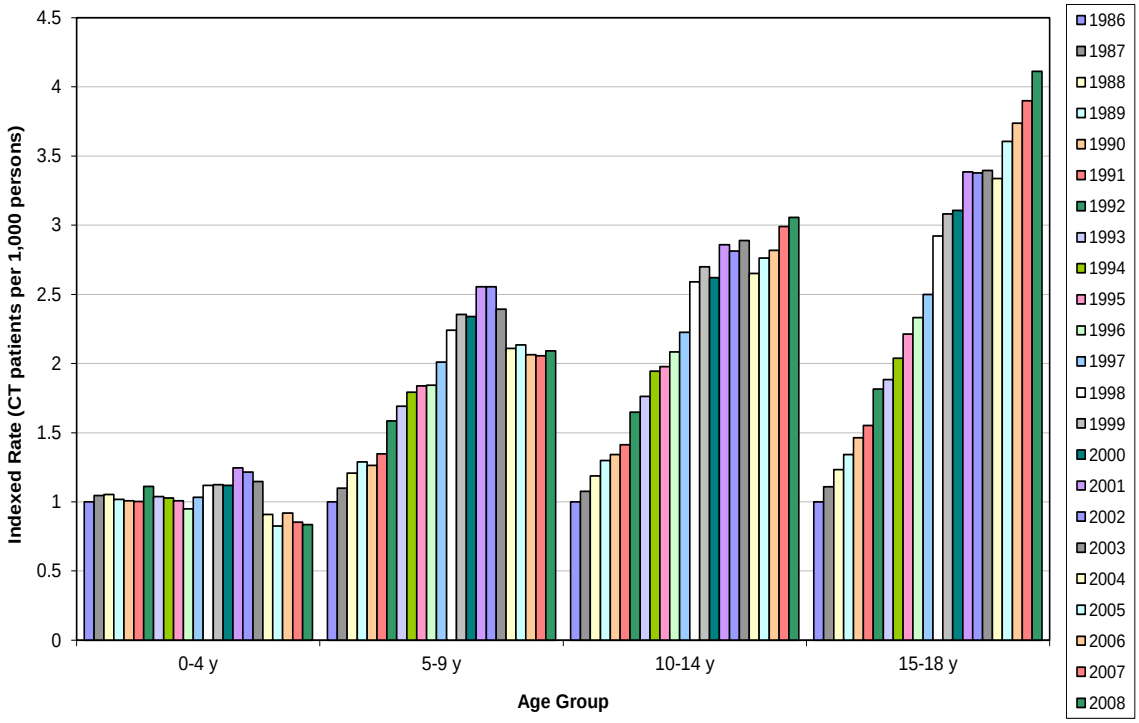

Figure 7.7: Indexed rate of the number of patients for whom CT services were billed to Medicare per 1,000 persons in Australia from 1986 to 2008 for persons aged 0 to 18 years relative to the imaging rate in 1986 (base of each index is the number of patients per 1,000 persons in the year 1986) (data provided by the Australian Department of Health and Ageing) (ABS, 2008a, June 2009; Medicare).

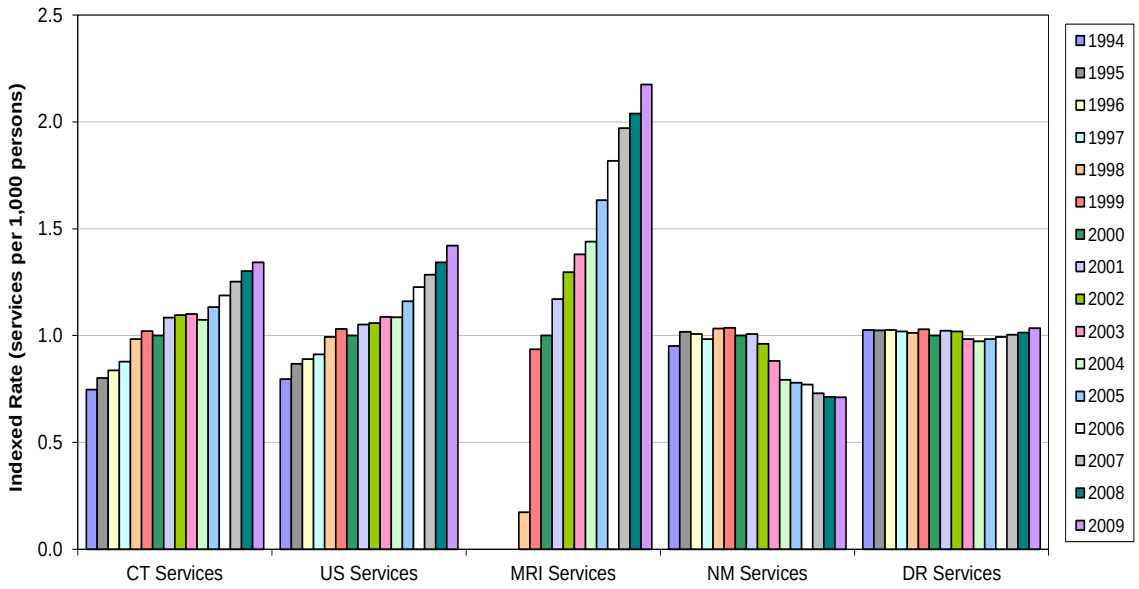

Figure 7.8: Indexed rate of the number of services for different diagnostic imaging modalities per 1,000 persons aged 0 to 24 years billed to Medicare in Australia from 1994 to 2009 relative to the imaging rate in 2000 (base of each index is the number of services per 1,000 persons in the year 2000) [CT = Computed Tomography, US = Ultrasound, MRI = Magnetic Resonance Imaging, NM = Nuclear Medicine, DR = Diagnostic Radiology] (ABS, 2008a, June 2009; Medicare).

24% in South Australia, 27% in Queensland, to 44% in New South Wales[i]. This variation highlights the challenges of assessing imaging trends and reinforces the importance of qualifying estimates of non-Medicare imaging statistics.

Table 7.2: Gender and age distribution for paediatric CT imaging in Australia in 2008.

Category	No. CT Patients[a] (%)		Scaling Factor[b]	CT Imaging Rate (No. patients per 1,000 persons)[c]
0-18 y	58,183	(100)	2.7-3.3	30-36
Sex				
0-18 y, male	31,115	(53)	2.7-3.6	31-41
0-18 y, female	27,068	(47)	2.6-3.2	27-33
Age				
0-4 y	1,919	(3)	3.8-4.9	5-7
5-9 y	6,725	(12)	2.4-2.9	12-15
10-14 y	18,563	(32)	2.4-3.2	32-42
15-18 y	30,976	(53)	1.3[d]	34

[a] Patients for whom CT services were billed to Medicare in 2008 (data provided by the Australian Department of Health and Ageing).

[b] Scaling factor derived from billing data at the RCH from 2002 to 2008 to adjust the Medicare number of patients for those CT services that are not billed to Medicare. The range represents the mean ± 2*standard deviation. The scaling factor is calculated as 1+X/(100-X) where X is the percentage of patients not billed to Medicare. Using the scaling factor the actual number of patients aged 0-18 years having a CT scan in 2008 is closer to three times 58,183 or about 175,000.

[c] Annual imaging rate calculated by dividing the number of CT patients billed to Medicare in 2008 (adjusted by the scaling factor) by the Estimated Resident Population at the midpoint of 2008, multiplied by 1,000 (ABS, 2008a, June 2009). The adjustment is made to include non-Medicare funded CT services.

[d] The published adult scaling factor has been used for the 15 to 18 year age range (Thomson and Tingey, 1997).

The CT usage profile for 2008 differs between Medicare and RCH data and neither matches the age distribution of the Australian population in the 0-18 year age group. Figure 7.9 shows the number of CT patients by year of age at the RCH as a percentage of all CT patients at RCH for 2008. Similarly, the percentage age distribution is shown for those CT patients billed to Medicare by all practices in Victoria. The largest percentage of CT imaging is performed at the RCH for patients less than one year old, while the older patients (15-18 years) constitute a greater proportion of the Medicare-billed CT services in Victoria. The Victorian population distribution is reasonably consistent across the 0-18 year age range.

Table 7.3 compares the average annual change in the CT imaging rate over the last 22 years with the change in the imaging rate in the last five years based on the RCH and Medicare data sources. The average annual change has been provided for both time periods to

[i] TM Cain [Royal Children's Hospital Melbourne] 2009, pers. comm., 13 April.

demonstrate the changing trend in recent years in some age groups.

7.4 Discussion

As Brenner and Hall (2007) state, the risk to the individual from diagnostic radiation exposure is small and in most cases for a properly justified procedure, the benefit to the individual will outweigh any risk. However, with increasing rates of CT usage the application of small levels of risk to a large population produces a health concern. Based on CT usage in 2007, it is estimated that 1.5% to 2.0% of all cancers in the US may be caused by CT imaging (Brenner and Hall, 2007). The total number of CT scans in the US has increased annually by 8% to 15% over the last seven to 10 years (Figure 7.1), which is a greater rate than population growth (Mettler et al., 2009, 2008; NCRP, 2009) and similar trends are seen in the UK (Hall and Brenner, 2008). This thesis shows that although the rate of increase is not as high as in the US (Figure 7.1), the use of CT imaging in Australia is increasing and at a much faster rate than population growth.

There have been expectations (Kalra et al., 2004a; Mettler et al., 2000; Rehani and Berry, 2000; Vock, 2005) that magnetic resonance imaging (MRI) may begin to lighten the workload in CT. In Australia, the Medicare data show that both MRI and CT services are increasing (Figure 7.1). However, over the past ten years MRI has only slowly increased from 15% to 20% of the total number of services. This slower than expected uptake may primarily be due to the restricted access, continued high cost and limited Medicare rebates for MRI scans.

Figure 7.3 demonstrates that the CT usage profile (Medicare) does not match the age distribution of the Australian population (ABS, June Quarter 2008). A greater percentage of CT scans are performed in an older, smaller percentage of the population. This is in agreement with recent demographic data from the US (Mettler et al., 2008). The New Zealand National Radiation Laboratory conducts a survey every ten years of CT usage. The most recent survey was conducted in 2007 (Stirling and Cotterill, 2008) and also demonstrates similar trends to the Australian data.

Furthermore, CT imaging rates for boys consistently exceed those for girls in the youngest age groups (0-14 years) (Figure 7.5). A similar trend was found in a US study of more than 300,000 health care records for children under the age of 18 years (Dorfman et al., 2011). CT was used more frequently for boys except in the 15-17 year age group. For Australia, over the larger age range from 15-64 years, women are scanned more than men (Figure 7.4). This could reflect that boys are more likely to require a CT scan than girls due to the activities being undertaken. From late adolescence onwards, it may be more likely for women to seek medical advice than men and therefore higher CT rates are seen in women. A recent study in Northern England found that the CT imaging rate was higher in males than females in all age groups up to 22 years of age, except infants (<1 year)

Table 7.3: The average annual change in the Australian CT imaging rate since 1987 and since 2004 for persons aged 0 to 18 years.

Age at Scan (years)	**Average annual change in CT imaging rate (patients per 1,000 persons)**[a]			
	1987-2009		**2004-2009**	
	RCH[b] (%)	**Australia**[c] (%)	**RCH**[b] (%)	**Australia**[c] (%)
0	***4.6***	-1.6	***3.9***	-8.2
1	***4.4***	-1.5	***5.5***	-6.6
2	***7.1***	-1.1	***8.5***	-5.4
3	***3.7***	1.0	***4.7***	-4.9
4	***5.8***	2.4	***3.4***	-1.4
5	3.5	***2.5***	-5.0	***-2.4***
6	3.7	***3.7***	-0.3	***-3.4***
7	3.0	***4.0***	-1.1	***-2.7***
8	4.2	***4.0***	5.7	***-1.7***
9	5.6	***3.9***	1.6	***-2.3***
10	6.1	***4.0***	0.8	***-2.1***
11	7.6	***4.6***	3.8	***0.3***
12	7.7	***5.4***	4.6	***0.4***
13	6.5	***5.9***	5.6	***2.2***
14	8.3	***6.2***	8.7	***2.9***
15	10.1	***6.4***	9.5	***3.4***
16	8.4	***6.7***	2.6	***3.9***
17	7.0	***7.0***	8.0	***3.9***
18	6.3	***6.8***	7.3	***4.5***
0-18	4.3	5.2	2.8	1.8

[a] Annual imaging rate calculated by dividing the number of patients undergoing CT procedures in that year by the Estimated Resident Population (ABS, 2008a, June 2009) in Victoria (for the RCH calculations) or Australia (for the Australia calculations) at the midpoint of the year, multiplied by 1,000.

[b] Number of patients undergoing CT examinations at the RCH.

[c] Number of patients undergoing CT examinations billed to Medicare in Australia (data provided by the Australian Department of Health and Ageing).

[d] Bolded and italicised figures represent those which the author believes best represent the actual situation in paediatric CT imaging trends.

(Pearce et al., 2011). Similarly, a large US trauma hospital also showed that imaging in children from infants to the mid-teen years was slightly more common in males and significantly higher for males aged 17 to 40 years (Boone and Brunberg, 2008).

Table 7.2 provides the scaled paediatric CT imaging rates for Australia in 2008. For every 1,000 persons aged 0-18 years, approximately 30-36 CT scans are performed annually. Based on Medicare billing alone, there are about 11 CT scans performed per 1,000 persons aged 0-18 years. Although there is little easily accessed published data on paediatric imaging rates to make comparisons, Ono et al. (2011b) have tabulated imaging rates for several countries for persons aged 0-15 years based on government department reports. For example, Ono et al. (2011b) quote the number of CT procedures per 1,000 persons (0-15 years) as being 10 for Sweden (in 2005), 7.6 for the UK (in 2006), 76-94 for the US (in 2006) and 32-34 for Japan (in 2006). The Australian paediatric CT imaging rate calculated in this thesis for 2008 compares favourably based on the Medicare data alone. The scaled paediatric imaging rate for Australia, which may better reflect actual practice, is lower than the US rate, comparable with the rate in Japan, but three times higher than imaging rates in the UK or Sweden. The CT imaging rate for the whole population in Australia for 2009 was estimated to be 95 CT services per 1,000 persons based on Medicare data. The CT imaging rate for the US population was 223 procedures per 1,000 population (Mettler et al., 2009; NCRP, 2009). For both children and the population as a whole, the Australian CT imaging rate appears to be much lower than the rate of imaging in the US.

Assessing the change in the CT imaging rate showed increased growth for all age groups in 1998 (Figure 7.6). This may coincide with the full introduction of helical scanning in Australia. Alternatively, it may be a result of bulk billing only being available for CT examinations conducted on scanners less than ten years old[ii]. If multiple sites replaced scanners at the same time, this could account for an increase in the number of services billed through Medicare. The Northern England study found that the CT imaging rate for young people 22 years and under increased dramatically between 1997 and 2000, which may also coincide with the introduction of helical scanning (Pearce et al., 2011). In this thesis, there is another apparent growth period in imaging rates for all age groups in 2001 which may reflect the wider availability of MDCT scanners in Australia at this time (Heggie, 2007). Furthermore, there is a decline in imaging rates in 2004, most significantly in the 0-4 year age group with a 16.6% decrease on the previous year and in the 5-15 year age group exhibiting a 7.6% decrease. This may be indicative of the heightened awareness at this time in the international community regarding the radiation risks of CT scanning, particularly in children. Since the turn of the century the 75-84 year age group have consistently had the highest imaging growth rate.

The paediatric CT imaging trends in Australia are more difficult to assess than adult

[ii] S Goergen [Southern Health] 2009, pers. comm., 14 April.

trends. This is because of the relatively small percentage of examinations included in the national health care system database. A survey of CT facilities in Australia found that on average 24% of CT examinations were non-Medicare funded for the Australian population (Thomson and Tingey, 1997). In this thesis, the CT imaging rates at a dedicated paediatric hospital were assessed and it was found that on average 65% of paediatric procedures were not billed to Medicare.

When averaged over the last 10 years, the percentage of non-Medicare funded procedures at the RCH was found to be higher in the youngest age group: 77% for the 0-4 year age group; 60% for the 5-14 year age group; and 57% for the 15-18 year age group. This implies that more children in the 0-4 year age group are imaged as public patients.

The distribution of CT services billed to Medicare across the age range 0-18 years demonstrates that the majority of funded services are performed on older adolescents (Figure 7.9). Conversely, at the RCH a greater percentage of CT patients are either very young (0-4 years) or early adolescents (10-15 years). More CT patients are less than one year old than any other age at the RCH. The reasons for this include that the RCH has a disproportionate number of very young sick patients; very young children may have a CT scan without general anaesthetic rather than an MRI scan with general anaesthetic when either modality could be used for diagnosis; and older patients who are able to tolerate an MRI scan without general anaesthetic are less likely to have a CT scan. Furthermore, older adolescents aged 17-18 years are more easily imaged at adult hospitals and less likely to attend a children's hospital. These trends in the younger age groups are reflected in data for a large Israeli health service (Chodick et al., 2006).

Due to the small number of paediatric CT examinations billed to Medicare, caution must be exercised when deriving imaging trends from Medicare data, particularly in the youngest age group. Therefore, in this thesis, data from a dedicated paediatric hospital was assessed and compared with the Medicare data. It was observed that trends differed between the data sets and were in fact opposite for some ages (Table 7.3).

In 2008, 57% of CT services for the 0-4 year age group billed to Medicare in Victoria were performed at the RCH compared to 12% for 5-14 year olds. Since only a small percentage of RCH services were billed to Medicare, the overall number of patients at the hospital undergoing CT examinations exceeded the number in the Medicare Victorian data for each single year of age in the 0-4 year range. Therefore, when assessing imaging trends it was considered justified to rely on the RCH data for trends in the 0-4 year age range and on national Medicare data for the older ages, 5-18 years (bolded and italicised figures in Table 7.3).

Using this premise, Table 7.3 shows that the average annual growth over the past 22 years in the CT imaging rate for single year of age in the range 0-18 years has varied from 2.5% to 7.1%, with an average of 5.1% per year (calculated using the data from RCH for

0-4 year olds and Medicare data for 5-18 year olds for the period 1987-2008). Although the CT imaging rate in this age group shows growth, it does not appear to be increasing at the same rate as the CT imaging rate in the overall Australian population. Studies from US institutions found that the average annual increase in CT imaging for 0-17 year olds was 8.2% (Wachtel et al., 2009) and the average annual increase in the percentage of emergency department visits that included CT imaging for 0-18 year olds was 12.7% (Wiest et al., 2002). A more recent study of nationwide trends in the US calculated an annual growth rate of 13.2% from 1995 to 2008 in the number of paediatric visits to the emergency department including a CT examination (Larson et al., 2011).

Interestingly, an assessment of the CT imaging rate for children and young people in the last five years shows that the trend of continuous growth is beginning to change. Over the past five years, the annual change in the CT imaging rate for paediatric age groups has ranged from -3.4% to 8.5% for single year of age and therefore has included some year-on-year decrease in usage (bolded and italicised figures in Table 7.3 for 2004 to 2008). A recent US study (Townsend et al., 2010) based on a survey of North American paediatric institutions similarly found that the utilisation of CT had decreased as a percentage of MRI, ultrasound and CT imaging between 2003 and 2007. From Table 7.3, the average change in CT imaging rate from 2004 to 2008 has now reduced to 1.7% per year for the age range 0-18 years (calculated using the data from RCH for 0-4 year olds and Medicare data for 5-18 year olds for the period 2004-2008).

Table 7.3 shows that for the 0-4 year age group, the annual growth in the CT imaging rate in recent years does not differ considerably from the average annual growth over the past 22 years based on RCH data. One reason for the continued increase in the imaging rate for the very young is the ability of new CT technology to perform CT angiography studies, particularly for infants less than one year old to assess for vascular abnormalities of the pulmonary veins and great vessels associated with congenital heart disease. Furthermore, faster scans allow CT scans of the brain in the case of trauma to be performed without general anaesthetic where previously the infant may have had an MRI scan or be placed under observation.

Based on the Medicare data in Table 7.3, the 11-18 year age range demonstrates slower growth over recent years and a decrease in the imaging rate is evident for 5-10 year olds. This may be indicative of a heightened awareness internationally of the potential radiation risks of CT scanning, particularly in children, and is similar to the trend found in a recent US study (Townsend et al., 2010). The series of articles in 2001 focussed attention on the incorrect use of adult parameters when scanning children and the increased radiation induced cancer risk that results (Brenner et al., 2001a; Donnelly et al., 2001; Paterson et al., 2001). The decrease in imaging rate in the 5-10 year age range and the slower growth for 11-18 years might suggest a reduction in non-essential or unjustified imaging in these age groups and/or an increased preference for MR imaging.

A preliminary result from a US study also demonstrated an apparent deceleration in growth for CT imaging of children (Wiest et al., 2002). Similar reductions in imaging in the 0-4 year age group have not been observed in this thesis. CT imaging for the youngest children may already have been more conservatively justified and hence the same magnitude of decrease is not observed in that age range.

7.5 Conclusions

This thesis significantly extends current knowledge of paediatric CT scanning trends in Australia. As stated by Pearce (2011) in an editorial on this work "*it is a welcome and important addition to the sparse literature*". It was found that the number of CT services provided in Australia is clearly increasing and is exceeding population growth. When analysing CT imaging rates using Medicare data, consideration must be given to the number of services not billed to this system. From this thesis it is evident that this is a significant percentage for 0-18 year olds. Based on combined data from Medicare and a dedicated paediatric hospital it appears that the rate of paediatric CT imaging growth has slowed in recent years and even demonstrates a reduction in some age brackets. Whilst it is encouraging that the imaging rate for children and young people is lower than that for adults, overall the imaging rate continues to increase. Some increase may be warranted due to improvements in the diagnostic power of CT. However, it is essential that every CT examination is justified and is of net benefit to the individual.

7.6 Publications Arising from this Chapter

1. **Brady, Z.**, Cain, T. M. and Johnston, P. N., *Paediatric CT imaging trends in Australia*, Journal of Medical Imaging and Radiation Oncology, 2011, 55:132-142 (Brady et al., 2011d).

   (a) The above paper led to a request for interview and citations in several media forums (Collins, 20 April 2011; Corderoy, 17 May 2011; Nafziger, 21 April 2011, Gastroenterology Update, 27 April 2011).

   (b) The editorial (Pearce, 2011) of the issue of the Journal of Medical Imaging and Radiation Oncology that this paper appeared in was dedicated to a discussion of the issues raised.

2. **Brady, Z.**, Cain, T. M. and Johnston, P. N., *Paediatric CT in Australia - trends and risk (EPSM ABEC 2010 Conference Proceedings)*, Australasian Physical & Engineering Sciences in Medicine, 2011, 34(1):110 (Brady et al., 2011a).

3. **Brady, Z.**, Cain, T. M. and Johnston, P. N., *Computed tomography - are we imaging more or less?* presented at the RANZCR/AIR/FRO/ACPSEM Combined Scientific Meeting, 2009, Brisbane, Australia *(Invited Speaker)* (Brady et al., 2009).

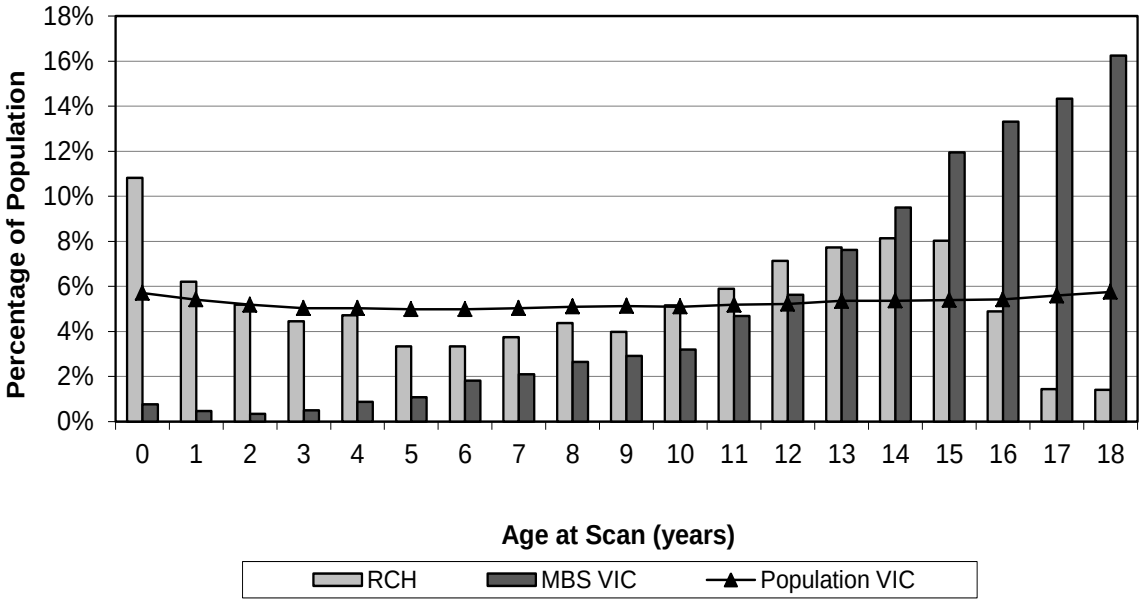

Figure 7.9: Percentage age distribution of computed tomography (CT) patients from 0 to 18 years billed to Medicare in Victoria (MBS VIC) and at the Royal Children's Hospital Melbourne (RCH) in 2008 (data provided by the Australian Department of Health and Ageing and the RCH). The percentage age distribution of the Victorian population in these age groups is also shown (ABS, 2008a, June 2009).

Chapter 8

Projected Cancer Risks for Paediatric CT in Australia

8.1 Introduction

Despite the prevalence of CT as a diagnostic imaging tool in hospitals today, the typical doses and associated radiation risks are not well understood. Primarily this is because the doses are not accurately known or easily calculated (see Chapter 5). Furthermore, there are large uncertainties, in addition to a lack of consensus, regarding the risk from radiation exposure at low doses. The United States National Research Council of the National Academies regularly reviews the available epidemiological and experimental research on the biological effects of ionising radiation (BEIR) and provides a framework for estimating cancer risk due to radiation exposure. The latest report, BEIR VII (NRC, 2006), was delivered in 2006 and provides age-, sex- and site-specific estimates of the lifetime attributable risk (LAR) associated with radiation exposure.

The Life Span Study (LSS) of the atomic bomb survivors is the principal source of data considered by the BEIR VII Committee along with medical and occupational radiation studies. The BEIR VII Report supports the linear no threshold (LNT) model as the best descriptor of the relationship between solid cancer incidence and low dose radiation exposure (NRC, 2006). A linear-quadratic model is used for leukaemia as it was found to provide substantially better agreement than the LNT model with the observed risk from exposure. The LNT theory is widely accepted (Brenner et al., 2003) as the most plausible model for radiation induced cancers for low dose exposures and is also adopted by the International Commission on Radiological Protection (ICRP) as the basis of the international system of radiation protection (ICRP, 2007b).

Cancer risk estimation based on BEIR VII modelling is limited by the uncertainties that exist from using the LSS data to derive radiation induced cancer risk. The sources of

uncertainty arise from transporting the cancer incidence and mortality from the Japanese atomic bomb survivors to a Western population. Furthermore, the LSS data is extrapolated to low dose and dose rate exposure situations. The risk modelling of BEIR VII is also affected by sampling variability in the model parameter estimates for the LSS data. Despite these inherent uncertainties, one of the most useful applications of the BEIR VII radiation risk models is for estimating the detriment from exposure situations where doses differ substantially across the body. Exposure from CT examinations falls within this scope. Other studies have also applied the BEIR VII attributable cancer risks to CT exposures on the basis that it is the best method currently available (Berrington de Gonzalez et al., 2009; Brenner et al., 2001a; Brenner and Hall, 2007; Einstein et al., 2007a; Smith-Bindman et al., 2009).

The aim of this part of the thesis was to assess the lifetime cancer incidence and mortality risks for Australian children attributable to radiation exposure from CT. By applying the BEIR VII risk models based on cancer incidence and mortality to the doses measured in this thesis, projected cancer risk estimates can be made.

8.2 Methods

The organ and tissue absorbed doses for CT brain, chest and abdomen/pelvis examinations were measured by thermoluminescence dosimetry (TLD) in a physical anthropomorphic phantom representing a 10 year old child (Chapter 3). These measurements were undertaken for typical CT protocols performed at the Royal Children's Hospital (RCH) Melbourne. The absorbed doses for organs and tissues for those malignancies identified in BEIR VII are given in Table 8.1. The BEIR VII lifetime incidence and mortality risks for males and females are provided in Table 8.2 for radiation exposure at 10 years of age.

Table 8.1: Organ and tissue absorbed doses measured by TLD for a 10 year old child.

Organ/Tissue	**Absorbed Dose (mGy)**		
	CT Brain	**CT Chest**	**CT Abdomen/Pelvis**
Stomach	0.07	4.8	8.9
Colon	0.03	0.52	8.0
Liver	0.12	10	8.5
Lung	0.46	9.9	4.1
Breast (Females)	0.27	9.1	1.3
Uterus (Females)	0.01	0.12	6.6
Ovary (Females	0.01	0.13	6.5
Prostate (Males)	0.01	0.06	5.8
Bladder	0.01	0.08	6.9
Other (Females)	2.7	5.2	3.7
Other (Males)	2.2	4.3	3.2
Bone Marrow	6.1	2.4	3.2

Table 8.2: Lifetime attributable risk (LAR) of site-specific solid cancer and leukaemia mortality for males and females for exposure at 10 years of age (NRC, 2006).

Cancer Site	**Incidence**[a]		**Mortality**[a]	
	Males % per Gy	**Females % per Gy**	**Males % per Gy**	**Females % per Gy**
Stomach	0.0055	0.0072	0.0030	0.0041
Colon	0.0241	0.0158	0.0117	0.0073
Liver	0.0043	0.0020	0.0031	0.0017
Lung	0.0216	0.0504	0.0219	0.0442
Breast	-	0.0712	-	0.0167
Uterus	-	0.0036	-	0.0008
Ovary	-	0.0073	-	0.0039
Prostate	0.0067	-	0.0012	-
Bladder	0.0150	0.0152	0.0032	0.0043
Other	0.0503	0.0523	0.0200	0.0220
Thyroid	0.0050	0.0275	-	-
All Solid[b]	0.1325	0.2525	0.0641	0.1051
Leukaemia	0.0120	0.0086	0.0071	0.0053
All Cancers[c]	0.1445	0.2611	0.0712	0.1104

[a] These estimates are obtained as combined estimates based on relative and absolute risk transport adjusted by a dose and dose rate effectiveness factor (DDREF) of 1.5 except for leukaemia, which is based on a linear-quadratic model (NRC, 2006).
[b] The category of all solid cancers includes all cancer sites except for leukaemia.
[c] The category of all cancers includes all solid cancers and leukaemia.

The absorbed dose to the bone marrow was used for leukaemia risk projections (NRC, 2006). BEIR VII uses the absorbed dose to the colon to determine the risk for the "other" cancers category, based on the same principle used in the LSS. In this thesis the absorbed dose used for the "other cancers" category is based on the methodology of Brenner et al. (2001c), where the doses are summed over radiosensitive organs and tissues not explicitly listed in the BEIR VII list and weighted according to ICRP 103 tissue weighting factors. A similar method is used in PCXMC risk assessments (Tapiovaara and Siiskonen, 2008). Therefore, the "other" organ and tissue absorbed dose (D_{other}) was calculated according to:

$$D_{other} = \frac{\sum_T w_T D_T}{\sum_T w_T} \tag{8.1}$$

where w_T is the ICRP 103 tissue weighting factor and D_T is the organ or tissue absorbed dose. These organs and tissues include the oesophagus, bone surface, brain, salivary glands, skin, adrenals, extrathoracic (ET) region, gall bladder, heart, kidney, lymph nodes, muscle, oral mucosa, pancreas, small intestine, spleen, thymus and testes (males).

The organ absorbed doses measured in this thesis were compared with absorbed doses measured in comparable studies. The absorbed doses were then multiplied by the BEIR VII

sex- and site-specific LARs for cancer mortality and incidence for radiation exposure at 10 years of age. Calculated site-specific lifetime attributable cancer risks were summed over the radiosensitive organs and tissues to give a total lifetime radiation-attributable cancer risk resulting from each type of CT examination assessed. These were compared with natural cancer incidence and mortality for the Australian population and as provided in ICRP 103 for a Euro-American population. The lifetime attributable risks for each CT examination calculated in this thesis are equivalent to the concept of "effective risk" proposed by Brenner (2008) or renamed "risk index" by Li et al. (2011a).

The calculated incidence and mortality risks for CT brain, chest and abdomen/pelvis examinations were then multiplied by the number of children aged 10 years undergoing these types of CT examinations in 2008 in Australia. The number of CT examinations was calculated from Medicare data supplied by the Australian Department of Health and Ageing, adjusted by previously derived (Chapter 7) scaling factors to account for the number of services not billed to Medicare. This provided a more realistic range of the actual number of patients undergoing CT examinations annually in Australia.

The calculated incidence and mortality risks for these types of CT examinations were also applied to the entire 0-18 year age group. The risks will be underestimated for infants, while overestimated for adolescents and hence will provide an intermediate estimate of the level of risk for the entire cohort. In addition to reduced CT parameters for younger, smaller children and higher site-specific radiation risk coefficients for younger children, there can also be variations in different organs with age. For example, almost all bone marrow is active (red bone marrow) at birth and with age gradually becomes inactive, with only about a third remaining active in adulthood (ICRP, 2002). Therefore, the bone marrow absorbed dose which directly correlates with leukaemia incidence will vary with age, particularly in childhood. The radiation risks calculated for a CT scan undertaken on a 10 year old child provide a reasonable benchmark for the average risk across the 0-18 year age band. Therefore, these calculated risks were applied to the number of CT examinations performed for the relevant body regions at the RCH in 2008 across the 0-18 year age range and more broadly to the Australian population aged 0-18 years undergoing CT scans (number of patients billed to Medicare in 2008 adjusted for the number not billed).

8.3 Results

There are a limited number of studies in the literature detailing organ and tissue absorbed doses for CT examinations on children (Brenner et al., 2001a; Brenner and Hall, 2007; Coursey et al., 2008; Fujii et al., 2007). This is due to the complexity of undertaking these types of measurements and the lack of resources and time for performing dosimetry experiments in the clinical environment. Furthermore, where studies exist, it is often difficult to make direct comparisons due to the number of differing variables that have

considerable effect on dose. These include the type of experimental or computational method, the representative age and type of anthropomorphic phantom used, the modelling of the CT scanner, if applicable, and/or the CT examination parameters (e.g. kV_p, mAs, collimation, pitch and scan length).

A comparison of the organ and tissue absorbed doses measured in this thesis with those from the literature is given in Table N.1 (Appendix N). The most regularly quoted risk estimates for paediatric CT are those calculated by Brenner et al. (2001a; 2007). The absorbed doses used in their first study (Brenner et al., 2001a) are considerably higher than those measured in this thesis. One of the assumptions of their initial study was that adult CT parameters were being used on children (Paterson et al., 2001) and the organ absorbed dose estimates were made accordingly. For a 10 year old, they calculated the brain dose to be 50 mGy from a CT head examination. This was decreased to 35 mGy in their subsequent study (Brenner and Hall, 2007), which is very close to the value measured in this thesis for a CT brain examination (34 mGy). Similarly, for a CT abdomen examination the absorbed doses to the stomach and liver were 30 and 28 mGy respectively (Brenner et al., 2001a), decreasing to 18 and 16 mGy in the second study (Brenner and Hall, 2007). However, these are approximately twice as high as the stomach and liver absorbed doses measured for the CT abdomen/pelvis examinations in this thesis (8.9 and 8.5 mGy, respectively).

Fujii et al. (2007) measured the organ absorbed doses in an anthropomorphic phantom representing a younger child (6 years) on the same type of scanner for a CT chest examination with slightly different parameters. Absorbed doses are comparable with those measured in this thesis except for the liver and stomach, which are lower. This is due to the increased scan length for the CT chest examination in this thesis, which would have included more of the liver and stomach in the scan volume. Coursey et al. (2008) also provided organ absorbed dose measurements for a CT chest examination in a phantom representing a younger child (5 years), which are comparable to this thesis. The breast absorbed dose is lower, which is most likely due to the age difference of the phantoms and the lower tube current used.

Using the organ absorbed doses measured in this thesis and the BEIR VII age-, sex- and site-specific LARs, the lifetime cancer incidence and mortality risks for a 10 year old child for a CT brain, chest or abdomen/pelvis examination were calculated and are given in Table O.1 (Appendix O). Natural site-specific cancer incidence and mortality risks for the Australian population (AIHW, 2009) and for a Euro-American population (ICRP, 2007b) are also provided for comparison. The site-specific lifetime cancer incidence and mortality risks are also shown in Figures 8.1 and 8.2. The overall lifetime attributable cancer risks for all solid cancers and leukaemia are shown in Figure 8.3 for males and females undergoing a CT examination at 10 years of age.

Another way of expressing the lifetime radiation induced cancer mortality risks is that

the risk of exposure for a CT head examination of a male 10 year old child is one in 10,100 (Table O.2, Appendix O). Similarly, the radiation risk for the same child from a CT chest examination is one in 2,700 and from a CT abdomen/pelvis examination is one in 2,800. The risk of exposure to a female child of the same age is one in 8,500 from a CT head examination, one in 1,300 for a CT chest examination and one in 2,100 for a CT abdomen/pelvis examination.

The potential number of fatal and non-fatal radiation induced cancers can be predicted by multiplying the calculated site- and sex-specific cancer incidence and mortality estimates by the number of paediatric CT examinations undertaken in Australia. Table 8.3 shows the predicted number of radiation induced malignancies from one year of CT scanning (based on 2008 figures) in Australia in the 0-18 year age range.

Table 8.3: Predicted number of radiation induced non-fatal and fatal cancers from CT brain, chest and abdomen/pelvis examinations undertaken on 0-18 year olds in Australia in 2008.

Examination	No. Incident Cancers	No. Fatal Cancers
CT Brain	∼15	<10
CT Chest	∼20	∼10
CT Abdomen/Pelvis	∼15	<10

[a] Calculations based on the number of patients for whom CT services were billed to Medicare in 2008 (data provided by the Australian Department of Health and Ageing). This number was adjusted by a scaling factor derived in Chapter 7 to take into account non-Medicare funded CT services.
[b] The number of CT examinations was multiplied by the LAR for "all cancers" calculated in this thesis based on site-specific organ absorbed doses measured with TLDs (Chapter 3) multiplied by the site- and sex-specific BEIR VII LARs for exposure at 10 years of age (NRC, 2006).
[c] Cancer risk projections detailed in this thesis should be considered with regard to the considerable and multi-faceted uncertainties involved in these types of estimates. However, albeit simplified, this is the best approach currently available.

8.4 Discussion

8.4.1 Limitations of Risk Modelling

Large uncertainties exist in the BEIR VII estimated cancer incidence and mortality lifetime risks attributable to radiation exposure. These risks predominantly rely on analyses of the cancer incidence and mortality in Japanese atomic bomb survivors who were exposed to intermediate radiation doses from gamma ray and neutron exposure. Uncertainties arise when extrapolating to the lower doses and dose rates typical of CT low energy X-ray photon exposures, from transporting these risks to a different population and from sampling variability in the model estimates based on the Life Span Study data.

The subjective confidence intervals for the LARs in BEIR VII cover at least an order of

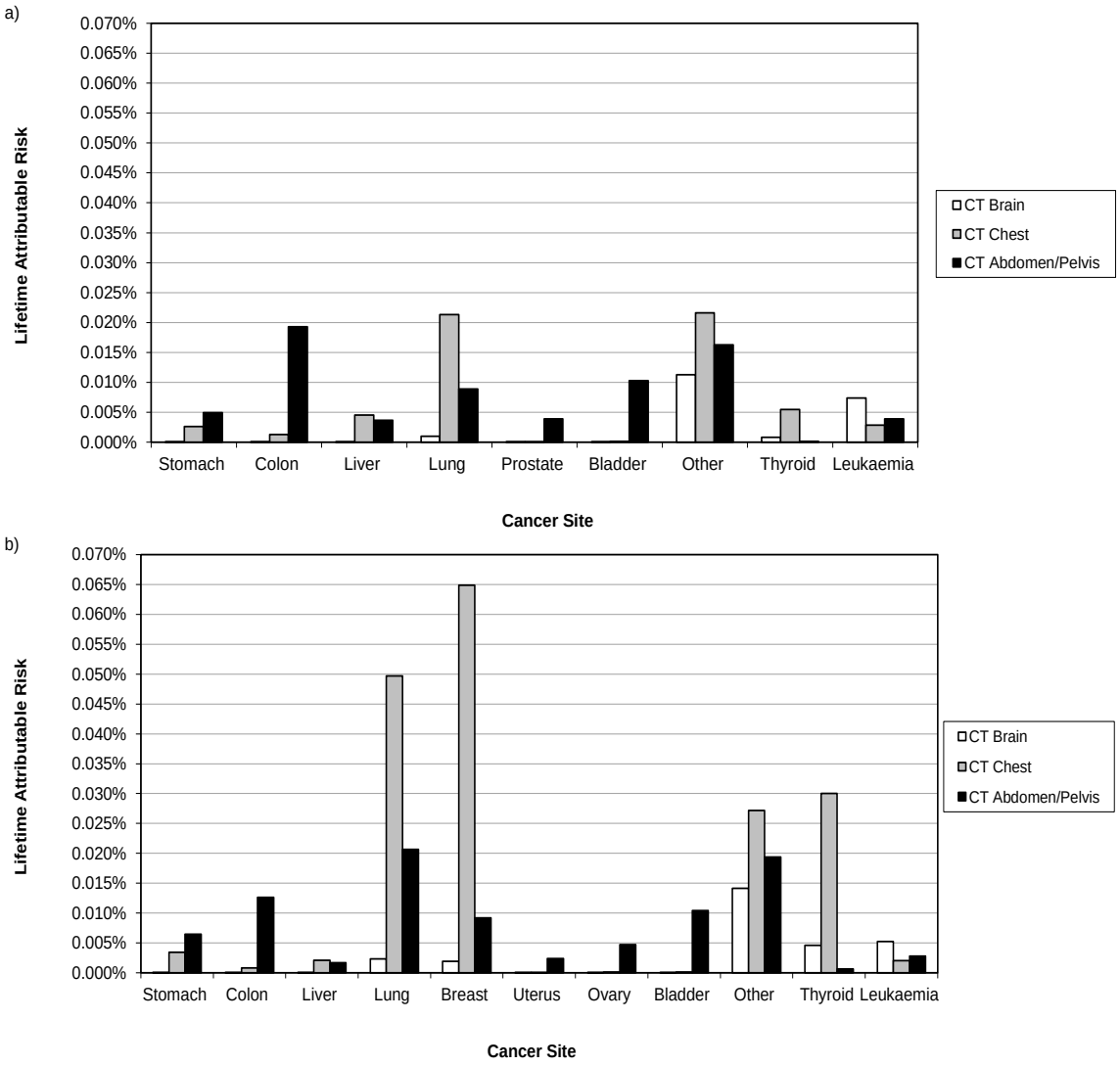

Figure 8.1: Site-specific lifetime attributable cancer incidence risks for a 10 year old undergoing a CT brain, chest or abdomen/pelvis examination for a) males and b) females.

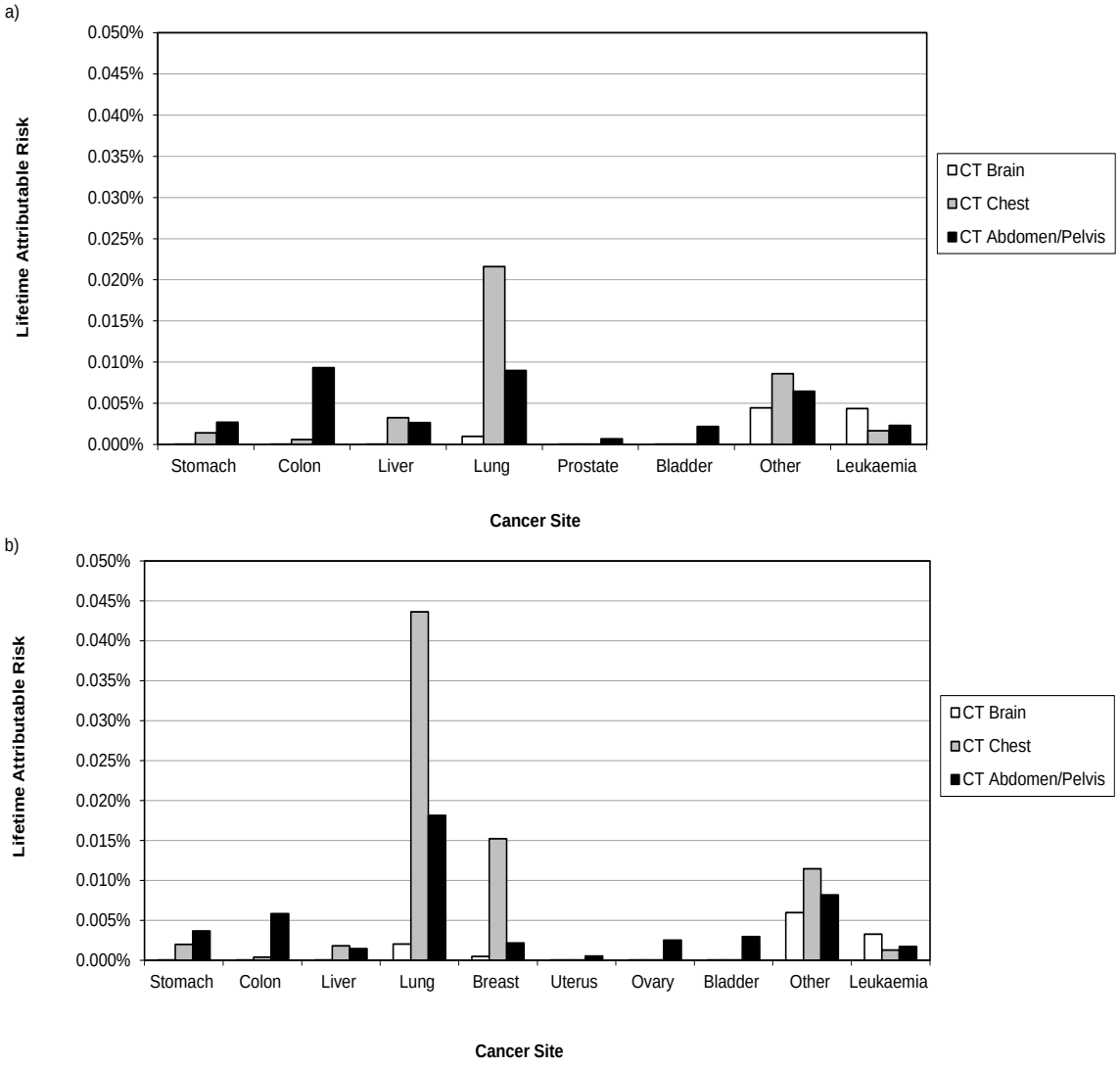

Figure 8.2: Site-specific lifetime attributable cancer mortality risks for a 10 year old undergoing a CT brain, chest or abdomen/pelvis examination for a) males and b) females.

magnitude and for site-specific risks can differ by a factor of two or more (NRC, 2006). These uncertainties are combined with the uncertainties in organ absorbed dose measurement when determining cancer risk estimates. Therefore, the cancer risk projections detailed in this thesis should be considered with regard to the considerable and multifaceted uncertainties involved.

Shuryak et al. (2010) have recently postulated that the risk modelling in BEIR VII is inconsistent with the observed relative risks of radiation induced cancer in the atomic bomb survivors in the Life Span Study. By modelling radiation initiation effects, as considered in BEIR VII, as well as radiation promotion of pre-existing premalignant cells, they show that relative radiation risk may in fact be underestimated in middle age. The proposed risk model still demonstrates a higher risk in the young, but it is somewhat lower than the risks estimated in BEIR VII. Overall, the risk of radiation induced cancer incidence is 37% lower for exposure at 10 years of age with the Shuryak et al. (2010) model. Furthermore, site-specific risks vary considerably with age. Colon cancer risk is higher in older age groups, while breast cancer risk decreases with increasing age. For exposure at 10 years of age, the initiation and promotion model estimates a decrease in cancer risk compared with an initiation only model of 78% for the colon, 59% for the stomach, 44% for the breast, 42% for the bladder, 37% for the liver and 14% for the lung. In terms of applying risk factors to patient populations undergoing CT examinations, they comment that the risk-benefit assessment will not be substantially affected even if the estimated risks are increased by a factor of two (Shuryak et al., 2010). This is based on the premise that the diagnostic benefit from a CT examination will far outweigh any small associated radiation risk (Brenner and Hall, 2007).

8.4.2 Comparison of Risks from CT Examinations

For the three types of CT examination considered for a 10 year old in this thesis, the greatest risk of death is from lung cancer in females from a chest examination (one in 2,300). This is a factor of two higher than the lung cancer mortality risk in males, which is the next highest risk (Figure 8.2). This reflects the LARs for cancer mortality for the lung, which are higher than any other site-specific mortality LAR for both males and females (Table 8.2). A relatively high breast cancer mortality LAR for females coupled with a high absorbed dose to this tissue from chest examinations places the breast in the high risk category.

For some radiation induced cancers, such as lung cancer, there is a poor prognosis and a greater likelihood that radiation induced cancer at this site will lead to death. However, for some radiation induced cancers, the lethality fraction is comparatively low, with relatively good survival for radiation induced cancer at these sites. It is more pertinent to discuss the incident cancers for these sites. An example is radiation induced thyroid cancer, which is rarely fatal (NRC, 2006). Considering the examinations on a 10 year old child, the highest

incident risk for thyroid cancer is for females undergoing a CT chest examination (one in 3,300). The risk of non-fatal breast cancer is also relatively high and combined with the high absorbed dose to the breast for a CT chest examination, the incidence risk of breast cancer is one in 1,500 for females.

Interestingly, due to the high radiation induced lung cancer mortality risks, even the CT brain examinations lead to some risk of dying from lung cancer due to the small absorbed dose measured for the lung for this examination. Although the lung absorbed dose measurement with the TLDs was low (0.46 mGy) it was confirmed by a CT-Expo (Stamm and Nagel, 2011b) calculation (0.48 mGy) and is considered to be a dose arising from scattered radiation. Overall, the CT brain examination risks are greatest from "other" malignancies, which are dominated by the absorbed dose to the brain. Leukaemia is the next highest fatal risk from CT brain examinations due to the amount of active bone marrow in the skull of children and the high absorbed dose to this region.

The estimated lifetime mortality risks are somewhat greater for females than for males, particularly for CT chest examinations (Figure 8.3). This is because of the substantially greater risks from the exposure of the lung in females compared with males (Table 8.2). The difference in lifetime mortality risks between sexes is less evident for the CT brain examination, as the risks for "other" cancers, which dominate the risk for this type of direct exposure of the brain, are quite similar between the sexes. The risk of fatal leukaemia is a relatively small component of the total cancer risk for all types of CT examination for both males and females.

The mortality risk from all cancers is about half the risk of cancer incidence. However, the site-specific risks are quite different and this explains why for males the highest cancer incidence is from CT abdomen/pelvis examinations, yet the highest cancer mortality is due to CT chest examinations (Figure 8.3). Comparing the number of site-specific induced cancers in males which progress to malignancy shows that more males potentially "die" from lung cancer than actually "have" lung cancer (Figure 8.4). This disparity is due to inherent uncertainties in the BEIR VII risk estimates. Figure 8.4 also shows that radiation induced lung cancer is the most likely type of cancer to progress to death for both males and females, followed by cancer of the liver.

8.4.3 Comparison of Calculated and Published Risks

Studies are beginning to emerge which use the BEIR V (Brenner et al., 2001a; Brenner and Hall, 2007) or BEIR VII (Berrington de Gonzalez et al., 2009; Smith-Bindman et al., 2009) cancer risk models to estimate the radiation induced cancer mortality for children and/or young adults from medical imaging. Tables 8.4 and 8.5 provide a summary of comparable results from this thesis and other studies for paediatric CT imaging.

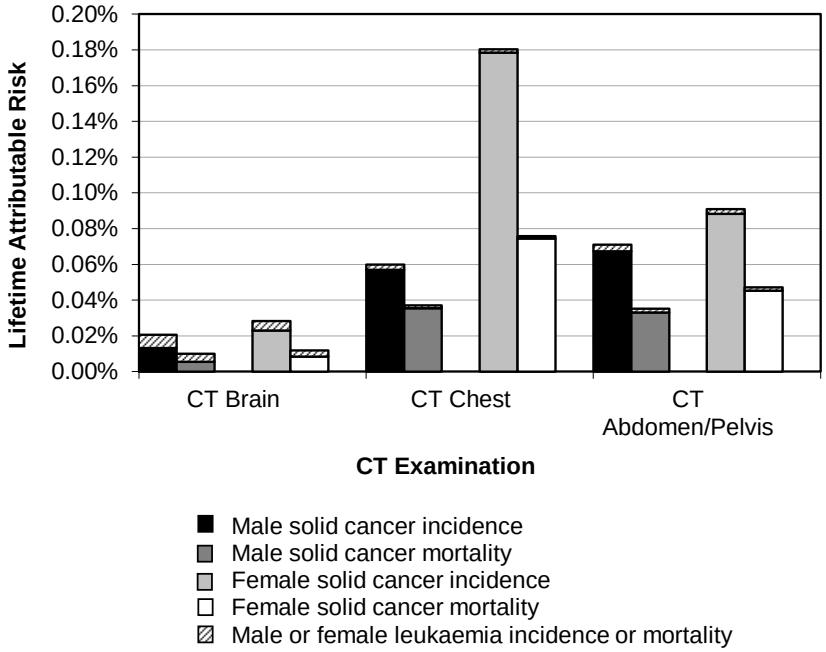

Figure 8.3: Lifetime attributable solid cancer and leukaemia risks for a 10 year old undergoing a CT brain, chest or abdomen/pelvis examination.

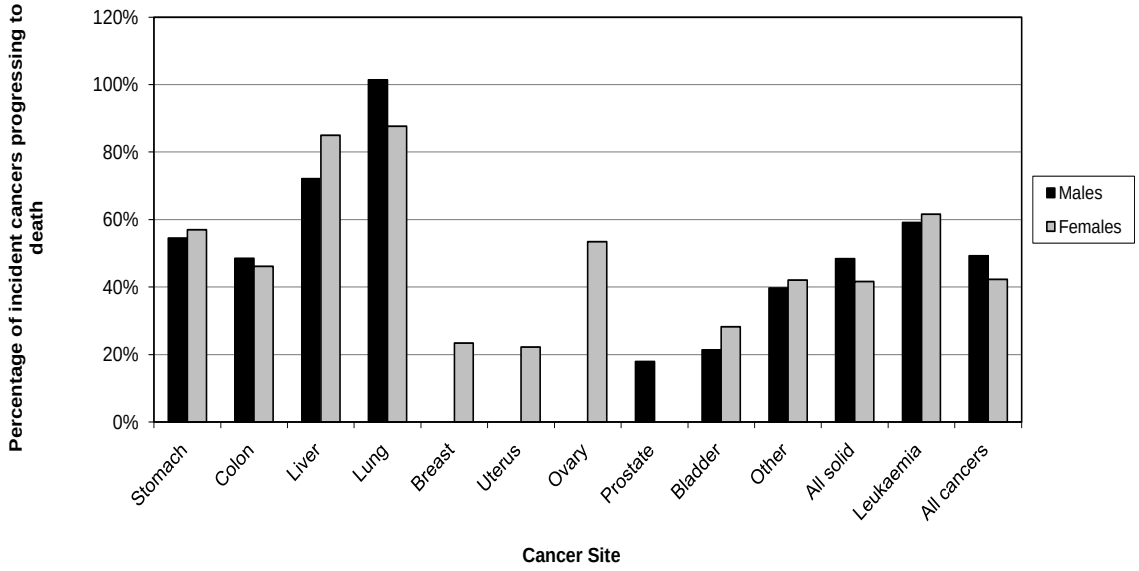

Figure 8.4: Percentage of site-specific radiation induced cancers progressing to cause death for males (black) and females (grey).

This thesis found that the radiation induced cancer mortality risk from CT brain examinations for a 10 year old child is lower than the risk estimated in two studies by Brenner et al. (2001a; 2007). In both studies, they found the risk to be about one in 4,000. The difference is readily explained by comparing the risk factors from the earlier BEIR V report (NRC, 1990) used by Brenner et al. (2001a; 2007) with the risks given in the current BEIR VII report (NRC, 2006) used in this thesis. For example, the sex-averaged lifetime mortality estimates for "other" cancers are lower by a factor of two in BEIR VII. Since this category of cancers are the highest contributor to radiation induced mortality for CT brain examinations due to the absorbed dose to the brain, the estimates from Brenner et al. (2001a; 2007) appear comparable with those from this thesis. The higher brain absorbed dose used by Brenner et al. (2001a) in their first study, which reflected the use of adult CT parameters on children, does not have a large effect on the total risk. This is because the brain absorbed dose is only one contributing organ amongst many to the category of "other" cancers and is not given a site-specific cancer risk.

The gender-averaged mortality risk from CT abdomen/pelvis examinations was found in this thesis to be about one in 2,450. Brenner et al. (2001a) found the risk for abdominal (excluding the pelvis) examinations to be about one in 800 based on the use of higher adult CT parameters (Paterson et al., 2001) and about one in 1,250 using lower organ absorbed doses (Brenner and Hall, 2007). The absorbed doses used were higher than those measured in this thesis (Table N.1, Appendix N), which when combined with the mostly higher risk factors in BEIR V leads to the conclusion that the risk estimates are fairly comparable with those from this thesis.

Two recent comprehensive studies (Berrington de Gonzalez et al., 2009; Smith-Bindman et al., 2009) estimate the age- and sex-specific cancer incidence risks attributable to CT radiation exposure in the US population applying BEIR VII risk factors (Table 8.5). The risks calculated in the current thesis for body examinations are considerably lower than those calculated for the US population. This is surprising since the risks calculated in this thesis are for a younger patient population in which the risks are expected to be higher due to increased radiosensitivity compared with adults, even young adults. Since the converse is true when comparing these studies, this may reflect the more optimised scan parameters used at the RCH, resulting in lower organ absorbed doses and consequently reduced overall risk.

The Smith-Bindman et al. (2009) study found the risk for females to be higher than for males from CT brain examinations although this was not found in the Berrington de Gonzalez et al. (2009) results. This was also an interesting finding of this thesis arising from the small lung dose measured from the CT brain examination. This dose combined with the high risk of radiation induced lung cancer in females, contributed to the disparity in overall risk between males and females. In general, the radiation induced cancer incidence risks from CT brain examinations calculated in this thesis were lower

than the US results for 15 year olds (Berrington de Gonzalez et al., 2009), but higher than the risks for 20 year olds (Smith-Bindman et al., 2009).

8.4.4 Projected Cancer Risks

The site- and sex-specific cancer incidence and mortality risks estimated in this thesis can be applied to the number of paediatric CT examinations undertaken in Australia to assess the potential number of fatal and non-fatal cancers induced (Table 8.3). The proportion of CT examinations conducted on children aged 5 to 14 years billed to Medicare in 2008 for the brain, chest and abdomen/pelvis are approximately 35%, 5-10% and 5-10% respectively (Medicare). This does not include examinations which combine any of these regions (for example chest/abdomen/pelvis). This breakdown of examinations is reflected in the RCH data for 2008 for children aged 10 years. The RCH data shows that a large percentage of the remaining examinations are conducted on extremities.

Other studies based on distributions of adult CT examinations have found that the proportion of head examinations is 30-40% (Berrington de Gonzalez et al., 2009; Brenner et al., 2001a; NCRP, 2009; Thomson and Tingey, 1997), chest examinations is 8-20% (Berrington de Gonzalez et al., 2009; NCRP, 2009; Thomson and Tingey, 1997) and abdomen/pelvis examinations is 20-32% (Berrington de Gonzalez et al., 2009; Brenner et al., 2001a). A recent assessment of a sample of children's health care records in the US, found that almost one-third of CT examinations were of the head (Dorfman et al., 2011). Abdomen and pelvis CT examinations were performed separately and therefore cannot be directly correlated with this thesis, although they accounted for 30% of the CT imaging (Dorfman et al., 2011). Chest CT examinations accounted for about 4% of all CT imaging (Dorfman et al., 2011).

A study of CT records in Northern England for patients under 22 years showed a much higher percentage of head and/or neck examinations (73%) although the cohort assessed was for an earlier time period (1993-2002) (Pearce et al., 2011). Chest imaging and abdomen/pelvis imaging each contributed to approximately 10% of all CT imaging (Pearce et al., 2011). Ono et al. (2011a) found 68% head imaging and 17% body imaging based on a Japanese survey of CT scanning in children. In Israel, about 55% of CT imaging was of the head in 0-18 year olds, and approximately 25% of the body, including pelvis, spine, chest and abdomen (Chodick et al., 2006). In this thesis, the following examination distribution for children has been used: 35% for head examinations and 10%[i] each for chest and abdomen/pelvis examinations.

In Australia, the total number of CT examinations undertaken on children aged 0-18 years billed to Medicare was 58,183 (males 31,115; females 27,068). These examinations need

[i]The upper values of these ranges have been used as these are still likely to underestimate the actual volume of CT examinations performed on these regions of the body. These examinations are often combined with other body regions and are difficult to categorise into this type of breakdown.

to be scaled by a factor of 3 (range 2.7 to 3.3) to account for those examinations not billed to Medicare (Chapter 7). Projected cancer risk estimates were then made based on this range, the breakdown of examinations according to body region in this age group and gender-averaged cancer incidence and mortality risks calculated for a 10 year old from organ absorbed doses measured in this thesis (Table 8.3). Due to the latency period for cancer to become apparent, these cancers will only be evident years after the CT examinations have been performed and hence will not be easily linked to the CT radiation exposure.

Despite the risk being lower from CT brain examinations than from body examinations, CT brain scans lead to an almost equivalent number of cancers in the Australian population as produced by each type of body scan. This is because of the much larger number of brain examinations performed in this age group in Australia. Overall, CT chest examinations lead to the greatest number of fatal radiation induced cancers.

Applying the same assumptions and risk estimates to the number of CT examinations performed at the RCH reveals that it would take more than one year of scanning to induce a fatal cancer from a single type of any of the examinations considered here. For all CT brain examinations currently performed at the RCH, one fatal cancer will be caused due to about seven years of CT scanning. It would take about five years of CT chest examinations to lead to one fatal cancer and about seven years of CT abdomen/pelvis examinations to result in one fatal cancer. These estimates assume the same CT imaging rates as performed at the RCH in 2008 and the same organ and tissue absorbed doses as measured in 2010 from standard protocols used on the RCH CT scanner.

The projected risks calculated in this thesis from CT scanning are much lower than the natural site-specific cancer mortality rates in Australia (Tables O.1 and O.2, Appendix O). For a 10 year old male undergoing CT examinations of the brain, chest or abdomen/pelvis the projected risks of radiation induced fatal cancer are about 2,020, 540 and 560 times lower respectively than the natural cancer mortality rate of one in five in Australia. For a 10 year old female the fatal cancer risks are about 1,420, 220 and 350 times lower from CT brain, chest and abdomen/pelvis examinations respectively than the natural cancer mortality rate of one in six in Australia.

The risk estimates provided in this thesis for the total number of CT examinations performed in the 0-18 year age group for Australia and at the RCH are based only on brain, chest and abdomen/pelvis examinations. It is assumed that these account for about 55% of all examinations in this age group (excluding those examinations that are combinations of these). To provide a very approximate estimate of the total predicted number of fatal cancers from one year of CT examinations, the risks can be assumed to be generally the same for the remaining 45% of examinations. Based on this assumption, it is predicted that up to 50 fatal cancers will be attributable to each year of paediatric CT scanning in Australia (based on current Australian trends and doses at the RCH) in addition to

the number of natural fatal cancers in this same group of children, which would be expected to be about 28,000-34,000[ii] over their lifetime. Similarly using this assumption and combining the risks from each type of examination, it is expected that each year of CT scanning of children aged 0-18 years at the RCH will lead to one fatal cancer. The number of natural fatal cancers for this cohort of children would be about 650. Overall, the estimated projected number of fatal cancers is only a very small (0.14%) percentage increase over the natural background rate.

8.4.5 Risks in Perspective

To put the risks from CT examinations in perspective, Table 8.6 shows the lifetime risk of dying from different causes in Australia. The mortality risk from a single CT examination at the age of 10 years is considerably lower than any of the other causes of death considered. The risks from CT examinations are only comparable when assessing causes of death in a narrow age range. For example, the risk of death from a CT chest or abdomen/pelvis examination for a 10 year old boy over his lifetime is roughly equivalent to half the risk of death from all other causes while he is aged 10-14 years. However, considering the boy's risk of death over his lifetime (to age 74 years) from all causes, the risk from the CT body examination is more than 700 times lower.

For a 10 year old girl, the risk of death from a CT chest examination over her lifetime is roughly equivalent to double the risk of death from all other causes while she is aged 10-14 years. It is noted that girls are at a much lower risk of dying in this age group than boys, yet their risk of radiation induced cancer is higher than boys undergoing the same CT examination. The girl's risk of death over her lifetime from a CT chest examination is more than 200 times lower than the risk of death (to age 74 years) from all other causes.

8.5 Conclusions

Based on current CT scanning rates and radiation doses, this thesis has shown that the radiation risks account for only a very small percentage increase over the natural cancer rate. The risks for the individual patient are small, particularly for a well optimised, justified examination. These risk estimates are based on absorbed doses measured at the RCH, which is a dedicated paediatric hospital. Therefore, it is expected that doses at this institution arise from best clinical practice and are already well optimised, hence presenting a best case scenario for risk projections. When considering the potentially wide variation in doses across Australia, these risks could in fact be much higher. In that case, when the risks are applied to the population there is the potential for a detrimental health impact to arise. It would be extremely challenging to detect this increased level

[ii] This range is based on the estimated range for the number of CT examinations performed on 0-18 year olds in Australia.

of risk in the population due to the high natural incidence of cancer and the sometimes lengthy latency period for radiation induced cancers to become evident. However, there are some epidemiological studies (Giles, 2004) commencing, including one in Australia (Brady et al., 2011f; Mathews and Chesson, 18 February 2009), which will be important in assessing current theoretical risk models at low radiation doses.

It is important to acknowledge the considerable uncertainties involved in projections of risk from radiation exposure and any use of these risk estimates must take these into account. It has been assumed that even at low doses of radiation there is a small (and theoretical) risk of cancer induction. The mechanistic risk model (NRC, 2006) on which these estimates are based considers that radiation risk decreases with increasing age, which may be inconsistent with models taking into account competing biological radiation effects such as cancer promotion (Shuryak et al., 2010). A further limitation of the estimates made here is that the risks for a 10 year old have been applied across the 0-18 year age range, which will underestimate the risk in the younger age groups and overestimate the risk in the older age groups. However, considering the assumptions and uncertainties involved in these risk estimates, this will give an adequate, albeit limited, indication of the paediatric risks.

Providing a better understanding of the lifetime attributable radiation risks for children undergoing CT examinations will hopefully lead to better justification for scans in the future. Furthermore, it will be a driver for undertaking dose optimisation at institutions where the doses are much higher. Overall, the risk due to radiation exposure for an appropriately justified and well optimised CT scan for an ill child hospitalised at the RCH, for example, will almost always be much lower than the risk associated with not performing the scan. The risk projections in this thesis must be considered in the context of the substantial diagnostic and/or treatment benefit gained from a justified and optimised CT scan.

8.6 Publications Arising from this Chapter

1. **Brady, Z.**, *Doses and risks in paediatric imaging in Australia*, presented at the Siemens Low Dose Academy, 2012, Sydney, Australia *(Invited Speaker)* (Brady, 2012a).

Table 8.4: Comparison of sex-averaged paediatric cancer mortality risks for CT brain and abdomen/pelvis examinations. Risk is expressed in terms of the number of patients undergoing CT examinations (in Australia for this study and in the US for the Brenner et al. studies (2001a; 2007)) that would lead to the development of one radiation-induced cancer.

	This Study[a]	**Brenner et al. (2001a)**[b]	**Brenner et al. (2007)**[c]
Age at exposure (years):	10	10	10
Examination			
CT Brain	9,300	4,000	4,000
CT Abdomen/Pelvis	2,450	800[d]	1,250[d]

[a] Cancer mortality risks for this thesis were calculated based on site-specific organ absorbed doses measured with TLDs (Chapter 3) multiplied by the site- and sex-specific BEIR VII LAR for exposure at 10 years of age (NRC, 2006).

[b] Brenner et al. (2001a) obtained paediatric organ absorbed doses by scaling adult organ absorbed doses reported in a 1989 British survey (Shrimpton et al., 1991) by relative age-dependent changes in effective dose estimated by Huda et al. (1997). These age-dependent organ absorbed doses were multiplied by the age-specific BEIR V LAR (NRC, 1990).

[c] Brenner et al. (2007) used paediatric organ absorbed doses from a 2000 US survey (CRCPD, 2006). These age-dependent organ absorbed doses were multiplied by the age-specific BEIR V LAR (NRC, 1990).

[d] These values are for abdomen examinations only (i.e. they do not include the pelvis).

Table 8.5: Comparison of male and female paediatric cancer incidence risks from CT brain, chest and abdomen/pelvis examinations. Risk is expressed in terms of the number of patients undergoing CT examinations (in Australia for this study and in the US for the Berrington de Gonzalez et al. (2009) and Smith-Bindman (2009) studies) that would lead to the development of one radiation-induced cancer.

	This Study		**Berrington de Gonzalez et al.**[a]		**Smith-Bindman et al.**[b]	
Gender:	Females	Males	Females	Males	Females	Males
Age at exposure (years):	10	10	15	15	20	20
CT Examination						
CT Brain	3,500	4,900	2,500	2,000	4,360	7,350
CT Chest	600	1,700	350	1,100	390	1,040
CT Abdomen/Pelvis	1,100	1,400	500	500	500	660

[a] Berrington de Gonzalez et al. (2009).

[b] Smith-Bindman et al. (2009).

[c] Cancer mortality risks for this thesis were calculated based on site-specific organ absorbed doses measured with TLDs multiplied by the site- and sex-specific BEIR VII LAR for exposure at 10 years of age (NRC, 2006).

[d] Berrington de Gonzalez et al. (2009) provide risk estimates for a range of ages, the younger age groups being 3 years and 15 years. The risk estimates for 15 year olds are provided in the Table above. The organ absorbed doses are calculated from technical parameters taken from a 2000 US survey (CRCPD, 2006) and input into CT-Expo (Stamm and Nagel, 2011b). The BEIR VII risk models were then applied, with minor modifications, and additional models were developed for sites not covered by BEIR VII.

[e] Smith-Bindman et al. (2009) conducted a retrospective patient dose survey and calculated effective dose using the dose length product (DLP) conversion method (Shrimpton et al., 2006). They confirmed the effective doses for a small subset of patients with the ImPACT CT Dosimetry Tool (ImPACT, 2011). The calculated effective dose was multiplied by the "all cancer" BEIR VII LAR. The youngest age that risk estimates are provided for is 20 years and these risks are given in the Table above.

Table 8.6: Lifetime risk of dying for the Australian population from various causes.

Cause of Death	Males	Females	Persons
CT brain examination at 10 years of age[a]	0.010%	0.012%	0.011%
CT chest examination at 10 years of age[a]	0.037%	0.076%	0.056%
CT abdomen/pelvis examination at 10 years of age[a]	0.035%	0.047%	0.041%
All causes combined[b,c]	25%	17%	25%
0-19 y	1.0%	0.72%	0.86%
0-4 y	0.63%	0.50%	0.56%
5-9 y	0.055%	0.049%	0.052%
10-14 y	0.063%	0.035%	0.049%
15-19 y	0.26%	0.13%	0.20%
60-64 y	4.2%	2.5%	3.3%
All neoplasms[b,d]	13%	8.3%	11%
Diseases of the circulatory system[b,e]	7.7%	3.6%	5.6%
External Causes[b,f]	3.2%	1.1%	2.2%
0-19 y	0.30%	0.13%	0.22%
0-4 y	0.056%	0.032%	0.044%
5-9 y	0.023%	0.012%	0.018%
10-14 y	0.032%	0.012%	0.022%
15-19 y	0.19%	0.08%	0.14%
60-64 y	0.23%	0.09%	0.16%
Diseases of the respiratory system[b,g]	1.9%	1.3%	1.6%
Endocrine, metabolic and nutritional diseases[b,h]	1.2%	0.76%	1.0%
Diseases of the digestive system[b,i]	1.3%	0.62%	0.93%
Diseases of the nervous system[b,j]	0.90%	0.66%	0.78%
Infectious and parasitic diseases[b,k]	0.49%	0.27%	0.38%
Diseases of the genitourinary system[b,l]	0.37%	0.29%	0.33%
Diseases of muscoskeletal system and connective tissue[b,m]	0.12%	0.19%	0.16%

[a] Cause of death from CT examinations is radiation induced cancer. Cancer mortality risks were calculated based on site-specific organ doses measured with TLDs (Chapter 3) multiplied by the site- and sex-specific BEIR VII Lifetime Attributable Risks (LAR) for exposure at 10 years (NRC, 2006).
[b] Risk of dying approximates the risk of contracting and dying of a disease if the risks at the time of estimation (2006) remain throughout the specified period and age range (0 to 74 years). Risk is expressed as a percent chance of dying from the disease (AIHW, 2008b). Causes of death are defined in terms of the International Classification of Diseases (ICD) Codes (WHO, 2004).
[c] All causes combined, ICD10. Age breakdowns for this category have also been given. For example, the risk of dying from all causes in the age group 0-19 years. The age group 60-64 years has been provided to allow comparison with an older age group. [d] All neoplasms, ICD10 C00-D48. [e] Diseases of the circulatory system, ICD10 I00-I99. For example, ischaemic heart diseases, pulmonary heart diseases, hypertensive diseases, etc. [f] External causes, ICD10 V01-Y98. For example, transport accident, drowning, assault, suicide, etc. Age breakdowns for this category have also been given. For example, the risk of dying from external causes in the age group 0-19 years. The age group 60-64 years has been provided for comparison with an older age group. [g] Diseases of the respiratory system, ICD10 J00-J99. For example, influenza, pneumonia, lung diseases due to external agents, etc. [h] Endocrine, metabolic and nutritional diseases, ICD10 E00-E90. For example, diseases of the thyroid gland, obesity, etc. [i] Diseases of the digestive system, ICD10 K00-K93. For example, diseases of the liver, appendix, stomach, etc. [j] Diseases of the nervous system, ICD10 G00-G99. For example, inflammatory diseases of the central nervous system, degenerative diseases of the nervous system, cerebral palsy, etc. [k] Infectious and parasitic diseases, ICD10 A00-B99. For example, intestinal infectious diseases, HIV, tuberculosis, etc. [l] Diseases of the genitourinary system, ICD10 N00-N99. For example, renal failure, diseases of the male and female genital organs and urinary system, etc. [m] Diseases of the muscoskeletal system and connective tissue, ICD10 M00-M99.
[n] All risks are quoted to two significant figures.

Chapter 9

Conclusions

The aim of this thesis was to assess the medical radiation exposure of children in Australia from CT examinations. Radiation risk coefficients that are specific to the site of cancer induction, the age at exposure and gender are made available in the BEIR VII Report (NRC, 2006). These risks are applied to organ absorbed doses in order to assess site-, age- and gender-specific radiation detriment. However, determining organ absorbed doses for CT exposure is complex, which is evidenced by the large number of, mostly indirect, methods currently available. Furthermore, few publications addressed experimental organ dosimetry methods in paediatric CT or the magnitude of organ absorbed doses for clinically used protocols. To provide a thorough assessment of the risks from paediatric CT in Australia, it was also necessary to use imaging rates to project radiation induced cancer risks for the population. However, there was no comprehensive analysis of paediatric CT imaging frequency in Australia.

This thesis addressed these objectives by:

1. Developing and implementing a method of organ dosimetry for paediatric CT exposures using a physical anthropomorphic phantom and high sensitivity TLDs.

2. Quantifying organ absorbed doses for typical paediatric CT examinations of the brain, chest and abdomen/pelvis for clinically used protocols.

3. Critically comparing computational dosimetry methods using TLD measured absorbed doses to assess their reliability for paediatric CT organ dosimetry feasible for clinical implementation.

4. Benchmarking CT doses at the RCH both nationally and internationally and developing an optimisation method for assessing CT parameter selection.

5. Identifying CT imaging frequencies and trends for the Australian paediatric population.

6. Projecting cancer risks for the population due to paediatric CT examinations based on measured organ absorbed doses, radiation risk coefficients and Australian imaging frequency.

There are few publications describing a methodology for TLD dosimetry for calculating mean organ absorbed doses and estimating effective dose for diagnostic radiology applications, particularly in the paediatric setting. This is perhaps due to the much lower doses typical of diagnostic imaging compared with radiotherapy and the lack of TLD dosimetry equipment and anthropomorphic phantoms in radiology departments. Even for this thesis it was necessary to draw upon resources from multiple sites, including radiotherapy centres, to undertake the TLD measurements. Furthermore, assessing organ absorbed doses in children instead of adults has additional considerations. Red bone marrow, as well as cortical and trabecular bone distributions vary with age. It is important to account for these variations when assessing the risk of leukaemia which depends on the absorbed dose to the red bone marrow and bone surfaces. In addition, experimental dosimetry in the low energy range typical of CT exposures is inherently difficult. Differences in mass energy absorption coefficients for different tissues must be considered and secondary electron equilibrium cannot be assumed for very small cavities, such as those containing bone marrow.

Another challenge was to identify a material or device with sufficient sensitivity to detect the low radiation doses encountered in paediatric CT. A relatively new, highly sensitive TLD material, which has yet to achieve broad implementation in diagnostic radiology dosimetry was selected. It was therefore necessary to develop a method for calibrating and using this TLD material in the diagnostic energy range. Due to the relatively linear energy and dose response of these TLDs it was possible to perform calibrations on a linear accelerator ensuring uniformity and reproducibility of output. This is a significant advantage associated with using these TLDs and a major improvement, which reduces the overall uncertainty typical in TLD dosimetry in the low energy and low dose range. MOSFETs were also investigated and found to be in reasonable agreement with TLDs, but overall offered a less accurate, although more practical, alternative for regular use in the clinical environment.

A systematic approach to TLD organ absorbed dose measurement and calculation was developed and employed for the three typical CT examinations of the brain, chest and abdomen/pelvis that were assessed in this thesis using clinical protocols at the RCH. A method for obtaining average organ absorbed dose measurements in an anthropomorphic phantom representing a child has been described. All organs and tissues considered to be at risk of stochastic radiation effects as defined in ICRP 103 have been considered. The highest measured organ absorbed doses were to the brain (33.6 mGy) for the CT brain examination, to the thyroid and ET region (10.9 mGy) for the CT chest examination and to the stomach (8.9 mGy) for the CT abdomen/pelvis examination. Furthermore,

absorbed doses were found to be more consistent for directly and fully irradiated organs, while organs on the periphery of the scan volume had a greater range of measured absorbed doses. These organs were also affected by the over-ranging length in helical scanning. For the organ absorbed doses derived from the TLD measurements, the $CTDI_{vol}$-normalised organ doses (in mGy to tissue per mGy of $CTDI_{vol}$ for the 16 cm dosimetry phantom) were 0.8 mGy/mGy for the brain for the CT brain examination and 0.7-0.9 mGy/mGy for directly irradiated organs for both the CT chest and abdomen/pelvis examinations.

The effective doses estimated from the TLD measured organ absorbed doses according to ICRP 103 were 1.4 mSv, 5.0 mSv and 4.8 mSv for the CT brain, chest and abdomen/pelvis examinations respectively. The ICRP 103 estimated effective dose was 22% lower for the CT brain examination, 16% higher for the CT chest examination and 4% lower for the CT abdomen/pelvis examination than the ICRP 60 estimated effective dose. This reflected the changes to the tissue weighting factors in ICRP 103 which are now lower for the brain when directly irradiated, higher for the breast and remainder organs and lower for the gonads.

Experimental dosimetry is not often a practical option in radiology clinical environments and a readily applied, indirect method of estimating organ absorbed doses is necessary for any type of risk assessment. Furthermore, it is useful to reliably estimate effective dose for planning and optimisation, particularly for CT protocol design. Therefore, several computational dosimetry methods were compared with the TLD measurements made in this thesis. There are only limited assessments in the literature of different CT dose calculation methods and these are mainly for adults, using theoretical, controlled exposure situations. For directly irradiated organs it was found that the computational methods varied by up to 31% from the measured organ absorbed doses for the CT brain and chest examinations and up to 49% for the abdomen/pelvis examination. Effective dose estimates using the ICRP 60 formalism using the various computational methods differed by -30% to 35% from the TLD derived effective doses. For ICRP 103 calculated effective doses, the variation ranged from -29% to 41% from the TLD doses. One of the key reasons for differences in dose calculations is due to the phantom used for either experimental dosimetry or Monte Carlo modelling. Children are more problematic to model than adults and several phantoms are required to adequately simulate anatomical differences over the age groups from newborn to adolescent. It was found that placement of the organs relative to other organs and also relative to the surface of the phantom had a significant effect on the absorbed dose.

A retrospective patient dose survey was also conducted to derive local diagnostic reference levels (DRLs) at the RCH for typical CT examinations in all paediatric age groups and to verify the measurements made in the anthropomorphic phantom with real patient data. The mean dose values from the patient dose survey were compared with national and international dose levels to identify areas of optimisation and to assess changes in CT doses

in Australia. The RCH DRLs were typically comparable to or lower than international values. In particular, the use of 80 kV_p for both chest and abdomen/pelvis imaging in young children lead to a significant dose saving. Scan lengths for body imaging is one area that can be reviewed for potential optimisation. Comparison of the RCH values with a 2001-2002 survey of Australian hospitals demonstrated that there were considerable dose reductions as a result of new technology and optimised protocols at the RCH. However, comparison with a more recent survey at another Australian hospital with a more advanced CT scanner showed that further dose reduction is achievable. The method of assessing patient CT doses described in this thesis will be useful to other practices undertaking similar retrospective audits. Furthermore, in the future it will allow evaluation of protocols on the new scanner to be installed at the RCH and ensure that the opportunity is used to further optimise dose.

A review of the literature revealed that there was little information regarding the number of CT examinations performed in Australia on children. There was a clear need for research to be conducted in this area. A comprehensive analysis of Australian Medicare and RCH records was undertaken in order to determine CT imaging rates in Australia that reflected current usage. Medicare is the best available resource for assessing imaging trends, although a major limitation is that it only captures CT services funded through the national health care system. It was found through analysis of RCH records that in the 0-18 year age range only one third of CT examinations are captured by Medicare. To address this shortcoming, scaling factors have been derived in this thesis in order to adjust Medicare data to take account of non-funded services. Overall, it was found that the growth in CT imaging of Australians of all ages is exceeding population growth at a significant rate. The average annual increase in the CT imaging rate for 0-18 year olds is estimated to be 5.1%. However, in recent years, growth in the imaging rate for 11-18 year olds has slowed, while for 5-10 year olds the imaging rate has declined.

Finally, by combining the measured organ absorbed doses and Australian CT imaging frequency, it was possible to make estimates of the number of cancers induced from the radiation exposure of children undergoing CT examinations. These risks were found to be much lower than similar estimates based on the US population and CT practice. One of the reasons for this is the much lower absorbed doses attributed to CT practice at the RCH and it also seems likely that there is a lower utilisation of CT imaging for children in Australia. Overall, it was found that there was only a very small percentage increase (approximately 0.14%) over the background natural cancer rate due to radiation induced cancers from CT imaging in the 0-18 year old Australian population.

There is sometimes an unreasonable level of anxiety associated with radiation exposure and its risks. This anxiety is understandably even greater for parents whose children are undergoing CT examinations. Often this concern will arise from a lack of awareness of the risks. This originates from misinformation, or even a knowledge deficit, in the medi-

cal profession regarding doses and risks and hence an inability to convey the appropriate information to patients. To some extent, this is because the information is not easily and readily available or is not directly applicable to their circumstances. For children's hospitals and other sites undertaking paediatric imaging in Australia there is little guidance on specific dose requirements.

This thesis significantly extends the knowledge base and methodology for assessing paediatric CT doses, risks and imaging trends in the Australian context. The trio of articles (Brenner et al., 2001a; Donnelly et al., 2001; Paterson et al., 2001) published in 2001 resulted in an increased awareness and focus on issues relating to children and CT. It is hoped that by conducting research in this area in Australia and developing a more in-depth understanding of paediatric CT dose, that it will similarly stimulate discussion and ultimately lead to dose reduction. Furthermore, it provides a useful basis for organ dosimetry that may be utilised in the epidemiological study assessing the effects of low doses of radiation to children from CT examinations that has commenced in Australia (Brady et al., 2011f; Mathews and Chesson, 18 February 2009).

Appendix A

Overview of CT Scanner Design, Technology and Dosimetry

A.1 CT X-ray Production and Detection

X-ray Tube Components and X-ray Production

The basic components of an X-ray tube consist of two electrodes: a filament (cathode) and target (anode), in a vacuum maintained typically by a glass housing (Figure A.1). Electrons are produced by the filament through thermionic emission when a current is applied. The electrons are accelerated towards the anode with the application of a high voltage (20-150 kV_p) across the electrodes. For CT, this is generally in the range 80-140 kV_p at discrete 20 kV_p intervals, although 120 kV_p is the most commonly used voltage in the clinical setting.

A focusing cup is placed around the filament to ensure that electrons are focused on the positive anode, rather than being attracted back to the gradually more positive filament, or dispersing due to repulsive forces between the electrons (space charge effect).

When an electron interacts with an atom in the anode, kinetic energy of the electron can be transferred to an orbiting atomic electron. This will cause excitation of the atom, or if the energy exceeds the binding energy of an orbital electron, ionisation may also occur. Electrons which have been excited to higher energy levels within an atom will drop back to the lower energy, ground state and in doing so emit characteristic photon radiation typically in the visible light to ultraviolet range. Where there is sufficient incident energy to ionise the atom, an electron is ejected usually from the inner K-shell leaving an electron hole or vacancy. One of the outer orbital electrons will quickly fill the vacancy and emit a characteristic X-ray photon with energy equal to the difference between the shells in the process. These emissions are dependent on the type of atom and the energy difference

between electron shells, hence the term "characteristic" radiation. The emitted radiation is at discrete energies and is readily evident in an X-ray spectrum as peaks.

When excess energy from the transition of an outer orbital electron to the inner shell vacancy is transferred to another atomic electron, this electron may be emitted from the atom as an Auger electron. The kinetic energy of the Auger electron will correspond to the difference between the energy available from filling the inner orbital vacancy and the Auger electron's binding energy.

Another inelastic scattering process produces bremsstrahlung or braking radiation. The nuclear electrostatic force causes the accelerated electrons to slow down or brake, and change direction. In doing so, they lose some of their kinetic energy in the form of X-ray photons. These photons have a full spectrum of energy from zero (the electron loses all of its energy) up to the maximum energy of the incident electrons (equivalent to the potential difference between the anode and cathode, i.e. the applied voltage). The energy of the photons is measured in electron volts (eV) which is a unit of energy equal to the amount of energy gained by an electron when accelerated across a potential difference of one volt (V).

Additional aluminium or copper filtration is added to the CT beam to filter out the low energy portion of the beam, which contributes to patient dose, but not to the image. Bow-tie filters are also used to shape the beam to account for beam hardening at the centre of the patient. For example, GE Healthcare (Waukesha, Wisconsin, US) scanners use different body and head filters depending on the body part being scanned (Toth, 2002). The bow-tie filters provide greater attenuation of the beam at the edges of the patient, which are thinner and therefore do not require a beam with the same penetrability needed for the more central thicker portion of a patient. The pre-patient filters will define the dose profile of the X-ray beam.

Figure A.2 demonstrates emission spectra for an X-ray tube operated at 120 kV_p, typical of CT scanners. Curve 1 shows that even without additional filtration, the tube aperture filters the softest (lowest energy) X-ray photons in the beam to a small extent. Curve 2 is a typical emission spectrum for a diagnostic X-ray unit and curve 3 for a CT scanner, with a more heavily filtered beam. It is also evident that the average effective energy of an X-ray beam is significantly less than the peak energy. The effective energy is much higher in CT applications compared with general radiography due to the additional beam filtration used.

The efficiency of X-ray production is relatively low and more than 99% of the incident electron energy is converted to heat. Therefore, X-ray tubes must have sufficient heat dissipation properties, particularly in the case of CT where there are high tube loadings. The anode must have a high melting point and its heat capacity will be a limiting factor for continuous operation and parameter selection when in use. The focal track of the

Figure A.1: Components of an X-ray tube (http://openlearn.open.ac.uk).

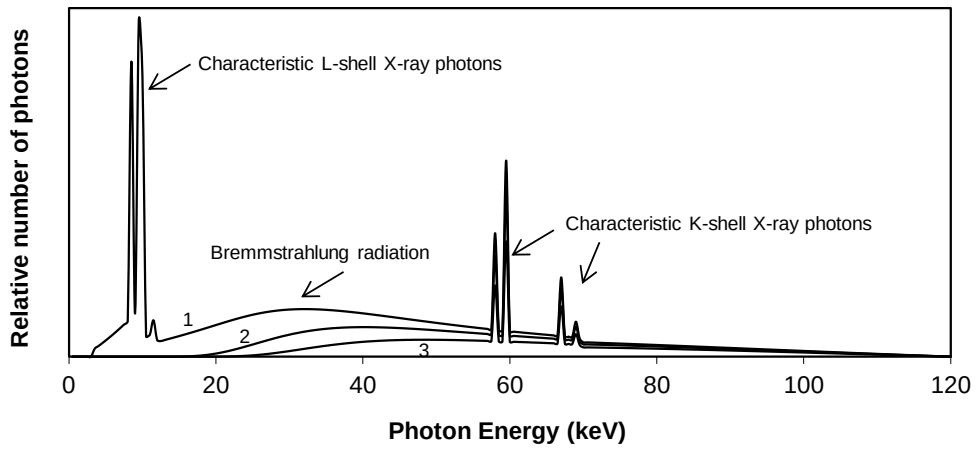

Figure A.2: Calculated X-ray emission spectra from a tungsten target produced at 120 kV_p. Maximum energy of emitted photons is 120 keV. All curves include inherent filtration from the tube aperture. Curve 1 is the typical spectrum with no additional filtration, curve 2 includes 2.5 mm aluminium additional filtration (typical general X-ray tube) and curve 3 shows the effect of 7 mm aluminium additional filtration (typical CT tube) (Reilly and Sutton, 1997).

anode is typically made of tungsten-rhenium for CT, as well as for general radiography applications. However, the metal focal track is usually brazed or deposited onto graphite for CT applications, which provides a higher heat capacity than a molybdenum body used in general X-ray tubes (Hsieh, 2003). Oil or water cooling can also be used in CT scanners to improve heat removal. Anodes will deteriorate over time with cracking and pitting occurring from electron bombardment and a disadvantage of the graphite based anode is an increased potential for these particles (Hsieh, 2003).

Two unique X-ray tube designs include the Straton tube (Schardt et al., 2004) (Siemens, Erlangen, Germany) and the liquid spiral groove bearing (Schmidt and Behling, 2000) (Philips Healthcare, Andover, Massachusetts, US). The Straton tube rotates the entire vacuum vessel containing both the anode and cathode, compared with a conventional design that rotates the anode only. This allows bearings to be placed outside the vacuum, which can then be lubricated. It also facilitates greater cooling of the anode by direct conductive cooling via an oil stream on the back anode surface (Kalendar, 2005). The Philips design replaces conventional ball bearings with a spiral groove, which use liquid metal lubrication. This anode is directly cooled by the bearing, increasing heat capacity.

CT Detectors

Very early scanners utilised monolithic sodium iodide crystal scintillators doped with thallium [NaI(Tl)] coupled with a photomultiplier tube (PMT). In these solid state detectors X-ray photons hit the scintillator material causing excitation and ionisation. During de-excitation, the atoms emit visible light (fluorescence) which is detected by the photocathode of the PMT. Interaction of the light photons results in the ejection of electrons, which are accelerated between dynodes creating an avalanche detected by the anode of the PMT. This amplified signal is proportional to the energy of ionising radiation incident on the detector. The scintillator material can be doped with an activator such as thallium to increase the probability of light emission (conversion efficiency).

Sodium iodide detectors in the early scanners intercepted the entire beam and therefore were very efficient (approximately 100% efficiency along the z-axis). However, they exhibited poor temporal response and suffered from afterglow from phosphorescence (delayed emission of light). These detectors were not suitable for later scanners which required large numbers of detector banks. Any drift in calibration or fault in a single detector would be propagated in the image as a ring artefact.

To overcome this problem, gaseous detectors were introduced in which a long metal chamber was subdivided into smaller chambers by septa to form a detector array across the patient. Each chamber was filled with xenon gas at a high pressure (10-30 atmospheres) and the septa enclosing each volume formed electrodes. As these were highly directional, scatter rejection was excellent (Bushberg et al., 2001). The interaction of X-ray photons with the gas causes ionisation and in the presence of a low applied voltage (200-350 V)

migration of the charges occurs before recombination can take place. The applied voltage also prevents secondary ionisations and the resulting current is measured with an electrometer.

As CT scanner design advanced, more flexibility in the design of the detector was needed than could be achieved by xenon detectors with their limited angular detection and bulkiness. Modern scanners have returned to scintillator material and now generally use solid state detectors, which exhibit improved detection efficiency and are capable of detection over a wider angle. Furthermore, ease of production is a necessity as modern scanners can have more than 800 detector elements in an array (across the patient in the scan plane) with multiple arrays and some scanners, with an entire ring of detectors, can exceed 4,800 individual detectors circling the patient (Bushberg et al., 2001).

Solid state detectors have a much higher density than gaseous detectors, making them more compact with higher detection efficiency. Detectors used in modern CT scanners consist of a ceramic or crystal scintillator coupled with photodiodes. The scintillator materials used today have much higher conversion efficiency than NaI used in the earlier detectors allowing PMTs to be replaced by photodiodes. These semiconductor diodes are reverse biased and do not amplify the light signal in the way that PMTs do. No electrical current flows in the diode until exposed to light, whereby the interaction of photons causes the production of electron-hole pairs, resulting in a current proportional to the light intensity.

Crystal scintillation detectors currently used include caesium iodide (CsI) and cadmium tungstate ($CdWO_4$), although ceramic scintillator solid state detectors, such as gadolinium oxysulfide (Gd_2O_2S) or yttrium gadolinium oxide (YGO) are preferred. Propriety names such as "ultra fast ceramic" (UFC) detector have been used for the Gd_2O_2S detector (Siemens, Erlangen, Germany). The disadvantages of the materials vary. For example, $CdWO_4$ is susceptible to radiation damage and CsI can have considerable afterglow (Fuchs et al., 2000). Furthermore, solid state detectors can lead to a ring artefact in the image when a detector element fails, whereas gas detectors are less susceptible to this effect.

The overall efficiency of a detector is the product of the quantum detection efficiency (QDE) and geometric detection efficiency (GDE). This represents the effectiveness of the detector in converting incident X-ray energy into a signal. It follows that an ideal detector will have an efficiency of one and utilise the entire incident beam, which will also optimise the dose to the patient. However, the detector efficiency does not equate to the overall dose efficiency of the system, which also requires the proportion of the beam actually used in the imaging process to be taken into account (discussed further in Section A.2).

The QDE or intrinsic efficiency of the detector is its ability to absorb and detect an incident photon and hence is the product of the absorption efficiency and conversion efficiency. For a detector with low QDE, photons will pass through without detection. The detection

efficiency is dependent on the linear attenuation coefficient of the detector and the detector thickness (Hsieh, 2003). Increasing the thickness or the linear attenuation coefficient of the material will increase the QDE. However, other factors, such as spatial resolution, will be affected by thicker detectors and hence must be taken into consideration in the design.

The GDE is a measure of the actual active area of the detector. Septa between detectors in both the scan plane and along the z-axis will subtract from the total active detection area. In addition, any post-patient collimators such as anti-scatter grids that are placed in front of the detector will partially block some of the primary X-ray beam. The GDE can be expressed as:

$$\text{Geometric detection efficiency (GDE)} = \frac{\text{Active detector area}}{\text{Total detector area}} \tag{A.1}$$

Conversely, some advantages of the septa between detector elements and post-patient collimators are to reduce cross-talk and increase scatter detection. In modern scanners which have multiple rows of detector arrays, there is an increase in the number of septa due to the larger number of detector elements which are in both the x-y and z-direction. This results in a decrease in detector efficiency compared with earlier scanners that consisted of a single detector array. Table A.1 lists properties of some common CT detectors. GE Healthcare (Waukesha, Wisconsin, US) have developed a new detector with a scintillator material consisting of a garnet gemstone and rare earth phosphor (∼1%). They claim that it has less afterglow by a factor of four and is 100 times faster than Gd_2O_2S.

Table A.1: Comparison of CT detector properties (from Heggie et al. (1997)).

Property	**Solid State**		**Xenon**
	Crystal $CdWO_4$	**Ceramic**	**30 atm**
Quantum detection efficiency (QDE)	95-100%	94-98%	50-60%
Geometric detection efficiency (GDE)	80%	80%	>90%
QDE x GDE	76-80%	75-78%	45-55%
Afterglow	∼0	<1%	∼0

A.2 CT Scanner Design

CT technology has rapidly advanced since the first scanner was installed at the Atkinson-Morley Hospital in Wimbledon, United Kingdom in 1971 (Prokop and Galanski, 2003). The different types of geometry utilised in scanners are identified by their "generation". However, the principle remains the same whereby a projection or view is formed from a set of rays at a particular angle passing through the body. A sinogram is then formed from the multiple projections over different angles around a slice of the body, from which

the final image is reconstructed.

CT Scanner Generations

The prototype first generation CT scanner (Figure A.3) developed by Godfrey Hounsfield was based on a translate-rotate principle. A pencil X-ray beam passed through the body and was detected by a single detector on the opposite side of the body. The X-ray tube and detector were coupled and hence moved together. The X-ray tube and detector were translated (160 times) across an entire slice to produce one complete projection. They were then rotated one degree to complete the next projection. This was continued until the body was scanned from 180 different angles. This type of scanner was restricted to imaging of the brain and the head was actually surrounded by a water bag to handle the change in flux in areas adjacent to the head (Beckmann, 2006; Bushberg et al., 2001). Each slice took 4.5 to 20 minutes to scan (Beckmann, 2006).

The next generation of scanner (Figure A.4) employed a small fan-beam of X-rays and was also known as a translate-rotate scanner. A linear array of detectors was used, but translation (six times) was still required as the fan beam was not wide enough to encompass the entire slice of the body to be imaged. Each rotation was increased to 30 degrees and a minimum scan time per slice of 18 seconds was achieved (Bushberg et al., 2001). This allowed whole body imaging as the timeframes were comparable to a breath hold, eliminating motion artefacts caused by the respiratory cycle.

Third generation scanners (Figure A.5) were based on a rotate-rotate movement where the tube and detectors move synchronously. A fan beam of X-rays was again utilised, but now encompassed the entire patient, hence avoiding translation movement of the tube and detectors. The number of detectors in the array increased (>800 in modern scanners) to accommodate the wider fan beam and were positioned along an arc. The X-ray tube and detector array still rotated together through a complete 360 degree revolution. In this type of scanner a single rotation could be obtained in seconds and in more modern scanners in under 0.5 second (Bushberg et al., 2001).

Scanners in the fourth generation (Figure A.6), termed rotate-stationary, incorporate a fixed ring of detectors fully encircling the patient. In modern scanners more than 4,800 detectors are located in the ring (Bushberg et al., 2001). The X-ray tube is positioned within the detector ring and rotates 360 degrees around the patient. The leading and trailing edge of the fan beam is used to calibrate the individual detectors during the scan. Each projection is derived from all rays acquired by a single detector for the various tube positions. Scanning times per rotation are approximately one second (Goldman, 2007b).

Fifth generation (Figure A.7) or cardiac scanners have no moving parts and hence are termed stationary-stationary. The X-ray tube is replaced with an electron gun and a

Figure A.3: First generation CT scanner (translate-rotate).

Figure A.4: Second generation CT scanner (translate-rotate).

Figure A.5: Third generation CT scanner (rotate-rotate).

tungsten anode ring surrounds the patient. The electron beam is magnetically steered towards the target and the X-ray fan beam intercepted by a ring of detectors. Four slices can be produced simultaneously in approximately 50 milliseconds, which allows fast frame rate movies of the beating heart (Bushberg et al., 2001). The very fast acquisition times result directly from the absence of moving components.

Helical Scanning

In the early nineties, advances in slip ring technology led to the introduction of helical scanning (sometimes referred to as spiral CT). The slip rings maintain electrical connection during continuous rotations to allow the X-ray tube to operate and data to be transferred without necessitating stopping between scan positions. Instead of the patient remaining stationary during a scan and stepping the table forward between rotations, the patient is moved continuously through the gantry and the X-ray tube rotates around the patient (Figure A.8).

The pitch describes the spacing between scanned points, such that contiguous slices will have a pitch of one (as is the case for axial sequential scanning). Pitch P is defined as:

$$P = \frac{\text{table feed per gantry rotation}}{\text{beam collimation}} \tag{A.2}$$

The beam collimation is simply the number of slices or sections multiplied by the slice width. For single row detector CT (SDCT) scanning the collimation is equivalent to the slice width. When the pitch is less than one, slices will be overlapped increasing patient dose, while for a pitch greater than one, gaps are produced in the spiral. The advantages of partial scanning along the z-axis with a pitch greater than one are faster scan times and less motion.

MDCT

One of the greatest advances in CT technology occurred in 1998 with the introduction of multiple row detector CT (MDCT) scanners. These scanners have the capability of acquiring multiple slices simultaneously (4, 8, 16, 32, 64, etc.), which better utilises the X-ray beam and optimises the heat loading of the tube. In 2008, the first 320 row MDCT scanner was installed in Australia (Stark, 2008). MDCT scanners are particularly beneficial for paediatric patients, trauma and cardiac imaging due to fast acquisition times (approximately 0.5 second rotation time). The multiple detector rows allow simultaneous measurements, which are reconstructed into multiple slices. MDCT scanners also allow increased scan length for the same scan time. More than 1,000 MDCT scanners had been installed worldwide by the end of the year 2000 (Prokop and Galanski, 2003).

Figure A.6: Fourth generation CT scanner (rotate-stationary).

Figure A.7: Fifth generation electron beam CT (stationary-stationary) (from Kalender (2005)).

Figure A.8: Helical CT scanning with different pitch factors (partially adapted from Goldman (2007b)).

In MDCT scanners the X-ray tube and detector configuration is typically of third generation scanner design. In addition to the multiple detector elements (array) in the scan plane, a bank of solid state detectors is also positioned along the z-axis (Figure A.9). The rows of detectors in the z-direction can be grouped together in various configurations to feed into single data acquisition channels. Technically, the number of data acquisition channels corresponds to each set of data projections. For example, GE "four slice" CT scanners have 16 rows of detectors along the z-axis, but only four data acquisition channels.

The detector configurations fall into three categories: uniform/mosaic/matrix; non-uniform/variable/adaptive; and hybrid. The uniform (or mosaic or matrix) detectors have detector elements of equal dimension (Figure A.10a). These are used in the GE Healthcare (Waukesha, Wisconsin, US) four and eight MDCT scanners and are continuing to find use in newer scanners (Cody and Mahesh, 2007; Flohr et al., 2005). Non-uniform (or variable or adaptive) configurations, initially used by Siemens (Erlangen, Germany) and Philips Healthcare (Andover, Massachusetts, US), increased detector efficiency by reducing the dead space between elements (Figure A.10b). Toshiba Medical Systems (Otawara, Tochigi, Japan) introduced the hybrid configuration used in several scanner designs today (Figure A.10c) (Cody and Mahesh, 2007; Flohr et al., 2005).

One of the major distinctions between SDCT and MDCT is the collimation of the X-ray beam. In both systems the X-ray beam is first collimated by the aperture of the X-ray tube housing. A fixed collimator is then located further away from the aperture, but before the patient, which limits penumbral effects (Section A.2) and defines the beam according to the desired slice width for SDCT or total beam collimation for MDCT. In MDCT the detector width or aperture defines the slice width instead of the pre-patient collimator. In SDCT scanners a post-patient collimator can be used at the detector to achieve very thin slices, which can be a geometric limitation of the design of the pre-patient collimator (Hsieh, 2003). An additional post-patient collimator in the form of an anti-scatter grid made of highly attenuating plates can be located in front of the detector. Both types of post-patient collimation will reduce dose efficiency, but improve image quality.

Over-Beaming

The finite size of the focal spot results in a penumbra at the edges of the X-ray beam with areas of reduced intensity (Figure A.11). With a single row array of detectors in SDCT, the detector extends beyond the beam width so that the entire X-ray beam is used (including the penumbra) to form the image (Figure A.12), unless post-patient collimation is used to better define narrow slice widths (Toth, 2002). In an MDCT system, the full X-ray beam including the penumbra is attenuated by the patient and hence contributes to dose, but the penumbral region does not expose the detectors (Figure A.12). Discarding the periphery of the beam in MDCT ensures uniform irradiation of the bank of detectors, preventing artefacts in the image and allowing three dimensional image reformations. This

Figure A.9: Single row detector CT (SDCT) with only one detector element along the z-axis and an array of detector elements across the patient and multiple row detector CT (MDCT) with multiple detector rows along the z-axis, while still retaining an array across the patient.

Figure A.10: Detector array designs (a) uniform, (b) non-uniform, (c) hybrid (adapted from Cody and Mahesh (2007)).

characteristic of MDCT is known as over-beaming (Heggie et al., 2006). The penumbra of an X-ray beam is constant and hence the "wasted dose" (Flohr et al., 2005; Lewis, 2005) will be greater for a narrow collimation (total beam width), defined by the number of slices multiplied by the slice width.

The dose efficiency of the scanner is a product of the detector efficiency (Section A.1) and the z-axis geometric efficiency. The efficiency along the z-axis is dependent on the amount of the beam used to form the image, which will be affected by post-patient collimation if present and particularly by over-beaming in MDCT scanners. This can be expressed as (Lewis, 2005; Toth, 2002):

$$\text{z-axis geometric efficiency} = \frac{\text{area under z-axis dose profile falling within active detectors}}{\text{area under total z-axis dose profile}} \tag{A.3}$$

Most modern scanners now display the z-axis geometric efficiency on the display console. For one type of 16 MDCT scanner, for example, a beam collimation of 10 mm will have a z-axis efficiency of 83%, while a collimation of 20 mm will have an efficiency of 97% (Lewis, 2005).

Dual Energy CT

A more recent development in CT scanner design is dual energy CT, which is now available for clinical use from several manufacturers. The method of using different CT energies to identify materials was recognised in the seventies, but previously limited by scanner design (Takahashi et al., 2008). The technique exploits the energy dependence of X-ray attenuation in different materials. Typically CT energy pairs of 80 kV_p and 140 kV_p are used (Coursey et al., 2010). Iodine is particularly suited to this technique with a k-edge at 33.2 keV, which maximises the photoelectric effect at the 80 kV_p beam energy (effective beam energy around 45-50 keV). At 140 kV_p, for iodine, the dominant X-ray interaction process is Compton scatter and therefore a distinct difference in the amount of attenuation will be evident. Muscle, for example, has a less distinct attenuation difference between the two different scanning energies (Coursey et al., 2010).

The difference in attenuation of some materials between two energies potentially allows characterisation of elemental composition by using this CT technique. For example, uric acid, iodine and calcium can be distinguished from soft tissue using two energies (Coursey et al., 2010). Uric acid detection in kidney stones has been demonstrated (Primak et al., 2007) and this concept has been extended to the characterisation of uric acid in gout (Bacani et al., 2009). Furthermore, it has been shown that urinary stones can be identified in a contrast scan using the dual energy method to produce an iodine subtracted image (Takahashi et al., 2008). This avoids a non-contrast scan and reduces patient dose as the

Figure A.11: Penumbra with reduced and inhomogeneous intensity caused by a finite focal size compared with a point source (adapted from Johns and Cunningham (1983)).

Figure A.12: For a single row detector array in an SDCT scanner the entire beam is used including the penumbra to generate the image (left). For a multiple rows of detectors in an MDCT scanner the penumbral region of the beam is discarded to ensure the detectors are uniformly irradiated (right).

dual energy scan dose is comparable to the dose for a single energy scan at 120 kV_p. These applications demonstrate the potential of dual energy techniques, although its use is not yet widespread.

Tube Current Modulation

An important technique for dose reduction, now available on most scanners, is the ability to alter the tube current during the CT scan (Gudjonsdottir et al., 2010). In 1981, Haaga et al. (1981) outlined the principle of tube current modulation, which was first introduced commercially by GE Healthcare (Waukesha, Wisconsin, US) in 1994 (McCollough et al., 2006). Techniques for modulating the tube current generally also include an automatic exposure control (AEC) that accounts for the overall patient size (AAPM, 2011). Three methods of modulation techniques are available and most modern scanners use a combination of these. They are typically labelled with proprietary names and are summarised in Table A.2. The three techniques involve algorithms for modulating the tube current based on the patient's size (AEC), angularly (in the x-y plane) or longitudinally (along the z-axis).

Table A.2: Automatic tube current modulation techniques for different manufacturers (AAPM, 2011; Lee et al., 2008b; Lewis, 2005).

Manufacturer	**Proprietary name**	**Modulation adjustment (x, y, z planes)**	**Method for control**	**User input**
Siemens	CARE Dose 4D	x, y, z	Scout and real time	Quality reference mAs
	CARE Dose	x, y		
GE	SmartmA	x, y, z	Scout	Noise index
	AutomA	z		
Philips	D-DOM	x, y	Scout	Reference image
	Z-DOM	z		
Toshiba	^{SURE}Exposure 3D	x, y, z	Scout	Standard deviation
	^{SURE}Exposure	z		

When taking into account the patient's size, the tube current is set to a single value for each patient so as to achieve the same level of noise for every patient regardless of their size. This method utilises the projection radiograph (also referred to as scout view) to determine the modulation required. In earlier systems, it could be achieved manually by the operator adapting the current for each patient based on their size prior to the scan. Using this technique independent of other modulation techniques will result in a single current for the entire scan. Hence, it is typically used in combination with the other modulation techniques.

Longitudinal modulation allows for tube current variations in anatomic regions along the z-axis. This is particularly useful for areas such as the abdomen, which require a higher

current to achieve the same level of noise as other low attenuation areas like the lung. The aim of longitudinal modulation is to achieve relatively uniform image quality and adapts the current to meet a user defined quantity, which is manufacturer dependent. The patient size is generally calculated from a single topogram (scout) view, which is the 2D radiograph taken prior to the actual CT scan.

Angular modulation takes into account the attenuation of photons at different angles through the body in the x-y plane. The current is varied to ensure a uniform photon flux on the detectors from all projections. The modulation typically varies sinusoidally and is based on the topogram view, or in some scanners is modulated in real time from the last 180°of projection data. For lateral projections the current will be higher, while for AP and posterior-anterior (PA) the current will be lower. For example, without modulation, the low attenuation in the AP direction through the shoulders results in a higher detected intensity, whereas the high attenuation provided by the shoulders in the lateral direction results in a lower detected intensity. The consequence of low measured beam intensity is increased image noise due to high statistical fluctuations (quantum noise). Therefore, current in the AP direction can reasonably be reduced, while in the lateral direction increased to maintain constant image noise and reduce dose. The benefits not only relate to dose savings, but also to a reduction in streak artefacts.

A.3 CT Image Formation and Display

Despite the variation in CT scanner and detector design, the same mathematical processes are applied in order to reconstruct the image from the measured data. The linear attenuation coefficient is determined from the detected X-ray beam intensities for each pixel (smallest 2D element in the image) by mathematical reconstruction of the data and displayed accordingly on a grey scale.

The attenuation of a beam of X-ray photons in a material is described by:

$$I = I_0 e^{-\mu t} \tag{A.4}$$

where I is the detected X-ray intensity, I_0 the initial X-ray intensity, μ is the linear attenuation coefficient, and t the absorber thickness. The initial or incident X-ray beam intensity can be determined from routine calibration scans.

When considering a polychromatic beam (as is the case with an X-ray beam) and an inhomogeneous object (human body) this equation becomes:

$$I = \int_0^{E_{\max}} I_0(E) e^{-\int_0^t \mu(E) ds} dE \tag{A.5}$$

The dependence on energy E is apparent and to overcome this each linear attenuation coefficient is normalised to water and scaled to calculate a value displayed on a gray scale. This quantity is referred to as the CT-number in Hounsfield Units (HU):

$$\mathrm{HU} = 1000\frac{\mu_{\mathrm{m}} - \mu_{\mathrm{water}}}{\mu_{\mathrm{water}}} \tag{A.6}$$

where μ_{m} and μ_{water} are the linear attenuation coefficients (measured in inverse centimetres) for the medium and water respectively. The linear attenuation coefficient for water (μ_{water}) is determined periodically by calibration scans of a phantom. A typical CT-number range for clinical use is from –1024 to +3071 HU, (cortical bone is between 600-3000, air is -1000 (Heggie et al., 1997)).

Numerous computational methods exist to calculate the linear attenuation coefficient for each pixel [$\mu(x, y)$]. These are broadly defined into two categories – iterative methods and back projection convolution methods (or equivalent Fourier techniques) (Webb, 1988).

Iterative methods

Iterative methods were utilised initially, but have since been replaced with the filtered back projection technique due to the considerable computation time required. However, there is currently a revival of iterative techniques with a new category of statistical iterative reconstruction methods starting to become available on the market (adaptive statistical iterative reconstruction (ASIR) and model based iterative reconstruction (MBIR), GE Healthcare; iterative reconstruction in image space (IRIS), Siemens; and iDose, Philips Healthcare) (Hara et al., 2009; Marin et al., 2010; Silva et al., 2010).

In the early iterative methods, the values of the linear attenuation coefficients for each pixel were approximated and adjusted iteratively until the calculated projections most closely resembled the measured projections. For a small matrix, the linear attenuation coefficients could be solved exactly using simultaneous equations. For example, Figure A.13 shows that for a 2x2 matrix, the four unknown linear attenuation coefficients (μ_1 - μ_4) can be easily calculated from the four equations.

For larger matrices, an estimate of each pixel value is made and compared with the true ray sum (S_n) until the accuracy reaches an acceptable level. However, for large matrices the computational power required for the substantial data sets still exceeds current capabilities.

Back Projection

The mathematician Johann Radon recognised in 1917 the basic principle that the internal structure of an object can be reconstructed from multiple projections of that object. This

method is commonly referred to as back projection. An infinite number of projections would be required to define the object completely. However, by combining the information from a finite number of projections, an accurate description of the object is possible. This is the premise of image formation in modern CT. The basis of this method is to "smear" the ray sum or line integral back along the same path in the image. As this is carried out for all rays, areas of higher attenuation will be reinforced and the image will begin to take form.

Figure A.14 shows the back projection of the ray sums (S_1 and S_2) in a single projection (P_1) for a simple 2x2 matrix with four pixels, each with a different linear attenuation coefficient (μ_1 - μ_4). As further projections are smeared across the matrix, the pixel values will more accurately reflect their true value.

For an image defined by a map of linear attenuation coefficients $\mu(x, y)$, the Radon transform is a series of line integrals (ray sums) through $\mu(x, y)$ defined by r and θ (e.g. $x = r\cos(\theta)$ and $y = r\sin(\theta)$) to give:

$$R\left[\mu\right](r,\theta) = \int_{-\infty}^{+\infty}\int_{-\infty}^{+\infty} \mu(x,y)\delta(x\cos\theta + y\sin\theta - r)dxdy \tag{A.7}$$

where δ is the Dirac delta function and Figure A.15 shows the co-ordinate system for the Radon transform.

Before reconstruction of the image, a display of the raw data acquired for each slice can be viewed as a sinogram $R(r, \theta)$). Since the sinogram $R(r, \theta)$ is known, the image can be reconstructed by finding $\mu(x, y)$. In order to reconstruct the image, the inverse Radon transform is applied. This effectively back projects the value of each ray sum into all pixels in that ray, as demonstrated in Figure A.14. The combination of all back projections produces an image of the object, which is only an approximation due to the finite number of projections. Heavy blurring will be evident in the reconstructed image and can be seen as a star-like artefact. Increasing the number of projections will improve the image quality, but spokes and blurring will always be apparent using this method.

These artefacts arise from the back projection process itself and are due to the functional dependence on the distance ($1/r$). The blurring can be removed by first filtering the data prior to applying the back projection. This modification of the reconstruction process is referred to as filtered back projection. A one-dimensional Fourier transform is applied to each projection, which is then multiplied by a kernel, before performing an inverse Fourier transform. Note that in the spatial domain the same function can be performed by convolving the spatial domain projection with a convolution kernel. Processing of the data is faster when performed in the frequency domain, hence the necessity of using Fourier transforms. The filtered projection (in the spatial domain) is then back projected onto the image matrix as usual. Various filters can be applied, the most common being a

Figure A.13: Iterative method for calculation of pixel linear attenuation coefficients (adapted from Kalendar (2005)).

Figure A.14: Back projection of two line integrals (S_1 and S_2) from a single projection (P_1). Repeating this process for all projections will eventually calculate the linear attenuation coefficients (μ_1 - μ_4).

Figure A.15: Radon transform.

ramp filter which effectively compensates for the inherent artefacts in the back projection method. Other filters, such as the Shepp-Logan and Hamming, can additionally be used to compensate for the increased noise at higher frequencies.

Helical CT Interpolation

For helical CT, an additional z-axis interpolation processing step is necessary to form a planar data set in the desired reconstruction plane. For SDCT, a planar data set is calculated for each location along the z-axis where data from either side of the reconstructed plane (separated by 360°) are weighted accordingly. This method is referred to as 360°linear interpolation (LI) (Hui, 1999; Kalendar, 2005). Similarly, utilising the redundancy in data from a 360°rotation (each line integral is measured twice as the tube moves around the patient), another method called 180°LI can also be used.

For MDCT, as the number of detector rows increases, the X-ray beam must be considered as a cone beam, rather than a planar 2D fan beam. Generally, scanners with greater than four rows require different reconstruction techniques to account for the cone beam (Kalendar, 2005) and these methods are reviewed in the literature (Flohr et al., 2005). The inherent problem with a wider beam is that objects that are not central to the detector array will be projected onto different detector rows. However, some MDCT scanners can utilise interpolation for narrow beam angles. Another technique called z-filtering is used in MDCT scanners, which uses the interpolation method, but does not restrict the calculation to the adjacent projections only (Flohr et al., 2005; van der Molen and Geleijns, 2007). A selectable width for z-filtering can be chosen retrospectively (Kalendar, 2005).

Over-Ranging

Additional data is acquired at each end of the desired scan volume to allow for interpolation and this results in the patient being exposed to radiation not displayed in the data set. Clinically, if the scan volume is selected to avoid critical (radiosensitive) organs or tissues then these may be inadvertently included. This feature of helical scanning is sometimes referred to as an end effect or over-ranging and typically requires an extra rotation at the start and end of the scan volume (Heggie et al., 2006), although the actual over-range length is also determined by factors such as the reconstruction section width (van der Molen and Geleijns, 2007). The extent of over-ranging depends on the table feed per rotation and will be greater for larger beam collimations and/or higher pitch (Schilham et al., 2010). However, it should be noted that over-ranging and over-beaming offset each other to some extent, since over-beaming is greater for narrow beam collimations (Section A.2). The effects of over-ranging are more pronounced in shorter scan lengths, often encountered in paediatric CT.

Some manufacturers are addressing over-ranging in newer scanners with a dynamic collimator with independent blades that block the over-ranging (Siemens and Philips Health-

care) or a hybrid reconstruction algorithm which allows image reconstruction beyond the conventional imaged volume (GE Healthcare) (Schilham et al., 2010).

Image Display

After reconstruction of the data and calculation of CT-numbers for each pixel, the image still requires digitisation of the information to be displayed in an image format of 2D pixels. A CT image is typically 512x512 pixels for adequate spatial resolution, although this also depends on the reconstructed field of view (Bushberg et al., 2001). For the range of CT numbers, 4096 shades of grey can be used to define each pixel to provide good contrast resolution (Kalendar, 2005). This equates to 12 bits ($4096=2^{12}$) of information per pixel to represent the data in a digital image format. This requires 315 kilobytes (kB) per image and a CT scan made up of a series of images will be many megabytes of data storage.

The human eye can only discern 30-90 shades of grey (Bushberg et al., 2001) and hence computer monitors, which can generally display 256 shades of grey (8 bits), are more than sufficient for viewing CT images. Furthermore, the grey scale range can be adjusted by the user with windowing and levelling. The window width defines the range of CT-numbers that will be allocated a shade of grey, while the level specifies the central CT-number around which the window is displayed. All CT-numbers falling outside of the window will be displayed as black (less than the minimum of the window) or white (greater than the maximum window value). Hence, the complete grey scale is assigned to a desired CT-number interval. Windowing and levelling is an interactive real time tool that can assist with displaying the image.

A.4 CT Image Quality

Optimum image quality is achieved by limiting noise and maximising resolution, both spatial and low contrast. Spatial and low contrast resolution are generally improved at the expense of one another. Therefore, a balance between the two is required without excessively limiting either resolving power. Furthermore, there are many causes of artefact, or systematic discrepancies, in an image. The reduction and/or elimination of these are essential to improving the quality of imaging.

Noise

The noise in an image is primarily due to quantum mottle (number of photons used to construct the image) and is stochastic in nature. Other sources of noise include electronic noise from the detector system and structural noise arising from the reconstruction process, although quantum noise is dominant (Goldman, 2007b). According to Poisson statistics, the quantum noise is quantified by the standard deviation (σ) of photons detected, which

is defined as:

$$\sigma = \sqrt{N} \tag{A.8}$$

where N represents the number of detected photons. The image noise is hence proportional to $1\Big/\sqrt{N}$ and the signal to noise ratio (SNR) is defined as:

$$SNR = \frac{N}{\sigma} = \sqrt{N} \tag{A.9}$$

The noise can be reduced and the SNR improved by increasing the voltage or mAs (either the tube current or the scan time) while all other parameters are held constant. The square root dependence of the SNR is important, since the mAs must increase by a factor of four (large dose increase) to reduce the noise by a factor of two. Increasing the tube voltage will cause more photons to penetrate the patient and hence reach the detector, therefore decreasing the noise. The number of photons can also be increased (and hence the noise reduced) by selecting a thicker slice width.

Spatial Resolution

The ability to resolve small details in an image is a measure of the spatial resolution. The size of detector elements is one of the main limiting factors in the x-y (image) plane. The distance between the centre of each detector element (detector pitch) must be smaller by a factor of two or more than the smallest resolvable detail to ensure that the desired spatial resolution is achieved. The Nyquist frequency (F_N) determines the highest frequency that can be imaged and is represented by:

$$F_N = \frac{1}{2\Delta} \tag{A.10}$$

where Δ is the detector pitch. The detector aperture width will also cause blurring, by averaging the signal over that width. Blurring in the scan plane will additionally result from the penumbra due to the finite size of the focal spot and also from the continuous movement of the focus during the measurement (Hsieh, 2003; Huda and Slone, 2003; Kalendar, 2005).

Undersampling of the X-ray beam can lead to aliasing artefacts in the image and hence a decrease in spatial resolution. This has been addressed with the use of a flying focal spot and/or quarter detector shift. A flying focal spot design shifts the electron beam slightly during the rotation to move the focal position on the anode surface to obtain a separate set of projections offset from the first, which effectively interleaves the projections and increases the sampling rate. The alternative technique involves moving the detector

elements a quarter of a detector width from the central ray, which doubles the sampling rate as the offset equates to half the sampling distance between the ray paths in each 180°rotation.

The number of pixels used to display the image will also affect the spatial resolution. The pixel size is determined by the displayed field of view (FOV). The FOV can be the same as or smaller than the diameter of the field that was used to acquire the image. For a typical 512x512 matrix and a 35 cm displayed FOV, the pixel size is 0.7 mm. Therefore, the size of the FOV used for the reconstructed image will affect the spatial resolution.

Another important factor is the filter selection for reconstruction of the image. A bone algorithm can be used to provide better spatial resolution by accentuating higher frequencies. The use of this filter, however, is offset by the substantial increase in noise. Other filters are available such as a smoothing or soft tissue kernel, which blur the noise and provide better low contrast resolution.

In the z-direction the slice thickness determines the resolution. For SDCT detectors this is generally defined by the beam collimation, while for MDCT scanners it is equivalent to the detector aperture along the z-axis. The profile of the slice would ideally be rectangular, but instead tends to be more Gaussian in shape affecting spatial resolution. Larger slice thickness will decrease overall spatial resolution. However, narrow slices will capture fewer photons and therefore lead to increased noise. When selecting an appropriate slice thickness, the competing influences on spatial and contrast resolution must be taken into account. Furthermore, helical scanning with larger values of pitch, will cause the full width half maximum (FWHM) of the slice profile to increase.

Traditionally spatial resolution in the scan plane was much better than in the longitudinal direction. Detector element spacing in single row scanners was much smaller than the width of the detector in the z-axis direction, providing superior resolution in the scan plane. However, with MDCT scanners thinner slices are achievable and isotropic resolution in each direction is attainable. This allows multi-planar reformatting (MPR) of images in the coronal and sagittal planes and 3D image reconstructions.

Low Contrast Resolution

Low contrast detectability is one of the greatest advantages of CT, particularly compared with conventional radiography. The SNR in the CT images influences the ability to resolve low contrast objects. Contrast is therefore affected by factors contributing to noise in the image. One of the simplest ways of decreasing noise is to increase the mAs. However, this is at the significant cost of increased dose to the patient.

To optimise low contrast resolution, ideally thicker slice width and larger pixel size should be used. These parameters provide better counting statistics in each voxel (volume element) by increasing SNR and allow differentiation between similar attenuation coefficients.

However, the selection of these factors degrades the spatial resolution and a compromise between the two is required depending on the clinical indications and the diagnostic information sought. Low spatial resolution will also obscure small low contrast objects.

The reconstruction algorithm can be used to improve the contrast by using a smooth filter which blurs the noise and hence is useful for imaging soft tissue where low contrast detectability is essential. As discussed previously, better spatial resolution will be achieved using a different filter, such as the bone filter, which enhances noise, but decreases low contrast detectability.

Artefacts

The presence of artefacts can seriously degrade the image quality and may even affect the ability to extract diagnostic information from an image. Even more problematic is the capacity of some artefacts to actually mimic pathology, which may lead to incorrect diagnosis. There are various sources of artefacts in a CT image including those from physics-based processes, from the patient and from the scanner itself and some of these have already been discussed in previous sections. Artefacts will manifest in the reconstructed image as streaks, shading, rings and distortion (Barrett and Keat, 2004). These can be removed by either eliminating or suppressing the source of the artefact or correcting for the effect.

The CT X-ray beam transmitted through a patient is polychromatic, or has a spectrum of energies, and selective attenuation of the lower energy photons occurs as it is transmitted through the patient. Hence, the average photon energy will increase with the distance travelled through the patient. This process is called beam hardening and occurs more through the thicker central parts of the patient. This effect is evidenced in the image by a brighter ring towards the edge of the image and is referred to as a cupping artefact. As previously discussed, a bow-tie filter addresses this issue and correction algorithms can also be used.

Streaking in the image can occur from photon starvation due to high attenuation of the beam. This can occur, for example, in transverse imaging where the shoulders highly attenuate the X-ray beam. This results in an insufficient number of photons reaching the detector and hence very low contrast resolution for these projections. This artefact can be addressed using a modulated tube current (Section A.2). Alternatively a software correction can be applied to smooth the projection above a selected attenuation threshold.

Each voxel is a finite volume and can therefore be composed of more than one tissue type. These will all contribute to the effective attenuation coefficient calculated for that voxel and the resulting CT-number will be a weighted average representing all component tissues. Artefacts arising from this averaging, called the partial volume effect, can easily be overcome by using a thin slice, which is particularly necessary where the anatomy is

changing quickly. However, decreasing the slice width is accompanied by an increase in noise.

Patient based artefacts arise from the presence of metallic objects, such as pacemakers, hip implants, or dental fillings. The CT-number calculated for a metallic object will be outside the possible range as a result of the increased density. This can cause quite significant streaking in the reconstructed image. Apart from attempting to avoid imaging of metallic objects, the artefact can be corrected using a software correction. However, the resulting image will still have limited detail in the area immediately surrounding the metal object.

Patient motion results in streaking and shading and can be due to both voluntary and involuntary motion. Voluntary motion, particularly in paediatric patients, can be reduced by using positioning aids and minimising scanning time or even using a general anaesthetic. Shorter scan times also allow the patient to hold their breath, minimising any motion attributable to the respiratory cycle. Organ movement, particularly the heart, can cause motion artefacts. This motion can be compensated for with software algorithms and placing less weighting on the beginning and end projections which tend to display greatest discrepancies (Barrett and Keat, 2004). With larger, obese patients there is the possibility that they will be outside the limits of the scan plane. This leads to hyperdense artefact areas in the image.

It is evident that the possible sources of artefacts in a reconstructed image are numerous. However, these are generally treated successfully and have a minimal effect on image quality. As Barrett and Keat (2004) state, design features and software corrections can minimise some types of artefacts, but careful patient positioning and optimum selection of scanning parameters are the most important factors in avoiding CT artefacts.

A.5 Formalism for CT Dosimetry

The radiation dose to the patient from a CT examination is dependent on the individual scanner design and geometry, as well as the technical factors used. CT dose quantities have been defined that allow evaluations of scanner and protocol performance. However, these quantities do not represent the dose to an individual patient, but rather are calculated using two standardised polymethyl methacrylate (PMMA) homogeneous phantoms (16 cm and 32 cm diameter) and are intended to be indicative of patient dose. Using standardised measures allows a relative comparison between different protocols on a single scanner or between different scanners by the same or other manufacturers. Furthermore, comparisons can be made between sites and across jurisdictions.

The CT dosimetry formalism based on the CT dose index (CTDI) is the most commonly used today. However, the International Atomic Energy Agency (IAEA) have recently adopted (Einstein et al., 2007b) the terminology detailed by the International Commission

on Radiation Units and Measurement (ICRU) in Report 74 (ICRU, 2005). This uses more precise definitions recognising, for example, that dosimetry measurements are of air kerma rather than absorbed dose (Einstein et al., 2007b). A brief outline of the dosimetry quantities currently displayed on CT scanners follows.

Ideally, the dose profile of a single rotation consisting of N slices or sections with width T, would be rectangular. However, due to scattered radiation and beam divergence (penumbral effect) the profile exhibits tails (Figure A.16). The FWHM of the dose distribution will be greater for larger patients and wider beam collimations due to increased scatter (Kalendar, 2005).

For multiple contiguous rotations of the X-ray tube the tails in each dose profile will contribute to adjacent regions and therefore the peak dose cannot be used as an accurate descriptor of the dose distribution (Figure A.17). Instead, the multiple scan average dose (MSAD) was defined to properly account for the contribution from all scan regions to a central portion of the multiple scan dose profile. The MSAD is typically determined from measurements with thermoluminescence dosimeters (TLDs) and has units of gray (Gy) (one gray is the absorption of one joule (J) of energy per unit mass (kg) of the medium) (Bauhs et al., 2008).

In 1981 the CTDI, which can be measured using a pencil ionisation chamber, was suggested as a measure to approximate the MSAD (Shope et al., 1981). It represents the area under the dose profile as a function of position along the z-axis, $D(z)$, divided by the total beam collimation, which is the number of sections or slices (N) multiplied by the section width (T) in each rotation:

$$\mathrm{CTDI} = \frac{1}{NT}\int_{-\infty}^{+\infty} D(z)dz \tag{A.11}$$

Due to the symmetry of dose deposition from the tails of adjacent rotations, a measurement can be made of a single rotation only, which will be equivalent to the dose in that volume including the contributions from the tails of all adjacent rotations (Goldman, 2007a). This assumes that the measurement device captures the entire tail for the single rotation being measured.

To standardise the quantity so that it is a useful comparative measure and based on the commercial availability of ionisation chambers for the measurement, a variety of CTDI quantities have been suggested. The most commonly used today is the CTDI_{100}, which utilises a 100 mm long ionisation chamber to perform the measurement. It is defined as:

$$\mathrm{CTDI}_{100} = \frac{1}{NT}\int_{-50mm}^{+50mm} D(z)dz \tag{A.12}$$

Figure A.16: Radiation dose distribution for a single X-ray tube rotation showing tails from scattered radiation and beam divergence.

Figure A.17: Radiation dose distribution from multiple adjacent rotations of the X-ray tube showing tails from scattered radiation and beam divergence.

where N is the number of sections/slices acquired per rotation and T is the section thickness, as previously used. Using a 100 mm long ionisation chamber, the CTDI_{100} is measured in air at the isocentre of the scanner for a single rotation centred on the chamber and calculated using:

$$\mathrm{CTDI}_{100} = \frac{fCXL}{NT} \tag{A.13}$$

where f is the conversion factor from exposure to an absorbed dose in air (8.76 mGy/R), C is the calibration factor for the electrometer used with the ionisation chamber, X is the measured exposure in Roentgen (1 R = 2.58 x 10^{-4} C/kg) acquired from a single 360°rotation with beam profile NT, and L is the active length of the ionisation chamber. The L/NT normalisation factor accounts for partial volume irradiation of the ionisation chamber.

For most modern scanners a standard 100 mm pencil ionisation chamber is long enough to intercept the length of both tails in a single profile. However, with fan beams becoming wider in newer scanner designs, this concept is being challenged (Bauhs et al., 2008; Geleijns et al., 2009; Goldman, 2007a).

The dose distribution in the x-y plane depends on the attenuation provided by the patient's body. CT is quite different from plain projection radiography, because of the 360°exposure of the patient. In projection radiography the patient will receive the highest dose proximal to the X-ray tube, whereas in CT the dose will be significantly higher around the entire periphery of the patient. For a CT scan, the dose towards the centre of the body will be approximately half of the dose at the patient's surface due to self-shielding. However, it has been shown that for small phantoms representing paediatric sizes or equivalent to an adult head, the dose is nearly uniformly deposited throughout the phantom (Nickoloff, 2002; Nickoloff et al., 2003).

To take into account the varying depth dose distribution, CTDI measurements are made in PMMA phantoms and weighted to account for the non-uniform dose to the centre. Two standardised phantoms are used representing an adult head (16 cm diameter) and an adult body (32 cm diameter to represent the abdomen). Both phantoms are 15 cm in length. The head phantom can also be used to represent a child's body. Another quantity, the weighted CTDI ($\mathrm{CTDI}_{\mathrm{w}}$), is used to take into account the dose at the periphery ($\mathrm{CTDI}_{100,\mathrm{p}}$) and the centre ($\mathrm{CTDI}_{100,\mathrm{c}}$) of the phantoms. It is an average of the absorbed dose in the x-y plane and is calculated using:

$$\mathrm{CTDI}_{\mathrm{w}} = \tfrac{2}{3}\mathrm{CTDI}_{100,\mathrm{p}} + \tfrac{1}{3}\mathrm{CTDI}_{100,\mathrm{c}} \tag{A.14}$$

These quantities have not taken into account the pitch (P) or spacing of the rotations for

helical scanning as a result of the table feed during each rotation (l). For helical CT, the pitch is defined as in equation A.2 as:

$$P = \frac{\text{table feed per gantry rotation}}{\text{beam collimation}} = \frac{I}{NT} \tag{A.15}$$

A volumetric CTDI (CTDI_{vol}) is used to take account of the pitch and is given by:

$$\text{CTDI}_{\text{vol}} = \frac{\text{CTDI}_{\text{w}}}{\text{P}} \tag{A.16}$$

This parameter is now displayed on all CT consoles and represents an average absorbed dose over the x-y-z planes. However, it does not take into account the length of the scanned region (L) for the entire CT scan. The dose length product (DLP) provides a better indicator of the total amount of radiation deposited in the patient and is typically measured in mGy·cm:

$$\text{DLP} = \text{CTDI}_{\text{vol}} \cdot L \tag{A.17}$$

DLP is displayed with CTDI_{vol} on the control console. They are useful, real time measures for comparing protocols. However, it is important to understand that DLP and CTDI_{vol} reflect the scan parameters used in the protocols and are measured in phantoms. They should not be used for risk assessments (Frush et al., 2003; ICRP, 2007a).

Appendix B

Effective Dose Computation

The mean organ or tissue absorbed dose (D_T) is the mean total energy imparted in a tissue or organ (ε_T) divided by the mass of that organ or tissue (m_T), given by (ICRP, 2007b):

$$D_T = \frac{\varepsilon_T}{m_T} \tag{B.1}$$

Absorbed dose is measured in joules per kilogram ($\mathrm{J{\cdot}kg^{-1}}$) or gray (Gy). The equivalent dose (H_T) is calculated from the mean organ and tissue absorbed doses due to radiation R in organ or tissue T ($D_{T,R}$) by multiplying by a radiation weighting factor (w_R) dependent on the type of radiation, given by (ICRP, 2007b):

$$H_T = \sum_R w_R \cdot D_{T,R} \tag{B.2}$$

For X-ray photons, the radiation weighting factor is one (ICRP, 1991, 2007b). Effective dose is defined as the sum of the equivalent doses in specific organs and tissues weighted by a tissue weighting factor (w_T), which accounts for varying organ radiosensitivity and was defined in ICRP Publication 60 (ICRP 60 (ICRP, 1991)) as:

$$E = \sum_T w_T \cdot H_T = \sum_T w_T \sum_R w_R \cdot D_{T,R} \tag{B.3}$$

such that $\sum w_T = 1$. The values of the tissue weighting factors, from the first ICRP Recommendations (ICRP Publication 26) to the two recent revisions (ICRP Publications 60 and 103) are shown in Table B.1.

ICRP Publication 103 (ICRP 103 (ICRP, 2007b)) later included sex-specific definitions of equivalent dose when calculating these using the hybrid phantom models for Reference

Table B.1: Tissue weighting factors from ICRP Publications 26, 60 and 103 (ICRP, 1977, 1991, 2007b).

Organ or Tissue	ICRP 26	ICRP 60	ICRP 103
Bone marrow (red)	0.12	0.12	0.12
Colon	-	0.12	0.12
Lung	0.12	0.12	0.12
Stomach	-	0.12	0.12
Breast	0.15	0.05	0.12
Remainder Tissues	0.30	0.05	0.12
Gonads	0.25	0.20	0.08
Bladder		0.05	0.04
Oesophagus	-	0.05	0.04
Liver	-	0.05	0.04
Thyroid	0.03	0.05	0.04
Bone surface	0.03	0.01	0.01
Brain	-	-	0.01
Salivary glands	-	-	0.01
Skin	-	0.01	0.01
Total	**1**	**1**	**1**

Male and Female. According to ICRP 103, the effective dose (E) is an average of the dose for males and females, given by (ICRP, 2007b):

$$E = \sum_T w_T \left[\frac{H_T^M + H_T^F}{2} \right] \tag{B.4}$$

where w_T is the tissue weighting factor and H_T^M, H_T^F are the equivalent doses for organs or tissues T of the male and female (M, F) respectively. ICRP 103 includes the prostate in the equivalent dose for males and the uterus/cervix for females. An earlier, different sex-specific effective dose definition was given in ICRP Publication 74 (ICRP, 1996b) as:

$$E = w_{breast} H_{breast,F} + \sum_{T \neq breast} w_T \left[\frac{H_{T,M} + H_{T,F}}{2} \right] \tag{B.5}$$

Some authors (Hunold et al., 2003; Nishizawa et al., 2008; Stamm and Nagel, 2011a) use this definition of effective dose, with Stamm and Nagel (2011a) stating that the contribution of breast dose is not taken into account for males as the stochastic risk is negligible due to the small size of the organ. However, Nagel (2002) also comments that excluding the breast in the calculation of the dose to a male may cause issues if it is not clearly stated and defined, particularly since the tissue weighting factors consequently sum to less than one for males.

The tissue weighting factors are sex- and age-averaged values for the specified tissues

and organs, including the male and female breast and the gonads (testes and ovaries). Therefore, it is stated in ICRP 103 (ICRP, 2007b) that it is not reasonable to treat the contribution of the male and female doses separately when considering effective dose and equation (B.3) should be used. It is pertinent to use equation (B.4) when determining sex-averaged equivalent doses for the effective dose calculation. An analysis of the age-averaging of ICRP 60 tissue weighting factors found that the effective dose did not change considerably if age dependent factors were used (Almen and Mattsson, 1996). However, when calculating effective dose for children, the age-averaging of the tissue weighting factors should be recognised.

The organs included in the effective dose calculation are divided into primary and remainder organs based on epidemiological information regarding radiation induced cancer risk. Table B.2 lists the primary and remainder organs and tissues according to ICRP Publications 26, 60 and 103.

Table B.2: Primary and remainder organs for effective dose computation as listed in ICRP Publications 26, 60 and 103 (ICRP, 1977, 1991, 2007b).

	Primary organs and tissues	**Remainder organs and tissues**
ICRP 26	Red bone marrow, lung, breast, gonads, thyroid, bone surface	The five most highly irradiated other organs and tissues
ICRP 60	Red bone marrow, colon, lung, stomach, breast, gonads, bladder, oesophagus, liver, thyroid, bone surface, skin	Adrenals, brain, upper large intestine, kidney, muscle, pancreas, small intestine, spleen, thymus, uterus
ICRP 103	Red bone marrow, colon, lung, stomach, breast, gonads, bladder, oesophagus, liver, thyroid, bone surface, skin, brain, salivary glands	Adrenals, kidney, muscle, pancreas, small intestine, spleen, thymus, uterus/cervix, extrathoracic (ET) region, gall bladder, heart, lymphatic nodes, oral mucosa, prostate

In ICRP 60 the remainder dose is the weighted average of the equivalent dose of all remainder tissues and organs. However, if a single one of the remainder organs or tissues received an equivalent dose in excess of the highest dose for the non-remainder organs and tissues then a specific weighting factor of 0.025 should be applied to that organ or tissue and a weighting factor of 0.025 applied to the average dose in the rest of the remainder. In ICRP 103, the remainder dose is sex-specific such that the equivalent dose for the remainder (H_{rmd}) for males (M) is given by:

$$H_{rmd}^{M} = \frac{1}{13} \sum_{T}^{13} H_{T}^{M} \tag{B.6}$$

And for females (F) is given by:

$$H_{rmd}^{F} = \frac{1}{13} \sum_{T}^{13} H_{T}^{F} \tag{B.7}$$

where T are the remainder tissues specified in ICRP 103 (ICRP, 2007b). There are 12 common remainder tissues, with the addition of the prostate for males and the uterus/cervix for females.

In ICRP Publication 69 (ICRP, 1995) the ICRP 60 effective dose definition was clarified by the ICRP by removing the upper large intestine from the list of remainder organs as it was already included in the colon in the primary list of organs. The colon equivalent dose was then defined as the mass average of the doses to the upper and lower large intestine of the gastrointestinal tract. Furthermore, the extrathoracic airways were added to the remainder in ICRP Publication 71, although the change to effective dose is negligible (ICRP, 1996b)

In this thesis, equation (B.3) is used to calculate effective dose. The organs and tissues specified in the definition of effective dose according to ICRP 60 (without inclusion of subsequent changes) and the revised recommendations in ICRP 103 are both utilised and indicated accordingly.

Appendix C

Introduction to Thermoluminescence Dosimetry

C.1 Thermoluminescence Dosimetry

One of the most accurate methods for dose measurement is thermoluminescence dosimetry. Thermoluminescence is the property of an insulating (or semiconductor) crystal to emit light when heated after being exposed to ionising radiation. When an insulator absorbs energy during irradiation, some electrons will be raised from the valence band (outer most band filled with electrons) to the conduction band (lowest empty energy band). A positive hole is left in the valence band and most electrons will immediately return to this band and emit visible light via either fluorescence (instantaneous emission) or phosphorescence (delayed emission). Prior to this recombination, the free electron and hole can move independently in their respective bands.

When impurities are added to the crystal, electrons may be caught in traps when moving between the valence and conduction bands. When electrons are trapped in these impurity levels, the material must be stimulated by some form of radiation to release the electron by raising it to the conduction band from where it can return to the valence band. If visible or infra-red stimulation is required the subsequently emitted photon radiation is called optically stimulated luminescence (OSL). When heat is applied, the resulting luminescence is called thermoluminescence. The amount of light measured is proportional to the amount of ionising radiation absorbed by the material. Hence, a measurement of exposure can be made.

Common forms (Cember and Johnson, 2009) of thermoluminescence material include LiF, CaF_2:Mn, $CaSO_4$:Tm, $Li_2B_4O_7$:Cu, LiF:Mg,Ti. These are provided in various forms (Johns and Cunningham, 1983) including powder, rods, or chips and are referred to as thermoluminescence dosemeters (TLDs). Lithium fluoride (LiF, effective atomic number

8.31) is most commonly used for personal dosimetry and medical applications as it has similar characteristics to tissue (effective atomic number 7.64) (Johns and Cunningham, 1983). Its response range is from 10^{-5} Gy to 10^{3} Gy and over such a wide range TLDs can vary in sensitivity. This can be problematic for radiotherapy applications where LiF:Mg,Ti is commonly used. The dose response of the TLD material is linear–supralinear–sublinear, with supralinearity evident above 1 Gy (Moscovitch and Horowitz, 2007). Therefore, it is always necessary to calibrate to a known dose and calculate relative sensitivities.

For reproducibility of measurement, it is essential that a protocol for using TLDs is established and followed closely. Prior to use, TLDs require annealing to remove any residual effects of previous irradiations (Khan, 2003). After irradiation, the TLD is again heated, typically in a TLD reader specifically designed for the purpose. The TLDs are placed in a carousel or on a planchet and heated in the reader to a reproducible temperature at a uniform rate. The light emitted is measured by a photomultiplier tube, which is then converted to an electrical current and amplified. The results produce a glow curve where the area under this curve is proportional to the total dose received by the TLD.

Peaks in the glow curve are representative of the different binding energies of electrons in different trapping sites. By measuring the total light output and calibrating to a known dose of radiation the dose received by each TLD can be calculated. There will be some spontaneous fading of the TLD, since even at room temperature some electrons will fall out of traps to the valence band (Cember and Johnson, 2009).

C.2 Advantages and Disadvantages

Thermoluminescence dosimetry is widely employed in medical dosimetry applications for assessing dose to both patients and occupationally exposed personnel. The tissue equivalence of a range of TLD materials and the various physical forms available provide flexibility in its use (Kron et al., 1999). In addition, due to the small size of some forms of TLD (for example, chips and rods) it is possible to insert TLDs into locations where ion chambers or other types of radiation detectors cannot be used. This may include direct insertion into tissue or cavities of the body (Khan, 2003). It is common for radiotherapy departments to have TLD capabilities for experimental dose assessment (Johns and Cunningham, 1983). TLDs are also used in diagnostic radiology applications (Broadhead et al., 1997; Dong et al., 2002), although less frequently. Due to the small size of a TLD chip they can be used without affecting image quality.

TLD cards are commonly used for personnel dosimetry. TLD materials are sufficiently robust and have minimal fading allowing them to be distributed amongst personnel for a period of time, commonly three months. They are used as a passive dosemeter accumulating dose over the wearing period to provide a cumulative assessment of exposure. Using different filtration materials in the holder for the TLD card allows energy discrim-

ination. One disadvantage compared to a film dosemeter is that an image is not formed. For example, it is simpler to assess on film if the dosemeter has been uniformly directly irradiated or whether an exposure is predominantly attributable to scattered radiation. Ring dosimeters can be utilised for assessing dose to the hands in the laboratory when using unsealed radioactive sources or in some high dose fluoroscopy procedures such as interventional cardiology or angiography where the clinician's hands are close to the primary X-ray beam. One of the disadvantages of TLDs for personnel dosimetry can be the occurrence of spurious signals from contaminants (Al-Haj et al., 2007), although overall they are relatively impervious.

A significant disadvantage of TLD dosimetry is that it is labour intensive and not real time. It is essential that the annealing, including cool down, and read out processes are reproducible to avoid significant systematic errors arising. Furthermore, repeat calibration is necessary to continually assess the effects of the radiation and thermal history of individual TLDs. To some extent, automatic readers have reduced the time involved in reading out TLDs. However, dosimetry with TLDs typically remains a multi-day process.

Despite some limitations thermoluminescence dosimetry remains the gold standard for radiation dosimetry.

C.3 High Sensitivity TLDs

A different type of TLD material is now finding application in lower dose medical dosimetry typical of diagnostic radiology applications. Lithium fluoride doped with magnesium, copper and phosphorous (LiF:Mg,Cu,P) has a much lower detection range and higher sensitivity. The glow curve consists of three low temperature peaks (70-160°C), a main dosimetry peak at about 220°C and a high temperature peak at 300°C (Moscovitch and Horowitz, 2007). Duggan et al. (2004) contend that LiF:Mg,Cu,P is equal to or superior to any other detector used for in vivo dosimetry in the low energy range.

LiF:Mg,Cu,P is 10-35 times more sensitive than conventional TLD material (LiF:Mg,Ti) used for medical dosimetry (Davis et al., 2003; Dong et al., 2002; Glennie, 2003; Kron et al., 1996; Moscovitch and Horowitz, 2007). Additionally, LiF:Mg,Cu,P does not exhibit the supralinearity with dose typical of LiF:Mg,Ti and the signal has minimal short term fading after irradiation (Bos, 2001; Harris et al., 1997; Luo and Rotunda, 2006; Moscovitch and Horowitz, 2007; Olko et al., 1993; Ramlo et al., 2007). The dose response of LiF:Mg,Cu,P is linear–sub-linear, with linearity extending from 1 μGy to 10 Gy (Moscovitch, 1999). As shown in Figure C.1 the energy response is relatively linear (Duggan, 2002; Duggan et al., 2004; Kron et al., 1996), particularly when compared with LiF:Mg,Ti.

The mass energy absorption coefficient ratio for LiF to air increases with decreasing energy in the low keV region (Moscovitch and Horowitz, 2007). As Moscovitch and Horowitz (2007) state, it may be expected that the response of LiF is correspondingly higher in

this region. Furthermore, since both LiF:Mg,Ti and LiF:Mg,Cu,P have the same effective atomic number the response would be expected to be the same (Moscovitch and Horowitz, 2007). This is in fact not the case (Figure C.1). The thermoluminescence response of LiF:Mg,Ti is higher at lower photon energies. Moscovitch and Horowitz (2007) explain that this is due to the supralinearity of LiF:Mg,Ti and the "microscopic dose distribution within photon induced secondary electrons". Without the supralinearity, LiF:Mg,Cu,P response in the lower keV region is lower.

Figure C.1 also shows an under-response of LiF:Mg,Cu,P at about 190 keV, which again is not predicted by the ratio of mass energy absorption coefficients. Olko et al. (1993) confirmed the hypothesis of Pradhan and Bhatt (1989) that the thermoluminescence efficiency of LiF:Mg,Cu,P is directly related to the density of ionisation. In the main CT diagnostic energy range, between 50 and 120 keV, the dominant photon interaction process for low Z elements changes from the photoelectric effect to Compton scattering (Johns and Cunningham, 1983). This is accompanied by a change in the ionisation density resulting from the different secondary electron energies and ranges. Using lineal energy (mean track-averaged linear energy transfer) Olko et al. (1993) showed that there is a maximum in ionisation density in LiF:Mg,Cu,P at about 80 keV, which correlates with a saturation in thermoluminescence response (Moscovitch, 1999). This corresponds with the experimentally identified local minimum in thermoluminescence response (Horowitz and Olko, 2004; Olko et al., 1993, 1994). The theoretical minimum is lower than that found experimentally and modelled by Duggan et al. (2004), who provide a good summary of the range of minimum responses found experimentally (50-190 keV).

Overall, the sensitivity and linear energy and dose response of LiF:Mg,Cu,P in the low keV and dose region make it a suitable choice for dosimetry in diagnostic radiology. Dosimetric studies using the high sensitivity TLD material are starting to emerge in this field (Brisse et al., 2009b; Dong et al., 2002; Duggan et al., 2003; Loubele et al., 2009; Theodorakou and Horrocks, 2003).

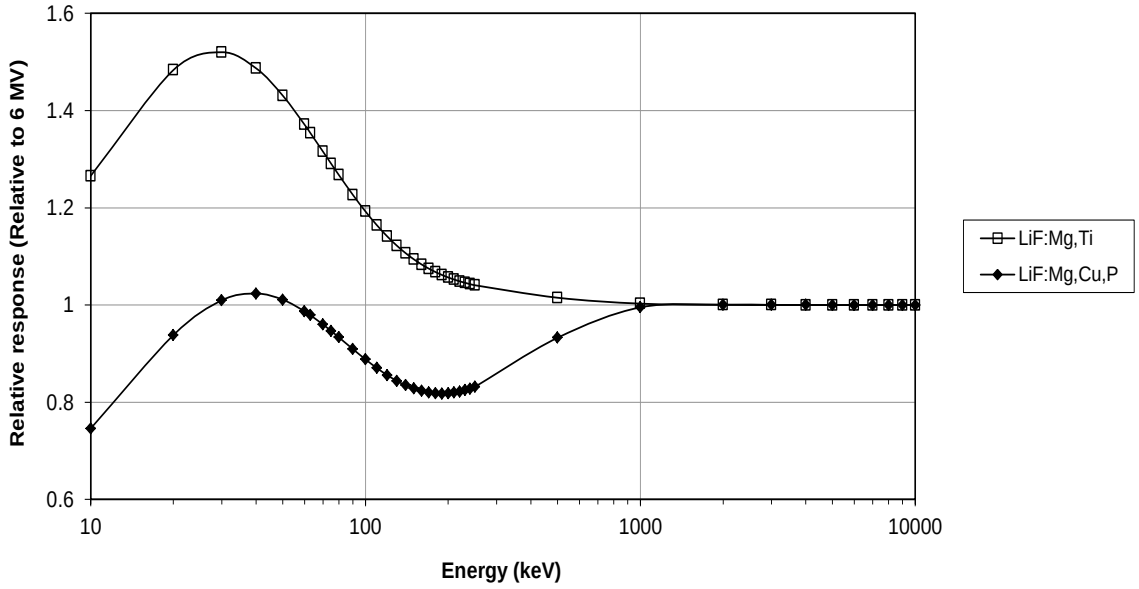

Figure C.1: Energy response for LiF:Mg,Ti and LiF:Mg,Cu,P chips based on energy fit models provided by Duggan et al. (2004).

Appendix D

International Paediatric CT Diagnostic Reference Levels

Table D.1: Comparison between paediatric CT diagnostic reference levels (DRLs) from Europe (2000 (Shrimpton and Wall, 2000) and 2001 (Bongartz et al., 2004; Shrimpton et al., 2005)), the United Kingdom (UK 2003 (Shrimpton et al., 2005, 2006)), Switzerland (2005 (Verdun et al., 2008)), Germany (2006 (Galanski et al., 2007)), and Greece (2009 (Yakoumakis et al., 2009)).

Region	**Age**[a] **(years)**	**$CTDI_{vol}$ (mGy)**[b]				**DLP (mGy·cm)**[b]					
		Europe 2001	**UK 2003**	**Switz. 2005**	**Germany 2006**	**Europe 2000**	**Europe 2001**	**UK 2003**	**Switz. 2005**	**Germany 2006**	**Greece 2009**
Head	0-1 (<1)	31	30	20	33	300	333	270	270	390	
	5 (1-5)	47	45	30	40	600	374	470	420	520	650[d]
	10 (5-10)		50	40	50	750		620	560	710	975
	15 (10-15)	60	65	60	60		1050	930	1000	920	
Chest	0-1 (<1)	12[c]	12	5	3.5	200	156[c]	200	110	55	
	5 (1-5)	12[c]	13	8	5.5	400	152[c]	230	200	110	336[d]
	10 (5-10)		20	10	8.5	600		370	220	210	578
	15 (10-15)	10*	14*	12	6.8*			580*	460	205*	
Abdomen	0-1 (<1)			7	5	170			130	145	
	5 (1-5)			9	8	250			300	255	840[d]
	10 (5-10)			13	13	500			380	475	1120
	15 (10-15)	15*	14*	16	10*			560*	500	500*	

[a] Age groups relate to UK and European DRLs (Bongartz et al., 2004; Shrimpton and Wall, 2000; Shrimpton et al., 2005, 2006). Bracketed age groups are for Switzerland and Germany (Galanski et al., 2007; Verdun et al., 2008).

[b] Calculated values of $CTDI_{vol}$ and DLP for CT on children relate to the 16 cm dosimetry phantom, except for those values marked with an asterisk (*) which relate to the 32 cm dosimetry phantom. Shrimpton et al. (2000) assume that practice for children aged over 10 years will be broadly similar to that for adult patients and hence the adult reference values are used. It is not defined in the Swiss study whether values are in terms of the 16 cm or 32 cm phantom (Verdun et al., 2008). It is assumed, based on the methodology and values obtained that it is the smaller phantom.

[c] Dose data for chest examinations originally referred to the 32 cm dosimetry phantom and have been corrected by multiplication by a factor of about two in order to allow comparison with corresponding data referring to the 16 cm dosimetry phantom, as recommended in NRPB Report 67 (Shrimpton et al., 2005).

[d] Calculated values of DLP use a 12 cm phantom, instead of the 16 cm CT dosimetry phantom, for 5 year olds (Yakoumakis et al., 2009).

Appendix E

Phantom Composition and Dimensions

Table E.1: CIRS Model 706-D anthropomorphic phantom materials (10 year old child) (CIRS, 2006).

	C	**O**	**H**	**N**	**Ca**	**P**	**Mg**	**Cl**	**Al**	**Physical Density (g/cc)**	**Electron Density (x10^{23} g/cc)**
Bone	0.4015	0.3406	0.0507	0.0106	0.1545	0.0000	0.0413	0.0005	0.0000	1.54	4.878
Soft tissue	0.5744	0.2459	0.0847	0.0165	0.0000	0.0000	0.0762	0.0019	0.0000	1.05	3.434
Spinal cord	0.5427	0.2659	0.0736	0.0217	0.0000	0.0000	0.0937	0.0022	0.0000	1.07	3.448
Spinal disks	0.4627	0.3082	0.0675	0.0188	0.0000	0.0000	0.1407	0.0020	0.0000	1.15	3.694
Lung	0.6336	0.2046	0.0832	0.0315	0.0000	0.0000	0.0000	0.0137	0.0329	0.20	0.650
Brain	0.5360	0.2649	0.0816	0.0153	0.0000	0.0000	0.0998	0.0019	0.0000	1.07	3.470

Table E.2: Comparison of elemental composition of CIRS and PCXMC anthropomorphic phantoms of a 10 year old child.

	C	**O**	**H**	**N**	**Ca**	**P**	**Mg**	**Cl**	**Al**	**Physical Density (g/cc)**
Bone (CIRS)	0.4015	0.3406	0.0507	0.0106	0.1545	0.0000	0.0413	0.0005	0.0000	1.54
Skeleton (PCXMC)	0.2548	0.4789	0.0734	0.0306	0.1036	0.0587	-	-	-	1.40
Soft tissue (CIRS)	0.5744	0.2459	0.0847	0.0165	0.0000	0.0000	0.0762	0.0019	0.0000	1.05
Soft tissue (PCXMC)	0.2266	0.6353	0.1045	0.0249	0.0024	0.0077	-	-	-	1.04
Lung (CIRS)	0.6336	0.2046	0.0832	0.0315	0.0000	0.0000	0.0000	0.0137	0.0329	0.20
Lung (PCXMC)	0.1023	0.7575	0.1013	0.0287	0.0024	0.0077	-	-	-	0.296

[a] In PCXMC the number of elements has been reduced from that in Cristy and Eckerman (1987) by grouping the elements Na, Mg, P, S and Cl together and treating them as phosphorus (Tapiovaara and Siiskonen, 2008). All elements of atomic number from that of K or higher have been grouped together and treated as calcium.

Table E.3: Characteristics of CIRS, CT-Expo and PCXMC anthropomorphic phantoms representing children.

	CIRS phantom 10 yo	**CT-Expo phantom 7 yo**	**PCXMC phantom 10 yo**
Weight (kg)	32	22	32
Total height (cm)	140	115	140
Trunk height (cm)	52	43	51
Trunk thickness (cm)	17	18	17
Trunk width (cm) (no arms)	20	33	24
Leg length (cm)	-	51	66

[a] Zankl et al. (1991).
[b] Tapiovaara and Siiskonen (2008).

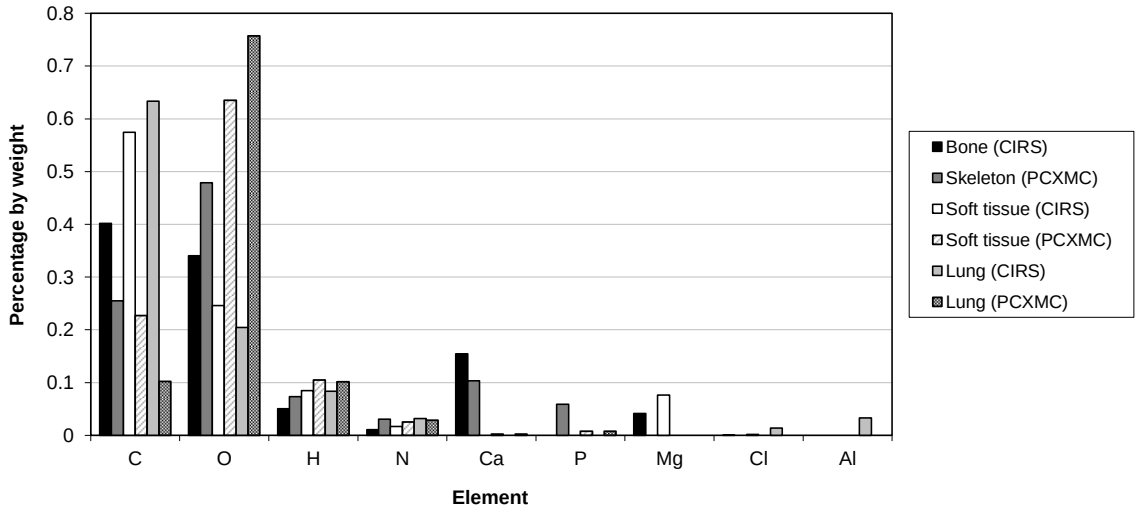

Figure E.1: Comparison of elemental composition of CIRS and PCXMC phantoms of a 10 year old child.

Appendix F

TLD Phantom Measurement Locations

Table F.1: Measurement locations in anthropomorphic phantoms from various studies for determining effective dose.

Organ/Tissue	**This Study**	**Groves et al.**	**Hunold et al.**	**Hurwitz et al.**	**Hollingsworth et al.**	**Kawaura et al.**	**Scalzetti et al.**	**Scalzetti et al. Scaled**[b]
ICRP Publication:	ICRP 60, 103	ICRP 60	ICRP 60	ICRP 60	ICRP 60	ICRP 60	ICRP 60, 103	
Dosimetry Method:	TLD	TLD	TLD	MOSFET	MOSFET	Photodiodes	NA	
Bone marrow (red)	10	1	20	4	5	8		
Colon	4	6	8		1	5	14	7
Lung	10	3	12	2	3	2	34	16
Stomach	6	3	2	2	1	1	13	6
Breast	4	3	2	2	2	1	4	2
Gonads	4	5	8		2	2	4	2
Bladder	3	3	2		1	1	6	3
Oesophagus	3	3	4	2	1	2	3	1
Liver	9	3	2	2	1	2	19	9
Thyroid	2	3	2	2	1	1	2	1
Bone surface	0[c]	3				4[d]		
Brain	6	3					16	8
Salivary glands	2						3	1
Skin	6	3	4			2		
Sub-Total	*69*	*42*	*66*	*16*	*18*	*31*	*118*	*56*

[a] Groves et al. (2004); Hunold et al. (2003); Hurwitz et al. (2007b); Hollingsworth et al. (2007); Kawaura et al. (2006); Scalzetti et al. (2008).

[b] Since the Scalzetti et al. (2008) recommendations for TLD placement is the only reference to address the organs and tissues in ICRP 103 (ICRP, 2007b), the number of measurement locations has been scaled to the number of TLDs available for this thesis to allow comparison.

[c] The absorbed dose to the bone surface was calculated from the bone marrow absorbed dose.

[d] Kawaura et al. (2006) place some photodiodes directly in locations to estimate the bone surface absorbed dose (e.g. ribs), while also using some measurements from the bone marrow (e.g. sternum). In total 10 measurement locations are used to determine the bone surface absorbed dose, with some overlap with the bone marrow measurement locations.

[e] The absorbed dose to the ET region was approximated by the thyroid absorbed dose.

Table F.1: Measurement locations in anthropomorphic phantoms. (continued)

Organ/Tissue	**This Study**	**Groves et al.**	**Hunold et al.**	**Hurwitz et al.**	**Hollingsworth et al.**	**Kawaura et al.**	**Scalzetti et al.**	**Scalzetti et al. Scaled**
ICRP Publication:	ICRP 60, 103	ICRP 60	ICRP 60	ICRP 60	ICRP 60	ICRP 60	ICRP 60, 103	
Dosimetry Method:	TLD	TLD	TLD	MOSFET	MOSFET	Photodiodes	NA	
Remainder Tissues								
Adrenals	2	3		2			2	1
ET region	0[e]							
Gall bladder	2						3	1
Heart	1[f]						8	4
Kidneys	3	3			1		16	8
Lymphatic nodes	0[g]							
Muscle	0[h]	2						
Oral mucosa	0[i]						4	2
Pancreas	2	3					4	2
Prostate	1						2	1
Small intestine	2	3			1	1	16	8
Spleen	2	3		2		1	8	4
Thymus	2	1		2			2	1
Uterus/cervix	2	3				1	2	1
Lens[j]	2						2	1
Sub-Total	*21*	*21*		*6*	*2*	*3*[m]	*69*	*34*
Total in phantom	**90**	**65**[k]	**66**	**22**[l]	**20**	**34**	**187**	**90**

[a] Groves et al. (2004); Hunold et al. (2003); Hurwitz et al. (2007b); Hollingsworth et al. (2007); Kawaura et al. (2006); Scalzetti et al. (2008).

[f] The TLD placed in the heart was also used as a fourth TLD for the oesophagus calculation. The heart is not specified on the CIRS phantom.

[g] The absorbed dose to the lymphatic nodes was approximated by the muscle absorbed dose.

[h] The absorbed dose to the muscle was calculated from the absorbed dose to all soft tissue measured by the TLDs.

[i] The absorbed dose to the oral mucosa was approximated by the salivary glands absorbed dose.

[j] The lens of the eye is not listed by the ICRP (1991; 2007b) as one of the tissues and organs to be considered for stochastic risk. However, it has been included so that deterministic effects can be assessed.

[k] Groves et al. (2004) use a total of 65 TLDs in the phantom. However, they do not individually specify the locations of these. It could only be determined where 63 of these had been placed and these are listed in the Table above.

[l] Hurwitz et al. (2007b) state that a total of 20 MOSFETs were used for effective dose determination. However, the total number for the locations listed in the study is 22.

[m] Kawaura et al. (2006) use some measurement locations from the main organs/tissues to estimate remainder organ absorbed doses. The thymus absorbed dose is approximated from the sternum/clavicles bone marrow absorbed dose; the pancreas absorbed dose is approximated by the transverse colon absorbed dose; and the adrenals and kidney absorbed doses are approximated by one of the liver absorbed dose measurement locations.

Figure F.1: TLD locations shown with white markers on the physical anthropomorphic phantom representing a 10 year old child used for measurements in this thesis.

Appendix G

Factors for Red Bone Marrow and Bone Surface Dosimetry

Table G.1: Active marrow in bone groups expressed as percentage of active marrow in the whole body for different ages (derived from Cristy (Cristy, 1981; Cristy and Eckerman, 1987)).

Skeletal Region	**Percentage of Active Marrow by Mass**	
	10 yo	**40 yo**
Skull (cranium + mandible)	12.72	8.32
Scapulae	2.89	2.85
Clavicles	0.89	0.79
Ribs + sternum	13.02	19.22
Upper spine (cervical vertebrae C1-C5)	1.80	2.66
Middle spine (cervical vertebrae C6-C7 + all thoracic vertebrae)	11.79	17.41
Lower spine (lumbar vertebrae L1-L4)	6.63	9.79
Pelvis (sacrum + os coxae + lumbar vertebra L5 + 50% of upper half of femora)	28.73	33.31
Upper leg (50% of upper half of femora)	4.72	3.35
Middle leg (lower half of femora)	6.14	0
Lower leg (tibiae, fibulae, patellae + ankle and foot bones)	5.51	0
Upper arm (upper half of humeri)	2.49	2.29
Middle arm (lower half of humeri)	1.62	0
Lower arm (radii and ulnae + wrist and hand bones)	1.06	0
Skeleton (total)	100.01	99.99

[a] Highlighted regions indicate the locations selected for bone marrow measurement in the anthropomorphic phantom used in this thesis.

Table G.2: Red bone marrow dose enhancement factors for individual bones weighted over the CT spectrum (derived from King and Spiers (1985)) using the bone matching described in Eckerman and Stabin (2000).

Skeletal Region (RBM Measurement Location)	**Bone Matching**[a]	**Dose Enhancement Factor 9 yo**[b]
Skull	Parietal Bone	0.28
Scapulae	0.6 iliac crest + 0.4 lumbar vertebra L3	0.10
Ribs	Ribs	0.07
Middle spine	0.5 cervical vertebra C4 + lumbar vertebra L3	0.14
Lower spine	Lumbar vertebra L3	0.10
Pelvis	0.6 iliac crest + 0.4 lumbar vertebra L3	0.10

[a] Matching of bone sets in King and Spiers (1985) to the bone measurement locations used in this thesis using the method of Eckerman and Stabin (2000)

[b] For tabulated dose enhancement factors for individual bones, the closest age provided is nine years old, which it is assumed will be very similar to the factors for a 10 year old, the age group considered in this thesis.

Table G.3: Percentage distribution by mass of active marrow (Cristy and Eckerman, 1987), inactive marrow and trabecular bone (Eckerman and Stabin, 2000) in different bones for a 10 year old child.

Skeletal Region	**Percentage Distribution by Mass**		
	Active Marrow in Each Bone to Total Active Marrow	**Inactive Marrow in Each Bone to Total Inactive Marrow**	**Trabecular Bone in Each Bone to Total Trabecular Bone**
Skull (cranium + mandible)	12.72	7.16	5.2
Scapulae	2.89	1.64	0.8
Clavicles	0.89	0.53	0.2
Ribs + sternum	13.02	3.42	2.7
Upper spine (cervical vertebrae C1-C5)	1.80	0.47	11.3
Middle spine (cervical vertebrae C6-C7 + all thoracic vertebrae)	11.79	3.10	25.6
Lower spine (lumbar vertebrae L1-L4)	6.63	1.74	7.3
Pelvis (sacrum + os coxae + lumbar vertebra L5 + 50% of upper half of femora)	28.73	11.87	6.8
Upper leg (50% of upper half of femora)	4.72	3.31	13.1
Middle leg (lower half of femora)	6.14	10.08	14.1
Lower leg (tibiae, fibulae, patellae + ankle and foot bones)	5.51	40.05	5.7
Upper arm (upper half of humeri)	2.49	1.74	2.7
Middle arm (lower half of humeri)	1.62	2.64	2.3
Lower arm (radii and ulnae + wrist and hand bones)	1.06	12.25	2.1
Skeleton (total)	100.01	100	99.9

[a] Highlighted regions indicate the locations selected for bone marrow measurement in the anthropomorphic phantom used in this thesis.

Table G.4: Derived mass of active marrow, inactive marrow and trabecular bone to give total spongiosa mass in different bones for a 10 year old child.

Skeletal Region	**Mass (g)**			
	Active Marrow	**Inactive Marrow**	**Trabecular Bone**	**Spongiosa (Total)**
Skull (cranium + mandible)	80.14	45.11	23.92	149.16
Scapulae	18.21	10.33	3.68	32.22
Clavicles	5.61	3.34	0.92	9.87
Ribs + sternum	82.03	21.55	12.42	115.99
Upper spine (cervical vertebrae C1-C5)	11.34	2.96	51.98	66.28
Middle spine (cervical vertebrae C6-C7 + all thoracic vertebrae)	74.28	19.53	117.76	211.57
Lower spine (lumbar vertebrae L1-L4)	41.77	10.96	33.58	86.31
Pelvis (sacrum + os coxae + lumbar vertebra L5 + 50% of upper half of femora)	181.00	74.78	31.28	287.06
Upper leg (50% of upper half of femora)	29.74	20.85	60.26	110.85
Middle leg (lower half of femora)	38.68	63.50	64.86	167.05
Lower leg (tibiae, fibulae, patellae + ankle and foot bones)	34.71	252.32	26.22	313.25
Upper arm (upper half of humeri)	15.69	10.96	12.42	39.07
Middle arm (lower half of humeri)	10.21	16.63	10.58	37.42
Lower arm (radii and ulnae + wrist and hand bones)	6.68	77.18	9.66	93.51
Skeleton (total)	630	630	460	1720

[a] Highlighted regions indicate the locations selected for bone marrow measurement in the anthropomorphic phantom used in this thesis.

Table G.5: Derived percentage distribution by mass of bone spongiosa in terms of active marrow, inactive marrow and trabecular bone for a 10 year old child.

Skeletal Region	**Percentage Distribution by Mass (to Total Spongiosa in Each Bone)**		
	Active Marrow	**Inactive Marrow**	**Trabecular Bone**
Skull (cranium + mandible)	54	30	16
Scapulae	57	32	11
Clavicles	57	34	09
Ribs + sternum	71	19	11
Upper spine (cervical vertebrae C1-C5)	17	4	78
Middle spine (cervical vertebrae C6-C7 + all thoracic vertebrae)	35	9	56
Lower spine (lumbar vertebrae L1-L4)	48	13	39
Pelvis (sacrum + os coxae + lumbar vertebra L5 + 50% of upper half of femora)	63	26	11
Upper leg (50% of upper half of femora)	27	19	54
Middle leg (lower half of femora)	23	38	39
Lower leg (tibiae, fibulae, patellae + ankle and foot bones)	11	81	8
Upper arm (upper half of humeri)	40	28	32
Middle arm (lower half of humeri)	27	44	28
Lower arm (radii and ulnae + wrist and hand bones)	7	83	10
Skeleton (total)	37	37	27

Table G.6: Percentage distribution by mass of spongiosa and ratio of mass energy absorption coefficients (ICRU, 1992) to tissue for bone measurement locations used in this thesis.

Skeletal Region (RBM Measurement Location)	**Spongiosa Percentage Distribution by Mass**	**Ratio of Mass Energy Absorption Coefficients (Spongiosa/Tissue)**[a]
Skull	9	1.33
Scapulae	2	1.20
Ribs	7	1.19
Middle spine	12	2.54
Lower spine	5	2.03
Pelvis	17	1.19

[a] Spectrum weighted ratio of mass energy absorption coefficients for spongiosa using values for adult red and yellow marrow and values for a 10 year old child for cortical bone.

Appendix H

Tube Current Modulation – Phantom

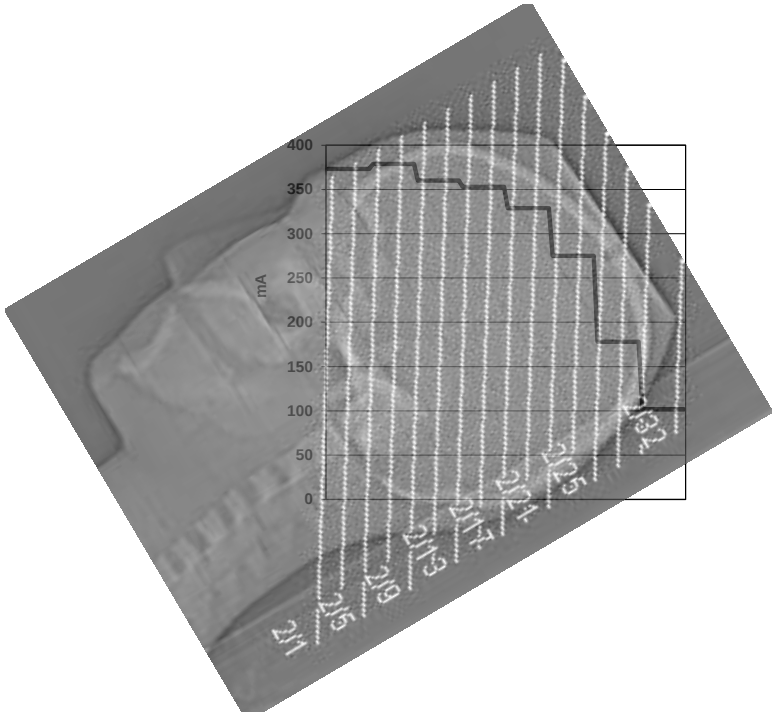

Figure H.1: Modulated tube current for CT brain examination superimposed on a lateral topogram view.

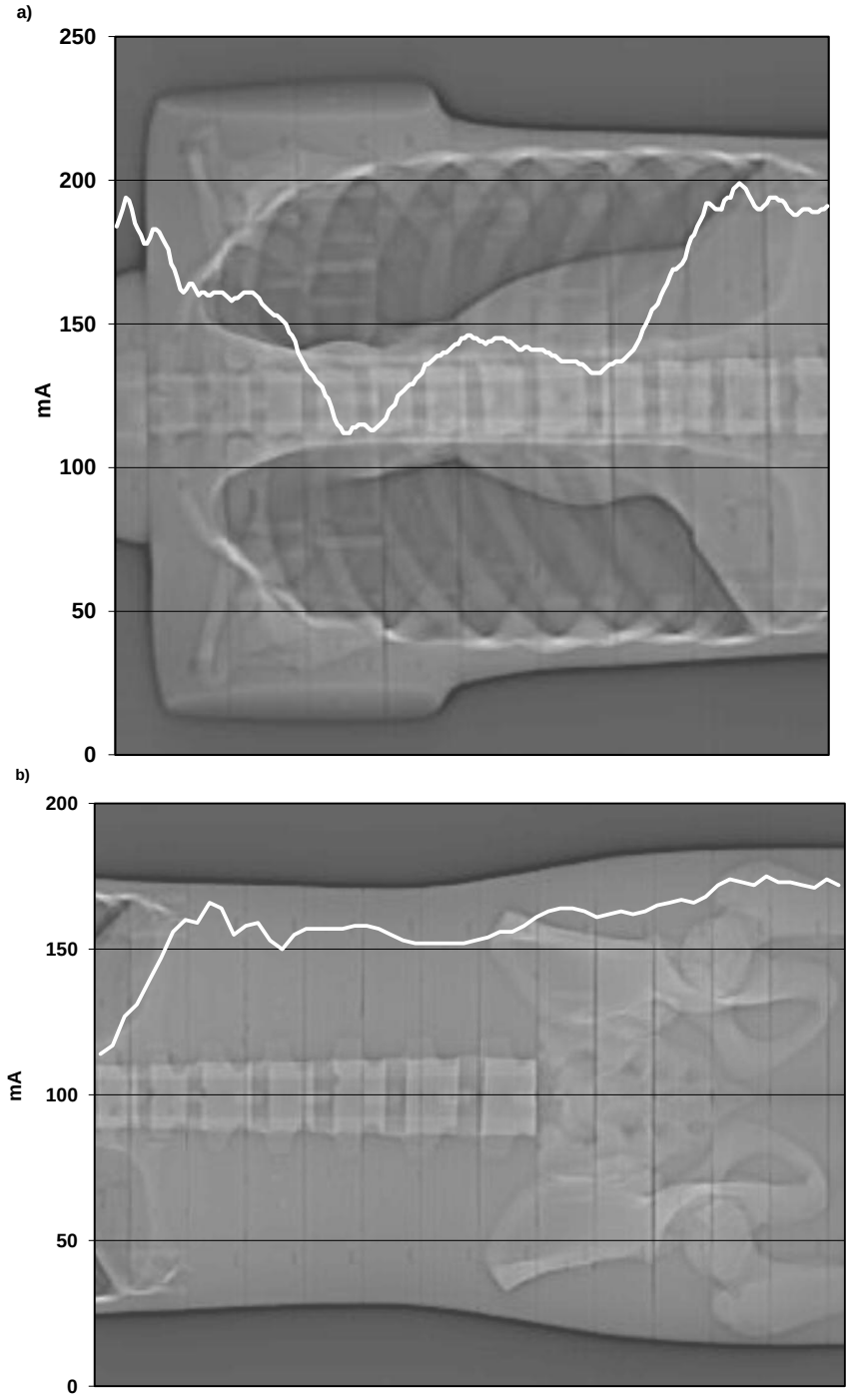

Figure H.2: Modulated tube current for a) CT chest examination and b) CT abdomen/pelvis examination. Both are superimposed on anterior-posterior (AP) topogram views.

Appendix I

Organ and Tissue Absorbed Doses – Phantom

Table I.1: TLD measured organ and tissue absorbed doses in an anthropomorphic phantom of a 10 year old child for a CT brain examination.

Organ/Tissue	**Absorbed Dose (mGy)**[a] **Mean±2σ**	**Absorbed Dose (mGy) Range (Min, Max)**[b]	**Absorbed Dose (mGy)/ 100 mAs**[c]	**Absorbed Dose (mGy)/ $CTDI_{vol}$ (mGy)**[d]
Bone Marrow	6.1±0.3	-	2.7	0.15
Colon	0.026±0.001	(0.012,0.034)	<0.1	<0.01
Lung	0.46±0.02	(0.22,1.15)	0.2	0.01
Stomach	0.068±0.003	(0.044,0.105)	<0.1	<0.01
Breast	0.27±0.01	(0.27,0.28)	0.1	<0.01
Remainder	0.49±0.02	-	0.2	0.01
Gonads	0.0127±0.0006	-	<0.1	<0.01
Bladder	0.0111±0.0006	(0.0087,0.0134)	<0.1	<0.01
Oesophagus	0.48±0.02	(0.16,0.97)	0.2	0.01
Liver	0.118±0.005	(0.070,0.160)	<0.1	<0.01
Thyroid	1.67±0.07	(1.29,2.05)	0.7	0.04
Bone Surface	5.0±0.2	-	2.2	0.13
Brain	33.6±1.4	(25.9,41.2)	14.6	0.84
Salivary Glands	2.7±0.1	(1.6,3.7)	1.1	0.07
Skin	2.0±0.3	(10.5,43.6)	0.9	0.05
Adrenals	0.094±0.005	(0.081,0.108)	<0.1	<0.01
ET Region	1.67±0.07	(1.29,2.05)	0.7	0.04
Gall Bladder	0.054±0.003	(0.045,0.063)	<0.1	<0.01
Heart	0.51±0.02	-	0.2	0.01
Kidney	0.064±0.003	(0.048,0.090)	<0.1	<0.01
Lymph Nodes	0.53±0.02	-	0.2	0.01
Muscle	0.53±0.02	-	0.2	0.01
Oral Mucosa	2.7±0.1	(1.6,3.7)	1.1	0.07
Pancreas	0.084±0.004	(0.061,0.108)	<0.1	<0.01
Prostate	0.0087±0.0007	-	<0.1	<0.01
Small Intestine	0.023±0.001	(0.021,0.024)	<0.1	<0.01
Spleen	0.156±0.007	(0.127,0.186)	<0.1	<0.01
Thymus	0.47±0.02	(0.39,0.55)	0.2	0.01
Uterus / Cervix	0.0126±0.0009	(0.0112,0.0139)	<0.1	<0.01
Eye Lenses	19.3±0.9	(14.0,24.6)	8.4	0.48
Testes	0.0115±0.0007	(0.0111,0.012)	<0.1	<0.01
Ovaries	0.0139±0.0008	(0.0138,0.0141)	<0.1	<0.01

[a] Errors are expressed as two standard deviations of the combined random and systematic errors.
[b] Minimum and maximum measured absorbed doses have been provided for organs and tissues in which multiple TLD measurements were averaged to calculate the absorbed dose.
[c] mAs (actual mAs, not effective mAs) normalised absorbed dose.
[d] $CTDI_{vol}$ (16 cm dosimetry phantom) normalised absorbed dose.

Table I.2: TLD measured organ and tissue absorbed doses in an anthropomorphic phantom of a 10 year old child for a CT chest examination.

Organ/Tissue	**Absorbed Dose (mGy)**[a] **Mean±2σ**	**Absorbed Dose (mGy) Range (Min, Max)**[b]	**Absorbed Dose (mGy)/ 100 mAs**[c]	**Absorbed Dose (mGy)/ CTDI$_{\mathrm{vol}}$ (mGy)**[d]
Bone Marrow	2.4±0.1	-	2.9	0.42
Colon	0.52±0.03	(0.12,1.04)	0.6	0.09
Lung	9.9±0.4	(8.4,11.4)	12.1	1.73
Stomach	4.8±0.2	(1.6,9.8)	5.9	0.83
Breast	9.1±0.4	(8.9,9.3)	11.2	1.59
Remainder	4.4±0.2	-	5.4	0.76
Gonads	0.080±0.004	-	0.1	0.01
Bladder	0.080±0.004	(0.058,0.092)	0.1	0.01
Oesophagus	9.2±0.4	(8.5,10.1)	11.3	1.60
Liver	10.5±0.5	(9.1,11.7)	12.9	1.83
Thyroid	10.9±0.5	(10.4,11.4)	13.4	1.91
Bone Surface	3.4±0.2	-	4.1	0.59
Brain	0.22±0.01	(0.11,0.39)	0.3	0.04
Salivary Glands	1.32±0.06	(0.99,1.66)	1.6	0.23
Skin	1.38±0.09	(6.78,10.21)	1.7	0.24
Adrenals	5.1±0.3	(2.7,7.6)	6.3	0.89
ET Region	10.9±0.5	(10.4,11.4)	13.4	1.91
Gall Bladder	2.7±0.2	(1.8,3.6)	3.4	0.48
Heart	8.6±0.4	-	10.6	1.50
Kidney	1.80±0.09	(0.90,2.83)	2.2	0.31
Lymph Nodes	2.5±0.1	-	3.1	0.45
Muscle	2.5±0.1	-	3.1	0.45
Oral Mucosa	1.32±0.06	(0.99,1.66)	1.6	0.23
Pancreas	6.4±0.3	(3.6,9.1)	7.8	1.12
Prostate	0.057±0.005	-	<0.1	0.01
Small Intestine	0.36±0.02	(0.34,0.37)	0.4	0.06
Spleen	9.2±0.4	(8.5,9.9)	11.3	1.60
Thymus	9.3±0.4	(9.2,9.5)	11.5	1.63
Uterus / Cervix	0.115±0.008	(0.089,0.141)	0.1	0.02
Eye Lenses	0.191±0.009	(0.185,0.197)	0.2	0.03
Testes	0.029±0.003	(0.028,0.029)	<0.1	<0.01
Ovaries	0.131±0.007	(0.128,0.134)	0.2	0.02

[a] Errors are expressed as two standard deviations of the combined random and systematic errors.
[b] Minimum and maximum measured absorbed doses have been provided for organs and tissues in which multiple TLD measurements were averaged to calculate the absorbed dose.
[c] mAs (actual mAs, not effective mAs) normalised absorbed dose.
[d] CTDI$_{\mathrm{vol}}$ (32 cm dosimetry phantom) normalised absorbed dose. These can be divided by a factor of approximately 2 to give absorbed dose normalised to the 16 cm dosimetry phantom.

Table I.3: TLD measured organ and tissue absorbed doses in an anthropomorphic phantom of a 10 year old child for a CT abdomen/pelvis examination.

Organ/Tissue	**Absorbed Dose (mGy)**[a] **Mean±2σ**	**Absorbed Dose (mGy) Range (Min, Max)**[b]	**Absorbed Dose (mGy)/ 100 mAs**[c]	**Absorbed Dose (mGy)/ CTDI$_{vol}$ (mGy)**[d]
Bone Marrow	3.2±0.1	-	4.0	0.71
Colon	8.0±0.4	(6.0,8.6)	9.8	1.75
Lung	4.1±0.2	(0.5,7.5)	5.0	0.90
Stomach	8.9±0.4	(8.6,9.6)	10.9	1.96
Breast	1.29±0.06	(1.26,1.32)	1.6	0.28
Remainder	4.9±0.2	-	6.0	1.08
Gonads	3.7±0.2	-	4.6	0.82
Bladder	6.9±0.3	(6.1,7.8)	8.4	1.51
Oesophagus	3.3±0.1	(0.4,7.0)	4.0	0.72
Liver	8.5±0.4	(7.3,9.8)	10.4	1.87
Thyroid	0.24±0.01	(0.20,0.28)	0.3	0.05
Bone Surface	3.6±0.2	-	4.4	0.78
Brain	0.033±0.001	(0.020,0.051)	<0.1	<0.01
Salivary Glands	0.117±0.005	(0.083,0.151)	0.1	0.03
Skin	1.7±0.1	(7.2,9.4)	2.0	0.36
Adrenals	6.9±0.3	(6.0,7.7)	8.4	1.51
ET Region	0.24±0.01	(0.20,0.28)	0.3	0.05
Gall Bladder	8.6±0.5	(8.2,9.0)	10.5	1.89
Heart	1.02±0.05	-	1.2	0.22
Kidney	8.3±0.4	(8.1,8.4)	10.1	1.81
Lymph Nodes	2.8±0.1	-	3.4	0.61
Muscle	2.8±0.1	-	3.4	0.61
Oral Mucosa	0.117±0.005	(0.083,0.151)	0.1	0.03
Pancreas	8.7±0.4	(8.7,8.7)	10.6	1.90
Prostate	5.8±0.4	-	7.1	1.27
Small Intestine	8.5±0.4	(7.6,9.4)	10.4	1.87
Spleen	7.9±0.4	(7.7,8.0)	9.6	1.73
Thymus	0.81±0.04	(0.64,0.98)	1.0	0.18
Uterus / Cervix	6.6±0.4	(6.2,7.0)	8.1	1.45
Eye Lenses	0.040±0.002	(0.039,0.041)	<0.1	<0.01
Testes	0.99±0.05	(0.90,1.09)	1.2	0.22
Ovaries	6.4±0.3	(6.2,6.7)	7.9	1.41

[a] Errors are expressed as two standard deviations of the combined random and systematic errors.
[b] Minimum and maximum measured absorbed doses have been provided for organs and tissues in which multiple TLD measurements were averaged to calculate the absorbed dose.
[c] mAs (actual mAs, not effective mAs) normalised absorbed dose.
[d] CTDI$_{vol}$ (32 cm dosimetry phantom) normalised absorbed dose. These can be divided by a factor of approximately 2 to give absorbed dose normalised to the 16 cm dosimetry phantom.

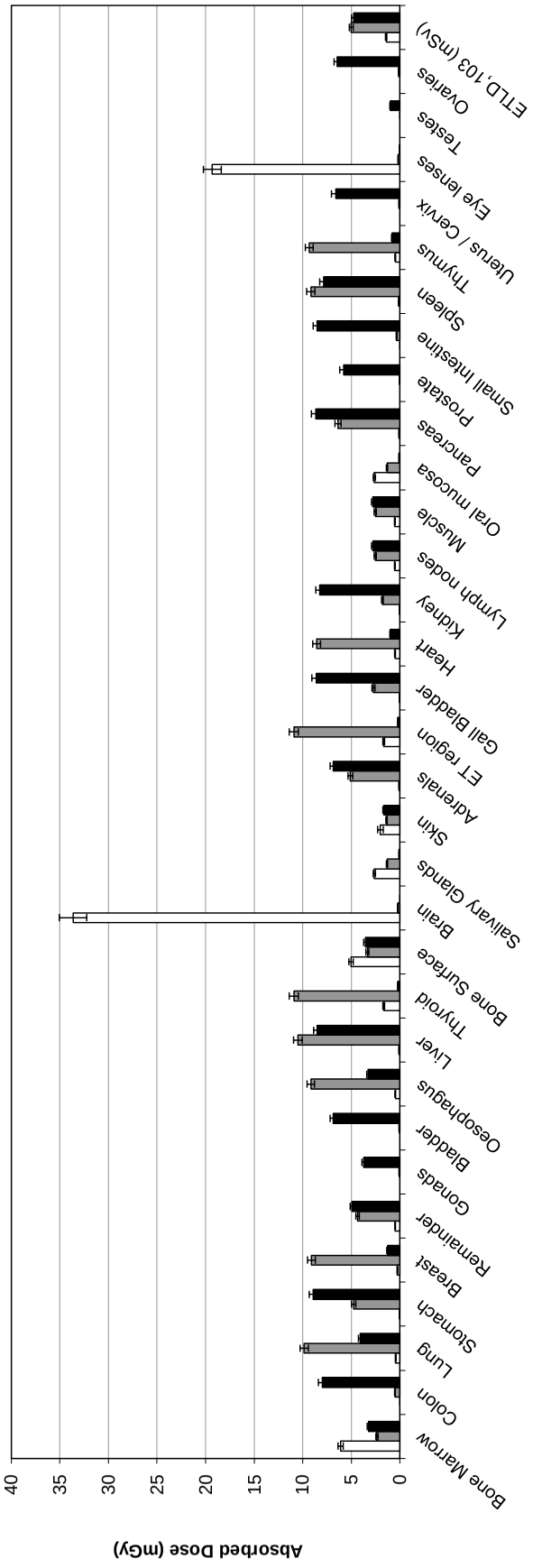

Figure I.1: Mean organ and tissue absorbed doses measured with TLDs loaded in a CIRS anthropomorphic phantom of a 10 year old child for CT brain (white), CT chest (grey) and CT abdomen/pelvis (black) examinations. Effective dose according to the ICRP 103 definition is also shown for each CT examination. Error bars are two standard deviations.

Appendix J

Phantom Scan Regions

Figure J.1: Phantom diagrams with scan lengths indicated for CT brain, chest and abdomen/pelvis examinations. a) physical phantom representing a 10 year old child, b) CT-Expo computational phantom representing a 7 year old child, c) ImPACT computational phantom representing an adult, d) PCXMC computational phantom representing a 10 year old child, e) PCXMC simulated "radiograph" for examination conditions shown in d).

Appendix K

Paediatric Fitting Parameters and Conversion Coefficients

Table K.1: Organ and effective dose normalised to 100 mAs for the ORNL 10 year old and UF 11 year old phantoms as provided in Lee et al. (2007a).

Organ/Tissue	**Head**		**Chest**		**Abdomen**		**Pelvis**	
	ORNL 10 yo	**UF 11 yo**	**ORNL 10 yo**	**UF 11 yo**	**ORNL 10 yo**	**UF 11 yo**	**ORNL 10 yo**	**UF 11 yo**
Testes	0.00	0.00	0.02	0.00	0.07	0.06	11.07	8.23
Bone Marrow	2.11	1.88	3.38	2.63	1.82	2.33	2.94	3.15
Colon	0.00	0.01	0.54	0.45	4.87	6.86	6.97	6.48
Lungs	0.10	0.14	12.63	12.04	1.55	2.96	0.06	0.03
Stomach	0.01	0.03	7.14	5.92	10.59	11.12	0.60	0.17
Urinary bladder	0.00	0.00	0.08	0.02	0.48	0.30	11.25	12.16
Liver	0.01	0.04	7.97	7.21	9.90	10.85	0.46	0.13
Oesophagus	0.10	0.21	10.02	8.99	2.89	3.69	0.09	0.04
Thyroid	0.76	0.5	2.78	5.22	0.07	0.37	0.00	0.01
Skin	1.60	1.72	2.37	1.58	1.43	1.71	1.55	1.74
Bone surface	6.45	8.11	7.09	5.01	2.98	3.59	3.16	5.42
Adrenals	0.01	0.03	9.83	4.94	8.81	9.90	0.22	0.17
Brain	14.65	13.94	0.13	0.10	0.01	0.02	0.00	0.00
ET region	0.76	1.96	2.78	1.33	0.07	0.18	0.00	0.00
SI wall	0.00	0.01	0.64	0.47	5.91	10.26	6.80	4.36
Kidney	0.01	0.02	4.74	2.55	10.88	12.30	0.71	0.33
Muscle	0.07	0.81	4.93	1.78	3.35	2.02	4.44	2.70
Pancreas	0.01	0.02	8.86	2.63	9.19	11.32	0.39	0.31
Spleen	0.02	0.04	8.85	7.53	9.94	11.78	0.36	0.12
Thymus	0.12	0.23	12.68	10.79	0.31	0.59	0.02	0.01
Effective Dose (male)	0.76	0.74	4.42	3.82	3.36	4.05	4.18	3.55

Table K.2: Fitting parameters for estimating organ doses according to equation (5.1) for CT chest examinations as given by Li et al. (2011a).

Organ/Tissue	α_T **(cm^{-1})**	β_T	**Organ/Tissue**	α_T **(cm^{-1})**	β_T
Lungs	-0.050	3.42	Stomach	-0.052	3.20
Heart	-0.041	3.30	Pancreas	-0.101	3.50
Thymus	-0.047	3.36	Small intestine	-0.200	3.96
Thyroid	-0.016	2.76	Large intestine	-0.204	4.01
Breast	-0.038	3.02	Urinary bladder	-0.163	1.01
Oesophagus	-0.047	3.25	Prostate	-0.175	1.19
Trachea-bronchi	-0.045	3.27	Testes	-0.250	1.80
Eyes	-0.179	1.72	Ovaries	-0.157	1.00
Brain	-0.153	1.70	Uterus	-0.152	0.78
Pharynx-Larynx	-0.096	3.50	Vagina	-0.146	0.35
Liver	-0.064	3.39	Residual soft tissue	-0.103	2.88
Gallbladder	-0.126	4.06	Bone surface	-0.082	3.25
Kidneys	-0.091	3.26	RBM	-0.054	2.09
Adrenals	-0.066	3.24	Skin	-0.096	2.34
Spleen	-0.063	3.33			

Table K.3: Exponential regression coefficients for size-corrected, scanner-independent organ absorbed dose estimates according to equation (5.3) for abdominal CT as given by Turner et al. (2011).

Organ/Tissue	A_0	B_0
Liver	3.824	-0.0120
Stomach	3.780	-0.0113
Adrenals	4.029	-0.0128
Kidney	3.969	-0.0124
Pancreas	3.715	-0.0122
Spleen	3.514	-0.0111
Gall Bladder	3.994	-0.0115

Table K.4: Normalised effective dose per dose length product (DLP) coefficients for adults and paediatric patients for several body regions (Shrimpton et al., 2006).

Scan Area	k **(mSv·mGy^{-1}·cm^{-1})**				
	0 yo[a]	**1 yo**[a]	**5 yo**[a]	**10 yo**[a]	**Adult**[b]
Head and neck	0.013	0.0085	0.0057	0.0042	0.0031
Head	0.011	0.0067	0.0040	0.0032	0.0021
Neck	0.017	0.012	0.011	0.0079	0.0059
Chest	0.039	0.026	0.018	0.013	0.014
Abdomen and pelvis	0.049	0.030	0.020	0.015	0.015
Trunk	0.044	0.028	0.019	0.014	0.015

[a] All paediatric conversion coefficients are for DLP values derived from the 16 cm dosimetry phantom.
[b] All adult conversion coefficients are for DLP values derived from the 32 cm dosimetry phantom, except for the head and/or neck which are based on the 16 cm dosimetry phantom.

Table K.5: Normalised effective dose per dose length product (DLP) for adults and paediatric patients for several body regions and ICRP 60 and ICRP 103 (Deak et al., 2010).

Scan Area	k **(mSv·mGy^{-1}·cm^{-1})**				
	Newborn	**1 yo**	**5 yo**	**10 yo**	**Adult**
ICRP Publication 60					
Head[b]	0.0077	0.0047	0.0031	0.0023	0.0016
Neck[b]	0.0228	0.0189	0.0137	0.0107	0.0057
Chest[c]	0.0651	0.0427	0.0291	0.0217	0.0136
Abdomen[c]	0.0817	0.0522	0.0354	0.0249	0.0155
Pelvis[c]	0.0876	0.0564	0.0380	0.0283	0.0167
ICRP Publication 103					
Head[b]	0.0085	0.0053	0.0035	0.0027	0.0019
Neck[b]	0.0206	0.0166	0.0120	0.0094	0.0051
Chest[c]	0.0706	0.0467	0.0314	0.0234	0.0145
Abdomen[c]	0.0804	0.0514	0.0349	0.0246	0.0153
Pelvis[c]	0.0672	0.0431	0.0294	0.0216	0.0129

[a] All conversion coefficients are for an X-ray tube voltage of 120 kV_p.
[b] For head and neck regions, the conversion coefficients are for DLP values derived from the 16 cm dosimetry phantom.
[c] For all body regions for both adults and children, the conversion coefficients are for DLP values derived from the 32 cm dosimetry phantom.

Table K.6: Fitting parameters for calculating size-dependent DLP conversion coefficients according to equation (5.5) (Chapple et al., 2002).

Scan Area	$\mathbf{y_0}$ **(mSv·mGy^{-1}·cm^{-1})**	$\mathbf{A_1}$ **(mSv·mGy^{-1}·cm^{-1})**	$\mathbf{t_1}$ **(cm)**
Head	0.00351	0.877	14.2
Chest	0.00736	0.272	4.07
Abdomen	0.00832	0.811	2.87
Pelvis	-0.0419	0.114	25.3

[a] Conversion coefficients derived using these fitting parameters and equation (5.5) are for DLP values derived from the 16 cm dosimetry phantom.

Table K.7: Normalised effective dose per weighted CTDI ($CTDI_w$) for adults and paediatric patients for several body regions (Shrimpton, 2004).

Scan Area	k_w **(mSv·mGy^{-1})**				
	0 yo[a]	**1 yo**[a]	**5 yo**[a]	**10 yo**[a]	**Adult**[b]
Head and neck	0.173	0.153	0.113	0.0880	0.0707
Head	0.0882	0.0735	0.0526	0.0417	0.0278
Neck	0.0869	0.0812	0.0769	0.0632	0.0591
Chest	0.354	0.316	0.284	0.264	0.383
Abdomen and pelvis	0.632	0.568	0.499	0.458	0.659
Trunk	0.967	0.853	0.769	0.708	1.03

[a] All paediatric conversion coefficients are for $CTDI_w$ values derived from the 16 cm dosimetry phantom.

[b] All adult conversion coefficients are for $CTDI_w$ values derived from the 32 cm dosimetry phantom, except for the head and/or neck which are based on the 16 cm dosimetry phantom.

Appendix L

RCH Patient Dose Survey – CT Examination Parameters

Table L.1: Set examination parameters and mean values for tube current, scan length, $CTDI_{vol}$ and DLP from a survey of patient records for typical CT examinations.

Examination	Age Group[a]	Set Parameters						Scan Values (Mean)			
		kV_p	Q_{ref}[b] (mAs)	Rotation time (s)	Pitch	Detector Configuration	Beam Collimation (mm)	Effective mAs[b]	Scan Length (cm)	$CTDI_{vol,16}$[c] (mGy)	DLP_{16}[c] (mGy·cm)
CT Brain	**0-6 m**	120	150	0.75	axial	12x1.5 mm	18	91	12.7	17.07	217
	6 m-3 y	120	150	0.75	axial	12x1.5 mm	18	105	14.4	19.43	281
	3-6 y	120	200	0.75	axial	12x1.5 mm	18	159	14.5	29.98	435
	6-10 y	120	240	0.75	axial	12x1.5 mm	18	212	15.3	39.76	608
	>10 y	120	270	0.75	axial	12x1.5 mm	18	235	15.3	44.35	679
	Combined	**120**	**-**	**0.75**	**axial**	**12x1.5 mm**	**18**	**160**	**14.4**	**30.12**	**444**
CT Chest	**<5 y**	80	65	0.5	1	16x1.5 mm	24	65	18.8	2.98	57
	5-10 y	100	80	0.5	1	16x1.5 mm	24	109	28.7	10.31	296
	>10 y	120	80	0.5	1	16x1.5 mm	24	157	34.6	22.90	799
	Combined	**-**	**-**	**0.5**	**1**	**16x1.5 mm**	**24**	**110**	**27.4**	**12.06**	**384**
CT	**<5 y**	80	80	0.5	1.25	16x1.5 mm	24	72	32.0	3.30	107
Abdomen/	**5-10 y**	100	80	0.5	1.25	16x1.5 mm	24	103	39.6	9.62	384
Pelvis	**>10 y**	120	60	0.5	1.25	16x1.5 mm	24	102	46.9	14.92	702
	Combined	**-**	**-**	**0.5**	**1.25**	**16x1.5 mm**	**24**	**92**	**39.5**	**9.28**	**398**

[a] Age groups are defined in terms of months (m) or years (y).

[b] Q_{ref} is the Imaging Quality Reference mAs, which is a Siemens specific setting used for automatic tube current modulation (CARE Dose 4D), which is set by the user for each protocol. This value is adjusted based on image quality requirements and the amount of noise acceptable in the image. It is defined in terms of the effective mAs (actual mAs divided by pitch).

[c] Dose indicators for CT chest and abdomen/pelvis examinations were displayed on the CT scanner as $CTDI_{vol,32}$ and DLP_{32}. These have been multiplied by a factor of 2.08 according to the methodology of Huda et al. (2010) to give $CTDI_{vol,16}$ and DLP_{16}. The dose indicators for the CT brain examinations were already displayed in terms of $CTDI_{vol,16}$ and DLP_{16} and therefore do not require correction.

Appendix M

RCH Patient Dose Survey – Age and Gender Demographics

Table M.1: Gender and age distribution for patients included in the RCH dose survey.

Category	CT Brain						CT Chest				CT Abdomen/Pelvis			
	0-6 m	**6 m-3 y**	**3-6 y**	**6-10 y**	**>10 y**	**Total**	**<5 y**	**5-10 y**	**>10 y**	**Total**	**<5 y**	**5-10 y**	**>10 y**	**Total**
	No.(%)	**No.(%)**	**No.(%)**	**No.(%)**	**No.(%)**	**No.(%)**	**No.(%)**	**No.(%)**	**No.(%)**	**No.(%)**	**No.(%)**	**No.(%)**	**No.(%)**	**No.(%)**
All	20 (100)	20 (100)	20 (100)	20 (100)	20 (100)	100 (100)	20 (100)	20 (100)	20 (100)	60 (100)	20 (100)	20 (100)	20 (100)	60 (100)
Sex														
Male	10 (50)	12 (60)	12 (60)	15 (75)	12 (60)	61 (61)	11 (55)	17 (85)	10 (50)	38 (63)	10 (50)	12 (60)	14 (70)	36 (60)
Female	10 (50)	8 (40)	8 (40)	5 (25)	8 (40)	39 (39)	9 (45)	3 (15)	10 (50)	22 (37)	10 (50)	8 (40)	6 (30)	24 (40)
Age														
0 y	20 (100)	4 (20)				24 (24)	5 (25)			5 (8)	2 (10)			2 (3)
1 y		12 (60)				12 (12)	9 (45)			9 (15)	5 (25)			5 (8)
2 y		3 (15)	1 (5)			4 (4)	3 (15)			3 (5)	4 (20)			4 (7)
3 y		1 (5)	6 (30)			7 (7)	1 (5)			1 (2)	6 (30)			6 (10)
4 y			7 (35)			7 (7)	0 (0)			0 (0)	2 (10)			2 (3)
5 y			5 (25)			5 (5)		2 (10)		2 (3)	1 (5)	3 (15)		4 (7)
6 y			0 (0)	0 (0)		0 (0)		3 (15)		3 (5)		5 (25)		5 (8)
7 y			1 (5)	2 (10)		3 (3)		5 (25)		5 (8)		1 (5)		1 (2)
8 y				5 (25)		5 (5)		3 (15)		3 (5)		4 (20)		4 (7)
9 y				8 (40)		8 (8)		5 (25)		5 (8)		6 (30)		6 (10)
10 y				4 (20)		4 (4)		2 (10)	1 (5)	3 (5)		1 (5)	1 (5)	2 (3)
11 y				1 (5)	4 (20)	5 (5)			2 (10)	2 (3)			2 (10)	2 (3)
12 y					5 (25)	5 (5)			0 (0)	0 (0)			0 (0)	0 (0)
13 y					4 (20)	4 (4)			2 (10)	2 (3)			4 (20)	4 (7)
14 y					0 (0)	0 (0)			3 (15)	3 (5)			3 (15)	3 (5)
15 y					4 (20)	4 (4)			4 (20)	4 (7)			4 (20)	4 (7)
16 y					1 (5)	1 (1)			4 (20)	4 (7)			3 (15)	3 (5)
17 y					2 (10)	2 (2)			3 (15)	3 (5)			3 (15)	3 (5)
18 y					0 (0)	0 (0)			1 (5)	1 (2)			0 (0)	0 (0)

[a] Age groups are defined in terms of months (m) or years (y).

Appendix N

Comparison of Doses for Typical Paediatric CT Examinations

Table N.1: Comparison of measured organ and tissue absorbed doses from this thesis with values in the literature.

	CT Brain		**CT Chest**			**CT Abdomen/ Pelvis**	**CT Abdomen**
	This Study	**Brenner et al.**[a]	**This Study**	**Fujii et al.**[b]	**Coursey et al.**[c]	**This Study**	**Brenner et al.**[a]
CT Scanner	Siemens Sensation 16	-	Siemens Sensation 16	Siemens Sensation 16	GE LightSpeed 16	Siemens Sensation 16	-
Device/Method	TLD	Survey[a]	TLD	Photodiode	MOSFET	TLD	Survey[a]
Phantom Age (years)	10	10	10	6	5	10	10
Tube voltage (kV_p)	120	-	120	120	120	120	-
Dose Modulation	Care Dose 4D	-	Care Dose 4D	Care Dose 4D	None	Care Dose 4D	-
Current x time (mAs)	259	462 (340)[a]	78	51	33	80	404 (240)[a]
Tube rotation time (s)	0.75	-	0.5	0.5	0.5	0.5	-
Beam collimation (mm)	18	-	24	24	20	24	-
Pitch	axial	-	1	1.125	1.375	1.25	-
Scanned length (cm)	16	11	27	20	-	37	14
Organ/Tissue				**Absorbed Dose (mGy)**			
Stomach	0.07	-	4.8	2.9	3.7	8.9	30 (18)[a]
Colon	0.03	-	0.52	0.4	-	8.0	9 (5)[a]
Liver	0.12	-	10	5.7	4.0	8.5	28 (16)[a]
Lung	0.46	-	9.9	7.5	4.3	4.1	-
Breast (Females)	0.27	-	9.1	6.5	4.0	1.3	-
Uterus (Females)	0.01	-	0.12	-	-	6.6	-
Ovary (Females	0.01	-	0.13	0.1	-	6.5	10 (6)[a]
Prostate (Males)	0.01	-	0.06	-	-	5.8	-
Bladder	0.01	-	0.08	0.1	-	6.9	-
Brain	34	50 (35)[a]	0.22	0.1	-	0.03	-
Bone Marrow	6.1	5 (5)[a]	2.4	2.4	3.6	3.2	8 (4)[a]

[a] Brenner et al. (2001a) obtained paediatric organ absorbed doses by scaling adult organ absorbed doses reported in a 1989 British survey (Shrimpton et al., 1991) by relative age-dependent changes in effective dose estimated by Huda et al. (1997). Although this method has inherent problems for estimating specific absorbed doses, including averaging over 120 different scanners, they are listed here as the risk estimates calculated by Brenner et al. (2001a) are quoted frequently in the literature (cited 929 times by 22 May 2010). Values in brackets in the Table are from a newer study by Brenner et al. (2007) based on a US survey (CRCPD, 2006) from 2000.

[b] Fujii et al. (2007).

[c] Coursey et al. (2008).

Appendix O

Cancer Incidence and Mortality Risks

Table O.1: Natural male and female cancer incidence and mortality risks compared with those from CT radiation exposure at 10 years of age, expressed as a percentage risk.

Cancer Site	Incidence					Mortality				
	Australia[a]	ICRP 103[b]	This Study[c]			Australia[a]	ICRP 103[b]	This Study[c]		
			CT Brain	CT Chest	CT AP[d]			CT Brain	CT Chest	CT AP[d]
Males										
Stomach	1.37%	1.71%	0.0000%	0.0026%	0.0049%	0.69%	1.05%	0.0000%	0.0014%	0.0027%
Colon	4.74%	3.74%	0.0001%	0.0013%	0.0193%	1.29%	1.67%	0.0000%	0.0006%	0.0094%
Liver	0.84%	0.64%	0.0001%	0.0045%	0.0037%	0.73%	0.51%	0.0000%	0.0033%	0.0026%
Lung	6.25%	7.76%	0.0010%	0.0213%	0.0089%	4.90%	6.81%	0.0010%	0.0216%	0.0090%
Prostate	17.1%	-	0.0000%	0.0000%	0.0039%	2.74%	-	0.0000%	0.0000%	0.0007%
Bladder	1.85%	3.61%	0.0000%	0.0001%	0.0103%	0.58%	0.74%	0.0000%	0.0000%	0.0022%
Thyroid	0.35%	0.20%	0.0008%	0.0055%	0.0001%	0.05%	-	-	-	-
Leukaemia	1.50%	1.28%	0.0073%	0.0028%	0.0039%	0.85%	0.69%	0.0043%	0.0017%	0.0023%
All Cancers[f]	41.7%	49.2%	0.0206%	0.0598%	0.0712%	18.8%	21.2%	0.0099%	0.0372%	0.0353%
Females										
Stomach	0.74%	1.02%	0.0000%	0.0034%	0.0064%	0.47%	0.68%	0.0000%	0.0020%	0.0037%
Colon	5.00%	3.98%	0.0000%	0.0008%	0.0126%	1.25%	1.79%	0.0000%	0.0004%	0.0058%
Liver	0.37%	0.40%	0.0000%	0.0021%	0.0017%	0.39%	0.36%	0.0000%	0.0018%	0.0015%
Lung	4.17%	4.75%	0.0023%	0.0497%	0.0207%	3.23%	3.94%	0.0020%	0.0436%	0.0181%
Breast	11.1%	12.6%	0.0019%	0.0649%	0.0092%	2.63%	3.40%	0.0005%	0.0152%	0.0022%
Uterus	1.92%	-	0.0000%	0.0000%	0.0024%	0.11%[d]	-	0.0000%	0.0000%	0.0005%
Ovary	1.30%	2.12%	0.0000%	0.0001%	0.0047%	0.93%	1.23%	0.0000%	0.0001%	0.0025%
Bladder	0.70%	1.29%	0.0000%	0.0001%	0.0104%	0.29%	0.37%	0.0000%	0.0000%	0.0030%
Thyroid	1.06%	0.49%	0.0046%	0.0300%	0.0007%	0.07%	-	-	-	-
Leukaemia	1.15%	0.99%	0.0053%	0.0020%	0.0028%	0.66%	0.59%	0.0032%	0.0013%	0.0017%
All Cancers[f]	33.3%	44.4%	0.0284%	0.1804%	0.0910%	16.7%	19.3%	0.0117%	0.0757%	0.0471%

[a] Natural cancer incidence and mortality risks for the Australian population in 2006 are provided by the Australian Institute of Health and Welfare (AIHW, 2008a, 2009). The average life expectancy for Australian men and women is 79 and 84 years respectively (ABS, 2008b). The AIHW provides risks to attained age of 75 years or 85 years. The risks in the above Table for men are an average of the risks to attained age 75 years and 85 years and for women the risks are for an attained age of 85 years. [b] Male and female Euro-American cancer incidence and mortality annual rates are provided by age (five year brackets) and cancer site in ICRP 103 (2007b). Risks were summed for each age group to 79 years for men and to 84 years for women (ABS, 2008b). The risks in each five year age interval were assumed constant. [c] Cancer incidence and mortality risks for this thesis were calculated based on site-specific organ doses measured with TLDs (Chapter 3) multiplied by the site- and sex-specific BEIR VII Lifetime Attributable Risks (LAR) for exposure at 10 years (NRC, 2006). [d] CT AP = CT Abdomen/Pelvis. [e] Mortality risk for uterine cancer in Australia in 2006 from the AIHW's Ovarian Cancer Overview (AIHW, 2010). [f] "All cancers" includes solid cancers and leukaemia listed in the Table above as well as "other" solid cancers not listed. [g] Natural cancer incidence and mortality risks are given to two significant figures <1% and three significant figures for risks ≥1%. Risks from CT examinations are given to four decimal places (precision below one in a million is unnecessary).

Table O.2: Natural male and female cancer incidence and mortality risks compared with those from CT radiation exposure at 10 years of age. Risk is expressed in terms of the number of people in the population for whom one will develop non-radiation related cancer (Australia and ICRP columns) and the number of patients undergoing CT scans that would lead to the development of one radiation-induced cancer.

Cancer Site	**Incidence**					**Mortality**				
	Australia[a]	ICRP 103[b]	This Study[c]			Australia[a]	ICRP 103[b]	This Study[c]		
			CT Brain	CT Chest	CT AP[d]			CT Brain	CT Chest	CT AP[d]
Males										
Stomach	73	59	2,677,100	38,100	20,300	100	96	4,908,100	69,900	37,300
Colon	0	27	1,570,600	79,600	5,200	78	60	3,235,100	163,900	10,700
Liver	100	200	1,969,200	22,200	27,300	136	200	2,731,400	30,800	37,800
Lung	16	13	101,400	4,700	11,300	20	15	100,000	4,600	11,100
Prostate	6	-	17,211,100	2,618,700	25,800	37	-	96,095,500	14,620,900	144,100
Bladder	54	28	6,006,900	837,100	9,700	200	100	28,157,500	3,924,000	45,500
Thyroid	300	500	119,800	18,300	828,200	1,900	-	-	-	-
Leukaemia	67	78	13,600	35,100	25,700	100	100	23,000	59,300	43,400
All Cancers[f]	2	2	4,900	1,700	1,400	5	5	10,100	2,700	2,800
Females										
Stomach	100	98	2,045,000	29,100	15,500	200	100	3,591,300	51,200	27,300
Colon	20	25	2,395,600	121,400	7,900	80	56	5,185,000	262,700	17,100
Liver	300	300	4,233,700	47,700	58,600	300	300	4,980,800	56,100	69,000
Lung	24	21	43,500	2,000	4,800	31	25	49,500	2,300	5,500
Breast	9	8	51,400	1,500	10,900	38	29	219,100	6,600	46,400
Uterus	52	-	22,071,500	2,411,200	42,000	1,000[e]	-	99,321,600	10,850,500	189,200
Ovary	77	47	9,833,100	1,045,300	21,200	100	81	18,405,600	1,956,500	39,800
Bladder	100	100	5,927,900	826,100	9,600	300	300	20,954,400	2,920,200	33,900
Thyroid	94	200	21,800	3,300	150,600	1,300	-	-	-	-
Leukaemia	87	100	19,000	49,000	35,900	200	200	30,800	79,400	58,200
All Cancers[f]	3	2	3,500	600	1,100	6	5	8,500	1,300	2,100

[a] Natural cancer incidence and mortality risks for the Australian population in 2006 are provided by the Australian Institute of Health and Welfare (AIHW, 2008a, 2009). The average life expectancy for Australian men and women is 79 and 84 years respectively (ABS, 2008b). The AIHW provides risks to attained age of 75 years or 85 years. The risks in the above Table for men are an average of the risks to attained age 75 years and 85 years and for women the risks are for an attained age of 85 years. [b] Male and female Euro-American cancer incidence and mortality annual rates are provided by age (five year brackets) and cancer site in ICRP 103 (2007b). Risks were summed for each age group to 79 years for men and to 84 years for women (ABS, 2008b). The risks in each five year age interval were assumed constant. [c] Cancer incidence and mortality risks for this thesis were calculated based on site-specific organ doses measured with TLDs (Chapter 3) multiplied by the site- and sex-specific BEIR VII Lifetime Attributable Risks (LAR) for exposure at 10 years (NRC, 2006). [d] CT AP = CT Abdomen/Pelvis. [e] Mortality risk for uterine cancer in Australia in 2006 from the AIHW's Ovarian Cancer Overview (AIHW, 2010). [f] "All cancers" includes the solid cancers and leukaemia listed in the Table above as well as "other" solid cancers not listed. [g] Natural cancer incidence and mortality risks are given to two significant figures <1% and three significant figures for risks ≥1%. Risks from CT examinations are given to four decimal places (precision below one in a million is unnecessary). [h] Risks greater than 1 in 100 have been rounded to the nearest whole number. Risks equal to and above 1 in 100 have been rounded to the nearest 100.

Bibliography

AAPM, American Association of Physicists in Medicine. *AAPM CT Lexicon Version 1.1.* College Park, Maryland, US, 2011. [cited on page(s): 197]

ABS, Australian Bureau of Statistics. *Australian Historical Population Statistics (Cat. No. 3105.0.65.001).* Canberra, Australian Capital Territory, Australia, 2008a. [cited on page(s): 141, 142, 145, 146, 147, 148, 150, 155]

ABS, Australian Bureau of Statistics. *Deaths (Cat. No. 3302.0).* Canberra, Australian Capital Territory, Australia, 2008b. [cited on page(s): 266, 267]

ABS, Australian Bureau of Statistics. *Population by Age and Sex, Australian States and Territories (Cat. No. 3201.0).* Canberra, Australian Capital Territory, Australia, June 2009. [cited on page(s): 141, 142, 145, 146, 147, 148, 150, 155]

ABS, Australian Bureau of Statistics. *Australian Demographic Statistics.* Canberra, Australian Capital Territory, Australia, June Quarter 2008. [cited on page(s): 149]

Academie des Sciences Academie Nationale de Medecine, *Dose-effect relationships and estimation of the carcinogenic effects of low doses of ionizing radiation.* 30 March 2005. [cited on page(s): 15]

ACR, American College of Radiology. *CT Accreditation Program Requirements.* 13 September 2010. [cited on page(s): 30]

AIHW, Australian Institute of Health and Welfare. *Cancer in Australia: An Overview 2008.* Canberra, Australian Capital Territory, Australia, 2008a. [cited on page(s): 266, 267]

AIHW, Australian Institute of Health and Welfare. *GRIM (General Record of Incidence of Mortality) Books.* Canberra, Australian Capital Territory, Australia, 2008b. [cited on page(s): 175]

AIHW, Australian Institute of Health and Welfare. *ACIM (Australian Cancer Incidence and Mortality) Books.* Canberra, Australian Capital Territory, Australia, 2009. [cited on page(s): 161, 266, 267]

AIHW, Australian Institute of Health and Welfare. *Ovarian Cancer in Australia, an Overview 2010.* Canberra, Australian Capital Territory, Australia, 2010. [cited on page(s): 266, 267]

Al-Haj, A., Lagarde, C., and Mahyoub, F. *A comparative study on the susceptibility of LiF:Mg,Ti (TLD-100) and LiF:Mg,Cu,P (TLD-100H) to spurious signals in thermoluminescence dosimetry.* Radiation Protection Dosimetry, 2007, 125(1-4):399–402. [cited on page(s): 219]

Alessio, A. M. and Phillips, G. S. *A pediatric CT dose and risk estimator.* Pediatric Radiology, 2010, 40(11):1816–21. [cited on page(s): 32, 115, 117]

Almen, A. and Mattsson, S. *On the calculation of effective dose to children and adolescents.* Journal of Radiological Protection, 1996, 16(2):81–89. [cited on page(s): 215]

Ambrose, J. *Computerized transverse axial scanning (tomography). 2. clinical application.* British Journal of Radiology, 1973a, 46(552):1023–47. [cited on page(s): 19]

Ambrose, J. *Computerized transverse axial scanning of the brain.* Proceedings of the Royal Society of Medicine, 1973b, 66(8):833–4. [cited on page(s): 19]

Ambrose, J. and Hounsfield, G. *Computerized transverse axial tomography.* British Journal of Radiology, 1973, 46(542):148–9. [cited on page(s): 19]

Ambrose, J. A. *The usefulness of computerized transverse axial scanning in problems arising from cerebral haemorrhage, infarction or oedema.* British Journal of Radiology, 1973c, 46(549):736. [cited on page(s): 19]

ANS, American Nuclear Society. *Health Effects of Low-Level Radiation - Position Statement 41.* June 2001. [cited on page(s): 15]

Arch, M. E. and Frush, D. P. *Pediatric body MDCT: a 5-year follow-up survey of scanning parameters used by pediatric radiologists.* AJR. American Journal of Roentgenology, 2008, 191(2): 611–7. [cited on page(s): 31]

Aroua, A., Besancon, A., Buchillier-Decka, I., Trueb, P., Valley, J.-F., Verdun, F. R., and Zeller, W. *Adult reference levels in diagnostic and interventional radiology for temporary use in Switzerland.* Radiation Protection Dosimetry, 2004, 111(3):289–295. [cited on page(s): 134]

ARPANSA, Australian Radiation and Protection Nuclear Safety Agency. *Safety Guide: Radiation Protection in Diagnostic and Interventional Radiology.* Yallambie, Victoria, Australia, 2008a. [cited on page(s): 112]

ARPANSA, Australian Radiation and Protection Nuclear Safety Agency. *Code of Practice for the Radiation Protection in the Medical Applications of Ionizing Radiation.* Yallambie, Victoria, Australia, 2008b. [cited on page(s): 111, 112]

ARPANSA, Australian Radiation and Protection Nuclear Safety Agency. *National Diagnostic Reference Level Survey.* Yallambie, Victoria, Australia, 2011. URL http://www.arpansa.gov.au/services/ndrl/index.cfm. [cited on page(s): 112, 130]

Bacani, A. K., McCollough, C. H., Glazebrook, K. N., Bond, J. R., Michet, C. J., Milks, J., and Manek, N. J. *Dual energy computed tomography for quantification of tissue urate deposits in tophaceous gout: help from modern physics in the management of an ancient disease.* Rheumatology International, 2009. [cited on page(s): 195]

Baerlocher, M.O. and Detsky, A.S. *Discussing radiation risks associated with CT scans with patients.* JAMA: The Journal of the American Medical Association, 2010, 304(19):2170–2171. [cited on page(s): 27]

Baerlocher, M.O. and Detsky, A.S. *Informed consent for radiologic procedures - reply.* JAMA: The Journal of the American Medical Association, 2011, 305(9):888–890. [cited on page(s): 27]

Bagg, S. A., Steenburg, S. D., and Ravenel, J. G. *Handling of outside trauma studies: a survey of program directors.* Journal of the American College of Radiology, 2008, 5(5):657–63. [cited on page(s): 27]

Barrett, J. F. and Keat, N. *Artifacts in CT: recognition and avoidance.* Radiographics, 2004, 24 (6):1679–91. [cited on page(s): 206, 207]

Bartolotta, A., Brai, M., Caputo, V., DiLiberto, R., DiMariano, D., Ferrara, G., Puccio, P., and Santamaria, A. S. *The response behaviour of LiF:Mg,Cu,P thermoluminescence dosimeters to high-energy electron beams used in radiotherapy.* Physics in Medicine and Biology, 1995, 40(2): 211–220. [cited on page(s): 41]

Bauhs, J. A., Vrieze, T. J., Primak, A. N., Bruesewitz, M. R., and McCollough, C. H. *CT dosimetry: comparison of measurement techniques and devices.* Radiographics, 2008, 28(1):245–53. [cited on page(s): 208, 210]

Beckmann, E. C. *CT scanning the early days.* British Journal of Radiology, 2006, 79(937):5–8. [cited on page(s): 189]

Bentley, R. E. *Monograph I: NMI Technology Transfer Series; Uncertainty in Measurement: The ISO Guide.* Australian Government - National Mesaurement Institute, Canberra, Australian Capital Territory, Australia, 2005. [cited on page(s): 43]

Bernier, M. O., Rehel, J. L., Brisse, H. J., Wu-Zhou, X., Caer-Lorho, S., Jacob, S., Chateil, J. F., Aubert, B., and Laurier, D. *Radiation exposure from CT in early childhood: a French large-scale multicentre study.* British Journal of Radiology, 2012, 85(1009):53–60. [cited on page(s): 92]

Berrington de Gonzalez, A. and Darby, S. *Risk of cancer from diagnostic X-rays: estimates for the UK and 14 other countries.* Lancet, 2004, 363(9406):345–51. [cited on page(s): 16]

Berrington de Gonzalez, A., Mahesh, M., Kim, K. P., Bhargavan, M., Lewis, R., Mettler, F., and Land, C. *Projected cancer risks from computed tomographic scans performed in the United States in 2007.* Archives of Internal Medicine, 2009, 169(22):2071–7. [cited on page(s): 19, 158, 166, 168, 169, 174]

Blackwell, C. D., Gorelick, M., Holmes, J. F., Bandyopadhyay, S., and Kuppermann, N. *Pediatric head trauma: Changes in use of computed tomography in emergency departments in the United States over time.* Annals of Emergency Medicine, 2007, 49(3):320–324. [cited on page(s): 22, 23]

Blecher, C. M. *Alarm about computed tomography scans is unjustified [letter].* Medical Journal of Australia, 2010, 192(12):723–4. [cited on page(s): 15]

Bolch, W. E., Shah, A. P., Watchman, C. J., Jokisch, D. W., Patton, P. W., Rajon, D. A., Zankl, M., Petoussi-Henss, N., and Eckerman, K. F. *Skeletal absorbed fractions for electrons in the adult male: considerations of a revised 50 um definition of the bone endosteum.* Radiation Protection Dosimetry, 2007, 127(1-4):169–173. [cited on page(s): 52]

Bongartz, G, Golding, S J, Jurik, A G, Leonardi, M, Meerten, E van Persign van, Rodriguez, R, Schneider, K, Calzado, A, Geleijns, J, Jessen, K A, Panzer, W, Shrimpton, P C, and Tosi, G. *European Guidelines for Multislice Computed Tomography.* Funded by the European Commission, 2004. [cited on page(s): 31, 112, 113, 224]

Boone, J. M. and Brunberg, J. A. *Computed tomography use in a tertiary care university hospital.* Journal of the American College of Radiology, 2008, 5(2):132–8. [cited on page(s): 151]

Boone, J. M., Geraghty, E. M., Seibert, J. A., and Wootton-Gorges, S. L. *Dose reduction in pediatric CT: a rational approach.* Radiology, 2003, 228(2):352–60. [cited on page(s): 29, 122]

Bos, A.J.J. *High sensitivity thermoluminescence dosimetry.* Nuclear Instruments and Methods in Physics Research B, 2001, 184:3–28. [cited on page(s): 219]

Bower, M. W. and Hintenlang, D. E. *The characterization of a commercial mosfet dosimeter system for use in diagnostic x-ray (abst).* Health Physics, 1998, 75(2):197–204. [cited on page(s): 35, 71, 75]

Brady, Z. *Radiation - a risky business?* Presented at the Medical Imaging Nurses Association Victorian State Conference, Melbourne, Victoria, Australia, 2010. [cited on page(s): 11]

Brady, Z. *Doses and risks in paediatric imaging in Australia.* Presented at the Siemens Low Dose Academy, Sydney, New South Wales, Australia, 2012a. [cited on page(s): 10, 172]

Brady, Z. *DLP practical breakdown - how best to adjust parameters to reduce dose.* Presented at the Siemens Low Dose Academy, Sydney, New South Wales, Australia, 2012b. [cited on page(s): 11, 138]

Brady, Z. and Einsiedel, P. *A Computed Tomography wish list, from a medical physicist's perspective (invited Editorial).* Australasian Physical & Engineering Sciences in Medicine, 2012, 35:1–5. [cited on page(s): 10]

Brady, Z., Cain, T.M., and Johnston, P.N. *Computed tomography - are we imaging more or less?* Presented at the RANZCR/AIR/FRO/ACPSEM Combined Scientific Meeting, Brisbane, Queensland, Australia, 2009. [cited on page(s): 11, 154]

Brady, Z., Ackland, H.M., and Varma, D.K. *Too much radiation in trauma?* Presented at the SWAN XVIII Trauma Conference, Sydney, New South Wales, Australia, 2010a. [cited on page(s): 11]

Brady, Z., Cain, T.M., and Johnston, P.N. *Calculations of effective dose for paediatric CT examinations.* Presented at the 16th International Conference on Solid State Dosimetry, Sydney, New South Wales, Australia, 2010b. [cited on page(s): 11, 64]

Brady, Z., Cain, T. M., and Johnston, P. N. *Paediatric CT in Australia - trends and risk (EPSM ABEC 2010 conference proceedings).* Australasian Physical & Engineering Sciences in Medicine, 2011a, 34(1):110. [cited on page(s): 11, 154]

Brady, Z., Cain, T. M., and Johnston, P. N. *Effective dose calculation in CT using high sensitivity TLDs (EPSM ABEC 2010 conference proceedings).* Australasian Physical & Engineering Sciences in Medicine, 2011b, 34(1):111. [cited on page(s): 11, 64]

Brady, Z., Cain, T. M., and Johnston, P. N. *Assessing CT protocols in a paediatric hospital using a patient dose survey (EPSM ABEC 2011 conference proceedings).* Australasian Physical & Engineering Sciences in Medicine, 2011c, 34(4):590. [cited on page(s): 11, 138]

Brady, Z., Cain, T. M., and Johnston, P. N. *Paediatric CT imaging trends in Australia.* Journal of Medical Imaging and Radiation Oncology, 2011d, 55:132–142. [cited on page(s): 10, 154]

Brady, Z., Cain, T.M., and Johnston, P.N. *Differences in using the International Commission on Radiological Protection's publications 60 and 103 for determining effective dose in paediatric CT examinations.* Radiation Measurements, 2011e, 46(12):2031–2034. [cited on page(s): 10, 64]

Brady, Z., Wallace, A.B., Wilkinson, L., Heggie, J.C.P., Hayton, A., Einsiedel, P., Forsythe, A., and Mathews, J. D. *Introduction to the Australian study of low dose radiation - assessing the effects of CT scans in childhood (EPSM ABEC 2011 conference proceedings).* Australasian Physical & Engineering Sciences in Medicine, 2011f, 34(4):611. [cited on page(s): 92, 172, 181]

Brady, Z., Cain, T. M., and Johnston, P. N. *Justifying referrals for paediatric CT (accepted).* Medical Journal of Australia, 2012a. [cited on page(s): 10, 33]

Brady, Z., Cain, T. M., and Johnston, P. N. *Comparison of organ dosimetry methods and effective dose calculation methods for paediatric CT.* Australasian Physical & Engineering Sciences in Medicine, 2012b. doi: 10.1007/s13246-012-0134-4. [cited on page(s): 10, 104]

Brady, Z., Ramanauskas, F., Cain, T. M., and Johnston, P. N. *Assessment of paediatric CT dose indicators for the purpose of optimisation (accepted).* British Journal of Radiology, 2012c. [cited on page(s): 10, 138]

Brenner, D., Elliston, C., Hall, E., and Berdon, W. *Estimated risks of radiation-induced fatal cancer from pediatric CT.* AJR. American Journal of Roentgenology, 2001a, 176(2):289–96. [cited on page(s): 5, 6, 19, 22, 23, 24, 31, 35, 153, 158, 160, 161, 166, 168, 169, 173, 181, 264]

Brenner, D. J. *Estimating cancer risks from pediatric CT: going from the qualitative to the quantitative.* Pediatric Radiology, 2002, 32(4):228–3. [cited on page(s): 19, 28]

Brenner, D J. *Effective dose: a flawed concept that could and should be replaced.* British Journal of Radiology, 2008, 81(967):521–523. [cited on page(s): 160]

Brenner, D. J. and Hall, E. J. *Computed tomography - an increasing source of radiation exposure.* New England Journal of Medicine, 2007, 357(22):2277–84. [cited on page(s): 5, 19, 32, 149, 158, 160, 161, 165, 166, 168, 173, 264]

Brenner, D. J. and Hricak, H. *Radiation exposure from medical imaging: time to regulate?* JAMA: The Journal of the American Medical Association, 2010, 304(2):208–9. [cited on page(s): 13, 26]

Brenner, D. J., Elliston, C. D., and Hall, E. J. *Estimates of the cancer risks from pediatric CT radiation are not merely theoretical: Comment on "point/counterpoint: In x-ray computed tomography, technique factors should be selected appropriate to patient size. against the proposition".* Medical Physics, 2001b, 28(11):2387–2388. [cited on page(s): 22]

Brenner, D. J., Elliston, C. D., Hall, E. J., and Berdon, W. E. *Response to the statement by The Society for Pediatric Radiology on radiation risks from pediatric CT scans.* Pediatric Radiology, 2001c, 31:389–391. [cited on page(s): 23, 159]

Brenner, D. J., Doll, R., Goodhead, D. T., Hall, E. J., Land, C. E., Little, J. B., Lubin, J. H., Preston, D. L., Preston, R. J., Puskin, J. S., Ron, E., Sachs, R. K., Samet, J. M., Setlow, R. B., and Zaider, M. *Cancer risks attributable to low doses of ionizing radiation: Assessing what we really know.* Proceedings of the National Academy of Sciences of the United States of America, 2003, 100(24):13761–13766. [cited on page(s): 13, 14, 15, 157]

Brink, J. A. and Amis, E. S. *Image Wisely: A campaign to increase awareness about adult radiation protection.* Radiology, 2010, 257(3):601–602. [cited on page(s): 32]

Brink, J. A., Goske, M. J., and Patti, J. A. *Informed consent for radiologic procedures.* JAMA: The Journal of the American Medical Association, 2011, 305(9):888–890. [cited on page(s): 27]

Brisse, H. J., Brenot, J., Pierrat, N., Gaboriaud, G., Savignoni, A., De Rycke, Y., Neuenschwander, S., Aubert, B., and Rosenwald, J. C. *The relevance of image quality indices for dose optimization in abdominal multi-detector row CT in children: experimental assessment with pediatric phantoms.* Physics in Medicine & Biology, 2009a, 54(7):1871–92. [cited on page(s): 30]

Brisse, H. J., Robilliard, M., Savignoni, A., Pierrat, N., Gaboriaud, G., De Rycke, Y., Neuenschwander, S., Aubert, B., and Rosenwald, J. C. *Assessment of organ absorbed doses and estimation of effective doses from pediatric anthropomorphic phantom measurements for multidetector row CT with and without automatic exposure control.* Health Physics, 2009b, 97(4): 303–14. [cited on page(s): 6, 35, 36, 99, 220]

Brix, G., Lechel, U., Veit, R., Truckenbrodt, R., Stamm, G., Coppenrath, E. M., Griebel, J., and Nagel, H. D. *Assessment of a theoretical formalism for dose estimation in CT: an anthropomorphic phantom study.* European Radiology, 2004, 14(7):1275–84. [cited on page(s): 7, 42, 80, 81, 96, 102]

Broadhead, D. A., Faulkner, K., Rawlings, D.J., and Chapple, C. L. *Automated thermoluminescent dosimetry for simple radiographic procedures.* Journal of Radiological Protection, 1997, 17(1): 17–24. [cited on page(s): 44, 218]

Broder, J. S. *CT utilization: the emergency department perspective.* Pediatric Radiology, 2008, 38 Suppl 4:S664–9. [cited on page(s): 26]

Bushberg, J. T., Seibert, J. A., Leidholdt, E. M. Jr., and Boone, J. M. *The Essential Physics of Medical Imaging.* Lippincott Williams & Wilkins, Baltimore, USA, 2001. [cited on page(s): 20, 186, 187, 189, 191, 203]

Campbell, J., Kalra, M. K., Rizzo, S., Maher, M. M., and Shepard, J. A. *Scanning beyond anatomic limits of the thorax in chest CT: findings, radiation dose, and automatic tube current modulation.* AJR. American Journal of Roentgenology, 2005, 185(6):1525–30. [cited on page(s): 28]

Caon, M., Bibbo, G., and Pattison, J. *An EGS4-ready tomographic computational model of a 14-year-old female torso for calculating organ doses from CT examinations.* Physics in Medicine & Biology, 1999, 44(9):2213–25. [cited on page(s): 80]

Caracappa, P. F., Chao, T. C., and Xu, X. G. *A study of predicted bone marrow distribution on calculated marrow dose from external radiation exposures using two sets of image data for the same individual.* Health Physics, 2009, 96(6):661–74. [cited on page(s): 51]

Carlton, R. R. and Adler, A. M. *Principles of Radiographic Imaging: An Art and a Science.* Delmar Publishers, New York, US, 1996. [cited on page(s): 19]

Cember, H. and Johnson, T.E. *Introduction to Health Physics.* The McGraw-Hill Companies, Inc., US, 2009. [cited on page(s): 217, 218]

Chapple, C. L., Willis, S., and Frame, J. *Effective dose in paediatric computed tomography.* Physics in Medicine & Biology, 2002, 47(1):107–15. [cited on page(s): 35, 36, 83, 85, 88, 96, 258]

Chodick, G., Ronckers, C., Ron, E., and Shalev, V. *The utilization of pediatric computed tomography in a large Israeli Health Maintenance Organization.* Pediatric Radiology, 2006, 36(6): 485–490. [cited on page(s): 27, 152, 169]

Chodick, G., Kim, K. P., Shwarz, M., Horev, G., Shalev, V., and Ron, E. *Radiation risks from pediatric computed tomography scanning.* Pediatric Endocrinology Reviews, 2009, 7(2):29–36. [cited on page(s): 31]

Christner, J. A., Kofler, J. M., and McCollough, C. H. *Estimating effective dose for CT using dose-length product compared with using organ doses: consequences of adopting international commission on radiological protection publication 103 or dual-energy scanning.* AJR. American Journal of Roentgenology, 2010, 194(4):881–9. [cited on page(s): 37, 62, 63, 81]

Chwals, W. J., Robinson, A. V., Sivit, C. J., Alaedeen, D., Fitzenrider, E., and Cizmar, L. *Computed tomography before transfer to a level I pediatric trauma center risks duplication with associated increased radiation exposure.* Journal of Pediatric Surgery, 2008, 43(12):2268–2272. [cited on page(s): 27]

CIRS, Computerized Imaging Reference Systems. *ATOM pediatric ten year old phantom, User Guide and Technical Information*, 2006. [cited on page(s): 40, 226]

Cody, D. D. and Mahesh, M. *AAPM/RSNA physics tutorial for residents: Technologic advances in multidetector CT with a focus on cardiac imaging.* Radiographics, 2007, 27(6):1829–37. [cited on page(s): 193, 194]

Cohen, M. D. *Pediatric CT radiation dose: How low can you go?* American Journal of Roentgenology, 2009, 192(5):1292–1303. [cited on page(s): 24]

Cohnen, M., Wittsack, H. J., Assadi, S., Muskalla, K., Ringelstein, A., Poll, L. W., Saleh, A., and Modder, U. *Radiation exposure of patients in comprehensive computed tomography of the head in acute stroke.* AJNR: American Journal of Neuroradiology, 2006, 27(8):1741–5. [cited on page(s): 42]

Collins, G. *CT scans decline for young patients*, 20 April 2011. URL www.6minutes.com.au. [cited on page(s): 154]

Cook, S. H., Fielding, J. R., and Phillips, J. D. *Repeat abdominal computed tomography scans after pediatric blunt abdominal trauma: missed injuries, extra costs, and unnecessary radiation exposure.* Journal of Pediatric Surgery, 2010, 45(10):2019–2024. [cited on page(s): 27]

Corderoy, A. *GPs get the go-ahead to order less risky scans.* The Sydney Morning Herald, Australia, 17 May 2011. [cited on page(s): 154]

Coursey, C., Frush, D. P., Yoshizumi, T., Toncheva, G., Nguyen, G., and Greenberg, S. B. *Pediatric chest MDCT using tube current modulation: effect on radiation dose with breast shielding.* AJR.

American Journal of Roentgenology, 2008, 190(1):W54–61. [cited on page(s): 28, 37, 75, 160, 161, 264]

Coursey, C. A., Nelson, R. C., Boll, D. T., Paulson, E. K., Ho, L. M., Neville, A. M., Marin, D., Gupta, R. T., and Schindera, S. T. *Dual-energy multidetector CT: how does it work, what can it tell us, and when can we use it in abdominopelvic imaging?* Radiographics, 2010, 30(4): 1037–55. [cited on page(s): 195]

Cranley, K., Gilmore, B.J., Fogarty, G.W.A., and Desponds, L. *IPEM Report No. 78: Catalogue of Diagnostic X-ray Spectra and Other Data.* The Institute of Physics and Engineering in Medicine, York, UK, 1997. [cited on page(s): 38]

CRCPD, Conference of Radiation Control Program Directors. *What's NEXT? Nationwide Evaluation of X-ray Trends: 2000 Computed Tomography.* 2006. [cited on page(s): 173, 174, 264]

Cristy, M. *Mathematical phantoms representing children of various ages for use in estimates of internal dose.* US Nuclear Regulatory Commission Rep. NUREG/CR-1159 (also Oak Ridge National Laboratory Rep. ORNL/NUREG/TM-367), Oak Ridge, US, 1980. [cited on page(s): 80]

Cristy, M. *Active bone marrow distribution as a function of age in humans.* Physics in Medicine & Biology, 1981, 26(3):389–400. [cited on page(s): 50, 234]

Cristy, M. and Eckerman, K. F. *Specific absorbed fractions of energy at various ages from internal photon sources (I. Methods).* Oak Ridge National Laboratory, Report ORNL/TM-8381/V1, Oak Ridge, US, 1987. [cited on page(s): 50, 52, 80, 84, 85, 86, 88, 226, 234, 236]

CT-Dose. National Institute of Radiation Hygiene, Herlev, Denmark. [cited on page(s): 81]

CT scans decline for young patients. Gastroenterology Update, 27 April 2011. [cited on page(s): 154]

Davis, S. D., Ross, C. K., Mobit, P. N., Van der Zwan, L., Chase, W. J., and Shortt, K. R. *The response of LiF thermoluminescence dosemeters to photon beams in the energy range from 30 kV x rays to 60Co gamma rays.* Radiation Protection Dosimetry, 2003, 106(1):33–43. [cited on page(s): 41, 219]

de Campo, J. F. and de Campo, M. P. *Is informed consent necessary for computed tomography in children and young adults? [letter].* Medical Journal of Australia, 2010, 192(7):423. [cited on page(s): 27]

Deak, P., van Straten, M., Shrimpton, P. C., Zankl, M., and Kalender, W. A. *Validation of a Monte Carlo tool for patient-specific dose simulations in multi-slice computed tomography.* European Radiology, 2008, 18(4):759–72. [cited on page(s): 80]

Deak, P. D., Smal, Y., and Kalender, W. A. *Multisection CT protocols: Sex- and age-specific conversion factors used to determine effective dose from dose-length product.* Radiology, 2010, 257(1):158–166. [cited on page(s): 62, 85, 88, 95, 96, 115, 117, 257]

DoH, Radiation Safety Section, Victorian Department of Health, Australia. *Radiation Safety Standard: Computed Tomography Scanners.* Melbourne, Victoria, Australia, 2007. [cited on page(s): 55]

Dong, S. L., Chu, T. C., Lan, G. Y., Wu, T. H., Lin, Y. C., and Lee, J. S. *Characterization of high-sensitivity metal oxide semiconductor field effect transistor dosimeters system and LiF:Mg,Cu,P thermoluminescence dosimeters for use in diagnostic radiology.* Applied Radiation and Isotopes, 2002, 57(6):883–91. [cited on page(s): 41, 71, 75, 76, 218, 219, 220]

Donnelly, L. F. *Lessons from history.* Pediatric Radiology, 2002, 32(4):287–92. [cited on page(s): 23]

Donnelly, L. F. *Reducing radiation dose associated with pediatric CT by decreasing unnecessary examinations.* AJR. American Journal of Roentgenology, 2005, 184(2):655–7. [cited on page(s): 22, 25, 26]

Donnelly, L. F. and Frush, D. P. *Fallout from recent articles on radiation dose and pediatric CT.* Pediatric Radiology, 2001, 31(6):388. [cited on page(s): 22]

Donnelly, L. F., Emery, K. H., Brody, A. S., Laor, T., Gylys-Morin, V. M., Anton, C. G., Thomas, S. R., and Frush, D. P. *Minimizing radiation dose for pediatric body applications of single-detector helical CT: strategies at a large children's hospital.* AJR. American Journal of Roentgenology, 2001, 176(2):303–6. [cited on page(s): 6, 22, 24, 29, 31, 153, 181]

Dorfman, A. L., Fazel, R., Einstein, A. J., Applegate, K. E., Krumholz, H. M., Wang, Y., Christodoulou, E., Chen, J., Sanchez, R., and Nallamothu, B. K. *Use of medical imaging procedures with ionizing radiation in children: A population-based study.* Archives of Pediatrics & Adolescent Medicine, 2011. [cited on page(s): 22, 27, 149, 169]

Dougeni, E., Faulkner, K., and Panayiotakis, G. *A review of patient dose and optimisation methods in adult and paediatric CT scanning.* European Journal of Radiology, 2012, 81(4):e665–e683. [cited on page(s): 111]

Duggan, L. *Clinical use of LiF:Mg,Cu,P: Critical evaluation of an ultrasensitive material for thermoluminescence dosimetry.* Medical Physics, 2002, 29(10):2457–2457. [cited on page(s): 42, 219]

Duggan, L. and Kron, T. *Glow curve analysis of long-term stability of LiF:Mg,Cu,P as compared to LiF:Mg,Ti.* Radiation Protection Dosimetry, 1999, 85(1-4):213–216. [cited on page(s): 41]

Duggan, L., Warren-Forward, H., Smith, T., and Kron, T. *Investigation of dose reduction in neonatal radiography using specially designed phantoms and LiF:Mg,Cu,P TLDs.* British Journal of Radiology, 2003, 76(904):232–7. [cited on page(s): 6, 42, 220]

Duggan, L., Hood, C., Warren-Forward, H., Haque, M., and Kron, T. *Variations in dose response with x-ray energy of LiF:Mg,Cu,P thermoluminescence dosimeters: implications for clinical dosimetry.* Physics in Medicine & Biology, 2004, 49(17):3831–45. [cited on page(s): 41, 42, 43, 45, 219, 220, 221]

Eckerman, K. F. and Stabin, M. G. *Electron absorbed fractions and dose conversion factors for marrow and bone by skeletal regions.* Health Physics, 2000, 78(2):199–214. [cited on page(s): 51, 52, 235, 236]

Ehringfeld, C., Schmid, S., Poljanc, K., Kirisits, C., Aiginger, H., and Georg, D. *Application of commercial MOSFET detectors for in vivo dosimetry in the therapeutic x-ray range from 80 kV to 250 kV.* Physics in Medicine & Biology, 2005, 50(2):289–303. [cited on page(s): 75]

Einstein, A. J., Henzlova, M. J., and Rajagopalan, S. *Estimating risk of cancer associated with radiation exposure from 64-slice computed tomography coronary angiography.* JAMA: The Journal of the American Medical Association, 2007a, 298(3):317–23. [cited on page(s): 19, 158]

Einstein, A. J., Moser, K. W., Thompson, R. C., Cerqueira, M. D., and Henzlova, M. J. *Radiation dose to patients from cardiac diagnostic imaging.* Circulation, 2007b, 116(11):1290–305. [cited on page(s): 207, 208]

Fazel, R., Krumholz, H., Wang, Y., Ross, J., Chen, J., Ting, H., Shah, N., Nasir, K., Einstein, A., and Nallamothu, B. *Exposure to low-dose ionizing radiation from medical imaging procedures.* The New England Journal of Medicine, 2009, 361(9):849. [cited on page(s): 19]

FDA, US Food and Drug Administration. *FDA Safety Investigation of CT Brain Perfusion Scans: Initial Notification 8 October.* 2009a. [cited on page(s): 19]

FDA, US Food and Drug Administration. *FDA Safety Investigation of CT Brain Perfusion Scans: Update 8 December.* 2009b. [cited on page(s): 19]

FDA, US Food and Drug Administration. *FDA Safety Investigation of CT Brain Perfusion Scans: Update 9 November.* 2010a. [cited on page(s): 19]

FDA, US Food and Drug Administration. *Initiative to Reduce Unnecessary Radiation Exposure from Medical Imaging.* 2010b. [cited on page(s): 19]

Fenton, S. J., Hansen, K. W., Meyers, R. L., Vargo, D. J., White, K. S., Firth, S. D., and Scaife, E. R. *CT scan and the pediatric trauma patient–are we overdoing it?* Journal of Pediatric Surgery, 2004, 39(12):1877–81. [cited on page(s): 26]

Fill, U. A., Zankl, M., Petoussi-Henss, N., Siebert, M., and Regulla, D. *Adult female voxel models of different stature and photon conversion coefficients for radiation protection.* Health Physics, 2004, 86(3):253–72. [cited on page(s): 80, 82]

Flohr, T. G., Schaller, S., Stierstorfer, K., Bruder, H., Ohnesorge, B. M., and Schoepf, U. J. *Multi-detector row CT systems and image-reconstruction techniques.* Radiology, 2005, 235(3):756–73. [cited on page(s): 193, 195, 202]

Fricke, B. L., Donnelly, L. F., Frush, D. P., Yoshizumi, T., Varchena, V., Poe, S. A., and Lucaya, J. *In-plane bismuth breast shields for pediatric CT: effects on radiation dose and image quality using experimental and clinical data.* AJR. American Journal of Roentgenology, 2003, 180(2): 407–11. [cited on page(s): 28]

Frush, D. *Radiation safety.* Pediatric Radiology, 2009, 39(0):385–390. [cited on page(s): 24]

Frush, D. P. *Pediatric dose reduction in computed tomography.* Health Physics, 2008, 95(5):518–27. [cited on page(s): 24, 32]

Frush, D. P. and Yoshizumi, T. *Conventional and CT angiography in children: dosimetry and dose comparisons.* Pediatric Radiology, 2006, 36(Supplement 14):154–158. [cited on page(s): 71, 75]

Frush, D. P., Soden, B., Frush, K. S., and Lowry, C. *Improved pediatric multidetector body CT using a size-based color-coded format.* AJR. American Journal of Roentgenology, 2002, 178(3): 721–6. [cited on page(s): 30, 31]

Frush, D. P., Donnelly, L. F., and Rosen, N. S. *Computed tomography and radiation risks: what pediatric health care providers should know.* Pediatrics, 2003, 112(4):951–7. [cited on page(s): 19, 28, 35, 211]

Fuchs, T., Kachelriess, M., and Kalender, W. A. *Direct comparison of a xenon and a solid-state CT detector system: measurements under working conditions.* IEEE Transactions on Medical Imaging, 2000, 19(9):941–8. [cited on page(s): 187]

Fujii, K, Aoyama, T, Koyama, S, and Kawaura, C. *Comparative evaluation of organ and effective doses for paediatric patients with those for adults in chest and abdominal CT examinations.* British Journal of Radiology, 2007, 80(956):657–667. [cited on page(s): 6, 36, 39, 53, 54, 160, 161, 264]

Fujii, K, Aoyama, T, Yamauchi-Kawaura, C, Koyama, S, Yamauchi, M, Ko, S, Akahane, K, and Nishizawa, K. *Radiation dose evaluation in 64-slice CT examinations with adult and paediatric anthropomorphic phantoms.* British Journal of Radiology, 2009, 82(984):1010–1018. [cited on page(s): 6, 36, 60, 63]

Galanski, M., Nagel, H. D., and Stamm, G. *Paediatric CT exposure practice in the federal republic of Germany: results of a nationwide survey in 2005-2006.* Medizinische Hochschule Hannover, Hannover, Germany, 2007. [cited on page(s): 132, 133, 134, 135, 136, 224]

Geleijns, J., Van Unnik, J. G., Zoetelief, J., Zweers, D., and Broerse, J. J. *Comparison of two methods for assessing patient dose from computed tomography.* British Journal of Radiology, 1994, 67(796):360–5. [cited on page(s): 7, 44, 80, 96, 102]

Geleijns, J., Salvado Artells, M., de Bruin, P. W., Matter, R., Muramatsu, Y., and McNitt-Gray, M. F. *Computed tomography dose assessment for a 160 mm wide, 320 detector row, cone beam CT scanner.* Physics in Medicine & Biology, 2009, 54(10):3141–59. [cited on page(s): 210]

Geleijns, J., Wang, J., and McCollough, C. *The use of breast shielding for dose reduction in pediatric CT: arguments against the proposition.* Pediatric Radiology, 2010, 40(11):1744–1747. [cited on page(s): 28]

George, J, Eatough, J P, Mountford, P J, Koller, C J, Oxtoby, J, and Frain, G. *Patient dose optimization in plain radiography based on standard exposure factors.* British Journal of Radiology, 2004, 77(922):858–863. [cited on page(s): 112]

Ghotbi, N., Ohtsuru, A., Ogawa, Y., Morishita, M., Norimatsu, N., Namba, H., Moriuchi, H., Uetani, M., and Yamashita, S. *Pediatric CT scan usage in Japan: results of a hospital survey.* Radiation Medicine, 2006, 24(8):560–567. [cited on page(s): 27, 29]

Giles, J. *Study warns of 'avoidable' risks of CT scans.* Nature, 2004, 431(7007):391. [cited on page(s): 19, 172]

Glennie, G. D. *A comparison of TLD dosimeters: LiF:Mg,Ti and LiF:Mg,Cu,P for measurement of radiation therapy doses.* Medical Physics, 2003, 30(12):3262–3262. [cited on page(s): 219]

Goldman, L. W. *Principles of CT: radiation dose and image quality.* Journal of Nuclear Medicine Technology, 2007a, 35(4):213–25. [cited on page(s): 208, 210]

Goldman, L. W. *Principles of CT and CT technology.* Journal of Nuclear Medicine Technology, 2007b, 35(3):115–28. [cited on page(s): 189, 192, 203]

Goldman, L. W. *Principles of CT: multislice CT.* Journal of Nuclear Medicine Technology, 2008, 36(2):57–68. [cited on page(s): 89]

Goske, M. and Bulas, D. *Improving health literacy: informed decision-making rather than informed consent for CT scans in children.* Pediatric Radiology, 2009, 39(9):901–903. [cited on page(s): 27]

Goske, M. J., Applegate, K. E., Boylan, J., Butler, P. F., Callahan, M. J., Coley, B. D., Farley, S., Frush, D. P., Hernanz-Schulman, M., Jaramillo, D., Johnson, N. D., Kaste, S. C., Morrison, G., Strauss, K. J., and Tuggle, N. *The "Image Gently" campaign: increasing CT radiation dose awareness through a national education and awareness program.* Pediatric Radiology, 2008a, 38 (3):265–9. [cited on page(s): 24]

Goske, M. J., Applegate, K. E., Boylan, J., Butler, P. F., Callahan, M. J., Coley, B. D., Farley, S., Frush, D. P., Hernanz-Schulman, M., Jaramillo, D., Johnson, N. D., Kaste, S. C., Morrison, G., Strauss, K. J., and Tuggle, N. *The Image Gently campaign: working together to change practice.* AJR. American Journal of Roentgenology, 2008b, 190(2):273–4. [cited on page(s): 24, 25]

Groves, A. M., Owen, K. E., Courtney, H. M., Yates, S. J., Goldstone, K. E., Blake, G. M., and Dixon, A. K. *16-detector multislice CT: dosimetry estimation by TLD measurement compared with Monte Carlo simulation.* British Journal of Radiology, 2004, 77(920):662–5. [cited on page(s): 7, 42, 44, 47, 80, 102, 230, 231]

Gudjonsdottir, J., Ween, B., and Olsen, D. R. *Optimal use of AEC in CT: a literature review.* Radiol Technol, 2010, 81(4):309–17. [cited on page(s): 197]

Haaga, J. R. *Radiation dose management: weighing risk versus benefit.* AJR. American Journal of Roentgenology, 2001, 177(2):289–91. [cited on page(s): 29, 122]

Haaga, J. R., Miraldi, F., MacIntyre, W., LiPuma, J. P., Bryan, P. J., and Wiesen, E. *The effect of mAs variation upon computed tomography image quality as evaluated by in vivo and in vitro studies.* Radiology, 1981, 138(2):449–54. [cited on page(s): 197]

Hadley, J. L., Agola, J., and Wong, P. *Potential impact of the American College of Radiology appropriateness criteria on CT for trauma.* AJR. American Journal of Roentgenology, 2006, 186(4):937–42. [cited on page(s): 27]

Hall, E. J. and Brenner, D. J. *Cancer risks from diagnostic radiology.* British Journal of Radiology, 2008, 81(965):362–78. [cited on page(s): 19, 35, 149]

Hallil, A. *MOSFET CT Dosimetry Workshop: Introduction to MOSFET dosimetry - physics and application in diagnostic radiology and radiotherapy.* Duke University Medical Center, 12-13 June 2009. [cited on page(s): 73]

Hammer, G. P., Seidenbusch, M. C., Regulla, D. F., Spix, C., Zeeb, H., Schneider, K., and Blettner, M. *Childhood cancer risk from conventional radiographic examinations for selected referral criteria: results from a large cohort study.* AJR. American Journal of Roentgenology, 2011, 197 (1):217–23. [cited on page(s): 19]

Hara, A. K., Paden, R. G., Silva, A. C., Kujak, J. L., Lawder, H. J., and Pavlicek, W. *Iterative reconstruction technique for reducing body radiation dose at CT: feasibility study.* AJR. American Journal of Roentgenology, 2009, 193(3):764–71. [cited on page(s): 199]

Harris, C. K., Elson, H. R., Lamba, M. A. S., and Foster, A. E. *A comparison of the effectiveness of thermoluminescent crystals LiF:Mg,Ti, and LiF:Mg,Cu,P for clinical dosimetry.* Medical Physics, 1997, 24(9):1527–1529. [cited on page(s): 45, 219]

Hart, D. and Wall, B. F. *UK population dose from medical X-ray examinations.* European Journal of Radiology, 2004, 50(3):285–291. [cited on page(s): 21]

Hart, D., Wall, B.F., Shrimpton, P.C., Bungay, D., and Dance, D.R. *Reference Doses and Patient Size in Paediatric Radiology NRPB R-318.* National Radiological Protection Board, Chilton, UK, 2000. [cited on page(s): 122]

Heaney, D. E. and Norvill, C. A. *A comparison of reduction in CT dose through the use of gantry angulations or bismuth shields.* Australasian Physical & Engineering Sciences in Medicine, 2006, 29(2):172–8. [cited on page(s): 28, 59]

Heggie, J. C. P. *Patient doses in multi-slice CT and the importance of optimisation.* Australasian Physical & Engineering Sciences in Medicine, 2005, 28(2):86–96. [cited on page(s): 122]

Heggie, J. C. P. *Technical developments in radiology in Australasia dating from 1977.* Australasian Physical & Engineering Sciences in Medicine, 2007, 30(3):160–77. [cited on page(s): 151]

Heggie, J. C. P., Liddell, N. A., and Maher, K. P. *Applied Imaging Technology.* St. Vincent's Hospital, Melbourne, Australia, 1997. [cited on page(s): 15, 188, 199]

Heggie, J. C. P., Kay, J. K., and Lee, W. K. *Importance in optimization of multi-slice computed tomography scan protocols.* Australasian Radiology, 2006, 50(3):278–85. [cited on page(s): 28, 195, 202]

Hendee, W. R., Becker, G. J., Borgstede, J. P., Bosma, J., Casarella, W. J., Erickson, B. A., Maynard, C. D., Thrall, J. H., and Wallner, P. E. *Addressing overutilization in medical imaging.* Radiology, 2010, 257(1):240–245. [cited on page(s): 26]

Hollingsworth, C. L., Yoshizumi, T. T., Frush, D. P., Chan, F. P., Toncheva, G., Nguyen, G., Lowry, C. R., and Hurwitz, L. M. *Pediatric cardiac-gated CT angiography: assessment of radiation dose.* AJR. American Journal of Roentgenology, 2007, 189(1):12–8. [cited on page(s): 6, 37, 47, 71, 75, 230, 231]

Hopper, K. D. *Orbital, thyroid, and breast superficial radiation shielding for patients undergoing diagnostic CT.* Seminars in Ultrasound, CT & MR, 2002, 23(5):423–7. [cited on page(s): 28]

Horowitz, Y. and Olko, P. *The effects of ionisation density on the thermoluminescence response (efficiency) of LiF:Mg,Ti and LiF:Mg,Cu,P.* Radiation Protection Dosimetry, 2004, 109(4): 331–348. [cited on page(s): 220]

Hounsfield, G. N. *Computerized transverse axial scanning (tomography). 1. description of system.* British Journal of Radiology, 1973, 46(552):1016–22. [cited on page(s): 19]

Hricak, H., Brenner, D. J., Adelstein, S. J., Frush, D. P., Hall, E. J., Howell, R. W., McCollough, C. H., Mettler, F. A., Pearce, M. S., Suleiman, O. H., Thrall, J. H., and Wagner, L. K. *Managing radiation use in medical imaging: A multifaceted challenge.* Radiology, 2011, 258(3):889–905. [cited on page(s): 16, 92]

Hsieh, J. *Computed Tomography: Principles, Design, Artifacts, and Recent Advances.* SPIE Optical Engineering Press, Bellingham, USA, 2003. [cited on page(s): 186, 188, 193, 204]

Hubbell, J.H. and Seltzer, S.M. *Tables of X-Ray Mass Attenuation Coefficients and Mass Energy-Absorption Coefficients (Version 1.4)*, 2004. [cited on page(s): 45, 46, 75]

Huda, W. *Effective doses to adult and pediatric patients.* Pediatric Radiology, 2002, 32(4):272–9. [cited on page(s): 28]

Huda, W. and Slone, R. *Review of Radiologic Physics.* Lippincott Williams & Wilkins, Philadelphia, USA, 2003. [cited on page(s): 30, 204]

Huda, W., Atherton, J. V., Ware, D. E., and Cumming, W. A. *An approach for the estimation of effective radiation dose at CT in pediatric patients.* Radiology, 1997, 203(2):417–22. [cited on page(s): 173, 264]

Huda, W., Scalzetti, E. M., and Levin, G. *Technique factors and image quality as functions of patient weight at abdominal CT.* Radiology, 2000, 217(2):430–5. [cited on page(s): 29, 30]

Huda, W., Ravenel, J. G., and Scalzetti, E. M. *How do radiographic techniques affect image quality and patient doses in CT?* Seminars in Ultrasound, CT, and MRI, 2002, 23(5):411–422. [cited on page(s): 29]

Huda, W., Sterzik, A., and Tipnis, S. *X-ray beam filtration, dosimetry phantom size and CT patient dose conversion factors.* Physics in Medicine & Biology, 2010, 55(2):551–61. [cited on page(s): 114, 118, 121, 123, 135, 260]

Huda, W., Magill, D., and He, W. *CT effective dose per dose length product using ICRP 103 weighting factors.* Medical Physics, 2011, 38(3):1261–1265. [cited on page(s): 62]

Hui, H. *Multi-slice helical CT: Scan and reconstruction.* Medical Physics, 1999, 26(1):5–18. [cited on page(s): 202]

Hunold, P., Vogt, F. M., Schmermund, A., Debatin, J. F., Kerkhoff, G., Budde, T., Erbel, R., Ewen, K., and Barkhausen, J. *Radiation exposure during cardiac CT: effective doses at multi-detector row CT and electron-beam CT.* Radiology, 2003, 226(1):145–52. [cited on page(s): 44, 47, 214, 230, 231]

Hurwitz, L. M., Reiman, R. E., Yoshizumi, T. T., Goodman, P. C., Toncheva, G., Nguyen, G., and Lowry, C. *Radiation dose from contemporary cardiothoracic multidetector CT protocols with an anthropomorphic female phantom: Implications for cancer induction.* Radiology, 2007a, 245(3): 742–750. [cited on page(s): 71, 75]

Hurwitz, L. M., Yoshizumi, T. T., Goodman, P. C., Frush, D. P., Nguyen, G., Toncheva, G., and Lowry, C. *Effective dose determination using an anthropomorphic phantom and metal oxide semiconductor field effect transistor technology for clinical adult body multidetector array computed tomography protocols.* Journal of Computer Assisted Tomography, 2007b, 31(4):544–9. [cited on page(s): 47, 71, 75, 230, 231]

Hurwitz, L. M., Yoshizumi, T. T., Goodman, P. C., Nelson, R. C., Toncheva, G., Nguyen, G. B., Lowry, C., and Anderson-Evans, C. *Radiation dose savings for adult pulmonary embolus 64-MDCT using bismuth breast shields, lower peak kilovoltage, and automatic tube current modulation.* AJR. American Journal of Roentgenology, 2009, 192(1):244–53. [cited on page(s): 71, 75]

IAEA, International Atomic Energy Agency. *International Basic Safety Standards for Protection against Ionizing Radiation and for the Safety of Radiation Sources.* Vienna, Austria, 1996. [cited on page(s): 15]

ICRP, International Commission on Radiological Protection. *Recommendations of the International Commission on Radiological Protection. ICRP Publication 26.* Annals of the ICRP, 1977, 1(3):1–53. [cited on page(s): xvii, 214, 215]

ICRP, International Commission on Radiological Protection. *1990 Recommendations of the International Commission on Radiological Protection. ICRP Publication 60.* Annals of the ICRP, 1991, 21(1-3):1–201. [cited on page(s): xvii, 8, 37, 48, 53, 92, 111, 115, 139, 213, 214, 215, 231]

ICRP, International Commission on Radiological Protection. *Age-dependent doses to members of the public from intake of radionuclides: Part 3 ingestion dose coefficients. ICRP Publication 69.* Annals of the ICRP, 1995, 25(1):1–74. [cited on page(s): 49, 216]

ICRP, International Commission on Radiological Protection. *Radiological protection and safety in medicine. ICRP Publication 73.* Annals of the ICRP, 1996a, 26(2):1–47. [cited on page(s): 111, 112]

ICRP, International Commission on Radiological Protection. *Conversion coefficients for use in radiological protection against external radiation. ICRP Publication 74.* Annals of the ICRP, 1996b, 26(3-4):1–205. [cited on page(s): 214, 216]

ICRP, International Commission on Radiological Protection. *Diagnostic reference levels in medical imaging: review and additional advice. ICRP Supporting Guidance 2.* Annals of the ICRP, 2001, 31(4):33–52. [cited on page(s): 111, 112]

ICRP, International Commission on Radiological Protection. *Basic anatomical and physiological data for use in radiological protection: reference values. ICRP Publication 89.* Annals of the ICRP, 2002, 32(3-4):1–277. [cited on page(s): 49, 50, 52, 54, 81, 160]

ICRP, International Commission on Radiological Protection. *Low-dose extrapolation of radiation-related cancer risk. ICRP Publication 99.* Annals of the ICRP, 2005, 35(4):1–140. [cited on page(s): 13, 14]

ICRP, International Commission on Radiological Protection. *Human alimentary tract model for radiological protection. ICRP Publication 100.* Annals of the ICRP, 2006, 36:1–327. [cited on page(s): 81]

ICRP, International Commission on Radiological Protection. *Managing patient dose in multi-detector computed tomography (MDCT). ICRP Publication 102.* Annals of the ICRP, 2007a, 37 (1):1–79. [cited on page(s): 14, 24, 26, 28, 29, 211]

ICRP, International Commission on Radiological Protection. *The 2007 Recommendations of the International Commission on Radiological Protection. ICRP Publication 103.* Annals of the ICRP, 2007b, 37(2-4):1–332. [cited on page(s): xvii, 5, 8, 13, 14, 15, 16, 17, 19, 25, 26, 37, 47, 48, 49, 61, 91, 92, 115, 157, 161, 213, 214, 215, 216, 230, 231, 266, 267]

ICRP, International Commission on Radiological Protection. *Radiological protection in medicine. ICRP Publication 105.* Annals of the ICRP, 2007c, 37(6):1–64. [cited on page(s): 13, 25, 26, 91, 111, 112]

ICRP, International Commission on Radiological Protection. *Adult reference computational phantoms. ICRP Publication 110.* Annals of the ICRP, 2009, 39(2):1–164. [cited on page(s): 52, 54, 93]

ICRP, International Commission on Radiological Protection. *ICRP Statement on Tissue Reactions.* 2011. [cited on page(s): 59]

ICRU, International Commission on Radiation Units and Measurements. *Tissue Substitutes in Radiation Dosimetry and Measurement. ICRU Report No. 44.* Bethesda, MD, 1989. [cited on page(s): 45, 46]

ICRU, International Commission on Radiation Units and Measurements. *Photon, Electron, Proton and Neutron Interaction Data for Body Tissues. ICRU Report No. 46.* Bethesda, MD, 1992. [cited on page(s): 52, 53, 239]

ICRU, International Commission on Radiation Units and Measurements. *Patient Dosimetry for X-rays used in Medical Imaging. ICRU Report No. 74.* Bethesda, MD, 2005. [cited on page(s): 208]

ImPACT CT Scanner Dose Survey, Measurement Protocol, Version 5.0. St. George's Healthcare NHS Trust, London, UK, 1997. [cited on page(s): 39]

ImPACT CT Dosimetry Calculator, Version 1.0.4. St. George's Healthcare NHS Trust, London, UK, 27 May 2011. [cited on page(s): xviii, 49, 79, 81, 84, 85, 94, 95, 98, 105, 106, 107, 114, 174]

ImpactDose. IBA Dosimetry, Germany. [cited on page(s): 81]

Introduction to session I: helical CT and cancer risk. Pediatric Radiology, 2002, 32(4):242–4. [cited on page(s): 26]

IPEM, Institute of Physics and Engineering in Medicine. *Guidance on the Establishment and Use of Diagnostic Reference Levels for Medical X-ray Examinations, IPEM Report No. 88.* York, UK, 2004. [cited on page(s): 112, 113, 122]

IPSM, Institute of Physical Sciences in Medicine. *National Protocol for Patient Dose Measurements in Diagnostic Radiology. Dosimetry Working Party of the Institute of Physical Sciences in Medicine (IPSM).* Didcot, Oxfordshire, 1992. [cited on page(s): 43]

ISO, International Organization for Standardization. *Guide to the Expression of Uncertainty in Measurement.* Geneva, 1993 (corrected & reprinted, 1995). [cited on page(s): 43]

Jacob, K., Vivian, G., and Steel, J. R. *X-ray dose training: are we exposed to enough?* Clinical Radiology, 2004, 59(10):928–934. [cited on page(s): 32]

Jimenez, S., Jimenez, J. R., Crespo, M., Santamarta, E., Bousono, C., and Rodriguez, J. *Computed tomography in children with cystic fibrosis: a new way to reduce radiation dose.* Archives of Disease in Childhood, 2006, 91(5):388–90. [cited on page(s): 28]

Johns, H. E. and Cunningham, J. R. *The Physics of Radiology.* Charles C Thomas, Springfield, USA, 1983. [cited on page(s): 45, 50, 196, 217, 218, 220]

Jones, A. K., Pazik, F. D., Hintenlang, D. E., and Bolch, W. E. *MOSFET dosimeter depth-dose measurements in heterogeneous tissue-equivalent phantoms at diagnostic x-ray energies.* Medical Physics, 2005, 32(10):3209–3213. [cited on page(s): 71, 75]

Jones, D. G. and Shrimpton, P. C. *Normalized organ doses for x-ray computed tomography calculated using Monte Carlo techniques NRPB SR-250.* National Radiological Protection Board, Chilton, UK, 1993. [cited on page(s): 81]

Jones, D.G. and Shrimpton, P.C. *Survey of CT Practice in the UK. Part 3: normalised organ doses calculated using Monte Carlo techniques NRPB-R250.* National Radiological Protection Board, Chilton, UK, 1991. [cited on page(s): 81]

Kalendar, W. A. *Computed Tomography: Fundamentals, System Technology, Image Quality, Applications*. Publicis Corporate Publishing, Erlangen, Germany, 2005. [cited on page(s): 186, 192, 201, 202, 203, 204, 208]

Kalender, W. A., Schmidt, B., Zankl, M., and Schmidt, M. *A PC program for estimating organ dose and effective dose values in computed tomography*. European Radiology, 1999, 9(3):555–62. [cited on page(s): 79, 81]

Kalra, M. K., Maher, M. M., D'Souza, R., and Saini, S. *Multidetector computed tomography technology: current status and emerging developments*. Journal of Computer Assisted Tomography, 2004a, 28 Suppl 1:S2–6. [cited on page(s): 20, 149]

Kalra, M. K., Maher, M. M., Rizzo, S., and Saini, S. *Radiation exposure and projected risks with multidetector-row computed tomography scanning: clinical strategies and technologic developments for dose reduction*. Journal of Computer Assisted Tomography, 2004b, 28 Suppl 1:S46–9. [cited on page(s): 29]

Karsli, T., Kalra, M., Self, J., Rosenfeld, J., Butler, S., and Simoneaux, S. *What physicians think about the need for informed consent for communicating the risk of cancer from low-dose radiation*. Pediatric Radiology, 2009, 39(9):917–925. [cited on page(s): 27]

Kawaura, C., Aoyama, T., Koyama, S., Achiwa, M., and Mori, M. *Organ and effective dose evaluation in diagnostic radiology based on in-phantom dose measurements with novel photodiode-dosemeters*. Radiation Protection Dosimetry, 2006, 118(4):421–30. [cited on page(s): 47, 51, 53, 230, 231]

Keijzers, G. B. and Britton, C. J. *Doctors' knowledge of patient radiation exposure from diagnostic imaging requested in the emergency department*. Medical Journal of Australia, 2010, 193(8): 450–3. [cited on page(s): 32]

Khan, F.M. *The Physics of Radiation Therapy*. Lippincott Williams & Wilkins, USA, 2003. [cited on page(s): 218]

Khursheed, A., Hillier, M. C., Shrimpton, P. C., and Wall, B. F. *Influence of patient age on normalized effective doses calculated for CT examinations*. British Journal of Radiology, 2002, 75(898):819–30. [cited on page(s): 83, 84, 88, 91, 92]

Kim, J. E. and Newman, B. *Evaluation of a radiation dose reduction strategy for pediatric chest CT*. AJR. American Journal of Roentgenology, 2010, 194(5):1188–93. [cited on page(s): 29]

Kim, K. P., Lee, J., and Bolch, W. E. *CT dosimetry computer codes: their influence on radiation dose estimates and the necessity for their revision under new ICRP radiation protection standards*. Radiation Protection Dosimetry, 2011, 146(1-3):252–255. [cited on page(s): 80]

Kim, S., Frush, D., and Yoshizumi, T. *Bismuth shielding in CT: support for use in children*. Pediatric Radiology, 2010, 40(11):1739–1743. [cited on page(s): 28]

King, S. D. and Spiers, F. W. *Photoelectron enhancement of the absorbed dose from x rays to human bone marrow: Experimental and theoretical studies*. British Journal of Radiology, 1985, 58(688):345–356. [cited on page(s): 50, 51, 235]

Kleinerman, R. A. *Cancer risks following diagnostic and therapeutic radiation exposure in children*. Pediatric Radiology, 2006, 36 Suppl 14:121–5. [cited on page(s): 19]

Kleinman, P. L., Strauss, K. J., Zurakowski, D., Buckley, K. S., and Taylor, G. A. *Patient size measured on CT images as a function of age at a tertiary care children's hospital*. American Journal of Roentgenology, 2010, 194(6):1611–1619. [cited on page(s): 29, 122, 124]

Klig, J. E. *Issues of computerized tomography scans in children and implications for emergency care*. Current Opinion in Pediatrics, 2006, 18(3):231–3. [cited on page(s): 26]

Kramer, R., Zankl, M., Williams, G., and Drexler, G. *The calculation of dose from external photon exposures using reference human phantoms and Monte Carlo methods Part I: The male (ADAM) and female (EVA) adult mathematical phantoms.* National Research Center for Environment and Health (GSF), GSF Report S-885, Neuherberg, Germany, 1982. [cited on page(s): 80, 82]

Kramer, R., Vieira, J. W., Khoury, H. J., Lima, F. R., and Fuelle, D. *All about MAX: a male adult voxel phantom for Monte Carlo calculations in radiation protection dosimetry.* Physics in Medicine & Biology, 2003, 48(10):1239–62. [cited on page(s): 51, 52, 80]

Kron, T., Smith, A., and Hyodo, K. *Synchrotron radiation in the study of the variation of dose response in thermoluminescence dosimeters with radiation energy.* Australasian Physical & Engineering Sciences in Medicine, 1996, 19(4):225–36. [cited on page(s): 41, 219]

Kron, T., Duggan, L., Smith, T., Rosenfeld, A., Butson, M., Kaplan, G., Howlett, S., and Hyodo, K. *Dose response of various radiation detectors to synchrotron radiation.* Physics in Medicine & Biology, 1998, 43(11):3235–59. [cited on page(s): 44, 45]

Kron, T., DeWerd, L., Mobit, P., Muniz, J., Pradhan, A., Toivonen, M., and Waligorski, M. *A checklist for reporting of thermoluminescence dosimetry (TLD) measurements. Letter to the editor.* Physics in Medicine & Biology, 1999, 44(10):L15–7. [cited on page(s): 218]

Kuppermann, N. *Pediatric head trauma: the evidence regarding indications for emergent neuroimaging.* Pediatric Radiology, 2008, 38(Suppl. 4):S670–S674. [cited on page(s): 27]

Larson, D. B., Rader, S. B., Forman, H. P., and Fenton, L. Z. *Informing parents about CT radiation exposure in children: It's OK to tell them.* American Journal of Roentgenology, 2007, 189(2): 271–275. [cited on page(s): 27]

Larson, D. B., Johnson, L. W., Schnell, B. M., Goske, M. J., Salisbury, S. R., and Forman, H. P. *Rising use of CT in child visits to the emergency department in the United States, 1995-2008.* Radiology, 2011, 259(3):793–801. [cited on page(s): 22, 153]

Le Heron, J.C. *CTDOSE.* Christchurch, New Zealand, 1993. [cited on page(s): 79, 81]

Lechel, U., Becker, C., Langenfeld-Jager, G., and Brix, G. *Dose reduction by automatic exposure control in multidetector computed tomography: comparison between measurement and calculation.* European Radiology, 2009, 19(4):1027–34. [cited on page(s): 7, 42, 80, 100]

Lee, C. and Bolch, W. E. *Age-dependent organ and effective dose coefficients for external photons: a comparison of stylized and voxel-based paediatric phantoms.* Physics in Medicine & Biology, 2006, 51(18):4663–88. [cited on page(s): 80]

Lee, C., Park, S. H., and Lee, J. K. *Development of the two Korean adult tomographic computational phantoms for organ dosimetry.* Medical Physics, 2006a, 33(2):380–90. [cited on page(s): 80]

Lee, C., Shah, A. P., and Bolch, W. E. *An assessment of bone marrow and bone endosteum dosimetry methods for photon sources.* Physics in Medicine & Biology, 2006b, 51(21):5391–407. [cited on page(s): 7, 51, 52]

Lee, C., Williams, J. L., and Bolch, W. E. *Whole-body voxel phantoms of paediatric patients - UF Series B.* Physics in Medicine & Biology, 2006c, 51(18):4649–61. [cited on page(s): 80, 85, 86]

Lee, C., Lee, C., Staton, R. J., Hintenlang, D. E., Arreola, M. M., Williams, J. L., and Bolch, W. E. *Organ and effective doses in pediatric patients undergoing helical multislice computed tomography examination.* Medical Physics, 2007a, 34(5):1858–1873. [cited on page(s): 85, 86, 93, 94, 95, 100, 105, 106, 107, 255]

Lee, C., Lodwick, D., Hasenauer, D., Williams, J. L., and Bolch, W. E. *Hybrid computational phantoms of the male and female newborn patient: NURBS-based whole-body models.* Physics in Medicine & Biology, 2007b, 52(12):3309–33. [cited on page(s): 80]

Lee, C., Lodwick, D., Williams, J. L., and Bolch, W. E. *Hybrid computational phantoms of the 15-year male and female adolescent: applications to CT organ dosimetry for patients of variable morphometry.* Medical Physics, 2008a, 35(6):2366–82. [cited on page(s): 81]

Lee, C., Lodwick, D., Hurtado, J., Pafundi, D., Williams, J. L., and Bolch, W. E. *The UF family of reference hybrid phantoms for computational radiation dosimetry.* Physics in Medicine & Biology, 2010, 55(2):339–63. [cited on page(s): 81, 82]

Lee, C., Kim, K. P., Long, D., Fisher, R., Tien, C., Simon, S. L., Bouville, A., and Bolch, W. E. *Organ doses for reference adult male and female undergoing computed tomography estimated by Monte Carlo simulations.* Medical Physics, 2011, 38(3):1196–206. [cited on page(s): 80, 93, 94]

Lee, C. H., Goo, J. M., Ye, H. J., Ye, S. J., Park, C. M., Chun, E. J., and Im, J. G. *Radiation dose modulation techniques in the multidetector CT era: from basics to practice.* Radiographics, 2008b, 28(5):1451–9. [cited on page(s): 197]

Lee, C. I., Haims, A. H., Monico, E. P., Brink, J. A., and Forman, H. P. *Diagnostic CT scans: assessment of patient, physician, and radiologist awareness of radiation dose and possible risks.* Radiology, 2004, 231(2):393–8. [cited on page(s): 32]

Lewis, M. *Radiation dose issues in multi-slice CT scanning.* ImPACT Technology Update No. 3, UK, 2005. [cited on page(s): 24, 195, 197]

Lewis, M., Edyvean, S., Sassi, S., Kiremidjian, H., Keat, N., and Britten, A. *Estimating patient dose on current CT scanners: results of the ImPACT CT dose survey.* RAD Magazine, 2000, 26:17–18. [cited on page(s): 81]

Li, X., Samei, E., Segars, W. P., Sturgeon, G. M., Colsher, J. G., and Frush, D. P. *Patient-specific dose estimation for pediatric chest CT.* Medical Physics, 2008, 35(12):5821–5828. [cited on page(s): 81, 82, 83]

Li, X., Samei, E., Segars, W. P., Sturgeon, G. M., Colsher, J. G., and Frush, D. P. *Patient-specific radiation dose and cancer risk for pediatric chest CT.* Radiology, 2011a, 259(3):862–74. [cited on page(s): 63, 79, 81, 82, 83, 85, 86, 87, 96, 100, 106, 160, 256]

Li, X., Samei, E., Segars, W. P., Sturgeon, G. M., Colsher, J. G., Toncheva, G., Yoshizumi, T. T., and Frush, D. P. *Patient-specific radiation dose and cancer risk estimation in CT: part II. application to patients.* Medical Physics, 2011b, 38(1):408–19. [cited on page(s): 81, 82, 87]

Li, X., Samei, E., Segars, W. P., Sturgeon, G. M., Colsher, J. G., Toncheva, G., Yoshizumi, T. T., and Frush, D. P. *Patient-specific radiation dose and cancer risk estimation in CT: part I. development and validation of a Monte Carlo program.* Medical Physics, 2011c, 38(1):397–407. [cited on page(s): 80, 81, 82, 87]

Lindskoug, B. A. *The reference man in diagnostic radiology dosimetry.* British Journal of Radiology, 1992, 65(773):431–7. [cited on page(s): 88]

Linton, O. W. and Mettler, Jr. F. A. *National conference on dose reduction in CT, with an emphasis on pediatric patients.* AJR. American Journal of Roentgenology, 2003, 181(2):321–9. [cited on page(s): 24, 26]

Loubele, M., Bogaerts, R., Van Dijck, E., Pauwels, R., Vanheusden, S., Suetens, P., Marchal, G., Sanderink, G., and Jacobs, R. *Comparison between effective radiation dose of CBCT and MSCT scanners for dentomaxillofacial applications.* European Journal of Radiology, 2009, 71 (3):461–468. [cited on page(s): 220]

Lucaya, J., Piqueras, J., Garcia-Pena, P., Enriquez, G., Garcia-Macias, M., and Sotil, J. *Low-dose high-resolution CT of the chest in children and young adults: dose, cooperation, artifact incidence, and image quality.* AJR. American Journal of Roentgenology, 2000, 175(4):985–92. [cited on page(s): 29, 30]

Luo, L. Z. and Rotunda, J. E. *Performance of harshaw TLD-100H two-element dosemeter.* Radiation Protection Dosimetry, 2006, 120(1-4):324–30. [cited on page(s): 219]

Lupke, M., Goblet, F., Polivka, B., and Seifert, H. *Sensitivity loss of Lif:Mg,Cu,P thermoluminescence dosemeters caused by oven annealing.* Radiation Protection Dosimetry, 2006, 121(2): 195–201. [cited on page(s): 41]

Margo, J. *CT scans pose risk of cancer.* The Australian Financial Review, 12 March 2009. [cited on page(s): 26, 27]

Marin, D., Nelson, R. C., Schindera, S. T., Richard, S., Youngblood, R. S., Yoshizumi, T. T., and Samei, E. *Low-tube-voltage, high-tube-current multidetector abdominal CT: improved image quality and decreased radiation dose with adaptive statistical iterative reconstruction algorithm–initial clinical experience.* Radiology, 2010, 254(1):145–53. [cited on page(s): 199]

Martin, C J. *Effective dose: how should it be applied to medical exposures?* British Journal of Radiology, 2007, 80(956):639–647. [cited on page(s): 80, 83]

Mathews, J. D. and Chesson, J. *Seminar - do we need to re-evaluate the health effects of ionising radiation?* The University of Melbourne, School of Population Health, 18 February 2009. [cited on page(s): 172, 181]

McCollough, C. H. *CT dose: how to measure, how to reduce.* Health Physics, 2008, 95(5):508–17. [cited on page(s): 29]

McCollough, C. H. and Zink, F. E. *Performance evaluation of a multi-slice CT system.* Medical Physics, 1999, 26(11):2223–30. [cited on page(s): 89]

McCollough, C. H., Bruesewitz, M. R., and Kofler, Jr. J. M. *CT dose reduction and dose management tools: overview of available options.* Radiographics, 2006, 26(2):503–12. [cited on page(s): 24, 197]

McCollough, C. H., Christner, J. A., and Kofler, J. M. *How effective is effective dose as a predictor of radiation risk?* AJR. American Journal of Roentgenology, 2010, 194(4):890–6. [cited on page(s): 37, 61]

McDermott, A., White, R. A., Mc-Nitt-Gray, M., Angel, E., and Cody, D. *Pediatric organ dose measurements in axial and helical multislice CT.* Medical Physics, 2009, 36(5):1494–1499. [cited on page(s): 6, 36]

McLean, D., Malitz, N., and Lewis, S. *Survey of effective dose levels from typical paediatric CT protocols.* Australasian Radiology, 2003, 47(2):135–42. [cited on page(s): 139, 140]

McNitt-Gray, M. F. *AAPM/RSNA physics tutorial for residents: Topics in CT. radiation dose in CT.* Radiographics, 2002, 22(6):1541–53. [cited on page(s): 28]

Medicare Australia Health Statistics, 2011. URL www.medicareaustralia.gov.au. [cited on page(s): 145, 146, 147, 149, 169]

Mendelson, R. M., Fox, R. A., and de Klerk, N. H. *Alarm about computed tomography scans is unjustified [letter].* Medical Journal of Australia, 2010, 193(4):246. [cited on page(s): 15]

Merck, L. H., Hauck, M. G., Houry, D. E., Lowery-North, D. W., Hemphill, R. R., and Applegate, K. E. *Informed consent for computed tomography.* The American Journal of Emergency Medicine, 2011, 29(2):230–232. [cited on page(s): 27]

Mettler, F. A., Bhargavan, M., Faulkner, K., Gilley, D. B., Gray, J. E., Ibbott, G. S., Lipoti, J. A., Mahesh, M., McCrohan, J. L., Stabin, M. G., Thomadsen, B. R., and Yoshizumi, T. T. *Radiologic and nuclear medicine studies in the United States and worldwide: Frequency, radiation dose, and comparison with other radiation source 1950-2007.* Radiology, 2009, 253(2):520–531. [cited on page(s): 21, 149, 151]

Mettler, F. A. Jr., Wiest, P. W., Locken, J. A., and Kelsey, C. A. *CT scanning: patterns of use and dose.* Journal of Radiological Protection, 2000, 20(4):353–9. [cited on page(s): 22, 149]

Mettler, F. A. Jr., Thomadsen, B. R., Bhargavan, M., Gilley, D. B., Gray, J. E., Lipoti, J. A., McCrohan, J., Yoshizumi, T. T., and Mahesh, M. *Medical radiation exposure in the U.S. in 2006: preliminary results.* Health Physics, 2008, 95(5):502–7. [cited on page(s): 21, 149]

Miksys, N., Gordon, C. L., Thomas, K., and Connolly, B. L. *Estimating effective dose to pediatric patients undergoing interventional radiology procedures using anthropomorphic phantoms and MOSFET dosimeters.* AJR. American Journal of Roentgenology, 2010, 194(5):1315–22. [cited on page(s): 71, 75]

Moscovitch, M. *Personnel dosimetry using LiF:Mg,Cu,P.* Radiation Protection Dosimetry, 1999, 85(1-4):49–56. [cited on page(s): 219, 220]

Moscovitch, M. and Horowitz, Y. S. *Thermoluminescent materials for medical applications: LiF:Mg,Ti and LiF:Mg,Cu,P.* Radiation Measurements, 2007, 41(Supplement 1):S71–S77. [cited on page(s): 40, 41, 45, 218, 219, 220]

Moss, M. and McLean, D. *Paediatric and adult computed tomography practice and patient dose in Australia.* Australasian Radiology, 2006, 50(1):33–40. [cited on page(s): 21, 111, 126, 127, 139, 140]

Muhogora, W. E., Ahmed, N. A., AlSuwaidi, J. S., Beganovic, A., Ciraj-Bjelac, O., Gershan, V., Gershkevitsh, E., Grupetta, E., Kharita, M. H., Manatrakul, N., Maroufi, B., Milakovic, M., Ohno, K., Ben Omrane, L., Ptacek, J., Schandorf, C., Shaaban, M. S., Toutaoui, N., Sakkas, D., Wambani, J. S., and Rehani, M. M. *Paediatric CT examinations in 19 developing countries: frequency and radiation dose.* Radiation Protection Dosimetry, 2010, 140(1):49–58. [cited on page(s): 21, 22, 111]

Mukundan, S. Jr., Wang, P. I., Frush, D. P., Yoshizumi, T., Marcus, J., Kloeblen, E., and Moore, M. *MOSFET dosimetry for radiation dose assessment of bismuth shielding of the eye in children.* AJR. American Journal of Roentgenology, 2007, 188(6):1648–50. [cited on page(s): 28, 35, 37, 71, 75]

Na, Y. H., Zhang, J., Ding, A., and Xu, X. G. Mesh-based and anatomically adjustable adult phantoms and a case study in virtual calibration of a lung counter for female workers. In Xu, X.G. and Eckerman, K.F., editors, *Handbook of Anatomical Models for Radiation Dosimetry*, pages 347–375. Taylor and Francis Group LLC, Boca Raton, Florida, USA, 2010. [cited on page(s): 54]

Nafziger, B. *Is the growth of pediatric CT slowing down?*, 21 April 2011. [cited on page(s): 154]

Nagel, H. D., editor. *Radiation Exposure in Computed Tomography: Fundamentals, Influencing Parameters, Dose Assessment, Optimisation, Scanner Data, Terminology.* CTB Publications, Hamburg, Germany, 2002. [cited on page(s): 81, 96, 214]

Nair, R. R., Rajan, B., Akiba, S., Jayalekshmi, P., Nair, M. K., Gangadharan, P., Koga, T., Morishima, H., Nakamura, S., and Sugahara, T. *Background radiation and cancer incidence in Kerala, India-Karanagappally cohort study.* Health Physics, 2009, 96(1):55–66. [cited on page(s): 15]

Nawfel, R. D., Judy, P. F., Silverman, S. G., Hooton, S., Tuncali, K., and Adams, D. F. *Patient and personnel exposure during CT fluoroscopy-guided interventional procedures.* Radiology, 2000, 216(1):180–4. [cited on page(s): 42]

NCRP, National Council on Radiation Protection & Measurements. *Exposure of the US Population from Diagnostic Medical Radiation. NCRP Report 100.* Bethesda, US, 1989. [cited on page(s): 21]

NCRP, National Council on Radiation Protection & Measurements. *Ionizing Radiation Exposure of the Population of the United States. NCRP Report 160.* Bethesda, MD, US, 2009. [cited on page(s): 5, 13, 21, 143, 149, 151, 169]

Nickoloff, E. *Current adult and pediatric CT doses.* Pediatric Radiology, 2002, 32(4):250–60. [cited on page(s): 24, 30, 210]

Nickoloff, E. L. and Alderson, P. O. *Radiation exposures to patients from CT: reality, public perception, and policy.* AJR. American Journal of Roentgenology, 2001, 177(2):285–7. [cited on page(s): 21]

Nickoloff, E. L., Dutta, A. K., and Lu, Z. F. *Influence of phantom diameter, kVp and scan mode upon computed tomography dose index.* Medical Physics, 2003, 30(3):395–402. [cited on page(s): 24, 210]

Nievelstein, R., van Dam, I., and van der Molen, A. *Multidetector CT in children: current concepts and dose reduction strategies.* Pediatric Radiology, 2010, 40(8):1324–1344. [cited on page(s): 24, 28]

Nishizawa, K., Mori, S., Ohno, M., Yanagawa, N., Yoshida, T., Akahane, K., Iwai, K., and Wada, S. *Patient dose estimation for multi-detector-row CT examinations.* Radiation Protection Dosimetry, 2008, 128(1):98–105. [cited on page(s): 6, 35, 36, 39, 51, 53, 214]

NRC, National Research Council of the National Academies. Board on Radiation Effects Research. *Health Effects of Exposure to Low Levels of Ionizing Radiation (BEIR V).* Washington, DC, US, 1990. [cited on page(s): 168, 173]

NRC, National Research Council of the National Academies. Board on Radiation Effects Research. *Health Risks from Exposure to Low Levels of Ionizing Radiation: BEIR VII Phase 2.* Washington, DC, US, 2006. [cited on page(s): 14, 15, 16, 17, 18, 92, 111, 157, 159, 162, 165, 168, 172, 173, 174, 175, 177, 266, 267]

Oestmann, J.-W. *The role and impact of reference doses in diagnostic radiology: Problems and perspectives.* Radiation Protection Dosimetry, 1998, 80(1-3):21–22. [cited on page(s): 112]

Olko, P., Bilski, P., Ryba, E., and Niewiadomski, T. *Microdosimetric interpretation of the anomalous photon energy response of ultra-sensitive LiF:Mg,Cu,P TL dosemeters.* Radiation Protection Dosimetry, 1993, 47(1-4):31–35. [cited on page(s): 219, 220]

Olko, P., Bilski, P., and Michalik, V.M. *Microdosimetric analysis of the response of LiF thermoluminescent detectors for radiations of different qualities.* Radiation Protection Dosimetry, 1994, 52(1-4):405–408. [cited on page(s): 220]

Ono, K., Ban, N., Ojima, M., Yoshinaga, S., Akahane, K., Fujii, K., Toyota, M., Hamada, F., Kouriyama, C., Akiba, S., Kunugita, N., Shimada, Y., and Kai, M. *Nationwide survey on pediatric CT among children of public health and school nurses to examine a possibility for a follow-up study on radiation effects.* Radiation Protection Dosimetry, 2011a, 146(1-3):260–2. [cited on page(s): 169]

Ono, K., Yoshitake, T., Hasegawa, T., Ban, N., and Kai, M. *Estimation of the number of CT procedures based on a nationwide survey in Japan.* Health Physics, 2011b, 100(5):491–6. [cited on page(s): 151]

Osmond, M. H., Klassen, T. P., Wells, G. A., Correll, R., Jarvis, A., Joubert, G., Bailey, B., Chauvin-Kimoff, L., Pusic, M., McConnell, D., Nijssen-Jordan, C., Silver, N., Taylor, B., and Stiell, I. G. *CATCH: a clinical decision rule for the use of computed tomography in children with minor head injury.* Canadian Medical Association Journal, 2010, 182(4):341–8. [cited on page(s): 27]

Pages, J, Buls, N, and Osteaux, M. *CT doses in children: a multicentre study.* British Journal of Radiology, 2003, 76(911):803–811. [cited on page(s): 125]

Parker, M. S., Kelleher, N. M., Hoots, J. A., Chung, J. K., Fatouros, P. P., and Benedict, S. H. *Absorbed radiation dose of the female breast during diagnostic multidetector chest CT and dose reduction with a tungsten-antimony composite breast shield: preliminary results.* Clinical Radiology, 2008, 63(3):278–88. [cited on page(s): 28]

Partrick, D. A., Janik, J. E., Janik, J. S., Bensard, D. D., and Karrer, F. M. *Increased CT scan utilization does not improve the diagnostic accuracy of appendicitis in children.* Journal of Pediatric Surgery, 2003, 38(5):659–62. [cited on page(s): 32]

Paterson, A. and Frush, D. P. *Dose reduction in paediatric MDCT: general principles.* Clinical Radiology, 2007, 62(6):507–17. [cited on page(s): 26, 28, 29]

Paterson, A., Frush, D. P., and Donnelly, L. F. *Helical CT of the body: are settings adjusted for pediatric patients?* AJR. American Journal of Roentgenology, 2001, 176(2):297–301. [cited on page(s): 6, 22, 23, 24, 31, 153, 161, 168, 181]

Pearce, M. S. *Patterns in paediatric CT use: An international and epidemiological perspective.* Journal of Medical Imaging and Radiation Oncology, 2011, 55(2):107–109. [cited on page(s): 154]

Pearce, M. S., Salotti, J. A., McHugh, K., Metcalf, W., Kim, K. P., Craft, A. W., Parker, L., and Ron, E. *CT scans in young people in Northern England: trends and patterns 1993-2002.* Pediatric Radiology, 2011, 41(7):832–8. [cited on page(s): 92, 151, 169]

Peet, D. J. and Pryor, M. D. *Evaluation of a MOSFET radiation sensor for the measurement of entrance surface dose in diagnostic radiology.* British Journal of Radiology, 1999, 72(858):562–8. [cited on page(s): 71, 75]

Petoussi-Henss, N., Zanki, M., Fill, U., and Regulla, D. *The GSF family of voxel phantoms.* Physics in Medicine & Biology, 2002, 47(1):89–106. [cited on page(s): 80, 82]

Picano, E. *Informed consent and communication of risk from radiological and nuclear medicine examinations: how to escape from a communication inferno.* BMJ, 2004, 329(7470):849–51. [cited on page(s): 23, 27]

Pierce, D. A., Shimizu, Y., Preston, D. L., Vaeth, M., and Mabuchi, K. *Studies of the mortality of atomic bomb survivors. Report 12, part I. cancer: 1950-1990.* Radiation Research, 1996, 146 (1):1–27. [cited on page(s): 15]

Pradhan, A.S. and Bhatt, R.C. *Thermoluminescence response of LiF:Mg,Cu,P, and LiF TLD-100 to thermal neutrons, 241Am alphas and gamma rays (abst).* Radiation Protection Dosimetry, 1989, 27(3):185–188. [cited on page(s): 220]

Preston, D. L., Shimizu, Y., Pierce, D. A., Suyama, A., and Mabuchi, K. *Studies of mortality of atomic bomb survivors. Report 13: Solid cancer and noncancer disease mortality: 1950-1997.* Radiation Research, 2003, 160(4):381–407. [cited on page(s): 14]

Preston, R. J. *Update on linear non-threshold dose-response model and implications for diagnostic radiology procedures.* Health Physics, 2008, 95(5):541–6. [cited on page(s): 16]

Primak, A. N., Fletcher, J. G., Vrtiska, T. J., Dzyubak, O. P., Lieske, J. C., Jackson, M. E., Williams, Jr. J. C., and McCollough, C. H. *Noninvasive differentiation of uric acid versus non-uric acid kidney stones using dual-energy CT.* Academic Radiology, 2007, 14(12):1441–7. [cited on page(s): 195]

Prokop, M. and Galanski, M. *Spiral and Multislice Computed Tomography of the Body.* Thieme Medical Publishers, New York, USA, 2003. [cited on page(s): 188, 191]

PSR, Professional Services Review. *Report to the Professions 2008-09.* Canberra, Australian Capital Territory, Australia, 2010. [cited on page(s): 26]

Quinn, A. D., Taylor, C. G., Sabharwal, T., and Sikdar, T. *Radiation protection awareness in non-radiologists.* British Journal of Radiology, 1997, 70(829):102–106. [cited on page(s): 32]

Ramlo, M., Moscovitch, M., and Rotunda, J. E. *Further studies in the reduction of residual in harshaw TLD-100H (LiF:Mg,Cu,P).* Radiation Protection Dosimetry, 2007, 125(1-4):217–9. [cited on page(s): 41, 219]

RANZCR, The Royal Australian and New Zealand College of Radiologists. *Position Statement on Computed Tomography and Radiation Risks*, 2010. [cited on page(s): 24]

RCH, The Royal Children's Hospital Melbourne. *RCH Annual Financial Report 2007-2008.* Melbourne, Victoria, Australia, 2008. [cited on page(s): 113, 141]

Reed, M. H. *Imaging utilization commentary: a radiology perspective.* Pediatric Radiology, 2008, 38 Suppl 4:S660–3. [cited on page(s): 32]

Rehani, M. M. and Berry, M. *Radiation doses in computed tomography. the increasing doses of radiation need to be controlled.* BMJ, 2000, 320(7235):593–4. [cited on page(s): 20, 149]

Reilly, A.J. and Sutton, D. *Spectrum Processor.* The Institute of Physics and Engineering in Medicine, UK, 1997. [cited on page(s): 38, 43, 65, 185]

Rice, H. E., Frush, D. P., Harker, M. J., Farmer, D., and Waldhausen, J. H. *Peer assessment of pediatric surgeons for potential risks of radiation exposure from computed tomography scans.* Journal of Pediatric Surgery, 2007, 42(7):1157–1164. [cited on page(s): 32]

Risks and benefits in pediatric CT. MR/CT Committee of the Society of Pediatric Radiology. Pediatric Radiology, 2001, 31(6):387. [cited on page(s): 23]

Robinson, A., Hill, E., and Harpen, M. *Radiation dose reduction in pediatric CT.* Pediatric Radiology, 1986, 16(1):53–54. [cited on page(s): 22]

Rogers, L. F. *Taking care of children: check out the parameters used for helical CT.* AJR. American Journal of Roentgenology, 2001, 176(2):287. [cited on page(s): 22]

Saito, K., Wittmann, A., Koga, S., Ida, Y., Kamei, T., Funabiki, J., and Zankl, M. *Construction of a computed tomographic phantom for a Japanese male adult and dose calculation system.* Radiation and Environmental Biophysics, 2001, 40(1):69–75. [cited on page(s): 80]

Saxena, A. K., Prasad, K., and Kaza, R. K. *Reducing radiation dose to pediatric patients.* AJR. American Journal of Roentgenology, 2005, 185(6):1658. [cited on page(s): 31]

Scalzetti, E. M., Huda, W., Bhatt, S., and Ogden, K. M. *A method to obtain mean organ doses in a RANDO phantom.* Health Physics, 2008, 95(2):241–4. [cited on page(s): 47, 230, 231]

Schardt, P., Deuringer, J., Freudenberger, J., Hell, E., Knupfer, W., Mattern, D., and Schild, M. *New x-ray tube performance in computed tomography by introducing the rotating envelope tube technology.* Medical Physics, 2004, 31(9):2699–706. [cited on page(s): 186]

Schilham, A., van der Molen, A. J., Prokop, M., and de Jong, H. W. *Overranging at multisection CT: an underestimated source of excess radiation exposure.* Radiographics, 2010, 30(4):1057–67. [cited on page(s): 202, 203]

Schlattl, H., Zankl, M., and Petoussi-Henss, N. *Organ dose conversion coefficients for voxel models of the reference male and female from idealized photon exposures.* Physics in Medicine & Biology, 2007, 52(8):2123–45. [cited on page(s): 52]

Schmidt, T. and Behling, R. *MRC: a successful platform for future x-ray tube development.* MedicalMundi (published by Philips Healthcare), 2000, 44(2):50–55. [cited on page(s): 186]

Segars, W. P., Mahesh, M., Beck, T. J., Frey, E. C., and Tsui, B. M. *Realistic CT simulation using the 4D XCAT phantom.* Medical Physics, 2008, 35(8):3800–8. [cited on page(s): 81]

Sessions, J. B., Roshau, J. N., Tressler, M. A., Hintenlang, D. E., Arreola, M. M., Williams, J. L., Bouchet, L. G., and Bolch, W. E. *Comparisons of point and average organ dose within an anthropomorphic physical phantom and a computational model of the newborn patient.* Medical Physics, 2002, 29(6):1080–9. [cited on page(s): 71, 75]

Shiralkar, S., Rennie, A., Snow, M., Galland, R. B., Lewis, M. H., and Gower-Thomas, K. *Doctors' knowledge of radiation exposures is deficient.* BMJ, 2002, 324(7342):919. [cited on page(s): 32]

Shope, T. B., Gagne, R. M., and Johnson, G. C. *A method for describing the doses delivered by transmission x-ray computed tomography.* Medical Physics, 1981, 8(4):488–95. [cited on page(s): 208]

Shrimpton, P. C. and Edyvean, S. *CT scanner dosimetry.* British Journal of Radiology, 1998, 71 (841):1–3. [cited on page(s): 81]

Shrimpton, P. C. and Wall, B. F. *Reference doses for paediatric computed tomography.* Radiation Protection Dosimetry, 2000, 90(1-2):249–252. [cited on page(s): 31, 83, 114, 122, 135, 224]

Shrimpton, P. C. and Wall, B. F. *Effective dose and dose-length product in CT.* Radiology, 2009, 250(2):604–605. [cited on page(s): 83]

Shrimpton, P. C., Jones, D. G., Hillier, M. C., Wall, B. F., Le Heron, J. C., and Faulkner, K. *Survey of CT Practice in the UK. 2. Dosimetric Aspects NRPB Report 249.* National Radiological Protection Board, Chilton, UK, 1991. [cited on page(s): 173, 264]

Shrimpton, P. C., Hillier, M. C., Lewis, M. A., and Dunn, M. *Doses from Computed Tomography (CT) Examinations in the UK - 2003 Review Report NRPB-W67.* National Radiological Protection Board, Chilton, UK, 2005. [cited on page(s): 112, 115, 116, 122, 129, 133, 134, 135, 136, 224]

Shrimpton, P. C., Hillier, M. C., Lewis, M. A., and Dunn, M. *National survey of doses from CT in the UK: 2003.* British Journal of Radiology, 2006, 79(948):968–80. [cited on page(s): 21, 83, 85, 88, 96, 103, 111, 115, 117, 121, 174, 224, 257]

Shrimpton, P.C. *2004 CT Quality Criteria. appendix C: Assessment of Patient Dose in CT (also NRPB-PE/1/2004).* National Radiological Protection Board, Oxon, UK, 2004. [cited on page(s): 81, 82, 83, 85, 89, 96, 258]

Shuryak, I., Sachs, R. K., and Brenner, D. J. *Cancer risks after radiation exposure in middle age.* Journal of the National Cancer Institute, 2010, 102(21):1628–36. [cited on page(s): 17, 165, 172]

Sidhu, M., Coley, B., Goske, M., Connolly, B., Racadio, J., Yoshizumi, T., Utley, T., and Strauss, K. *Image Gently, Step Lightly: increasing radiation dose awareness in pediatric interventional radiology.* Pediatric Radiology, 2009, 39(10):1135–1138. [cited on page(s): 32]

Siegel, M. J., Schmidt, B., Bradley, D., Suess, C., and Hildebolt, C. *Radiation dose and image quality in pediatric CT: effect of technical factors and phantom size and shape.* Radiology, 2004, 233(2):515–22. [cited on page(s): 24, 115]

Siemens Sensation 16 Straton Manual, Year not available. [cited on page(s): 39, 43]

Silva, A. C., Lawder, H. J., Hara, A., Kujak, J., and Pavlicek, W. *Innovations in CT dose reduction strategy: application of the adaptive statistical iterative reconstruction algorithm.* AJR. American Journal of Roentgenology, 2010, 194(1):191–9. [cited on page(s): 199]

Singh, S., Kalra, M. K., Moore, M. A., Shailam, R., Liu, B., Toth, T. L., Grant, E., and Westra, S. J. *Dose reduction and compliance with pediatric CT protocols adapted to patient size, clinical indication, and number of prior studies.* Radiology, 2009, 252(1):200–208. [cited on page(s): 29, 31]

Sivit, C. J. *Contemporary imaging in abdominal emergencies.* Pediatric Radiology, 2008, 38 Suppl 4:S675–8. [cited on page(s): 32]

Smith, A., Shah, G. A., and Kron, T. *Variation of patient dose in head CT.* British Journal of Radiology, 1998, 71(852):1296–301. [cited on page(s): 42]

Smith-Bindman, R. *Is computed tomography safe?* New England Journal of Medicine, 2010, 363 (1):1–4. [cited on page(s): 19]

Smith-Bindman, R., Lipson, J., Marcus, R., Kim, K. P., Mahesh, M., Gould, R., Berrington de Gonzalez, A., and Miglioretti, D. L. *Radiation dose associated with common computed tomography examinations and the associated lifetime attributable risk of cancer.* Archives of Internal Medicine, 2009, 169(22):2078–86. [cited on page(s): 19, 21, 111, 158, 166, 168, 169, 174]

Snyder, W.S., Ford, M.R., Warner, G.G., and Fisher, H.L. *Estimates of absorbed fractions for monoenergetic photon sources uniformly distributed in various organs of a heterogeneous phantom.* Society of Nuclear Medicine, MIRD Pamphlet No. 5, New York, US, 1969. [cited on page(s): 80]

Sodickson, A., Baeyens, P. F., Andriole, K. P., Prevedello, L. M., Nawfel, R. D., Hanson, R., and Khorasani, R. *Recurrent CT, cumulative radiation exposure, and associated radiation-induced cancer risks from CT of adults.* Radiology, 2009, 251(1):175–84. [cited on page(s): 27]

Soye, J. A. and Paterson, A. *A survey of awareness of radiation dose among health professionals in Northern Ireland.* British Journal of Radiology, 2008, 81(969):725–729. [cited on page(s): 32]

Stamm, G. and Nagel, H. D. *CT-Expo V2.0: A Tool for Dose Evaluation in Computed Tomography, User's Guide.* Hannover, Germany, 2011a. [cited on page(s): 214]

Stamm, G. and Nagel, H. D. *CT-Expo V2.0.1: A Tool for Dose Evaluation in Computed Tomography.* Hannover, Germany, 2011b. [cited on page(s): xvii, 79, 81, 84, 85, 96, 97, 105, 106, 107, 128, 129, 166, 174]

Stark, J. *Super scanner gets right to the heart of the matter.* The Age, Australia, 2008. [cited on page(s): 191]

Stirling, G. and Cotterill, A. *Medical use of computed tomography (CT) and patient doses in New Zealand in 2007 (draft).* New Zealand National Radiation Laboratory, 2008. [cited on page(s): 149]

Strauss, K. J., Goske, M. J., Kaste, S. C., Bulas, D., Frush, D. P., Butler, P., Morrison, G., Callahan, M. J., and Applegate, K. E. *Image gently: Ten steps you can take to optimize image quality and lower CT dose for pediatric patients.* AJR. American Journal of Roentgenology, 2010, 194(4):868–73. [cited on page(s): 25, 28]

Street, M., Brady, Z., Van Every, B., and Thomson, K. R. *Radiation exposure and the justification of computed tomography scanning in an Australian hospital emergency department.* Internal Medicine Journal, 2009, 39(11):713–9. [cited on page(s): 27]

Studdert, D. M., Mello, M. M., Sage, W. M., DesRoches, C. M., Peugh, J., Zapert, K., and Brennan, T. A. *Defensive medicine among high-risk specialist physicians in a volatile malpractice environment.* JAMA: The Journal of the American Medical Association, 2005, 293(21):2609–2617. [cited on page(s): 26]

STUK, Radiation and Nuclear Safety Authority. *PCXMC Dose Calculations, Version 2.0.* Helsinki, Finland, 2008. [cited on page(s): xviii, 84, 85]

Suess, C. and Chen, X. *Dose optimization in pediatric CT: current technology and future innovations.* Pediatric Radiology, 2002, 32(10):729–34. [cited on page(s): 29, 30]

Sykes, P. J. and Day, T. K. *Requirements for identification of low dose and non-linear mutagenic responses to ionising radiation.* Dose Response, 2007, 5(4):308–14. [cited on page(s): 15]

Takahashi, N., Hartman, R. P., Vrtiska, T. J., Kawashima, A., Primak, A. N., Dzyubak, O. P., Mandrekar, J. N., Fletcher, J. G., and McCollough, C. H. *Dual-energy CT iodine-subtraction*

virtual unenhanced technique to detect urinary stones in an iodine-filled collecting system: a phantom study. AJR. American Journal of Roentgenology, 2008, 190(5):1169–73. [cited on page(s): 195]

Tapiovaara, M. and Siiskonen, T. *PCXMC: A PC-based Monte Carlo program for calculating patient doses in medical x-ray examinations (2nd ed.).* Finnish Centre for Radiation and Nuclear Safety, Report STUK-A139, Helsinki, 2008. [cited on page(s): 84, 86, 105, 106, 107, 159, 226, 227]

Theodorakou, C. and Horrocks, J. A. *A study on radiation doses and irradiated areas in cerebral embolisation.* British Journal of Radiology, 2003, 76(908):546–552. [cited on page(s): 220]

Thermo scientific materials and assemblies for thermoluminescent dosimetry: Product overview, 2007. [cited on page(s): 40]

Thomas, K. and Wang, B. *Age-specific effective doses for pediatric MSCT examinations at a large children's hospital using DLP conversion coefficients: a simple estimation method.* Pediatric Radiology, 2008, 38(6):645–656. [cited on page(s): 125]

Thomson, J. E. M. and Tingey, D. R. C. *Radiation doses from computed tomography in Australia.* Australian Radiation Laboratory, ARL/TR123, Yallambie, Victoria, Australia, 1997. [cited on page(s): 20, 139, 140, 148, 152, 169]

Toth, T. L. *Dose reduction opportunities for CT scanners.* Pediatric Radiology, 2002, 32(4):261–7. [cited on page(s): 184, 193, 195]

Townsend, B. A., Callahan, M. J., Zurakowski, D., and Taylor, G. A. *Has pediatric CT at children's hospitals reached its peak?* AJR. American Journal of Roentgenology, 2010, 194(5):1194–6. [cited on page(s): 22, 32, 153]

Turner, A. C., Zankl, M., DeMarco, J. J., Cagnon, C. H., Zhang, D., Angel, E., Cody, D. D., Stevens, D. M., McCollough, C. H., and McNitt-Gray, M. F. *The feasibility of a scanner-independent technique to estimate organ dose from MDCT scans: using CTDIvol to account for differences between scanners.* Medical Physics, 2010, 37(4):1816–25. [cited on page(s): 82]

Turner, A. C., Zhang, D., Khatonabadi, M., Zankl, M., DeMarco, J. J., Cagnon, C. H., Cody, D. D., Stevens, D. M., McCollough, C. H., and McNitt-Gray, M. F. *The feasibility of patient size-corrected, scanner-independent organ dose estimates for abdominal CT exams.* Medical Physics, 2011, 38(2):820–9. [cited on page(s): 79, 82, 83, 85, 87, 88, 96, 100, 101, 107, 256]

UNSCEAR, United Nations Scientific Committee on the Effects of Atomic Radiation. *Sources and Effects of Ionizing Radiation. volume I: Sources, Volume II: Effects.* New York, US, 2000. [cited on page(s): 14, 15, 20, 21]

UNSCEAR, United Nations Scientific Committee on the Effects of Atomic Radiation. *Sources and Effects of Ionizing Radiation. volume I.* New York, US, 2010a. [cited on page(s): 13, 20, 21, 22, 112]

UNSCEAR, United Nations Scientific Committee on the Effects of Atomic Radiation. *Report of the United Nations Scientific Committee on the Effects of Atomic Radiation, Official Records, General Assembly, Sixty-fifth Session, Supplement No. 46*, 2010b. [cited on page(s): 22]

van der Molen, A. J. and Geleijns, J. *Overranging in multisection CT: quantification and relative contribution to dose-comparison of four 16-section CT scanners.* Radiology, 2007, 242(1):208–16. [cited on page(s): 60, 69, 100, 115, 124, 202]

Varchena, V. *Pediatric phantoms.* Pediatric Radiology, 2002, 32(4):280–4. [cited on page(s): 39, 40]

Veit, R., Zankl, M., Petoussi, N., Mannweiler, E., Williams, G., and Drexler, G. *Tomographic anthropomorphic models, Part I: construction technique and description of models of an 8 week*

old baby and a 7 year old child. National Research Centre for Environment and Health (GSF), GSF Report 3/89, Neuherberg, Germany, 1989. [cited on page(s): 82, 84, 85]

Verdun, F. R., Lepori, D., Monnin, P., Valley, J. F., Schnyder, P., and Gudinchet, F. *Management of patient dose and image noise in routine pediatric CT abdominal examinations.* European Radiology, 2004, 14(5):835–41. [cited on page(s): 29, 30]

Verdun, F. R., Gutierrez, D., Vader, J. P., Aroua, A., Alamo-Maestre, L. T., Bochud, F., and Gudinchet, F. *CT radiation dose in children: a survey to establish age-based diagnostic reference levels in Switzerland.* European Radiology, 2008, 18(9):1980–6. [cited on page(s): 133, 134, 135, 137, 224]

Vock, P. *CT dose reduction in children.* European Radiology, 2005, 15(11):2330–40. [cited on page(s): 20, 24, 28, 149]

Wachtel, R. E., Dexter, F., and Dow, A. J. *Growth rates in pediatric diagnostic imaging and sedation.* Anesthesia & Analgesia, 2009, 108(5):1616–21. [cited on page(s): 153]

Wagner, L. K. *Practical dilemmas in implementing benefit-risk protocols.* Pediatric Radiology, 2002, 32(4):238–41. [cited on page(s): 32]

Wall, B. F., Kendall, G. M., Edwards, A. A., Bouffler, S., Muirhead, C. R., and Meara, J. R. *What are the risks from medical X-rays and other low dose radiation?* British Journal of Radiology, 2006, 79(940):285–94. [cited on page(s): 16, 19]

Wallace, A., Sibelle, K., Budd, R., Goergen, S., and Heggie, J. *A national dosimetric survey of common scanning procedures for paediatric CT examinations.* Australasian Physical & Engineering Sciences in Medicine, 2007a, 30(4):402. [cited on page(s): 126, 128]

Wallace, A., Sibelle, K., Stanley, M., Budd, R., and Goergen, S. *Paediatric CT dosimetry survey - a QUDI funded research project.* Presented at the RANZCR Annual Scientific Meeting, Melbourne, Victoria, Australia, 2007b. [cited on page(s): 126, 128]

Wallace, A. B., Goergen, S. K., Schick, D., Soblusky, T., and Jolley, D. *Multidetector CT dose: clinical practice improvement strategies from a successful optimization program.* Journal of the American College of Radiology, 2010, 7(8):614–24. [cited on page(s): 21, 111]

Wang, B., Xu, X. G., and Kim, C.-H. *Monte Carlo study of MOSFET dosemeter characteristics: dose dependence on photon energy, direction and dosemeter composition.* Radiation Protection Dosimetry, 2005, 113(1):40–46. [cited on page(s): 71, 75]

Watson, D. J. and Coakley, K. S. *Paediatric CT reference doses based on weight and CT dosimetry phantom size: local experience using a 64-slice CT scanner.* Pediatric Radiology, 2010, 40(5): 693–703. [cited on page(s): 126, 130, 131]

Webb, D.V., Solomon, S.B., and Thomson, J.E.M. *Background radiation levels and medical exposure levels in Australia.* Radiation Protection in Australasia, 1999, 16(1):7–14. [cited on page(s): 21, 139]

Webb, S. *The Physics of Medical Imaging.* CRC Press (Institute of Physics), Bristol, UK, 1988. [cited on page(s): 19, 199]

WHO, World Health Organization. *ICD-10 International Statistical Classification of Diseases and Related Health Problems: 10th Revision, 2nd Ed.* Geneva, 2004. [cited on page(s): 175]

Wiest, P. W., Locken, J. A., Heintz, Philip H., and Mettler, F. A. *CT scanning: A major source of radiation exposure.* Seminars in Ultrasound, CT, and MRI, 2002, 23(5):402–410. [cited on page(s): 22, 23, 32, 153, 154]

Wise, K. N. *Solid cancer risks from radiation exposure for the Australian population.* Australasian Physical & Engineering Sciences in Medicine, 2003, 26(2):52–61. [cited on page(s): 16]

Wise, K.N. and Thomson, J. E. M. *Changes in CT radiation doses in Australia from 1994 to 2002.* The Radiographer, 2004, 51(2):81–5. [cited on page(s): 7, 21, 139]

Xu, X. G., Taranenko, V., Zhang, J., and Shi, C. *A boundary-representation method for designing whole-body radiation dosimetry models: pregnant females at the ends of three gestational periods - RPI-P3, -P6 and -P9.* Physics in Medicine & Biology, 2007, 52(23):7023–44. [cited on page(s): 81]

Xu, X.G. and Eckerman, K.F., editors. *Handbook of Anatomical Models for Radiation Dosimetry.* CRC Press, Florida, US, 2010. [cited on page(s): 80, 81]

Yakoumakis, E., Karlatira, M., Gialousis, G., Dimitriadis, A., Makri, T., and Georgiou, E. *Effective dose variation in pediatric computed tomography: dose reference levels in Greece.* Health Physics, 2009, 97(6):595–603. [cited on page(s): 224]

Yoshizumi, T. *MOSFET CT Dosimetry Workshop: MOSFET calibration fundamentals.* Duke University Medical Center, 12-13 June 2009. [cited on page(s): 51]

Yoshizumi, T. T., Goodman, P. C., Frush, D. P., Nguyen, G., Toncheva, G., Sarder, M., and Barnes, L. *Validation of metal oxide semiconductor field effect transistor technology for organ dose assessment during CT: comparison with thermoluminescent dosimetry.* AJR. American Journal of Roentgenology, 2007, 188(5):1332–6. [cited on page(s): 35, 40, 42, 71, 72, 75, 76]

Yoshizumi, T.T., Sarder, M., Goodman, P. C., Frush, D. P., Barnes, L., and Nguyen, G. *Application of MOSFET technology in CT organ dose assessment (abst).* Medical Physics, 2003, 30:1422. [cited on page(s): 71, 76]

Zankl, M., Veit, R., Williams, G., Schneider, K., Fendel, H., Petoussi, N., and Drexler, G. *The construction of computer tomographic phantoms and their application in radiology and radiation protection.* Radiation and Environmental Biophysics, 1988, 27(2):153–64. [cited on page(s): 80]

Zankl, M., Panzer, W, and Drexler, G. *The calculation of dose from external photon exposures using reference human phantoms and Monte Carlo methods part VI: Organ doses from computed tomographic examinations.* National Research Center for Environment and Health (GSF), GSF Report 30/91, Neuherberg, Germany, 1991. [cited on page(s): 81, 82, 227]

Zankl, M., Panzer, W, and Drexler, G. *Tomographic anthropomorphic models, part II: Organ doses from computed tomographic examinations in paediatric radiology.* National Research Centre for Environment and Health (GSF), GSF Report 30/93, Neuherberg, Germany, 1993. [cited on page(s): 81, 82, 84, 85]

Zankl, M., Panzer, W., Petoussi-Henss, H., and Drexler, G. *Organ doses for children from computed tomographic examinations.* Radiation Protection Dosimetry, 1995, 57(1-4):393–396. [cited on page(s): 82, 84, 85]

Zankl, M., Fill, U., Petoussi-Henss, N., and Regulla, D. *Organ dose conversion coefficients for external photon irradiation of male and female voxel models.* Physics in Medicine & Biology, 2002, 47(14):2367–85. [cited on page(s): 86]

Zankl, M., Becker, J., Fill, U., Petoussi-Henss, N., and Eckerman, K.F. GSF male and female adult voxel models representing ICRP reference man - the present status. In *The Monte Carlo Method: Versatility Unbounded in a Dynamic Computing World.* American Nuclear Society, LaGrange Park, Illinois, US, 2005. [cited on page(s): 93]

Zhou, G. Z., Wong, D. D., Nguyen, L. K., and Mendelson, R. M. *Student and intern awareness of ionising radiation exposure from common diagnostic imaging procedures.* Journal of Medical Imaging and Radiation Oncology, 2010, 54(1):17–23. [cited on page(s): 32]